UNIVERSITY OF CALIFORNIA SAN DIEGO

The Materials Science of Skin: Experimental Characterization, Constitutive Modeling, and Tear Resistance

A dissertation submitted in partial satisfaction of the

requirements for the degree of Doctor of Philosophy

in

Engineering Sciences (Applied Mechanics)

by

Andrei Pissarenko

Committee in charge:

Professor Marc A. Meyers, Chair
Professor Shenqiang Cai
Professor Francesco Lanza di Scalea
Professor Juan C. Lasheras
Professor Michael T. Tolley

2019

The Dissertation of Andrei Pissarenko is approved, and is acceptable in quality and form for publication on microfilm and electronically:

_____

_____

_____

_____

_____

Chair

University of California San Diego

2019

DEDICATION

This work is dedicated to my family.

TABLE OF CONTENTS

LIST OF FIGURES

LIST OF TABLES

ACKNOWLEDGEMENTS

First and foremost, I would like to thank my advisor, Professor Marc André Meyers, for giving me the opportunity to spend my graduate studies in his group, and to conduct the research work that is presented in this dissertation. Your endless enthusiasm for science and discovery was a true inspiration for me, as well as the energy that you continue to infuse in every aspect of your life.

I want to thank my esteemed committee members Profs. Shenqiang Cai, Francesco Lanza di Scalea, Juan Lasheras, Michael Tolley, as well as Vlado Lubarda for their support, their time, and their valuable insights, which considerably improved the quality of my research. Prof. Cai, thank you for the time that you have allocated for me during some of our meetings, with advice that was instrumental to the success of my research. Prof. Lubarda, thank you for your kind support, and for the fruitful discussions we had together.

In the Meyers group, I was very fortunate to work and collaborate with some wonderful colleagues, from whom I have learnt a lot and that I am now glad to have as friends. I want to thank Dr. Vincent Sherman and Dr. Eric Hahn for everything they have done to make me feel welcome and integrated in the group, from the very beginning. The work we published on eggshells is, ironically, still my most successful contribution to this day! I am also grateful to Dr. Andrew Marquez, Dr. Tarah Sullivan, Dr. Bin Wang, Dr. Zezhou Li, Dr. Haocheng Quan, Rachel Flanagan, Audrey Velasco-Hogan, Josh Pelz, Gaia Righi, and Boya Li. Tarah and Bin, thank you for including me in some of your fascinating projects. Haocheng, thank you for going out of your way so many times to help me with microscopy imaging. We have traversed many challenges together, which forged our friendship and made us stronger. Dr. Wen Yang, thank you for being an exemplary collaborator, and mentor. I have truly learnt many valuables lessons

working by your side. Rachel and Audrey, your constant support and your kindness helped make some days feel more cheerful in some difficult times. I should also thank other collaborators and visitors of the group, with whom I have worked on several enriching projects. Jae-Young, your dedication to your work and your efficiency always impressed me, and I am thankful I got to learn from you and help you in the context of the woodpecker project. In this same project, collaborating with Prof. Pablo Zavattieri was a truly enriching experience; thank you for your more than enthusiastic support during this period. Carlos Ruestes, the value of the help and the support you provided throughout my graduate studies extends far beyond the work we produced on the collagen modeling project, thank you for being available, understanding, and human (!). Much of the microscopy imaging that we have obtained would have not been feasible without the precious help of Mason Mackey at the NCMIR, and Jennifer Santini at the BML. Lastly, I am thankful I got to share some good times and discussions with Zida "Kotachi" Liu, Keyur "KCB" Karandikar, Katya Evdokimenko, Marine Lapeyriere, Louis Guibert, and Boris Poyer.

Throughout my studies, for the skin project, I had the privilege to conduct research work at the Cavendish Laboratory at the University of Cambridge. This has been an inestimable opportunity, through which I got to work with some of the brightest researchers I have met. Special thanks to Dr. Kate Brown, for doing an incredible job at coordinating our "pig weeks". Your resourcefulness, kindness, and contagious optimism strengthened my beliefs in the quality of the research we produced. The success of our project would have not been possible without the help of the many people that made sure that we could have access to all the resources and facilities we needed. This includes Dr. Ben Butler (and his wife Krysa), Dr. Alun Williams, Dr. Bill Proud, Dr. Richard Langford, Andy Rayment, JJ Rickard, Eric Tapley, and Dr. Dan Tucker.

None of this would have been possible without the kind support of Profs. Ravichandran at Caltech, and François Hild and Pierre-Alain Boucard at the École Normale Supérieure de Cachan, that believed in me in very early stages of my research career, and helped me achieve goals I did not think were possible at the time.

Of the many things I learnt at UCSD, studying Portuguese has been a fantastically enriching experience. With a very dense scientific workload, these classes were a breath of fresh air in my curriculum. I am grateful to Denise Paladini and Cassia de Abreu for showing me how much I could learn in just a couple of years, and for strengthening my passion for Brazilian culture and for the people that represent it.

I want to use this opportunity to thank the wonderful new friends that I was lucky to meet at UCSD, and more generally in San Diego. You gave me the feeling of a family away from home, and I will never be thankful enough for this precious gift. Marghe, thank you for being the best friend I could hope for in this moment of my life, and for always anchoring me back to reality. Lorenzo, you are a caring and trustworthy friend, which I will always value. Keep the fire alive. Handa, your boundless positivity (except of course, when we go on our infinite rants) always propagates to others, and I'll always remember how we rescued my car from Victorville. Martina, your selfless dedication to your work and to others is something that we probably did not recognize enough at the time, and I wish that you find your balance. Jen, thank you for being the best roommate and cooking buddy I could have hoped for, I am so proud to see how much you have grown. Oytun, your ability to make things happen will always impress me, and I will fondly remember our long dinners at the "Villa Lamont". Ryan, I know that behind your reserved personality lies a true, genuine, kind heart. Thanks to Marine T., with whom we've shared countless memorable moments. Alice S., Vava , Elsa, Ludo, Alex B., Simone T., and

Andrew, thank you for being amazing friends. Olesya, Maya, and Anya, you have more than once shown your unconditional support, and have always been a sympathetic ear that I could rely on. My gratitude also goes to my extended Italian family: Alessandro, thank you for how much you have shared with us, and for helping me out in very difficult times. Mattia, your generosity and authenticity are qualities that I sincerely admire in you as a friend. Valeria, you are truly one of a kind. I am proud and thankful for all the moments we all shared together.

Ice hockey and beach volleyball were important activities that helped me stay healthy and focused during this very demanding experience. I am very thankful for all the great people I encountered through them. Many thanks to Mike Duffey, who was kind enough to give me time to play, and to the Baked Warrior and Silver Fox teams. We didn't win the Mall Cup, but we had a lot of fun. Phil Yeung, I have no words to express my gratitude for how much effort you put into each one of us and to doing the things you love, without ever expecting anything in return. You are an inspiration to all of us at the "Saturday Gentleman's Club"; my gratitude extends to all its members as well.

My adventure in the US started initially with my time at Caltech, and the friendships I forged during this period and during my repeated trips to Los Angeles proved to be long lasting ones. Thibault, it's incredible to reflect on how many times our paths have crossed. It's even more incredible to see how much dedication you put in pursuing your dreams; I am extremely proud and happy for you that you landed that position at JPL. Murat, my brother, it's hard to find words to describe how far our friendship extends, and how much it means to me. I am thankful for the countless memories we share, the battles we fought together on the court (and outside of it), and for the challenges we faced with each other's support. Laura, you are truly a magical being. I will never be grateful enough for everything you have done for me, and in

proving how meaningful our friendship was to you. You gave me one of the best birthday celebrations of my life.

To Baptiste, Igor, and Blanche, who crossed the pond to visit me in San Diego: thank you for letting me share a bit of my California experience with you.

Yana, your unconditional love and support, and the beliefs you placed in me gave me the wings I needed to fly. Words cannot express how thankful I am that you have always been there for me, patiently, despite all the sacrifices you and I had to make. We did this together, my love.

Last but not least, my infinite gratitude and love goes to my family. Mama, Papa, thank you for all the sacrifices you have made over the years to make sure I could always reach my ambitions. Thank you for giving me the best education I could hope for. Vania, thank you for finally coming to visit me, this meant a lot. I hope that I am making you proud. This work is also dedicated to my grandparents, whom I love dearly.

Financial support is key to the success of this work. The work presented in this dissertation was supported principally by a Multi-University Research Initiative through the Air Force Office of Scientific Research of the United States (AFOSR-FA9550-15-1-80009).

Chapter 1, in full, has been submitted for publication of the material as it may appear in Progress in Materials Science, and is authored by A. Pissarenko and M.A. Meyers. The dissertation author was the primary investigator and author of this paper.

Chapter 2, in full, is published in Acta Biomaterialia and is authored by A. Pissarenko, W. Yang. H. Quan, K.A. Brown, A. Williams, W.G. Proud, M.A. Meyers. The dissertation author was the primary investigator and author of this paper.

Chapter 3, in full, has been submitted for publication of the material as it may appear in Acta Biomaterialia, and was authord by A. Pissarenko, C.J. Ruestes, and M.A. Meyers. The dissertation author was the primary investigator and author of this paper.

Chapter 4, in full, is currently being prepared for submission for publication of the material, and is authored by A. Pissarenko, W. Yang, H. Quan, B. Poyer, K.A. Brown, A. Williams, and M.A. Meyers. The dissertation author was the primary investigator and author of this paper.

VITA

2019 Ph.D. Engineering Sciences (Applied Mechanics)

University of California San Diego, La Jolla, CA

Dissertation: The materials science of skin: experimental characterization, constitutive modeling, and tear resistance

Advisor: Professor Marc A. Meyers

2015 M.Res. Bioengineering

Imperial College of London, UK.

2014 M.S. Mechanical and Materials Science Engineering

École Normale Supérieure de Cachan, France

2012 B.S. Applied Sciences

École Normale Supérieure de Cachan, France

PUBLICATIONS

Pissarenko A, Yang W, Quan H, Poyer B, Brown KA, Williams A, Meyers MA, The toughness of porcine skin: quantitative measurements and microstructural characterization. In preparation.

Dike S, Yang W, Quan H, Pissarenko A, Meyers MA, On the Gular Sac Tissue of the Brown Pelican: Structural Characterization and Mechanical Properties. In preparation.

Pissarenko A, Ruestes CJ, Meyers MA, Constitutive description of skin dermis: through analytical continuum and coarse-grained approaches for multi-scale understanding. Submitted.

Pissarenko A, Meyers MA, The materials science of skin: analysis, characterization, and modeling. Submitted.

Pissarenko A, Yang W, Quan H, Brown KA, Williams A, Proud WG, Meyers MA, Tensile behavior and structural characterization of pig dermis. Acta Biomaterialia, vol 86, pp 77-95, 2019.

Jung J-Y, Pissarenko A, Trikanad AA, Restrepo D, Su FY, Marquez A, Gonzalez D, Naleway SE, Zavattieri P, McKittrick J, A natural stress deflector on the head? Mechanical and functional evaluation of the woodpecker skull bones. Advanced Theory and Simulations, 1800152, 2019.

Wang B, Sullivan TN, Pissarenko A, Zaheri A, Espinosa HD, Meyers MA, Lessons from the Ocean: Whale Baleen Fracture Resistance. Advanced Materials, 1804574, 2018.

Jung J-Y, Pissarenko A, Yaraghi NA, Naleway SE, Kisailus D, Meyers MA, McKittrick J, A comparative analysis of the avian skull: Woodpeckers and chickens, Journal of the Mechanical Behavior of Biomedical Materials, vol 84, pp 273-280, 2018.

Hahn EN, Sherman VR, Pissarenko A, Rohrbach SD, Fernandes DJ, Meyers MA, Nature's technical ceramic: the avian eggshell. Journal of the Royal Society Interface, vol 14, 126, 2017.

Sullivan TN, Pissarenko A, Herrera SA, Kisailus D, Lubarda VA, Meyers MA, A lightweight, biological structure with tailored stiffness: The feather vane. Acta Biomaterialia, vol 41, pp 27-39, 2016.

ABSTRACT OF DISSERTATION

The Materials Science of Skin: Experimental Characterization, Constitutive Modeling, and Tear Resistance

by

Andrei Pissarenko

Doctor of Philosophy in Engineering Sciences (Applied Mechanics)

University of California San Diego, 2019

Professor Marc André Meyers, Chair

Skin is the outermost layer of the body and acts as a primary protective barrier against external agents such as heat, light, infection, and injury. Additionally, skin regulates a broad range of physiological parameters and hosts several vital components. In order to fulfill these functions throughout life, skin must be able to withstand and recover from significant deformation as well as mitigate tear propagation that can occur during growth, movement, and

injuries affecting its integrity. Hence, characterizing the mechanical behavior of skin and understanding the underlying mechanisms of deformation at different spatial scales is essential in a large spectrum of applications such as surgery, cosmetics, forensics, biomimetics and engineering of protective gear or artificial grafts.

In this dissertation, a comprehensive list of experimental techniques that have been developed over the years to test skin's nonlinear elastic, viscoelastic, and dissipative properties are reviewed. To identify parameters affecting its behavior, a significant number of models have been developed, some of which are detailed here. The principal structural elements within the dermis, and especially the arrangement and orientation of the collagen fibrils and fibers, are presented; their incorporation into the constitutive models is discussed.

We conduct a detailed investigation of the evolution of the collagen architecture of the dermis as a function of deformation, which reveals new aspects that extend our understanding of the mechanical response of porcine skin. The dermis is found to have a tridimensional woven structure of collagen fibers, which evolves with deformation. After failure, we observe that the fibers have straightened and aligned in the direction of tension. Time-dependent and dissipative effects are quantitatively established. Digital image correlation techniques were implemented to quantify skin's anisotropy; measurements of the Poisson ratio and their evolution are reported for the first time. Based on new observations, we propose that fiber braiding is at least partially responsible for the monotonic increase of the tangent modulus of skin with strain, as well as its dissipative response to cyclical loads.

We incorporate these findings in a constitutive framework incorporating fibril stiffness, interfibrillar frictional sliding, and the effect of lateral fibers on the extension of a primary fiber, using analytical and coarse-grained modeling approaches. The representation of these important

physical processes that occur during deformation of the dermis represents an advance in our understanding of these phenomena.

Finally, we estimate the toughness of porcine skin by conduct two types of experiment on pre-notched specimens, placing the tissue under shear Mode III and opening Mode I. We obtain two distinct toughness values of $J_{IIIc} \approx 20.4\ kJ/m^2$ and $J_{Ic} = 30.4\ kJ/m^2$, indicating notable differences between these two modes of crack propagation. Digital image correlation is used to plot strain profiles around the tip of the crack, from which a strain-based criterion for crack propagation is established. The evaluation of the structure at the crack tip and regions undergoing more uniform states of deformation is conducted by *ex situ* transmission electron microscopy and *in situ* environmental scanning electron microscopy.

CHAPTER 1. MECHANICAL BEHAVIOR, STRUCTURE, AND CONSTITUTIVE MODELING OF SKIN: A REVIEW

1.1. Introduction

1.1.1. Functions and Structure of Skin

For most vertebrates, skin is the outermost layer of the body and acts as a first protective barrier against external agents such as heat, light, infection, and injury. It is also an important interface with our environment, hosting a myriad of sensors, glands, channels, and pores that enables organisms to feel touch, heat, pain, regulate their body temperature and hygrometry [1].

Its structure can be decomposed into three main regions, and it described by the schematic in Figure 1.1. The epidermis (50 μm -150 μm in thickness [2–4] for humans) is the external layer of the skin, and mainly fulfills the function of a barrier and exchange interface with the exterior [5]. Constant renewal and growth occurs in its sublayers where stem cells in the inner stratum basale differentiate into keratinocytes, which then migrate outwards and eventually decay as corneocytes, forming the stratum corneum, a tough keratinized layer [1,6]. The dermis (150 μm to 4 mm in thickness for humans [7,8]) supports the epidermis by providing it with nutrients and structural support via the papillary dermis, where wavy ridges facilitate exchanges. The reticular dermis comprises a variety of sensors, glands, and vessels, and accounts for most of the skin's mechanical properties in tension via a layered and dense arrangement of wavy collagen fibers (~60-80% of dry tissue weight), transverse straight elastin fibers (~1-4% of dry tissue weight), all embedded in a proteoglycan matrix commonly referred to as the ground substance [7–9]. The hypodermis (or subcutaneous layer) is the innermost layer of skin and is mostly composed of adipose tissue, in which adipocytes form clumps called

lobules, surrounded by a fibrocollagenous network. Its main functions are to provide thermal insulation, store energy, and absorb shocks [7,8]. Its loose connective tissue structure also enables it to minimize friction with neighboring muscle tissue. Its thickness varies greatly depending on the region of the body and the subject.

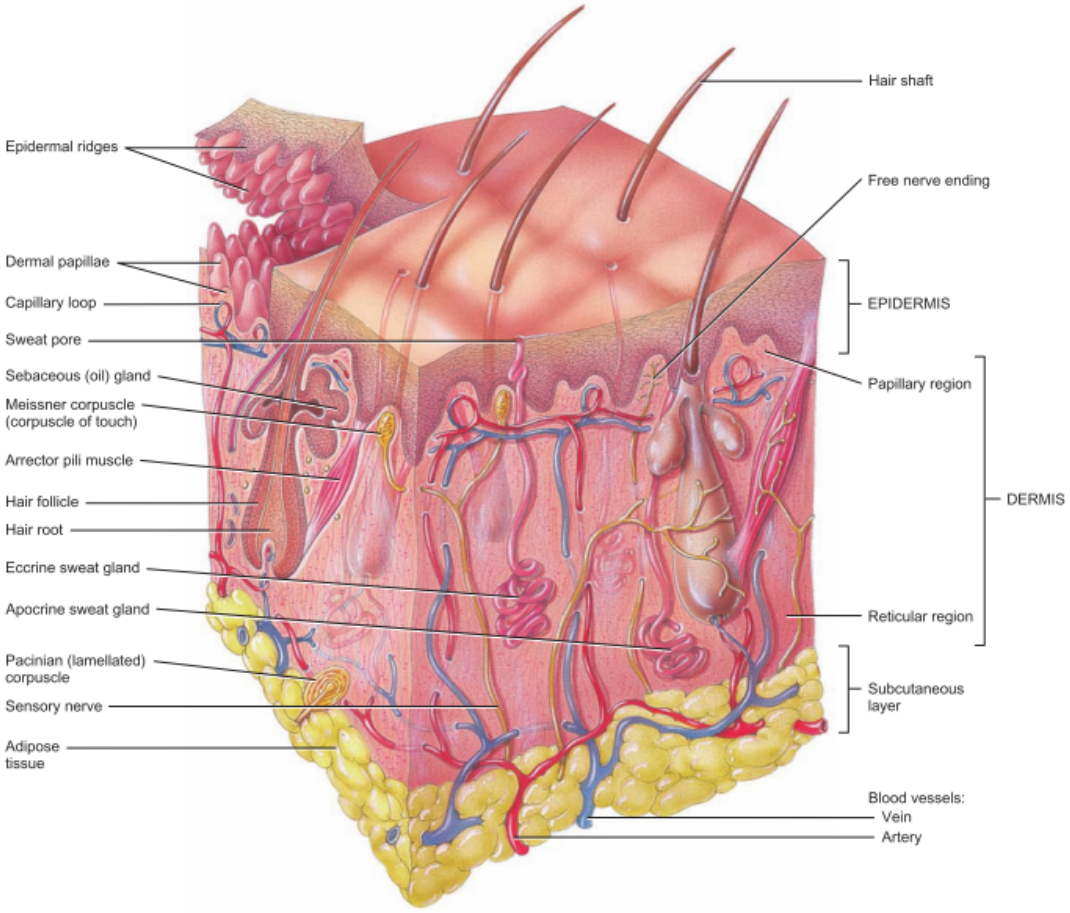

Figure 1.1 Rendering of the cross-section of mammal skin, showing the diversity of functional elements and structures present in the different layers. Dimensions and density vary among species, individuals, and genders. Note that proportions between different components is not maintained for the sake of clarity. Reprinted from [1].

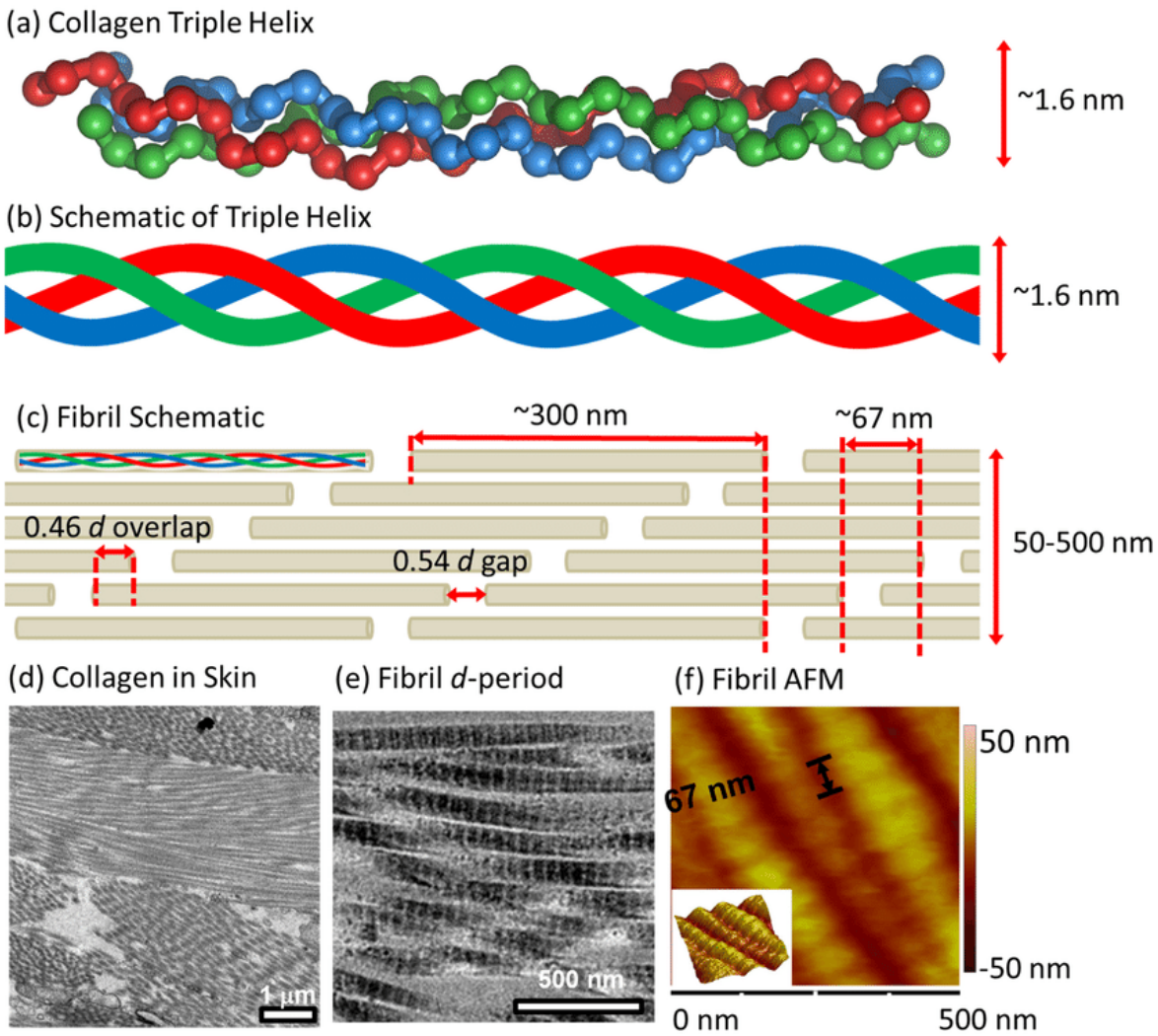

Figure 1.2. The full hierarchy of collagen in the dermis. (a,b) Tropocollagen chains form right handed triple helices. (c) Tropocollagen molecules form a quarter-staggered arrangement, with a characteristic d-period of 67 nm. This footprint of collagen fibrils makes them easily recognizable under Atomic Force Microscopy (AFM) (f) or Transmission Electron Microscopy (TEM) (e). (d) TEM of rabbit skin also shows collagen fibrils bundled together into fibers, with a circular/elliptical cross section and a high fibril density. Reprinted from [10].

Thus, skin can be considered a layered composite material [11], where, from a mechanical viewpoint, each layer fulfills a certain function: the hard keratinized surface of the epidermis enhances toughness, the dermis provides load-bearing [9] properties, the hypodermis provides shock absorption. In the case of tensile behavior, the dermis is the main contributing layer, and understanding the structural arrangement of its constitutive elements is a key factor towards describing the response of skin. Figure 1.2 shows the different structural levels of collagen fibers, exemplified here for rabbit skin. Starting with polypeptide chains formed in a triple-helix arrangement, tropocollagen molecules have a length of ~ 300 nm and a diameter of ~ 1.5 nm. These macromolecules arrange themselves into collagen fibrils, characterized by a d-period of 67 nm, which is the defining structure of collagen. The fibrils have diameters of ~ 50-300 nm and are organized into fibers with parallel fibrils, forming bundles with diameters ranging ~ 2-7 μm. At this organizational level the complexity of the arrangement is less well understood. Many models of skin tend to neglect out-of-plane components of the collagen network, suggesting a layered disposition, as in the work on rabbit skin of Sherman et al. [12]. On the other hand, Jor et. al [13] reported that collagen fibers in pig skin form a dense three-dimensional network with average angles of $\pm 45°$ with the surface of the skin (Figure 1.3). It is also likely that arrangements vary from species to species.

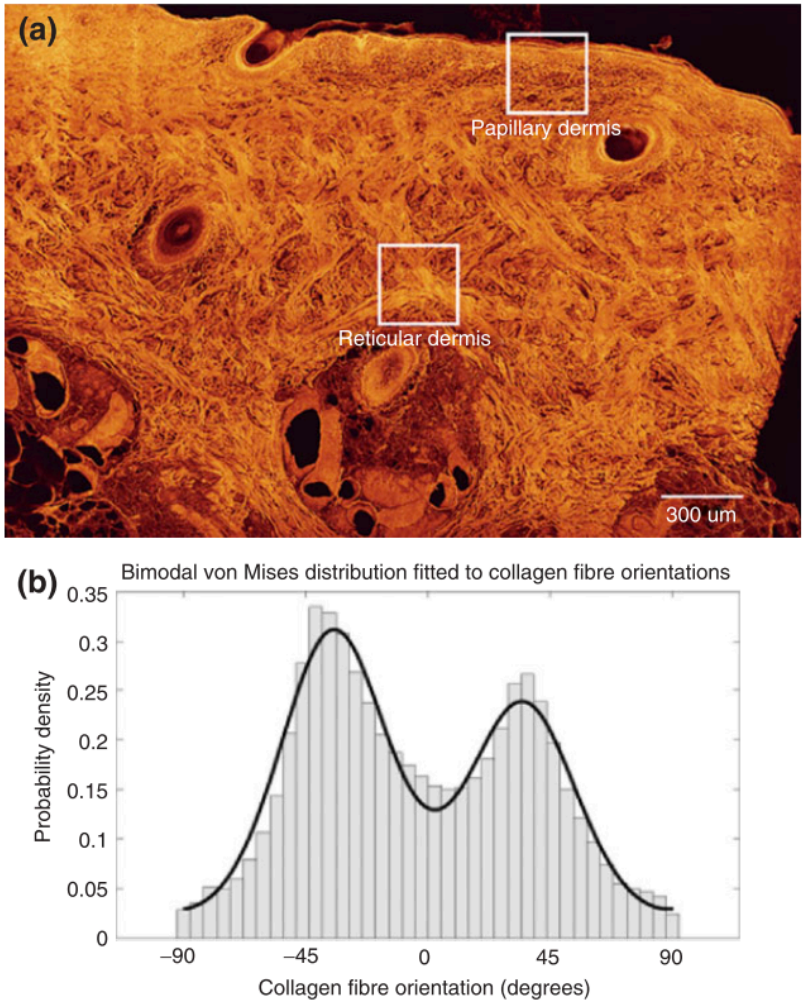

Figure 1.3.(a) Cross-sectional view of a pig skin sample using Confocal Microscopy, (b) A bi-modal analysis shows that the collagenous network in this plane seems to be organized in a lattice arrangement, with preferred angles $\pm 45°$. From Jor et al. [13].

In Figure 1.4, the structural arrangement of collagen fibers and collagen fibril size distributions in skin is compared with two other collagenous tissues: tendon and pelican pouch. On one hand, fibers in tendon form larger scale fascicles, and are highly aligned along the principal axis of the tissue, as the scanning electron micrograph Fig 1.4a and the optical micrograph Fig. 1.4b show [14,15]. Fibril diameter, as seen in the transmission electron micrograph of the cross-section of a human tendon Fig. 1.4c [16], follows a bimodal distribution

with an even repartition. The waviness and interweaving of collagen fibers in the dermis of pig skin is illustrated again in Fig. 1.4d-e. The cross-section of a collagen fiber in the dermis shows a more consistent distribution of collagen fibril diameters [17]. On the other hand, pelican pouch is an example of a soft tissue with a high level of collagen fiber curvature, as presented Fig. 1.4g-i, which considerably enhances the extensibility of the material, up to 400% (Dike S, unpublished data). The bimodal distribution parameters of collagen fibril diameters for five types of tendon in humans [16], pig skin [17], and pelican pouch are reported in Table 1.1. The bimodal fit corresponds to the following distribution function:

$$f(x) = \frac{A_S}{\sqrt{2\pi\sigma_S^2}} \exp\left(-\frac{(x-\mu_S)^2}{2\sigma_S^2}\right) + \frac{A_L}{\sqrt{2\pi\sigma_L^2}} \exp\left(-\frac{(x-\mu_L)^2}{2\sigma_L^2}\right) \quad (1.1)$$

With parameters A_S and A_L, the peaks of the small and larger diameter distributions, respectively, μ_S and μ_L the corresponding means, and σ_S and σ_L the standard deviations. The bimodal ratio $R = A_L/A_S$ can also be introduced. It gives information on the repartition between small and larger fibrils. For tendons, it varies between 0.82 and 3.34, hence the proportion is either even or in favor of larger diameters, which can go up to 125 nm for the mean value. Collagen fibrils in the pelican pouch have a significantly larger diameter, with 102 nm for μ_S and 171 nm for μ_L. Mean values μ_S and μ_L are often 50-70 nm apart and vary considerably across tissues. Skin falls in the middle, however large diameters are much rarer (16%) than smaller fibrils, with also narrower standard deviations, indicating more consistency in fibril size, as shown Fig. 1.4f. Skin is therefore a tissue with relatively curved collagen fibers, which contribute to its nonlinear elasticity, formed by bundles of collagen fibrils with a quite consistent diameter.

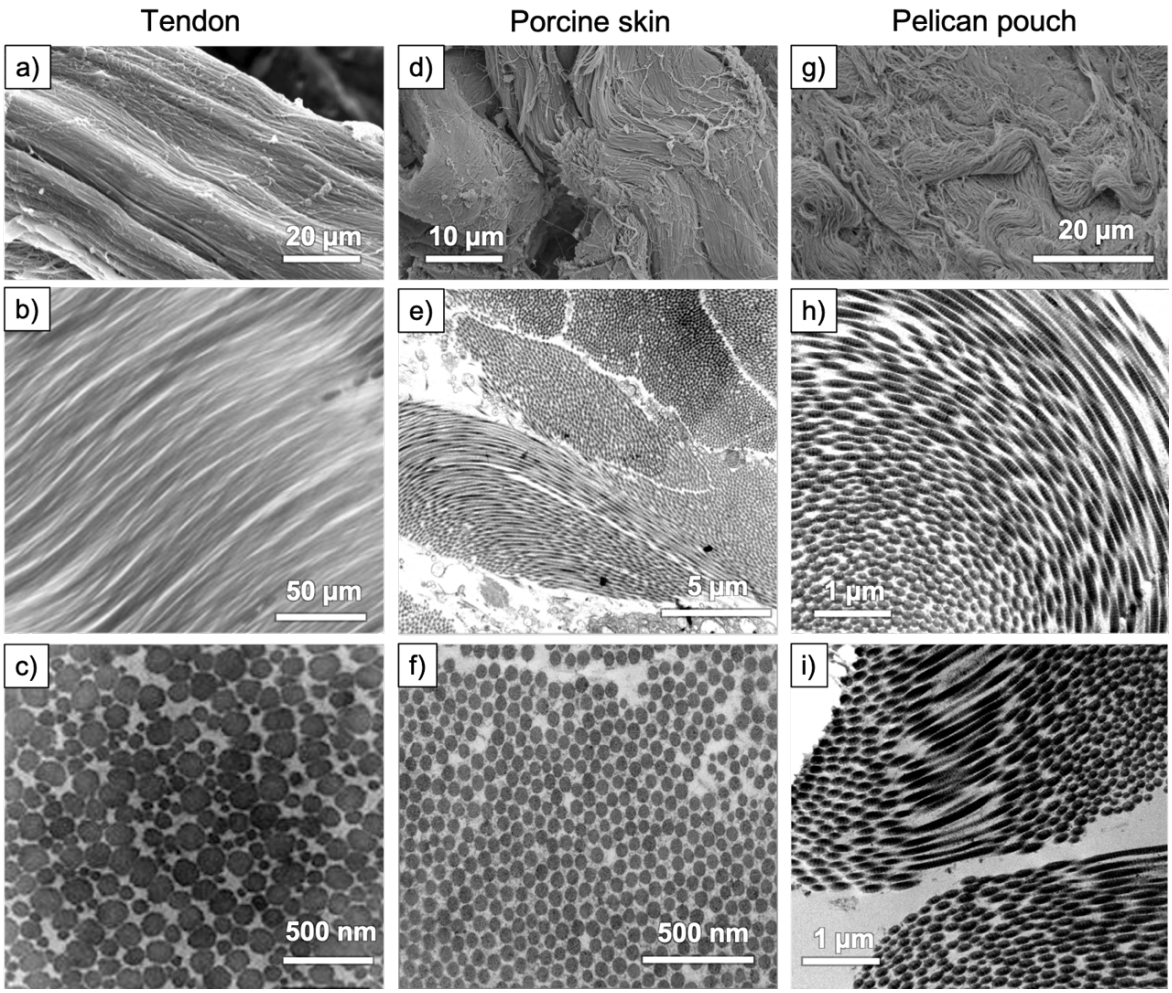

Figure 1.4.Comparison of collagen fiber arrangements in tendon, porcine skin, and pelican pouch. (a) Scanning electron micrograph (SEM) of human tendon [14] and (b) optical micrograph [15] of rat tendon in the longitudinal direction, showing a consistent alignment of fibrils. (c) Transmission electron micrograph (TEM) of a cross-section of a collagen fiber from human patellar tendon, showing a significant variation of collagen fibril diameter [16]. (d) SEM and (e) TEM of porcine dermis in the longitudinal section, showing highly curved collagen fibers going in and out of plane. (f) TEM of a cross-section of a collagen fiber in the dermis. The fibril diameter distribution is more consistent [17]. (g) SEM and (h) TEM of the pelican pouch skin in the longitudinal direction and (i) in the transverse direction. Collagen fibers show a much higher degree of curvature, as well as a bimodal distribution of fibril diameters (Dike S, unpublished data).

Table 1.1. Distribution parameters of collagen fibril diameters reported for human tendon (patellar, quadriceps, semitendinosus, ITB, ACL) [16], pig dermis [17], and pelican pouch (unpublished data). A bimodal distribution is assumed. Parameter R corresponds to the bimodal ratio, i.e. the ratio between the amplitudes of the large diameter peak A_L and the smaller diameter peak A_S.

Tissue		μ_1 **(nm)**	σ_1 **(nm)**	μ_2 **(nm)**	σ_2 **(nm)**	**R**
Tendon	Patellar	52.25	17.64	110.6	32.77	0.82
	Quadriceps	58.73	17.31	114.2	18.45	0.77
	Semitendinosus	75.16	34.44	124.6	23.01	1.32
	ITB	59.74	7.97	70.2	21.84	1.22
	ACL	61.08	13.2	66.94	25.88	0.87
Pig dermis		77.11	8.31	115.5	6.88	0.16
Pelican pouch		102.07	22.28	170.62	23.18	0.46

The organization of elastin in the dermis of skin is reported more rarely, mainly because of its low volume fraction in skin. It appears as straight fibrils, transversely connecting collagen fibers [18,19], as seen in the confocal image of pig skin, on Figure 1.5. As pointed out by Pittet et al. [19], the volume fraction of elastin decreases with age. Elastin fibers in older tissues become thicker and more fragmented, and show a greater affinity for calcium, affecting their ability to withstand large deformations [1].

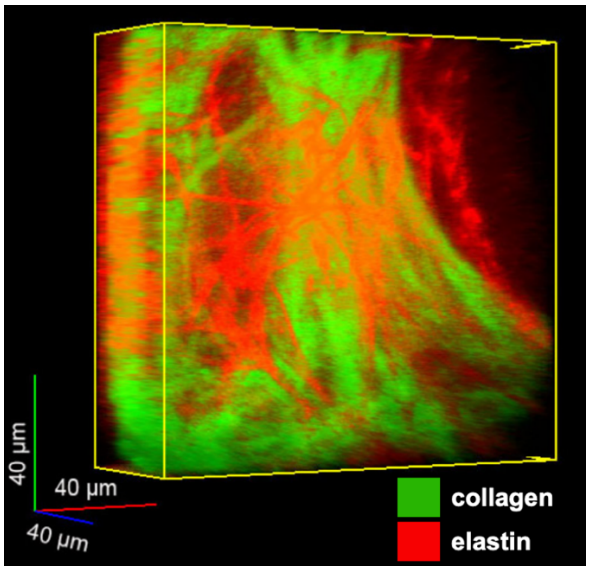

Figure 1.5. Multiphoton tomography of young human skin, showing collagen fibers in fluorescent green, and elastin in red. Elastin fibers are straight and thin, and interconnect collagen fibers transversely. From Pittet et al. [19].

1.1.2. On the Relevance of Studying Skin

Throughout life, skin must be able to withstand significant deformations, shocks, and mitigate propagation of tears that can occur during growth, movement, or injuries. Therefore, understanding the mechanisms of deformation at different spatial levels can be essential in areas ranging from cosmetics, surgery, forensics, armor design, and to biomimetic skin grafts, where our expanding knowledge can be extensively applied to improve current methods.

A classic example is the Pfannenstiel-Kerr incision [20], a C-section surgical procedure, performed in the transverse direction (perpendicular to the spine). It results in a reduction of the incised area and minimizes bleeding, and consequently in a decrease of the mortality rate of both mothers and their newborns, as well as in reduced scar tissue formation. Such improvements were partially made possible by the earlier discovery of Langer lines. First observed by anatomist and surgeon Guillaume Dupuytren in 1831, they were further characterized by Dr. Karl Langer in 1861 [12,21,22]. Both observed that by stabbing a cadaver using a stylet with circular cross-section in different locations of the body, the wound would stretch in one preferred direction and become elliptical, showing for the first time pre-existing axes of tension, and therefore defining skin's anisotropy and ability to adapt to loads; thus, the Langer lines. Said lines were later mapped for the human body by Cox [23] (see Figure 1.6), but can also be encountered in other species [24,25].

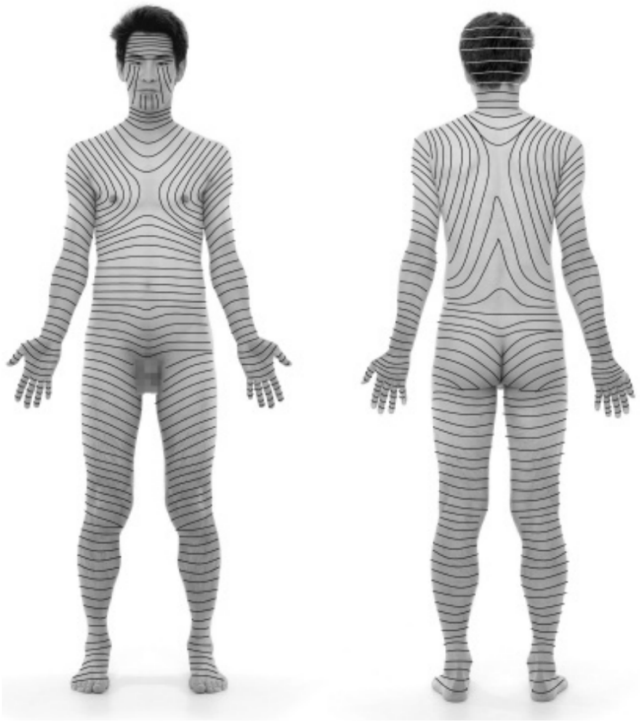

Figure 1.6. Langer lines indicating the direction of alignment of the collagen fibers. From Meyers and Chen [21].

The reduction of scar tissue formation is a vastly studied topic in plastic surgery and has known great improvements over recent years, thanks to an accrued knowledge of skin's mechanobiology [26]. New techniques involve stress-relieving implants or bandages that condition the mechanical environment of the healing region [27–29]; some of these solutions are presented in Figure 1.7. Recently, synthetic skin grafts have also been a flourishing area of research [30–33], where significant progress can be correlated with advances in tissue engineering and additive manufacturing.

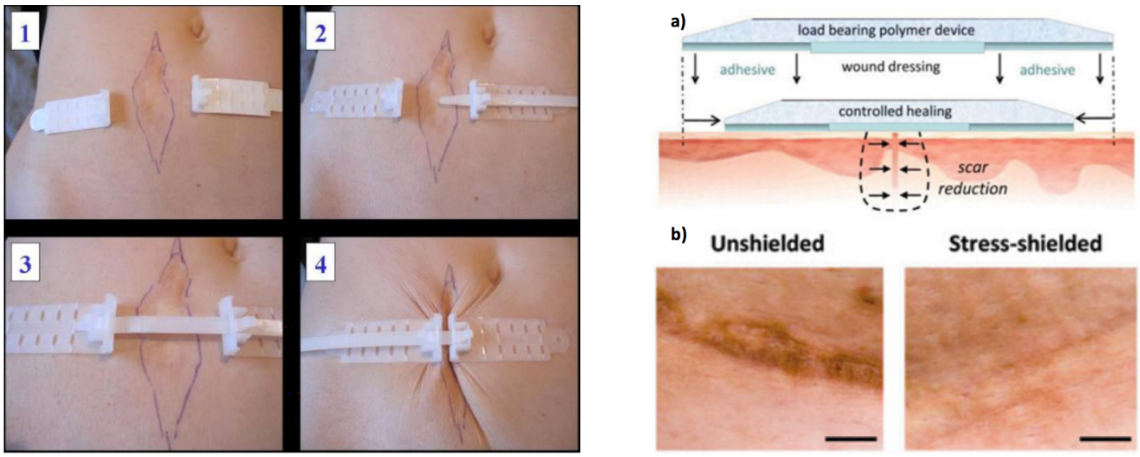

Figure 1.7. Examples of recent technologies to minimize scar tissue formation by locally relieving stress in the healing region. Left: TopClosure device (http://www.topclosure.com), where the healing scar is transversely closed by a pair of glued (or stapled) plates tied by a strap. Right: (a) Schematic illustration of the Stress-shielding device developed by G. Gurtner et al. [28,29]. The bandage-like taunt is placed after removal of sutures and applies a uniform compression on the wound. (b) Comparison of unshielded and shielded wound healing on swine skin; the scar is much less apparent in the stress-shielded cut.

Wearable devices are also a developing industry, aiming to improve self-monitoring of health indicators, varying from sports activities to the auto-regulation of chronic diseases [34,35]. Such advances have required the development of models of skin mechanics, either based on phenomenological observations or physical descriptions of the tissue. An important step of this process is characterizing the deformation mechanisms at different length scales such as macroscopic tensile tests, or microscopic observations.

The present chapter draws a non-exhaustive summary of the experimental techniques that have been implemented to characterize the behavior of skin under different types of loading, at a macroscopic scale. Tensile properties and testing (direct and indirect) are mainly emphasized because it is the most important and frequent type of load that skin experiences. Compressive loading of skin is less frequently studied, and is mainly relevant to cases following impact or blast injury. Second, associated models that have been developed based on these observations are discussed, outlining their strengths and limitations. A better understanding of the deformation mechanisms can be gained by taking a closer look at the microstructure of skin.

Although a valuable amount of work has been done on the properties of the epidermis, and more particularly the *stratum corneum*, our review is limited to the microstructure of the dermis, considered to account mostly for skin's mechanical behavior, especially at large strains. The current knowledge of the hierarchical arrangement of the forming components of skin constitutes a basis for physical models of skin mechanics, which use nano and microstructural features to describe the macroscale behavior.

1.2. Experimental Characterization of Skin Mechanics

Skin is an anisotropic, nonlinear, viscoelastic, tissue and subject-specific material, which consequently yields highly variable experimental results. Rodrigues [36] reported that measured values of the Young's modulus of human skin with *in vivo* tests can differ by four orders of magnitude. One main cause of variability is the lack of test standardization. Moreover, the Young's modulus is a measure of linear elasticity, which is not appropriate for a nonlinear material like skin. Studies in the literature generally report a local measurement of the slope of a given portion of the stress-strain curve, which we will refer to as tangent modulus further on.

Methods can vary by sample and setup size, sample attachment or gripping, the region that is tested, or whether the sample is preconditioned. Preconditioning was first introduced by Fung [37] and corresponds to a cyclic load applied at low strains until the tissue response becomes reproducible. This potentially reduces inter-sample variations due to relative orientation or pre-stress. Applied deformations cover continuous stretching, cyclic loading, relaxation, and creep, and are used as methods to characterize skin's nonlinear elasticity, viscoelasticity, and dissipative behavior.

Experimental testing of mammal skin can be categorized into two distinct methods: *in vivo* and *ex vivo* setups, where the sample is either tested directly on the subject, or excised from it

prior to testing, respectively. Among tested species we can find mice [38], rats [39,40], rabbits [12,41,42], swine/pigs (often preferred for the similarity of their skin with humans) [11,26,43–51], humans [46,52–82], cattle [83], and rhinoceros [84]. For obvious ethical restrictions, non-invasive *in vivo* testing is usually favored, especially for the characterization of human skin, yet *ex vivo* data on humans can also be found in the literature (where skin is excised from cadavers or surgical flaps), and provides more rigorous results in simple kinematics and geometries. These methods are discussed in the following section.

1.2.1. *In Vivo* Testing of Skin

One main advantage of *in vivo* experiments is that they are non-destructive, which ensures repeatability of tests and accessibility of samples with fewer ethical restrictions. Another important aspect is that skin *in vivo* is in its natural configuration, undergoing tensile loads dictated by its environment (along the Langer lines) and interfaces with other organs in the body. However, this is limited by the fact that damage and failure cannot be observed, which reduces the span of the obtained stress-strain curves. Also, sample accessibility is restricted, such that only methods contacting skin superficially can be applied.

1.2.1.1. Extensometry

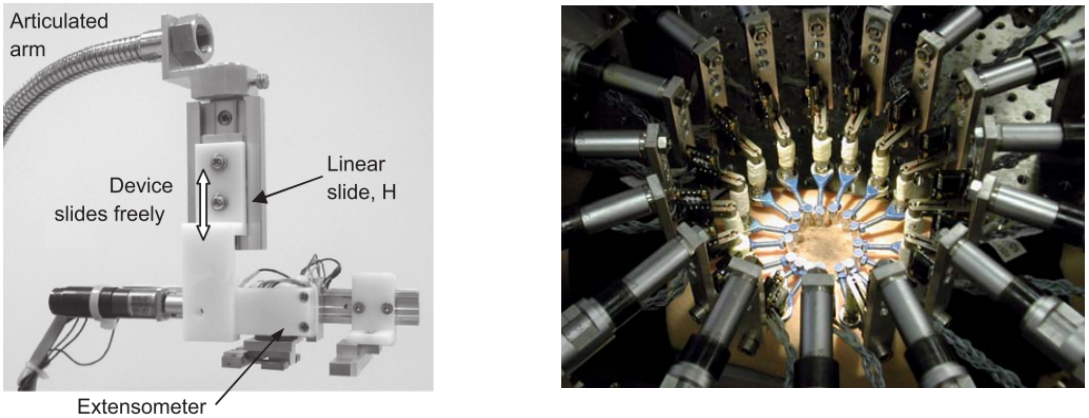

Figure 1.8. Left: Uniaxial shield pad extensometer developed by Lim et al. [46]. Right: Multiaxial extensometer setup used by Kvistedal et al. [59].

Classically, the principle of extensometry is to apply a relative displacement (either positive or negative) between two or more pads that are fixed on the surface of the tested material and to measure the resulting force (Figure 1.8.left). Mechanical properties of skin *in vivo* have been tested in uniaxial [85–87] and multiaxial geometry (Figure 1.8.right) [59]. Improvements of such systems also include the addition of circumferential shield guards [46], which minimize the effects of peripheral forces from the skin surrounding the tested region, or coupling with optical [59] or ultrasonic [88] tools to increase the accuracy of the measured deformation.

Tests can be run at low strain rates, and the obtained force-displacement curves can be used to compare variations due to changes in tested location or orientation. Because gauge dimensions in the *in vivo* configuration are difficult to estimate, quantitative assessment of the mechanical properties is often limited to linear or areal parameters [46,85], unless image-based strain calculation methods [59], or numerical simulations [46] are implemented.

Another extension of this method is the recent use of triaxial force-sensitive micro-robots. Flynn *et al.* [66,73] developed a protocol where a robotic probe is glued to the skin and applies a set of pre-defined deformations; a three-dimensional arrangement of force transducers allows for measurement of the reaction force. The tested region is isolated using a guard ring. They used this method to apply a range of in-plane and out-of-plane cyclic displacements in order to observe orientation-related variations in dissipated viscoelastic energy, for various locations of the forearm [66], and the face [73]. Out-of-plane deformations can be also assimilated to an extension of the indentation method (see paragraph 2.1.4. of this Chapter).

1.2.1.2. Torsion

Typical torsion (or shear inducing) devices consist of a friction head placed in contact with the surface of the skin and set in rotation by an actuator [58,89–91]. An example of a commercially available device, the Frictiometer®, is presented Figure 1.9a. A normal pressure and/or an adhesive can be applied to optimize friction, and a guard ring can be used to isolate the tested region [54,61]. By applying a certain torque (or angular displacement), the skin is set in rotation in the area between the friction head (disk) and the external ring (if present). The torque-angular displacement curve thus obtained can be used to qualitatively observe the skin's viscoelastic response and compare age, gender, location, and moisture-related variations in skin's elasticity. However, because torsion tests are not conducted along one specific alignment, they cannot be used to assess anisotropy. Quantitative estimation of an elastic modulus, E, can be done using equations that have been derived for unshielded mechanical tests by Vlasblom [92] and later applied by Sanders [90]:

$$E = \frac{2M(1+\nu)}{4eR_1^2\theta} \tag{1.2}$$

and by Leveque et al. for shielded tests [61]:

$$E = \frac{M}{2\pi \cdot 0.4eR_1R_2\theta} \tag{1.3}$$

where M is the applied moment, e the estimated skin thickness, R_1 the disk radius, R_2 the guard ring radius (for shielded tests), and θ the angular rotation at R_1. In Leveque's equation, the Poisson ratio ν is estimated to be equal to 0.25. It is important to note that the above equations correspond to linear approximations of the mechanical response of skin and therefore do not fully describe its nonlinear elastic behavior.

The torsion method is a rather easy and quick technique that is not too restrictive in terms of accessibility, and has, as a result, been widely used in the context of clinical dermatology [93]. Direct measurements of the angular rotation over time (for an imposed value of the applied torque), i.e. creep tests, tend to be preferred. Specific viscoelastic parameters are used to monitor skin's response, and were initially introduced by Boyer et al. [64]:

- U_E the immediate elastic deformation,
- U_V the viscoplastic deformation,
- $U_F = U_E + U_V$ the total deformation,
- U_R the immediate retraction,
- U_R/U_F the firmness parameter,
- U_A the viscoelastic retraction.

Figure 1.9b shows a typical deformation vs. time curve from a torsion test, where the above-mentioned parameters are indicated.

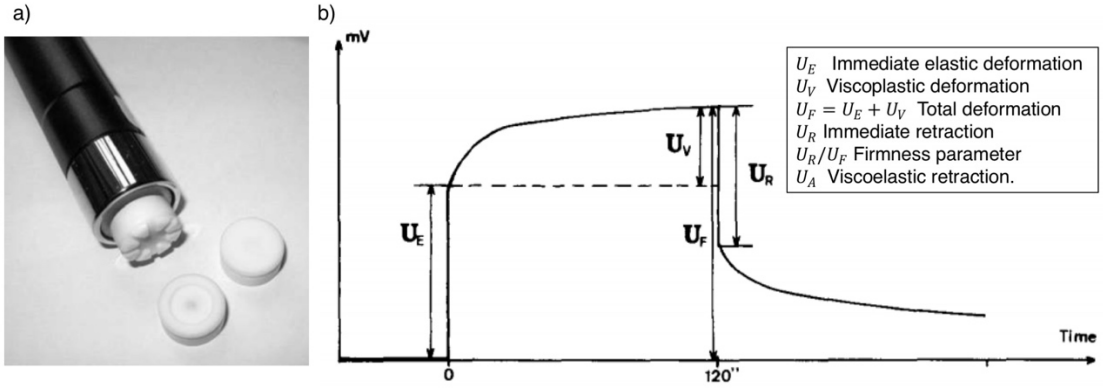

Figure 1.9. (a) Photograph of the Frictiometer® FR 700 (Courage-Khazaka, Köln, Germany), a clinically used torsion probe. (b) Typical deformation curve of a skin sample after torque application (t=0) and torque removal (t=120s) with a shielded torsion device, developed by Leveque et al. [61]. The angular displacement is linearly proportional to the measured voltage.

1.2.1.3. Suction

First introduced by by Grahame and Holt in 1969 [94] for experiments *in vivo*, the suction method consists of applying a negative pressure through a cylindrical or hemispherical cup mounted on the tested region, resulting in an upwards deformation of a dome of skin. The height of the raised dome is compared with the suction pressure, and a stress-strain curve can be obtained using Tregear's equation [95] for deforming hemispherical domes:

$$\sigma = \frac{pR^2}{4xe}\left(1 + \frac{x^2}{R^2}\right) \tag{1.4}$$

$$\epsilon = \frac{2x^2}{3R^2\left(1 + \frac{2x^2}{R^2}\right)} \tag{1.5}$$

where σ and ϵ are respectively the engineering stress and the engineering strain, p is the applied pressure, R the radius of the suction cup, e the estimated skin thickness and x the height of the deformed dome. The modulus of elasticity is then obtained by isolating the slope of a portion of the stress-strain curve [94]. The aperture of the suction cup has a non-negligible influence on the calculated parameters, as with a smaller diameter, only more superficial layers of the skin will deform [5].

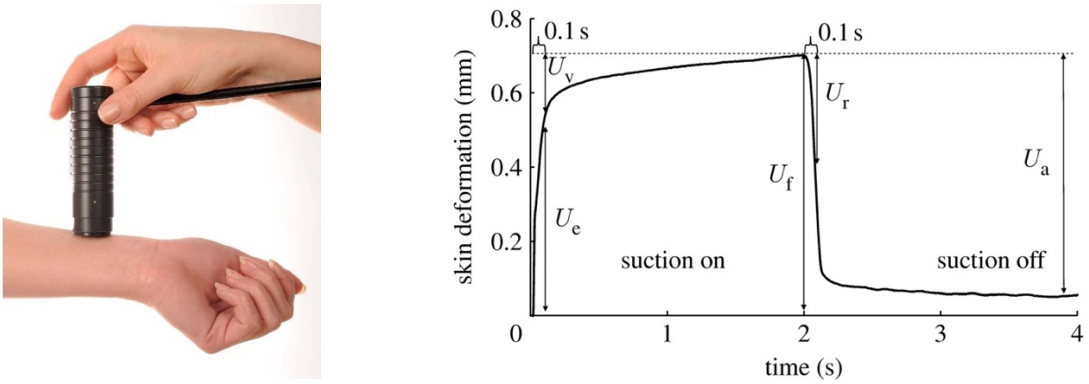

Figure 1.10. Left: Photograph of the Cutometer®, a clinically used suction device (http://www.courage-khazaka.de/index.php/en/products/scientific/140-cutometer). Right: Typical deformation curve from a suction test, obtained with the Cutometer® and reported by Gerhardt et al. [96]. Viscoelastic parameters are indicated on the graph.

In the same way as torsion tests, suction tests are simple to implement, and a broad range of regions can be tested. Clinical studies have shown that suction tests provide reliable indicators for skin aging [78,93,94], which explains its continuous development and use, such as the Cutometer® (Courage-Khazaka, Köln, Germany), or the DermaLab® (Cortex Technology, Hadsund, Denmark), presented in Figure 1.10. It is currently the most used non-invasive *in vivo* experimental technique in clinical dermatology [78,93,97–99], and, as in torsion tests, the parameters U_E, U_V, U_F, U_R, U_R/U_F from creep tests are favored to assess age, gender, or treatment-related changes.

1.2.1.4. Indentation Method

It can be considered that indentation is historically the first method to directly test dermal elasticity, with Schade's adaptation of the eye tonometer for skin, in 1912 [100]. It was subsequently refined in other studies [101,102]. Current setups are also adaptations of mechanical nanoindenters which are being widely used in the characterization of biological materials (see Figure 1.11).

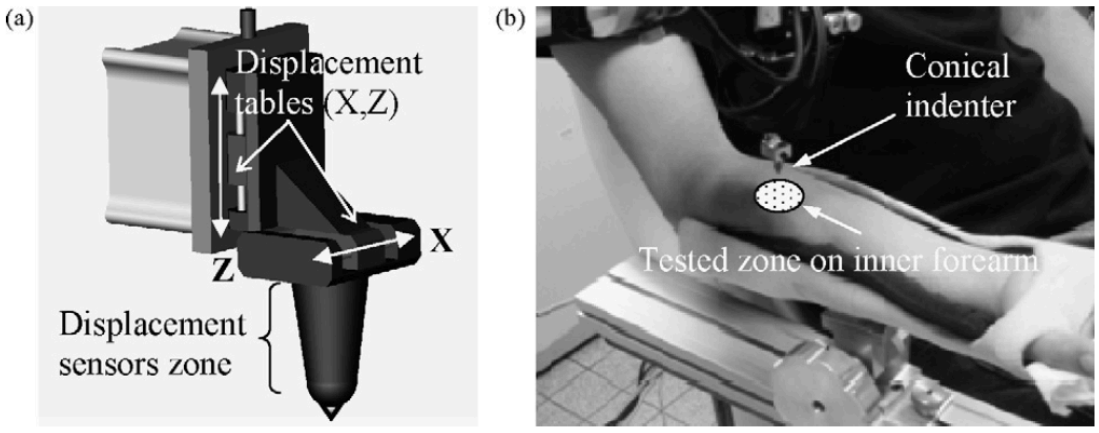

Figure 1.11. (a) schematic representation of the indentation device developed by Pailler-Mattei et al. [53]. (b) Positioning of the system of a subject's arm.

In this technique, a rigid indenter applies a controlled displacement δ at a given location on the subject's skin, and the normal force F_N is recorded. Controlling the applied force and recording the penetration depth is also feasible. From the obtained data, the indentation modulus E*, can be determined [53]:

$$E^* = \frac{\sqrt{\pi/A}}{2} \frac{dF_N}{d\delta}\Big|_{F_N=F_{max}} \tag{1.6}$$

where A is the projected contact area and F_{max} is the force at unloading. Elasticity parameters can be found via the following approximation:

$$E_{skin} = E^*(1 - \nu_{skin}^2) \tag{1.7}$$

where E_{skin} is the uniaxial elasticity modulus of skin, and ν_{skin} the Poisson ratio.

The indentation method is non-invasive and does not require any shielding of the tested area. However, depending on the penetration depth, the indenter size and geometry, other regions under the skin can affect the results [53,71]. Anisotropy of the tissue cannot be resolved with such techniques. Moreover, stress-strain curves are difficult to obtain because the geometry of the deforming region is hard to define. It was shown that pre-stress in the tissue affects the measured response as well [103].

Other less common *in vivo* experimental methods for skin testing include vibration/friction [63,96,104], and ballistometric [105,106] tests, to mention a few.

While *in vivo* methods have limitations (sample accessibility, limited deformation), they can also be useful non-invasive and non-destructive tools in a clinical context to monitor changes in mechanical properties of a patient's skin due to causes such as aging, wound healing, or radiation therapy. The obtained results and reported parameters vary widely, mainly due to lack of test standardization [36,93]. Depending on the parameters of the experimental setup,

e.g. suction cup diameter, or indenter shape and diameter, different layers of the skin and sometimes subcutaneous organs contribute to the deformation, which complicates obtaining consistent experimental results. The high inter-subject variability accentuates this problem.

1.2.2. *Ex Vivo* Testing of Skin

Although presenting some ethical restrictions, excising skin from a subject, either *post-mortem* or after surgery, gives researchers more freedom in terms of experimental techniques. More particularly, standardized mechanical testing methods become feasible, which usually improves the consistency and reliability of results. The deformation range can be extended to larger strains, which enable the characterization of additional mechanical processes such as irreversible deformations, damage, and tissue failure. When applying such techniques, one main obstacle to accurate measurements is commonly related to the fact that at high strains and high strain rates, the layer of fat covering the hypodermis lubricates the interface with the grips and contributes to additional slipping. Thus, specific gripping systems need to be designed to alleviate this problem. These designs are rarely communicated, and their performance is seldom quantified. Due to preexisting tension in skin, samples shrink differently after excision, implying that calculation of strains and stresses need to be addressed carefully when comparing *in vivo* and *ex vivo* results.

Most techniques described for *in vivo* experiments in the previous section have also been applied *ex vivo* (also reported as *in vitro* experiments). For example, Jee and Komvopoulos [107] reported data for the reduced elastic modulus of porcine skin from *in vitro* nano/microindentation methods, with a major emphasis on breed type variations. A more considerable amount of work has been conducted with tensile tests, as described in the following sections.

1.2.2.1. Uniaxial Tensile Testing

It is not surprising that uniaxial tensile testing protocols were also implemented for skin, as it is perhaps the most common mechanical test. Uniaxial testing machines are easily accessible, and the skin's anisotropy can be quantified by varying the direction of tension. One of the first reported uniaxial experiments on excised skin was conducted by Ridge et al. in 1966 [108], where deformation along and across the Langer lines of human cadavers was compared, showing skin's anisotropy. Since then, with the development of mechanical testing machines, a very broad range of experimental studies have focused on the influence of sample orientation and location [26,39,42,47,55,57], hydration [10,41], and strain rate [48], to mention some examples. Samples are preferably cut in a dumbbell shape, to maximize stress uniformity in the gauge region. Recently, Yang et al. [41] also performed tensile tests to observe the remarkable tear resistance of skin, using skin samples excised from rabbits (see Figure 1.12). Unlike most materials, skin mitigates the propagation of a pre-cut crack by blunting.

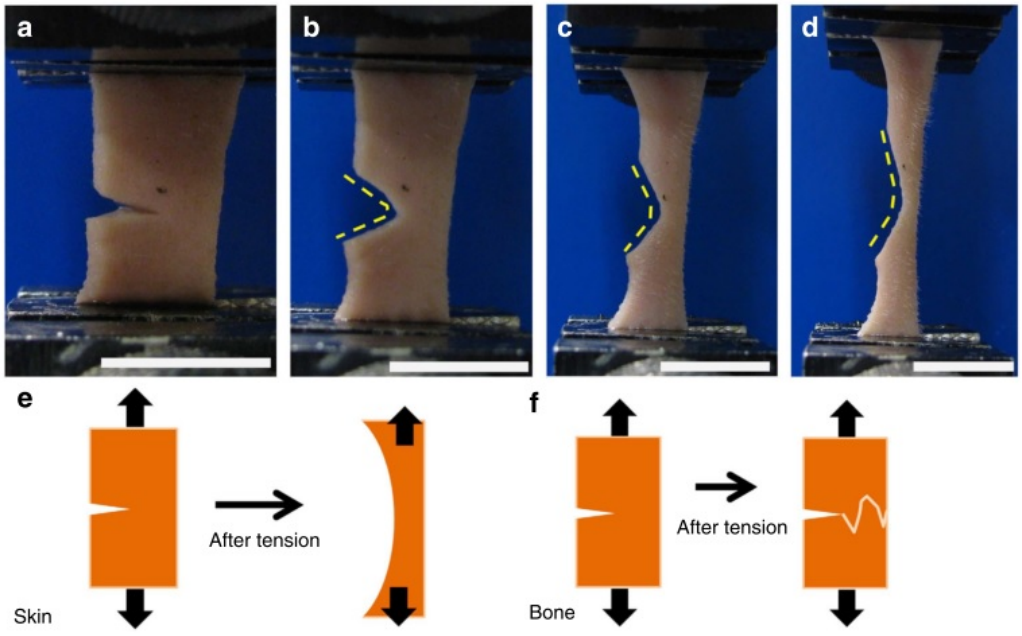

Figure 1.12. Tear resistance of rabbit skin in comparison to bone materials. From Yang et al. [41]

1.2.2.2. Biaxial Tensile Testing

Lanir and Fung [109] described in 1974 a biaxial testing setup, with the purpose of further characterizing the three-dimensional behavior of skin. The setup is shown in Figure 1.13. In their design, a small rectangular piece of the tissue is connected to a force-distributing platform at each side via a set of stapled silk threads. The displacements are controlled in both directions, and sample deformations are recorded on camera. The setup was used to perform tensile and relaxation tests on rabbit skin, after biaxial preconditioning, in the uniaxial (no load in one direction) and the biaxial directions (with one dimension kept constant), for different strain rates and controlled temperatures [42]. Their results are still being used for the construction of phenomenological and microstructural time-dependent models [110,111]. Schneider et al. [112] later used the same setup for the *ex vivo* characterization of human skin.

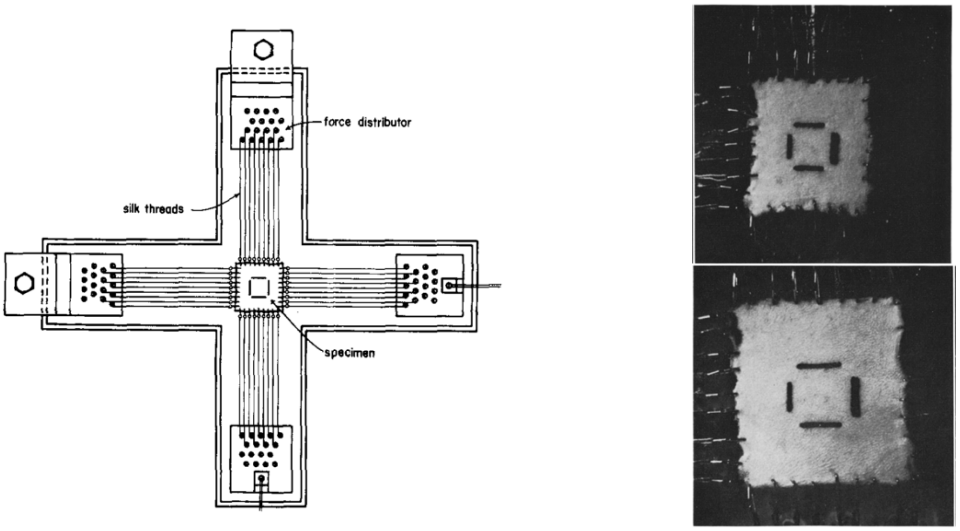

Figure 1.13. Biaxial stretching setup by Lanir and Fung [109]. Left: Schematic illustration of the setup, with specimen hooking and force distribution. Right: Photographs of undeformed (top) and biaxially stretched (bottom) rabbit skin sample. Marked lines are used to indicate that there was no rotation during stretching.

Biaxial testing produces loading that is closer to the *in vivo* conditions of skin, and provides additional insight into the mechanical parameters of the tissue. While it is possible to fully

resolve the mechanical properties of an incompressible isotropic material, it does not suffice to fully determine the constitutive equations a an anisotropic material like skin, as pointed out by Holzapfel and Ogden [113]. For a full experimental characterization, more general methods, combining different testing and measurement techniques, are recommended [114].

1.2.2.3. Bulge tests

Bulge tests (also sometimes referred to as diaphragm or inflation tests) were first introduced by Dick in 1951 [115], for measuring the deformation of human skin. As pointed out by Grahame and Holt [94], the principle is analogous to the suction method, because it consists of creating a difference in pressure between the inner side of the tissue and the outer side. In this case, it is effectuated by injecting a fluid (water [115], or porcine saline buffer (PBS) [62]) into a pressurization chamber, on top of which a circular portion of sample is clamped. With applied fluid pressure, the sample inflates and the external surface forms a bulge. By approximating the deformed bulge to a hemispherical cap, the stretches can be measured by estimating the changes in arc length [116], or by tracking markers on the surface of the tissue [62,117]. The stresses can be computed from the applied fluid pressure using thin-shell theory [62,116], or inverse finite-element analysis [118,119], depending on the assumptions on the deformation state. Assuming that the deforming tissue behaves like a thin membrane and that the radial stress is small compared to the in-plane stresses, a biaxial stress state is also reached in the material [116]. An additional interest of the method is that the injected fluid in the chamber can be also used to hydrate the sample or control its temperature to physiological levels.

Another challenging venture is the measurement of tensile properties of skin under dynamic loads, to characterize the strain rate sensitivity of the tissue and to study extreme loading conditions. Examples using Split Hopkinson Tensile Bar designs can be encountered [43], but their performance is limited by sample slipping and impedance mismatch. Shergold et al. [45] performed dynamic tests on pig skin in a compression Hopkinson bar using disk-shaped specimens with a thickness of ~ 2.3 mm and a diameter of 7 mm. With such a low thickness to diameter aspect ratio, friction at the contact surfaces is likely to create pressure differentials (the pressure in the center being higher thanin the periphery) and cause barreling, which is rarely taken into consideration in the experimental protocol. Moreover, dynamic compression is more representative of particular cases such as the response of skin to blast and impact.

1.2.3. Image/Ultrasound Based Measurement Techniques

A considerable obstacle to reliable and accurate measurements of the deformation of skin can come from the mismatch between the estimated deformation and the true deformation, partly due to sample slipping. Estimation of stresses can be complicated in the case of *in vivo* experiments due to the difficulty to resolve between deforming layers of the subject's body.

To address this issue, some researchers have coupled their experimental setups with image or ultrasound-based measurement techniques. These techniques can be used to quantify the error between the applied displacement and the average local displacements in the structure. But it can as well be a useful tool to observe localization of strains and tissue anisotropy, via two-dimensional mapping of strains. Moreover, ultrasound (or also OCT [5,120,121]) measurements can yield valuable out of plane visualization, which allows one to distinguish the different layers being deformed, or heterogeneities that can be indicators of health-related problems. A notable example is the application of elastography, i.e. a mechanical testing device

coupled to an imaging apparatus, to detect anomalies such as infections or skin cancer [120,122]. By measuring the degree of distortion under an applied load, local tissue stiffness can be qualitatively observed. Coutts et al. [88] describes an elastograph based on a uniaxial extensometer paired with an ultrasound probe, to distinguish deforming skin from the subcutaneous layer *in vivo* (Figure 1.14). The same concept has been used for suction devices [78], as a tool to measure simultaneously the bulge height and the deforming layers.

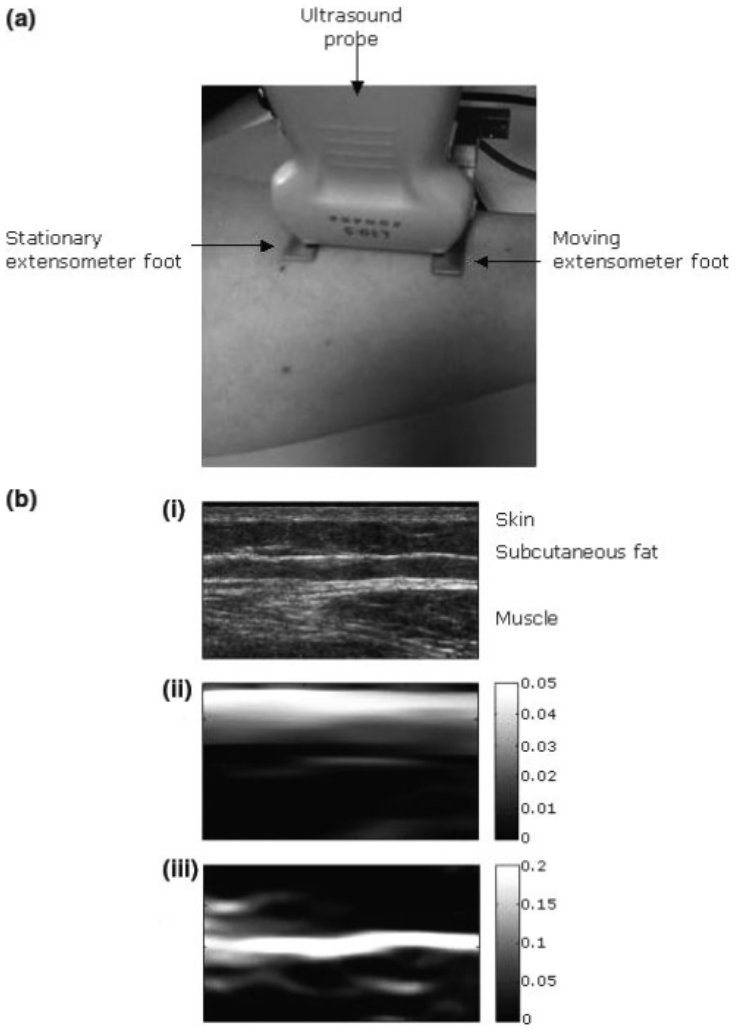

Figure 1.14. (a) Photograph of a uniaxial extensometer attached to forearm skin of a human subject, paired with an ultrasound probe for elastography. (b)(i) Ultrasound image with corresponding examples of (ii) tensile normal strain elastogram and (iii) shear strain elastogram. Reprinted from Coutts et al. [88].

A very common use of imaging techniques to quantify superficial deformation of skin is Digital Image Correlation (DIC). DIC consists of tracking specific markers, speckled randomly on the surface of the sample, during an applied deformation. The recorded sequence of images is then processed, and the local displacements are identified by cross-correlation, allowing for the calculation of strains. In addition, three-dimensional deformation can be determined by using a set of two cameras (Stereoscopic Image Correlation). In the context of skin's characterization, it is a very useful tool to observe the anisotropy of a sample, localization or uniformity of stresses, and the coherence between the imposed and real deformations. Figure 1.15 shows how DIC can be implemented to compare the macroscopic deformation, measured with a displacement sensor (DS), and the local strains via DIC, to account for sample slipping or localized deformations. By coupling a bulge tests with three-dimensional DIC (Figure 1.16), Tonge et al. [62] successfully quantified skin's anisotropy, evidenced by a difference in vertical and horizontal displacements of the sample, and an elliptical out-of-plane displacement contour.

To visualize how macroscopic deformations are distributed in the structure, other measurement techniques can be implemented. The reorganization of the collagenous network in skin has been observed *in situ* by Second Harmonic Generation coupled with DIC by Nesbitt et al. on mouse skin [123] and by Small Angle X-ray Scattering (SAXS) by Yang et al. [41] on rabbit skin. Both studies show that collagen fibrils gradually align towards the direction of tension, before eventually undergoing stretching, sliding, and delamination, which precedes fracture. This fiber recruitment process has also been recorded with *ex situ* SEM by Yang et al. [41] for rabbit skin (Figure 1.17), and earlier by Brown [68] for human skin. Tensile tests were interrupted at different increments of strain, and samples were fixed prior to SEM imaging.

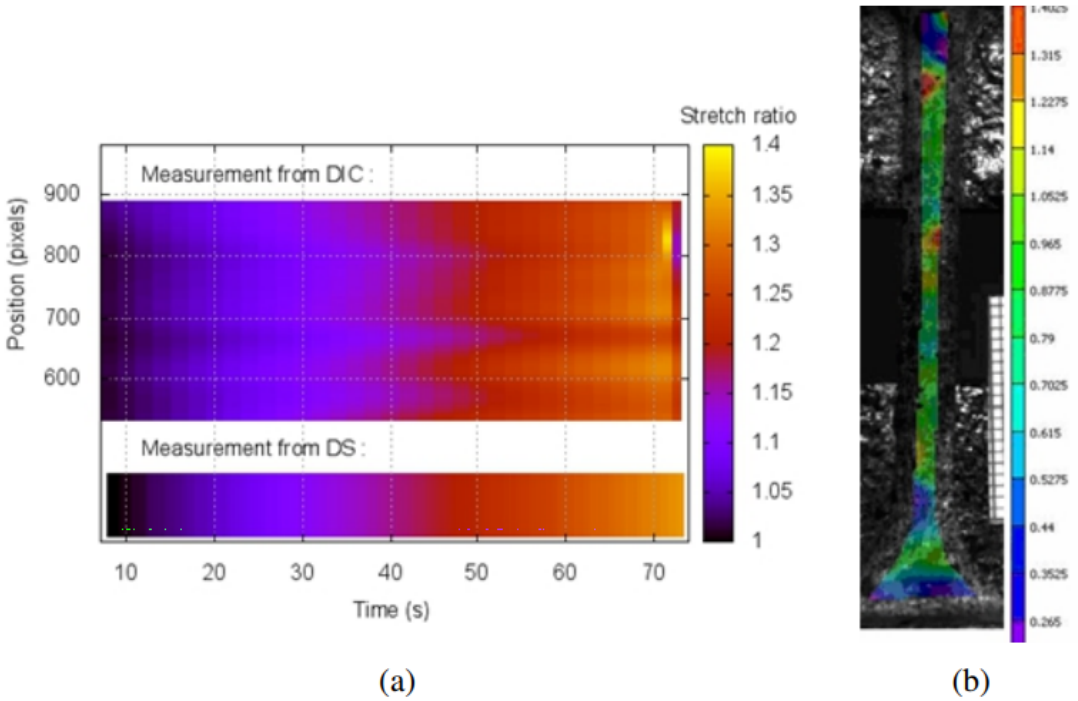

(a) (b)

Figure 1.15. (a) Comparison of stretch measurement from DIC and Displacement Sensor (DS) over the length of the specimen, throughout the duration of a given tensile test. (b) Distribution of local Lagrangian strains just before rupture of a dumbbell shaped skin sample. From Ni Annaidh et al. [55].

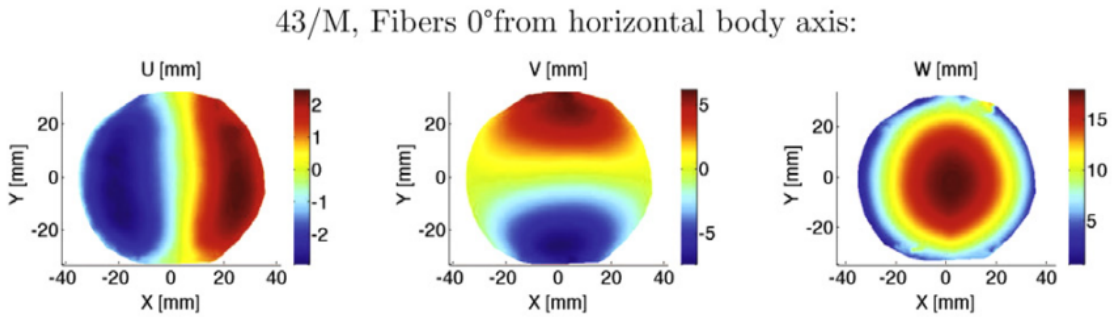

Figure 1.16. Three-dimensional DIC contours of displacement components in the body axis coordinates ((U, V): in-plane, W: out-of-plane) for a 43-year-old male from *in vivo* suction tests on human subjects. Anisotropy of the tissue is evident from the rotated U and V contours and the elliptical W contour. From Tonge et al. [62].

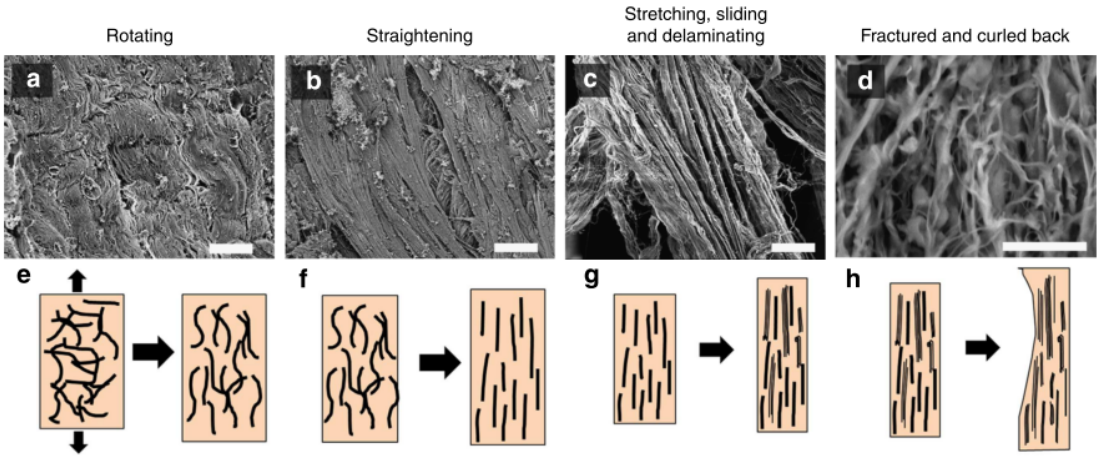

Figure 1.17. Collagen fiber recruitment and deformation during tension, visualized by *ex situ* SEM (a-d), and schematic illustration of the process of deformation (e-f). Reprinted from Yang et al. [41].

1.2.4. Summary of Experimentally Observed Features

It can be challenging to compare *in vivo* and *ex vivo* experimental results given the large differences in terms of protocol, sample configuration, and spanned deformations. However, good agreements have been observed when comparing low deformation curves, obtained from the same animal, for identical types of loadings [69]. An additional feature is the degradation of the skin in *ex vivo* testing, which starts immediately after removal from host. Preservation methods vary and this introduces additional variations in results.

With considerable variations due to specifics of the experimental protocol, e.g. boundary conditions, sample geometry, measurement accuracy, or spanned deformation, as well as inter-species and inter-subject variations, it is difficult to quantitatively obtain comparable mechanical parameters. A non-exhaustive summary of reported values of the tangent modulus of skin encountered in the literature is presented in Table 1.2. It highlights the high discrepancy between these results, and corroborates observations from Rodrigues et al. [36].

Table 1.2. Comparative analysis of reported tangent modulus, failure strain, and failure stress found in previous studies (ranked by chronological order). N.A.= Not Applicable; N.R. = Not Reported.

Reference	**Year**	**Tested Species - Region**	**Type of Experiment**	**Tangent Modulus E (MPa)**	**Failure Strain**	**Failure Stress (MPa)**
Jansen and Rottier [75]	1958	Human - Abdomen	*Ex vivo* – Uniaxial tension	2.9-54.0	0.17-2.07	1-24
Stark et al. [76]	1977	Human - Back	*In vivo & ex vivo* – Uniaxial tension	0.26-0.83	0.16-0.52	N.A.
Vogel and Hilgner [39]	1979	Rat – Dorsal Skin	*Ex vivo* – Uniaxial tension	35.2-36.9	0.63-0.86	10.6
Agache et al. [54]	1980	Human - Back	*In vivo* – Torsion	0.42-0.85	N.A.	N.A.
Dunn and Silver [124]	1983	Human - Abdomen and Thorax	*Ex vivo* – Uniaxial tension	0.1-18.8	1.0	7
Vogel [77]	1987	Human – N.R.	*Ex vivo* – Uniaxial tension	15-150	0.3-1.15	5-32
Haut [40]	1989	Rat – Dorsal Skin	*Ex vivo* – Dynamic tensile tests	4.4-11.1	0.52-1.25	1.2-3.2
Shadwick et al. [84]	1992	Rhinoceros – Back and Flanks	*Ex vivo* – Uniaxial tension	107.8-237.3	0.24-0.33	14.5-30.5
Diridollou et al. [78]	1998	Human – Forehead and Arm	*In vivo* – Suction	0.12-0.25	N.A.	N.A.
Ankersen et al. [47]	1999	Pig – Back and Abdomen	*Ex vivo* – Uniaxial tension	N.R.	0.49+/-0.28	14.5+/-7.0
Hendriks et al. [79]	2003	Human - Forearm	*In vivo* - Suction	0.056+/-0.021	N.A.	N.A.
Khatyr et al. [80]	2004	Human - Tibia	*In vivo* – Uniaxial tension	0.13-0.66	N.A.	N.A.
Ventre et al. [83]	2006	Calf/Bovine Skin - Back	*Ex vivo* – Uniaxial tension	50.11+/-7.47	0.59+/-0.06	16.80+/-1.95
Jacquemoud et al. [81]	2007	Human – Forehead and Arm	*Ex vivo* – Uniaxial tension	19.5-87.1	0.27-0.59	5.7-12.6
Jachowickz et al. [82]	2007	Human – Face and Forearm	*In vivo* – Indentation	0.007-0.033	N.A.	N.A.
Pailler-Mattei et al. [53]	2008	Human – Arm	*In vivo* – Indentation	0.0045-0.008	N.A.	N.A.
Zhou et al. [48]	2010	Pig – Abdomen	*Ex vivo* – Uniaxial tension	0.9-4.2	1.23-1.26	0.25-1.0
Lim et al. [43]	2011	Pig – Back and Abdomen	*Ex vivo* – Dynamic tensile tests	N.R.	0.16-0.30	0.1-0.8
Wong et al. [26]	2012	Pig – Eyelid, Back, Cheek, Forelimb, Abdomen, and Chest	*Ex vivo* – Uniaxial tension (scarred tissue)	0.121-0.532	N.R.	N.R.
Ni Annaidh et al. [55]	2012	Human – Back	*Ex vivo*– Uniaxial tension	83.3+/-34.9	0.54+/-0.17	21.6+/-8.4
Gallagher et al. [57]	2012	Human – Back	*Ex vivo*– Uniaxial tension	146-171	0.37-0.55	30-37
Sherman et al. [12]	2016	Rabbit – Back and Belly	*Ex vivo* – Uniaxial tension	11.5-40.4	0.74-1.33	4.52-16.75

Figure 1.18a. presents a typical stress-strain curve for skin, obtained from uniaxial tensile tests. The so-called J-curve is observed for a broad range of collagenous materials (tendon, arterial wall, epimysium [125]) and can be decomposed in three distinct regions, which are associated with different deformation mechanisms at the microstructural level:

- the toe region, where collagen fibers gradually align with the tensile direction;
- the heel region, where the rotation continues and aligned fibers start uncrimping;
- the linear region, where aligned and straightened fibers undergo stretching, sliding past each other, delaminating, and ultimately failing, causing macroscopic damage and failure.

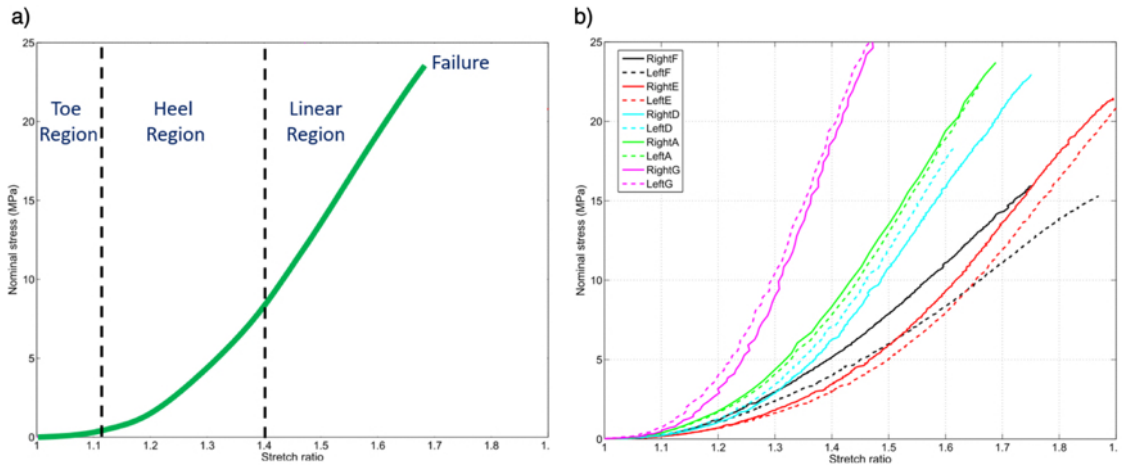

Figure 1.18. (a) Typical J-curve response of skin under uniaxial tension, showing three distinct regions. Depending on the isolated portion, the measurement of the tangent modulus can considerably vary. (b) Stress-stretch response from *in vitro* uniaxial tensile tests of adjacent samples human back skin, with similar orientation. Colors indicate different subjects while solid and dashed lines indicate samples to the right and left of the spinal line respectively, illustrating inter-subject and intra-subject variations. Adapted from Ni Annaidh et al. [55].

Thus, isolating a single value for the tangent modulus of a nonlinear curve depends highly on the portion of the stress-strain curve that is chosen (or accessible) to evaluate it, which affects the wide disparity in reported data that can be seen in Table 1.2. Moreover, tissue anisotropy, mainly caused by the distribution of collagen fibers, makes it impossible to fully describe the

response of skin under tensile loads, without prior knowledge of the structural arrangement of its constituents, or without a certain set of assumptions with respect to this arrangement.

Some further characterization of skin's nonlinear and anisotropic behavior needs to be implemented to yield a better description. Mechanical models that attempt to do so are developed further in this chapter. Even qualitatively, some important factors cause rather large variations to the experimental result. Figure 1.18b. shows that for identical experimental conditions, there can be important inter-sample variations, even for samples taken from the same species, or the same specimen.

1.2.4.1. Scaling of Skin Mechanics Across Species

It is rather common to expand results observed for a given animal to the behavior of human skin, but such considerations need to be addressed with caution. Although there are many commonalities in the structure of mammal skins, some fundamental differences can affect the mechanical behavior. Allometric considerations have to be made and a guiding parameter is that the volume (and therefore the mass M) increases with the cube of the radius R, assuming a spherical body. We consider an average thickness t of the skin and an average density ρ_s. Considering that skin envelops all internal organs, it must contain them without deforming too much itself. A schematic representation of the problem is given Figure 1.19a. By isolating the bottom hemispherical envelope of skin from the top part, the section of skin is subjected to the effect its own weight, as well as the internal forces at the interface with the upper half. The equilibrium of the isolated part can be expressed as follows:

$$2\pi R t \sigma_i = 2\pi R^2 t \rho_s g \tag{1.8}$$

Where σ_i is the internal normal stress at the interface. The mass of the lower envelope is equal to the product of its density ρ_s times the volume, where the volume of the hemispherical thin shell is approximated by $2\pi R^2 t$. Further simplification leads to the following relationship:

$$\sigma_i = \rho_S g R \tag{1.9}$$

Then, for a spherical body, we have:

$$R \propto \left(\frac{3}{4\pi} M\right)^{1/3} \tag{1.10}$$

Which leads us to the following allometric relationship:

$$\sigma_i \propto M^{1/3} \tag{1.11}$$

By considering an equivalent level of "sagging" strain for each species, this implies that the tangent modulus of skin should scale with body mass to an exponent of 1/3, assuming that $\sigma_i \propto E\varepsilon_i$. We compared this prediction to a set of experimental results collected in the literature, most of which are presented in Table 1.2. To avoid disparity, we gathered data for *ex vivo* uniaxial tensile experiments performed under similar conditions (strain rate, temperature, type and region of the sample) for all types of orientations (Figure 1.19b) from animals ranging from a rat ($M \approx 10^2\ g$) [39,40] to a rhinoceros ($M \approx 10^6\ g$) [84]. The most consistent parameter appears to be the slope of the linear region of the J-curve. A least-squares approach was used to fit two power laws: one with unrestricted parameters (blue dotted line) yields $y = 1.94x^{0.34}$ with an R-square coefficient of 0.86. For the second curve (red dotted line), the exponent was fixed to 1/3, as predicted by our approximation, and $y = 2.21x^{1/3}$ with an R-square coefficient of 0.84, showing a satisfying agreement with our prediction. This correlation is indeed fascinating and demonstrates that the slope of the linear region increases with the mass of the

animal and scales with an allometric exponent of 0.33, as predicted from a simple dimensional analysis.

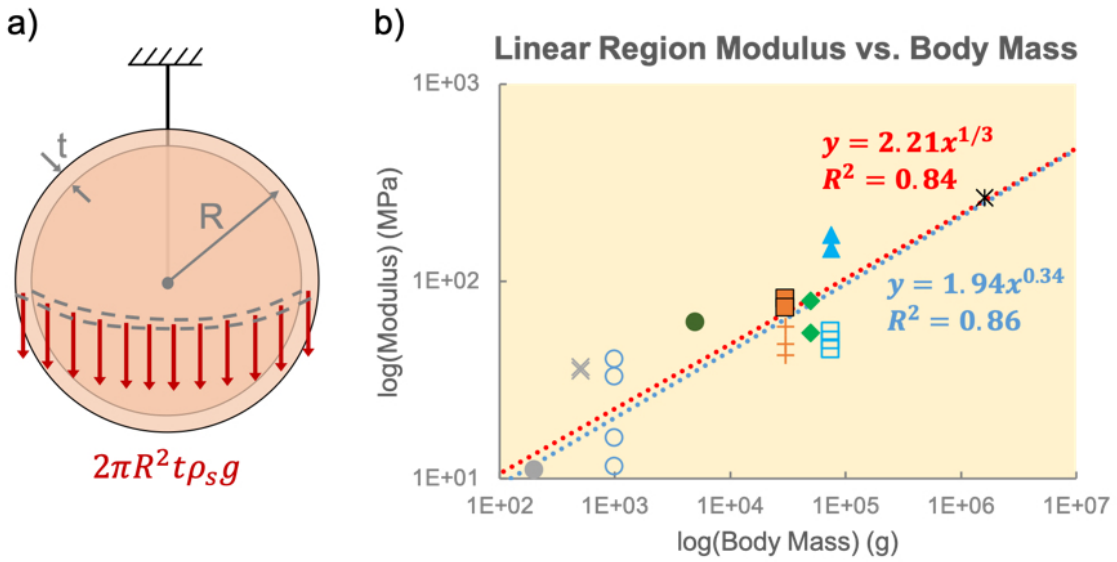

Figure 1.19. Simplified model of allometric scaling of skin elasticity across species. a) Schematic representation of a spherical body with an outer layer of skin. The skin envelope must be able to withstand its own weight with limited stretch; by isolating the top hemisphere we see that the total vertical force is proportional to the mass of the lower hemisphere. b) Logarithmic plot of the slope of the linear region of the stress-strain curve versus body mass. Data for *ex vivo* uniaxial tensile tests of rat (● - Haut [40], ✕ - Vogel [77]), rabbit (○ - Sherman et al [11]), cat (● - Veronda and Westmann [126]), pig(■ - Ankersen et al. [47], ┼ - Pissarenko et al. [17]), calf (◆- Ventre et al. [83]), human (□ - Ni Annaidh et al. [55], ▲ - Gallagher et al. [57]), and rhinoceros (✳ - Shadwick et al. [84]) skins. Blue and red dotted lines represent least-squares fit power law functions with unrestricted parameters and fixed exponent, respectively. Experiments were generally conducted with fresh skin, at ambient temperature, at strain rates around $10^{-2}s^{-1}$.

1.2.4.2. Alignment with the Langer Lines

The orientation dependence is perhaps the most fundamental mechanical characteristic of skin and can be directly linked to Langer's description of lines of pre-stress, and consequently skin's anisotropy. It has been repeatedly reported that when pulled along the principal alignment direction of collagen fibers (i.e. parallel to the Langer lines), skin exhibits a higher ultimate tensile stress and higher tangent modulus [43,47,55,108], illustrated here in Figure 1.20. The influence of the Langer lines on failure stretch are disputable, and region dependence needs to be taken into account, see section 2.4.3.

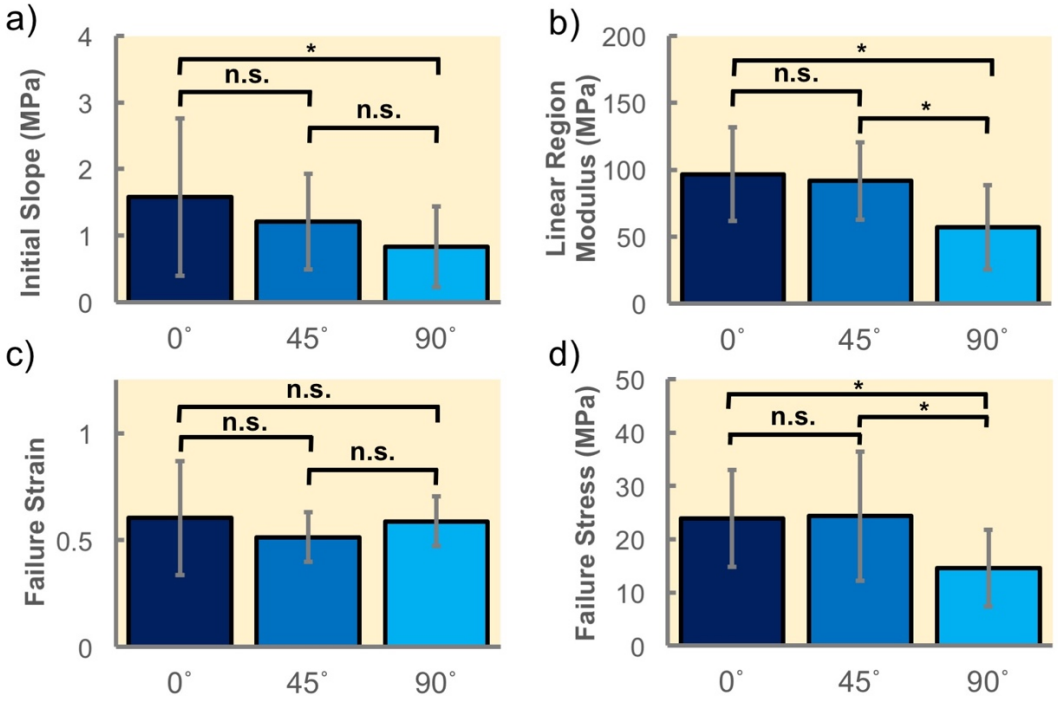

Figure 1.20. Influence of orientation on the (a) initial slope, (b) linear region modulus, (c) failure strain, and (d) failure stress for human back skin, tested uniaxially. Samples were taken parallel (0˚ - N=16), diagonally (45˚ - N=26), and perpendicularly (90˚ - N=14) to the Langer lines, mean values and standard deviations are shown. Comparisons where no statistically significant difference was observed are marked with an "n.s." symbol. Otherwise, asterisk (*) symbols are marked when $p < 0.05$. N designates the number of tested samples. Adapted from Ni Annaidh et al. [55].

1.2.4.3. Region Dependence

The findings of Agache et al. [54] exemplify how different locations of the body have varying responses to deformation, where the belly region needs to be highly deformable in the transverse direction while other areas such as the back tend to be thicker and stiffer in order to protect the spine. Values reported in Table 1.2. illustrate this suggestion, and particularly results reported by Ankersen et al. [47] where the back and belly regions of excised pig skin were tested uniaxially (see Figure 1.21). Their results demonstrate that location does not only affect elasticity but also the degree of anisotropy within the tissue, which can be understood by the fact that each region needs to sustain a different set of deformations of varying amplitudes. This

degree of anisotropy was shown to significantly vary between two comparable specimens as well by Lanir and Fung [42] from their biaxial testing experiments.

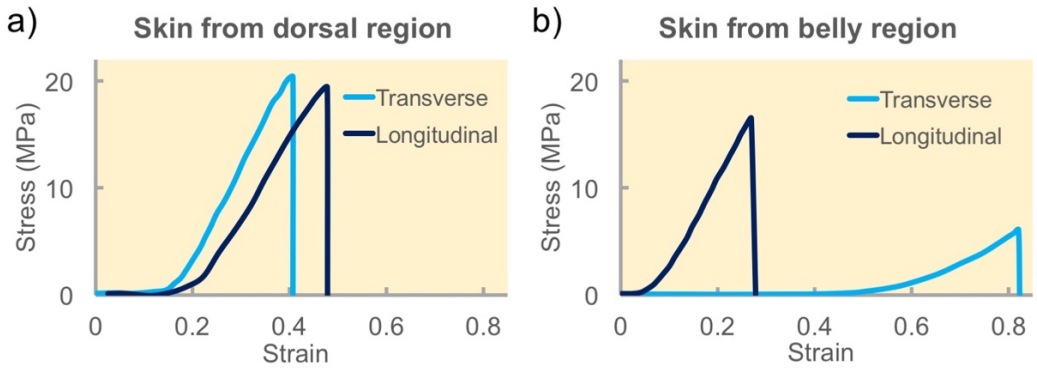

Figure 1.21. Stress-strain curves of pig skin tested in longitudinal (parallel to spine) and transverse (perpendicular to spine) directions via uniaxial tensile tests: (a) back, (b) belly, showing the influence of the tested region. Reproduced from Ankersen et al. [47].

1.2.4.4. Influence of Aging

Age is a significant factor affecting the mechanical response of skin. As mentioned previously, certain *in vivo* experimental techniques can be applied to assess the aging of the tissue depending on observable parameters such as apparent stiffness, or relaxation time. Boyer et al. [64] used the Cutometer® and an indentation device on human skin to show that apparent stiffness and the elasticity ratio U_R/U_E decrease with increasing age of subject, while the U_V/U_E ratio increases. Similar trends for U_V/U_E were reported from torsion tests on male and female subjects by Agache et al. [54]. However, the elasticity ratio appears to increase until the age of 30 before eventually decreasing, which agrees with some other reported findings [91,94]. It is worth noting that this increase is generally more pronounced amongst female subjects, which can be linked to morphological adaptations for pregnancy, pointing out the influence of gender on experimental measurements.

1.2.4.5. Hydration

Hydration is an external parameter of significant contribution to skin's elasticity. Its impact has been studied through variations of external humidity [41,62,127,128], or application of hydrating agents or water immersion [96,120,121,129,130], and reported for the first time by Christensen et al. [129]. They tested the external surface of skin with an electrodynamometer and noted a softening response after application of water and emollient. Later, Auriol et al. [131] performed *in vivo* suction experiments on human subjects and observed an increase up to 14% in skin's extensibility, depending on the time water was applied prior to testing, and this number rose to 21% when women were considered apart from men. Hydration mostly affects the stiffness of the stratum corneum [96,127], which for women represents a higher ratio of the total skin thickness, suggesting that its changes in mechanical response have a more perceptible effect on the overall response of the tissue. The mechanical sensitivity of the stratum corneum to humidity has been quantified by Levi et al. [127], who measured an increase in thickness and a decrease in Young's modulus with water content. Yang et al. [41] report a significant stiffening of rabbit skin after drying (Figure 1.22). The stiffness of the skin scales with the reduction in weight due to water loss. Dry skin, with a 35% reduction of weight due to dehydration, has a radically altered mechanical response. Nonetheless, Tonge et al. [62] report that variations in the humidity level of the testing chamber have no significant effect on bulge tests on human skin.

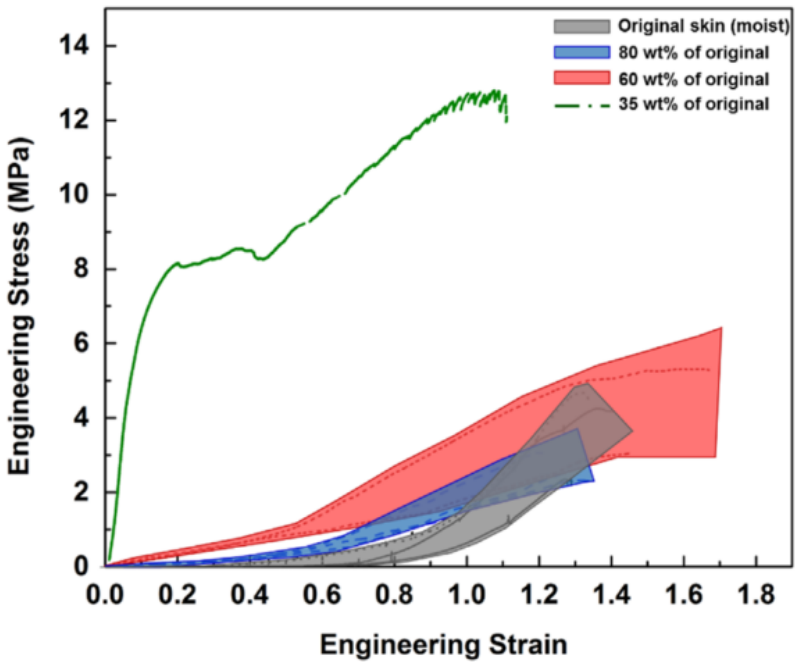

Figure 1.22. Stress-strain curves of original moist skin and dehydrated skin of different amounts. Adapted from Yang et al. [41].

1.2.4.6. Influence of Temperature

Thermal effects have also been studied, due to their notable interest in dermatological and surgical applications. Zhou et al. [48] tested uniaxially pig belly skin under temperatures ranging from 10°C to 60°C and observed a softening response, marked by a longer toe region and a decrease of the Young's modulus in the linear region with increasing temperature (Figure 1.23). According to their findings, high temperatures damage the tissue and denature collagen which loses its structural integrity and thus its mechanical properties, along with other effects such as changes in hydration and water intake.

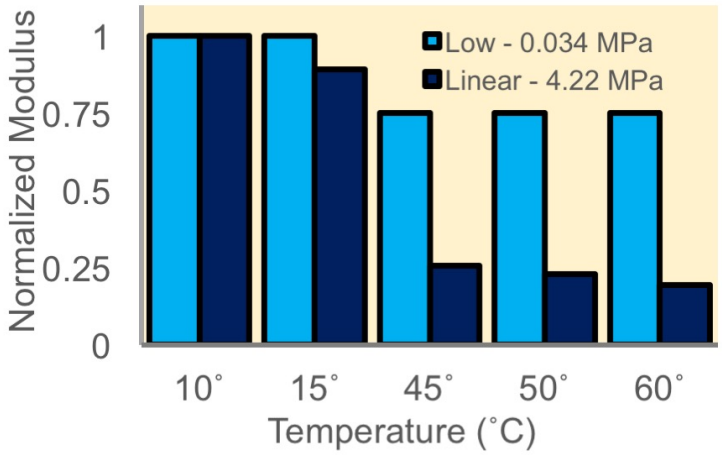

Figure 1.23. Influence of external temperature on tangent modulus in the low strain and linear regions of the J-curve, for tensile tests on pig skin at a strain rate of $0.01 s^{-1}$. Values are normalized by their maximum to highlight decreasing trend. Adapted from Zhou et al. [48].

1.2.4.7. Strain-Rate Sensitivity

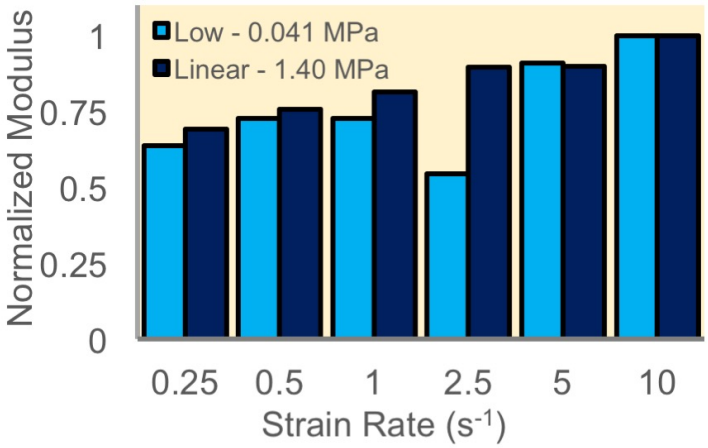

Figure 1.24. Influence of strain rate on tangent modulus in the low strain and linear regions of the J-curve, for tensile tests on pig skin at a temperature of 45˚C. Values are normalized by their maximum to highlight decreasing trend. Adapted from Zhou et al. [48].

The time-dependent behavior of skin can be observed by changing the strain rate of the applied load. Zhou et al. [48] conducted experiments on excised pig belly skin samples under uniaxial tension, with loading rates ranging from 0.25% s^{-1} to 10% s^{-1}. The reported curves (Figure 1.24) show a reduced toe region and, most importantly, a hardening response with increasing crosshead speed. The authors suggest that higher strain rates increase the shear

interactions between the structural elements of the dermis and alter the movement of internal fluids, thus affecting the viscoelasticity and dissipative behavior of the tissue. Strain-rate sensitivity of skin was suggested earlier by Finlay [58], who also stated that skin exhibits thixotropy. It was later validated by other studies involving uniaxial [17,43,132], biaxial [42] and compressive [11,45] tests.

1.2.4.8. Stress-Relaxation and Creep

Standardized measurements by the suction and torsion methods include time-dependent parameters, namely U_V, U_F, and U_R (Figures 1.9. and 1.10), which, depending on the controlled input (i.e. applied force or applied displacement), can be assimilated to creep or stress relaxation tests. Time-dependent parameters have shown to be a good indicator of skin aging [54], and location [61]. Direct stress-relaxation tests have been conducted by Lanir and Fung [42] with their biaxial testing setup, and show that the relaxation response is dependent of the strain or initial stress at which the sample is relaxed. This is comparable to the observations later made by Liu and Yeung [133], although the authors emphasize the fact that the stress relaxation rate varies according to the region of the J-curve that has been reached as well as the sample orientation (Figure 1.25). Relaxation curves are generally normalized by the maximum stress, which is why these results need to be addressed carefully because stress levels are different parallel and perpendicular to the spine due to of skin anisotropy.

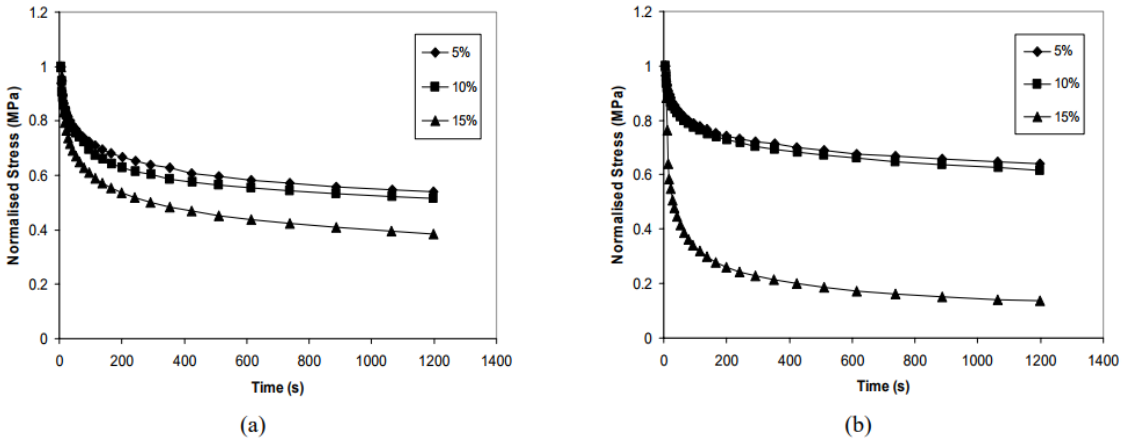

Figure 1.25. Stress relaxation trend of pig skin at different strains in (a) samples parallel to the spine, and (b) samples perpendicular to the spine direction. All stresses are normalized to the initial stress. From Liu and Yeung [133].

1.2.4.9. Irreversible Damage and the Mullins Effect

The changing relaxation behavior with repeated cycles or for different levels of relaxation stress suggests that the tissue undergoes irreversible deformations that start accumulating after stretching. This may principally be caused by fibers realigning permanently in the principal direction of tension and eventually sliding past each other [41,68,123]. A consequence of this damage-induced behavior is the Mullins effect, commonly encountered for filled rubber materials, which can be examined during cyclic tests at large deformations [134] (Figure 1.26a.). The non-overlapping loading curves imply a loss of viscoelastic energy [66] and material softening [51]. Upon reloading, the material follows the previous unloading curve, showing that there is no further damage. The typical responses for nonlinear elastic and nonlinear viscoelastic materials are shown in Figures 1.26b. and 1.26c., showing that the loading and unloading paths are different for the latter. In their study, Muñoz et al. [134] also showed that for each testing cycle, residual strains accumulate, mainly for deformations above 10%, indicating irreversible damages in the tissue at this level. Values of these remnant strains after each loading cycles are marked in the abscissa in Figure 1.26a.

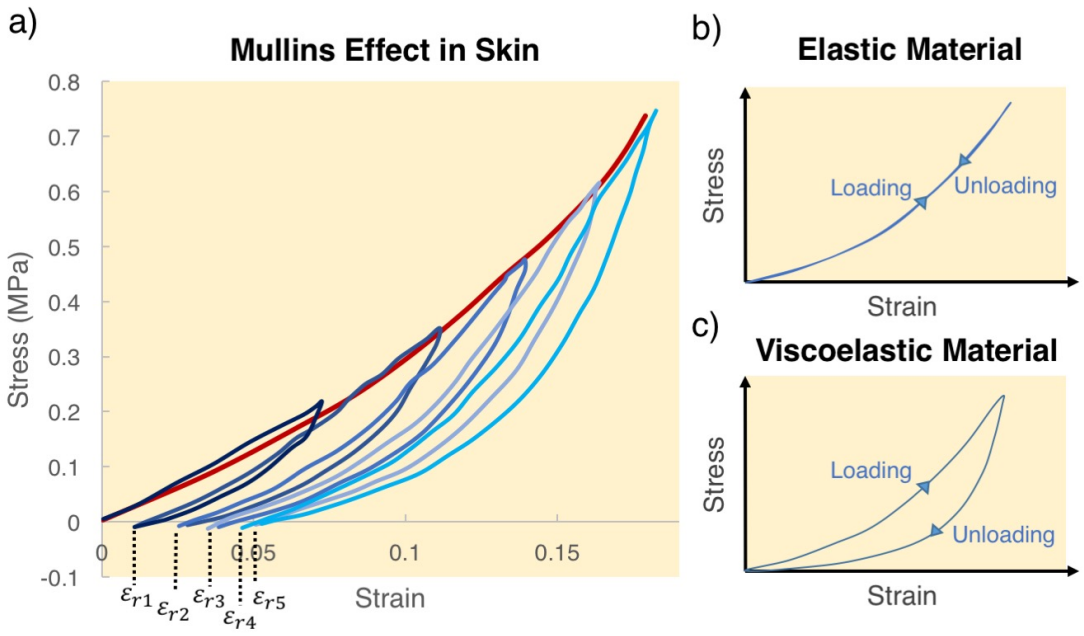

Figure 1.26. Illustration of the Mullins effect in mouse skin. (a) Experimental results obtained from the skin of an 18-month male mouse, adapted from Muñoz et al. [134]. The primary loading curve of the cyclic test (dark blue line) closely follows the monotonic one (red line), which describes an envelope curve for the cyclic test. Each reloading cycle then follows the previous unloading curve, a phenomenon called the Mullins effect. After each unloading cycle, remnant strains ε_r remain, indicating irreversible damage in the material. (b) For an elastic material, loading and unloading follow the same path. (c) In the case of a viscoelastic material, hysteresis can be observed, reflecting the dissipated viscoelastic energy.

In contrast, preconditioning consists of reaching overlapping hysteresis cycles at low strains (<10%) to ensure repeatability and reduce inter-sample variations [57,133], by maximizing fiber alignment, and has been first introduced by Fung [37].

1.2.4.10. Volume Changes

It is often assumed that biological tissues are incompressible, suggesting that no change in volume occurs during deformation. This has substantial consequences on the constitutive modeling of the material, where the incompressibility condition yields an additional relationship between the model invariants and reduces the material constants that need to be determined. As a result, the out-of-plane deformation component is sometimes neglected in experimental characterization, as it can be described by the in-plane components [7]. However,

recent studies involving image-based analyses of the lateral and out-of-plane deformations in skin during uniaxial *ex vivo* tensile tests report variations in the volume ratio J. Wahlsten et al. [135] measured a decrease of the volume ratio with increasing tensile deformation for murine and human skins [135], as illustrated in Figure 1.27. The authors attribute this trend to an outflow of the internal fluids, leading to volume loss, explaining also the irreversible cyclic behavior of the tissue.

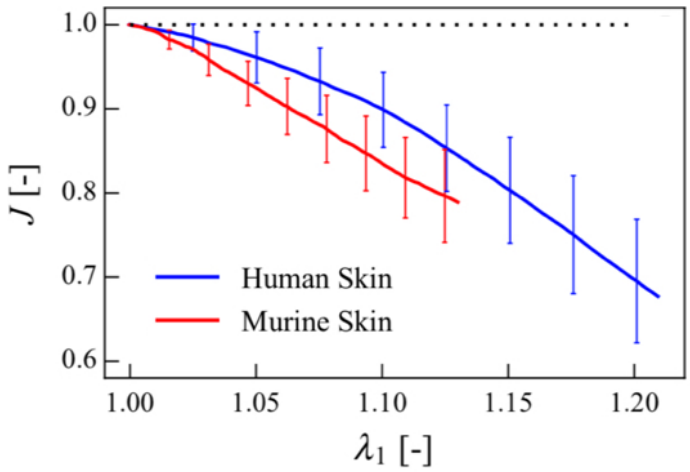

Figure 1.27. Loss of volume with applied stretch in human and murine skin samples during uniaxial tension tests, expressed by normalized volume change $J = V/V_0$. The dotted line indicates a constant volume ($J = 1$). Reproduced from [135].

It is more difficult to confirm that volume changes occur in the *in vivo* configuration. The out-of-plane deformation cannot be estimated using conventional imaging techniques, and different lateral constraints. Still, comparable trends in lateral contraction were reported [135]

1.2.4.11. Storage Conditions

Recently, Caro-Bretelle et al. [50] have pointed out the importance of storage conditions of skin samples prior to testing by quantifying the softening behavior after cyclic loading of pig skin, either fresh or stored under different conditions. Their results showed that conserving in saline solution or freezing the skin significantly and irreversibly alters the mechanical

properties, while cryopreservation appears as the only suitable method for maintenance, if not tested fresh.

The vast amount and variety of work that has been done on experimental characterization of skin's viscoelastic properties provides a broad framework to gain a better understanding of skin mechanics. It is clear that skin is a *nonlinear, anisotropic, viscoelastic* structural material that is sensitive to temperature, humidity, aging, UV exposure [136], radiation, as well as other external factors. Despite the complexity of providing a fully descriptive mechanical model for skin, researchers have attempted to predict its mechanical behavior under certain limited conditions and hypotheses. The following section describes some of the nonlinear elastic and viscoelastic models that have been implemented to this end.

1.3. Constitutive and Semi-Structural Models of Skin Mechanics

Experimental studies on skin's mechanical properties often report values for an elastic modulus. In most cases, it is calculated by isolating the slope of a quasilinear portion of the stress-strain curve, although some authors have their own way of estimating it. Nonetheless, the span of the measured curve varies from one study to another, yielding different possibilities for the calculated elastic modulus. Considering the skin's nonlinear and anisotropic behavior, limiting the description of the tissue response to a single linear parameter can be misleading, and can result in inconsistencies. It is therefore important to define and use more complete models that accurately describe skin mechanics, and incorporate its structural arrangement. Moreover, viscoelasticity and loading history dependent processes, such as damage, need to be considered. It is generally done by strain or stress-based linear decomposition of the elastic and viscous behaviors for viscoelasticity. The dissipative behavior, illustrated for example by the Mullins effect in loading-unloading experiments, is either described by the introduction of

dissipative factors in the energy function, or by including shearing or friction interactions between components of the structure.

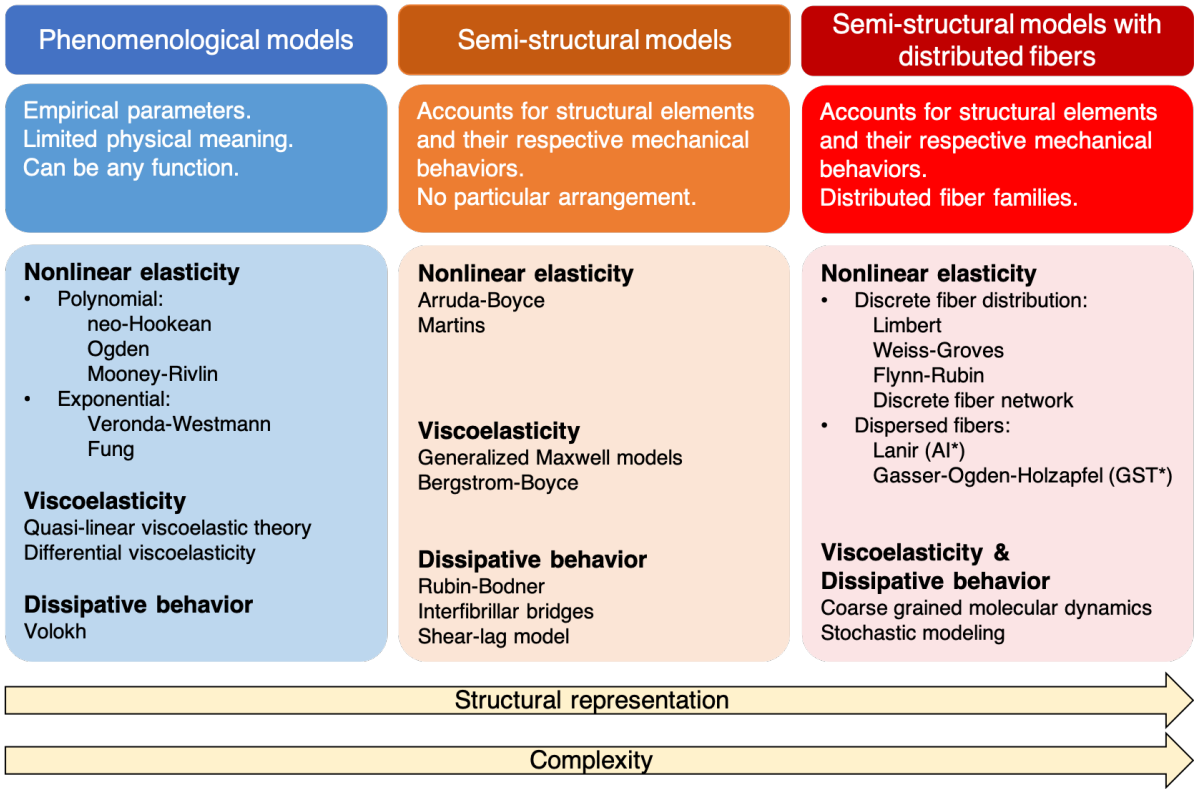

Figure 1.28. Summary of constitutive models used to represent the nonlinear elasticity, the viscoelasticity, and the dissipative behavior of skin, classified into three different categories. A few examples are listed for each category, some of which are presented in this review. Phenomenological models of nonlinear elasticity are not further developed, due to their inability to capture tissue anisotropy. As the complexity increases, the description of the materials structure and microscale behavior is improved. (*AI: angular integration; *GST: generalized structural tensors).

Figure 1.28 summarizes the most commonly encountered models for skin and other soft tissues, sorted in three main categories:

- phenomenological models, where the response is essentially based on empirical observations. For the most part, these models were initially introduced for the description of rubber-like materials and polymers, and their use was extended to biological tissues, as a first approximation and as an attempt to fit the J-curve. Although phenomenological descriptions of nonlinear elasticity have been widely used in the

literature to model the mechanical response of skin, mainly for their ease of implementation, several shortcomings limit their applicability, and the obtained parameters tend to lack physical meaning. Some examples are the Ogden model, the Mooney-Rivlin model, or the Fung model [49,52,125,137–139], as listed in the first column of Figure 1.28. Most of these descriptions are isotropic, and as a result fail to capture the anisotropy of the tissue, which eventually yields inconsistent results depending on sample orientation, location on the body, or testing conditions. The obtained parameters can lead to ambiguous interpretations, so the implementation of such models is not recommended, and is not further developed in this review. Nonetheless, hyperelastic constitutive laws can be encountered for the representation of the nonlinear elastic behavior of the ground matrix in semi-structural models, with some examples developed in the following section.

- In semi-structural models take into account the constituents of the material and include their respective mechanical behaviors, and potentially their relative interactions. An advantage of such a representation is that some characteristics of the material behavior can be attributed to some specific constituents, or their structure. the case of skin, this particularly involves the distinction between the contribution of the constitutive fibers, from the contribution of the ground matrix. For example, material anisotropy can be included by introducing preferred directions in the material, along which some families of fibers can be aligned, or viscoelasticity can be solely attributed to the surrounding matrix.
- semi-structural models with distributed fibers. In this category of models, the fibrous network of biological tissues is represented using fiber families with distributed

orientations, embedded in an isotropic matrix. The anisotropy of the tissue is thus mostly attributed to the splay of collagen fibers, and sometimes elastin. This distribution is either described by a discrete number of preferred directions, or by introducing fiber dispersion around the principal orientations. Dispersion can be represented using a pre-selected distribution function for the angular orientation of the fibers, integrated at each time step of the resolution, in which case the approach is called "angular integration" (AI), or directly incorporated into a generalized structure tensor, also referred to as the GST approach. These methods are further developed in the sections below.

Semi-structural models, due to their increased level of complexity, often introduce considerably more parameters, which can be associated with specific components or physical processes within the tissue. Their implementation requires some prior knowledge of the structure of skin, which can be identified using various microscopy imaging techniques such as scanning electron microscopy, transmission electron microscopy, histology, or second harmonic generation imaging. This information, along with some additional knowledge of the mechanical properties of the material constituents, obtained from small scale characterization, can be used to pre-set some constitutive parameters and consequently reduce the number of parameters to estimate.

Note that more complete representations of skin's behavior can be obtained by coupling different constitutive models for nonlinear elasticity, viscoelasticity, and dissipative behavior. The following sections provide a more detailed review of some of the models that have been successfully implemented for skin for each of these properties. Their respective advantages and limitations are also discussed, with the idea in mind to provide some guidelines for selecting the appropriate model, for given experimental conditions or specific testing criteria.

1.3.1. Continuum Description and Constitutive Framework

We start by assuming that the material is initially in a stress-free reference configuration Ω_0. The position of a material point in the reference state is described by its coordinates vector $\boldsymbol{X}$. In the deformed current configuration Ω, the spatial position of this point is described by $\boldsymbol{x} = \varphi(\boldsymbol{X})$. The deformation gradient $\boldsymbol{F}$ is defined as:

$$\boldsymbol{F}(\boldsymbol{X}) = \frac{\partial \varphi(\boldsymbol{X})}{\partial \boldsymbol{X}} \tag{1.12}$$

The local change in volume ratio is indicated by $J = \det(\boldsymbol{F})$. We also define the right Cauchy-Green deformation tensor $\boldsymbol{C} = \boldsymbol{F}^{\boldsymbol{T}}\boldsymbol{F}$, associated with the reference (Lagrangian) state, and the left Cauchy-Green deformation tensor $\boldsymbol{b} = \boldsymbol{F}\boldsymbol{F}^{\boldsymbol{T}}$, associated with the current (Eulerian) state. The isotropic component of the strain-energy function can be fully expressed by the strain invariants of $\boldsymbol{C}$ (or equivalently of $\boldsymbol{b}$), which are:

$$\begin{aligned} I_1 &= tr(\boldsymbol{C}) \\ I_2 &= \frac{1}{2}\left(tr(\boldsymbol{C})^2 - \ tr(\boldsymbol{C}^2)\right) \\ I_3 &= \det(\boldsymbol{C}) = J^2 \end{aligned} \tag{1.13}$$

For a fibrous tissue like skin, the splay in orientation of the collagen fiber network has a notable influence on the anisotropy of the material [13,114,140]. The arrangement of the fibers in the dermis can be approximated by defining n_f fiber families where each one follows a distinct principal alignment, equivalent to a peak in the orientation distribution profile. Let $\boldsymbol{n}_{0i}\ (i = 1..n_f)$ be the unit vector describing the main direction of fiber family i in the reference configuration. Accordingly, we define the structural tensors $\boldsymbol{B}_{0i}$ as:

$$\boldsymbol{B}_{0i} = \boldsymbol{n}_{0i} \otimes \boldsymbol{n}_{0i}\ \ (i = 1..n_f) \tag{1.14}$$

For each fiber family, two additional deformation invariants can be introduced

$$I_{4i} = \boldsymbol{C} : \boldsymbol{B_{0i}} = \lambda_i^2$$
$$I_{5i} = \boldsymbol{C^2} : \boldsymbol{B_{0i}} \tag{1.15}$$

λ_i denotes the stretch of the fibers oriented along $\boldsymbol{n}_{0i}$. For most semi-structural models presented below, it is the principal invariant that is used to characterize the contribution of the fibers to the deformation process. Other invariants associated with the relative interaction between the fiber families can be introduced, but these are generally neglected, either directly or by assuming material orthotropy or transverse anisotropy [9,141,142]. Tissue orthotropy is obtained when the principal material directions are orthogonal to each other, limiting the number of fiber families to three. For two fiber families (planar orthotropy), the normal to the plane formed by these two directions is also a preferred direction. Transverse isotropy is a special case of orthotropy, with only one principal fiber direction.

For dispersed fiber models, deviation around the principal orientation axis is incorporated, either by choosing a probability distribution function for the angular integration (AI) models, or by defining a set of generalized structure tensors for each fiber family for GST models. These concepts are further developed in the sections below, but an important notion is that this framework affects the expression of the deformation invariants associated with fiber deformation. For the sake of generality, the notations I_{4i} and I_{5i} are maintained in this subsection.

Following [114], the strain-energy function W of a fibrous biological tissue can be decomposed into an isotropic component, attributed to the ground substance, and the contribution of the fibers, such that:

$$W = W_m(\boldsymbol{C}) + \sum_{i=1}^{n_f} W_{fi}(\boldsymbol{C}, I_{4i}, I_{5i}) \tag{1.16}$$

Where n_f is the number of distinct fiber families in the model. The second Piola-Kirchhoff stress tensor $\boldsymbol{S}$, associated with the reference configuration, can be obtained by derivation of the strain-energy function W:

$$\boldsymbol{S} = 2\sum_{j=1}^{n_{inv}} \frac{\partial W}{\partial I_j}\frac{\partial I_j}{\partial \boldsymbol{C}} \tag{1.17}$$

With n_{inv} the total number of invariants considered in the model. The Cauchy stress tensor $\boldsymbol{\sigma}$, associated with the current state, is obtained by push-forward operation from the reference state [142]:

$$\boldsymbol{\sigma} = \frac{1}{J}\boldsymbol{F^T S F} = \frac{2}{J}\left[\sum_{j=1}^{n_{inv}} \frac{\partial W}{\partial I_j}\boldsymbol{F^T}\frac{\partial I_j}{\partial \boldsymbol{C}}\boldsymbol{F}\right] \tag{1.18}$$

In the following sections, some semi-structural and dispersed fiber models that have been implemented to represent the nonlinear elastic response of skin are presented, and the corresponding strain-energy function is provided.

1.3.2. Semi-Structural Models

1.3.2.1. The Arruda-Boyce Eight-Chain Model

The Arruda-Boyce constitutive equation [143], also referred to as the eight-chain model, was initially introduced to mimic the behavior of rubber-like elastomers at high levels of strain,

based on the entropy change upon stretching of macromolecules. The isotropic formulation is based on a cubic Representative Volume Element (RVE) consisting of eight freely-jointed chains starting from each corner and joining at the center. The initial length of each chain can be described by random walk: $r_0 = l\sqrt{N}$, with N the number of segments in the chain and l their length. The length of a fully extended chain is given by $r_L = Nl$, thus a "locking" stretch can be defined as:

$$\lambda_{lock} = \frac{r_L}{r_0} = \sqrt{N} \tag{1.19}$$

One can also express the stretch of a single chain: $\lambda_{chain} = \sqrt{I_1/3}$. The energy density function of such a system, with the hypothesis of material incompressibility, is the following:

$$W(\lambda_{chain}) = n\, k_B \Theta \left[\lambda_{lock}\lambda_{chain}\beta - \lambda_{lock}^2 \ln\left(\frac{sinh\,\beta}{\beta}\right)\right] \tag{1.20}$$

where n is the chain density, k_B the Boltzmann constant, Θ the absolute temperature and β is the inverse of the Langevin function: $\beta = \mathcal{L}^{-1}(\lambda_{chain}/\lambda_{lock})$, and $\mathcal{L}(\beta) = \coth\beta - 1/\beta$. The Arruda-Boyce model solely requires the identification of two parameters, the chain density n and the number of segments per chain N, which can potentially add physical meaning to the description.

In the context of skin mechanics, Bischoff et al. [144] implemented the isotropic Arruda-Boyce model to match experimental data reported in other studies [124,145,146]. The model has been shown to work particularly well at high strains. Interestingly, the anisotropic behavior of skin was also successfully captured by introducing an anisotropic stress-state, i.e. pre-existing stretches on the RVE.

The freely-jointed chain representation in the Arruda-Boyce model can also be replaced by a wormlike chain (WLC) model [110,111], which has a smoother curvature, and is therefore potentially better suited to mimic collagen in skin. In this case, the strain-energy function becomes:

$$W_{WLC} = \frac{k_B \Theta r_L}{4L_p}\left(2\left(\frac{\lambda_{chain}}{\lambda_{lock}}\right)^2 + \frac{1}{(1-\lambda_{chain}/\lambda_{lock})} - \frac{\lambda_{chain}}{\lambda_{lock}}\right) \tag{1.21}$$

Here L_p is the persistence length of a chain, i.e. its inherent stiffness.

The WLC model was implemented by Kuhl et al. [111] to simulate biaxial testing experiments conducted by Lanir and Fung [42] on rabbit skin, with the addition of transverse isotropy via a parallelepiped RVE with dimensions (a, b), and the effects of a surrounding matrix. The total energy density function of the tissue then becomes:

$$W_{Kuhl} = W_{bulk} + \gamma_{chain}\left(W_{WLC} + W_{rep}\right) \tag{1.22}$$

where W_{bulk} accounts for bulk effects due to the incompressibility of the matrix, γ_{chain} is the chain density per unit of length, and W_{rep} is a repulsive energy that ensures a stress-free reference configuration and prevents the chains from collapsing. Their expressions are as follows:

$$\begin{aligned} W_{bulk}(I_1, I_3) &= \kappa\left[I_1 - 3 + \frac{1}{\beta}\left(I_3^{-\beta} - 1\right)\right] \\ W_{rep} &= \frac{k_B \Theta}{4L_p}\left(\frac{1}{r_L} + \frac{1}{4r_0(1-\lambda_{lock}^{-1})^2} - \frac{1}{4r_0}\right)\overline{W}_{rep}(I_1, I_4) \end{aligned} \tag{1.23}$$

where $\overline{W}_{rep}(I_1, I_4)$ is a repulsion weighing factor characterized by the geometry of the representative volume element (RVE). Note that W_{bulk} has a form close to the neo-Hookean formulation. In this representation, the direction n_0 of transverse isotropy is the normal to the

square section of the RVE with sides b. I_4 is therefore the square of the stretch along the a-direction, and is not related to fiber stretch. The current fiber length is $r = \sqrt{I_4 a^2 + (I_1 - I_4)b^2}$. Thus, material parameters are the bulk modulus κ, the bulk parameter β, the persistence length L_p, the chain density γ_{chain}, the contour length r_L, and the dimensions of the parallelepiped RVE (a, b). Figure 1.29 shows that, after parameter identification, the transversely isotropic eight-chain model nicely captures the tissue's anisotropy and the J-curve elastic behavior. This framework can also be extended to material orthotropy by defining an RVE with three different lengths (a, b, c), as in the rheological model proposed by Bischoff et al. [147] to incorporate viscoelastic effects in skin, presented in section 3.4.2.

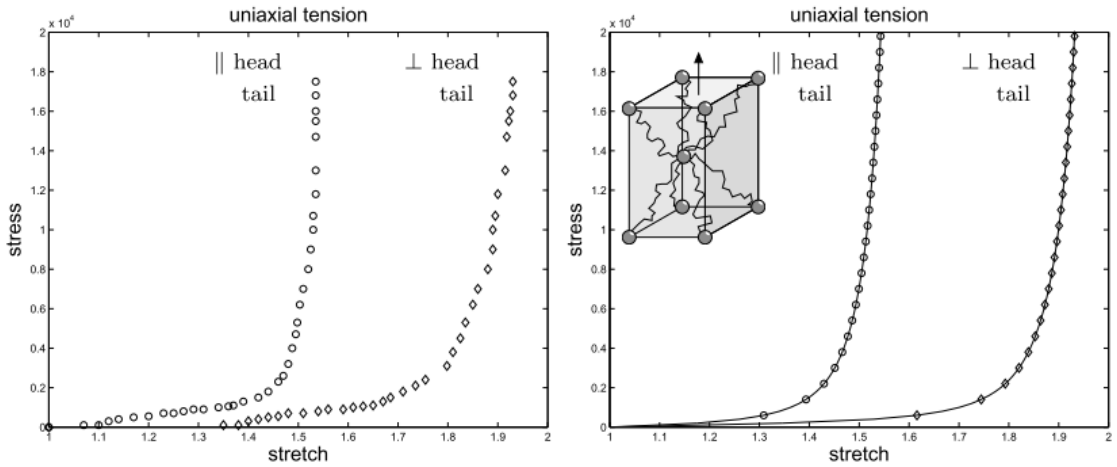

Figure 1.29. Anisotropy of rabbit skin. Left: Experimental results from biaxial tensile tests reported by Lanir and Fung [42]. Right: Simulation with a transversely isotropic eight-chain model using a worm-like chain description, by Kuhl et al. [111]. The model captures adequately the anisotropy of skin, as well as the curve shape.

The eight-chain model is a simple yet efficient way to represent a fibrous material. Some physical aspects can be integrated by assimilating the deformation of the chain with the straightening process of collagen fibers in the dermis, and the fiber arrangement is tridimensional, i.e. angular orientations in planes parallel and orthogonal to the dermis surface can be described. However, it can be challenging to physically interpret the nature of the

attachment points at the center and in the corners of the RVE, and fiber volume fraction is quite limited. Nonetheless, it offers interesting perspectives for synthetic material design that would replicate the behavior of skin tissue, with characteristics resembling truss-lattice architectures, see for example [148].

1.3.3. Semi-Structural Models with Discrete Fiber Distributions

1.3.3.1. The Weiss-Groves Model

Weiss et al. [149] proposed a transversely anisotropic hyperelastic model of collagenous tissues for the description of ligaments, accounting for the uncrimping process of collagen fibers. This formulation was later adapted for skin by Groves et al. [38], in an attempt to fit their data on uniaxial tensile tests on human and murine skin. In their model, three fiber families with distinct orientations are considered, and the out-of-plane direction is restricted. The strain-energy function is decomposed into the contribution of the matrix, represented by a Veronda-Westmann model, a volumetric component, and the contribution of the fibers, such that: $W_{Weiss} = W_{VW}(I_1, I_2) + W_{vol}(J) + \sum_{i=1}^{3} W_{fiber_i}(\lambda_i)$. More specifically, we have:

$$W_{VW}(I_1, I_2) = C_1\left(e^{C_2(I_1-3)} - 1\right) - \frac{C_1 C_2}{2}(I_2 - 3)$$
$$W_{vol}(J) = \frac{K}{2}(\ln J)^2 \tag{1.24}$$

For each fiber direction, the deformation depends on the fiber stretch λ_i, with $\lambda_i = \sqrt{I_{4i}}$:

$$\frac{\partial W_{fiber_i}(\lambda_i)}{\partial \lambda_i} = \frac{1}{\lambda_i}\begin{cases} 0, & \lambda_i \leq 1 \\ c_3\left[e^{c_4(\lambda_i - 1)} - 1\right], & 1 \leq \lambda_i \leq \lambda_{lock} \\ c_5\lambda_i + c_6, & \lambda_i \geq \lambda_{lock} \end{cases} \tag{1.25}$$

where λ_{lock} corresponds to the uncrimping stretch. Fibers are not given any compressive resistance, and the straightening process is described by an exponential function. Once fully

uncrimped, their behavior becomes linear elastic. Thus, fiber geometry, which dictates the process of deformation, is taken into account by associating different elasticity functions for different stretching states, in a piecewise fashion. The Weiss-Groves model requires initially the identification of fifteen parameters, which can be reduced to six if all three fiber families share the same properties.

Groves et al. [38] obtained parameters with a very good consistency, both for human and murine skin, despite a high inter-sample variability. The model was able to accurately reproduce skin anisotropy, with a lowest R-square coefficient of 98.4%. An example for human skin is shown in Figure 1.30. The piecewise function allows for a good description of the transition from the low-load regime in the toe region and the heel region to the linear portion of the J-curve. Hence, the Weiss-Groves model is an interesting approach for the comparison of specific areas of the deformation curve. The authors showed for example that main differences between samples from the same species is the degree of anisotropy (angular distribution), while differences between human and murine skin are seen with a shorter toe region for the latter. They attributed these differences mainly to the fiber network, the matrix conserving similar material properties.

It is important to observe that such a representation of skin suggests a layered arrangement of collagen fibers, parallel to the outer surface of the dermis. The model is therefore only transversely isotropic at the level of a single layer. Potential interactions between the three fiber families, which are generally not orthogonal to each other, are not considered. Moreover, the absence of an out-of-plane fiber component is in contradiction with several experimental observations, showing that the collagen network is initially tridimensional [13,17]. While this

description may provide satisfying predictions of in-plane deformations, it may face difficulties with data from compressive or shear tests.

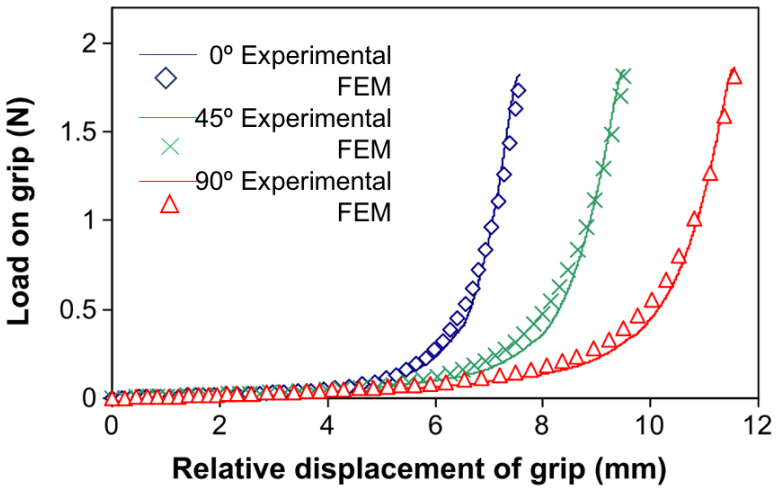

Figure 1.30. Load-displacement curve of a circular human skin sample from mastectomy, tested in three different orientations. Experimental measurements and FEM calculations. Tests were interrupted at a low load and relaxed for 30 seconds between each measurement to avoid irreversible deformations when changing orientations. Reprinted from Groves et al. [38].

1.3.3.2. The Limbert Model

The model proposed by Limbert [110] is the first to explicitly incorporate the contribution of inter-fiber and fiber-matrix shear into the deformation process of skin, although it can also be found in works on tendon by Szczesny and Elliott [150], Gao et al. [151] for the epimysium of skeletal muscles, and Peng et al. [152] for the annulus fibrosis. The formulation is based on the transversely isotropic model described by Lu and Zhang [153], who proposed a decoupling of the transformation gradient into volumetric, deviatoric, and shear components. In several other constitutive models, the shear energy is captured by the matrix/isotropic component but does not account for the influence of fiber deformation on the shearing interaction and does not make any distinction between shear occurring in the direction of local transverse anisotropy and the plane perpendicular to it. Considering an initial configuration where collagen fibers are

wavy and follow different orientations, it is reasonable to assume that the interaction with the surrounding substance, or with other fibers, changes as the fibers stretch and realign.

In the Limbert model, a pair of orthogonal fiber families is embedded in a compressible matrix. The strain energy function is obtained by summation of each contribution:

$$W_{Limbert} = W_{vol}(J) + \sum_{i=1}^{2} W_{dev}^{i}(\bar{\lambda}_i) + W_1^i(\alpha_{i1}) + W_2^i(\alpha_{i2}, \bar{\lambda}_i) \tag{1.26}$$

with $\bar{\lambda}_i = J^{-\frac{1}{3}}\sqrt{I_{4i}}$ the deviatoric stretch (without loss of volume) of fiber family i, and:

$$\begin{aligned} \alpha_{i1} &= \frac{I_1 I_{4i} - I_{5i}}{\sqrt{I_3 I_{4i}}} \\ \alpha_{i2} &= \frac{I_{5i}}{I_{4i}^2} \end{aligned} \tag{1.27}$$

are invariants associated with transverse shear (perpendicular to the direction of local transverse anisotropy) and in-plane shear (i.e. the plane containing fiber family i), respectively. The total set of invariants is obtained by orthogonal decomposition of the stress tensor into hydrostatic pressure, deviatoric fiber tension, and in-plane and out-of-plane shear, and by identifying the strain invariants that directly yield this decomposition after differentiation of the strain-energy function. A detailed demonstration is provided in [153]. The volumetric component is defined as follows:

$$W_{vol}(J) = \frac{1}{4}\kappa\,(J^2 - 2\,lnJ - 1) \tag{1.28}$$

for which κ is the bulk modulus of the matrix.

The deviatoric strain-energy associated with fiber stretch in family i is defined by:

$$W_{dev}^{i}(\bar{\lambda}_i) = \begin{cases} n_i\mu_{0i}\left(\bar{\lambda}_i^2 + \frac{2}{\bar{\lambda}_i} - 3\right) + \xi_{i0}n_i\, ln\left(\bar{\lambda}_i^{-r_{0i}^2}\right),\ if\ \bar{\lambda}_i \le 1 \\ n_i k_B\theta\frac{L_i}{4L_{pi}}\left(2\frac{\bar{\lambda}_i^2 r_{0i}^2}{L_i^2} + \left(1 - \frac{\bar{\lambda}_i r_{0i}}{L_i}\right)^{-1} - \frac{\bar{\lambda}_i r_{0i}}{L_i}\right) + \xi_{i0}n_i\, ln\left(\bar{\lambda}_i^{-r_{0i}^2}\right),\ if\ \bar{\lambda}_i \ge 1 \end{cases} \quad (1.30)$$

Each fiber family is therefore considered as a set of polymer chains, of density per unit volume n_i, and described by the Worm-Like Chain constitutive law in tension, with initial end-to-end length r_{0i}, contour length L_i, and persistence length L_{pi}. Note that this formulation associates a non-null stiffness to fibers in compression, using a neo-Hookean behavior, with shear moduli μ_{0i}. The last term in each loading case corresponds to a repulsion energy that ensures that the chain does not collapse onto itself, similarly to the model of Kuhl et al. [111]. $W_1^i(\alpha_{1i})$ corresponds to the isotropic shear energy, effective in a plane transverse to the direction of family i, to which a shear modulus μ_{i1} is associated:

$$W_1^i(\alpha_{i1}) = \frac{\mu_{i1}}{2}(\alpha_{i1} - 2) \quad (1.31)$$

$W_2^i(\alpha_{i2}, \bar{\lambda}_i)$ corresponds to an anisotropic shear energy associated with the fiber-fiber and fiber-matrix interactions, along the direction of transverse anisotropy:

$$W_2^i(\alpha_{i2},\ \bar{\lambda}_i) = \frac{\mu_{i2}}{2}(\alpha_{i2} - 1)^2\frac{1}{1 + a_i e^{-b_i(\bar{\lambda}_i - \bar{\lambda}_i^c)}} \quad (1.32)$$

The left part of Equation 1.32 describes a classical one dimensional shear energy, while the right term is a sigmoid function, implemented to adjust the interaction energy for different stretching states [110]. A suggested justification for this behavior is that when adjacent fibers are stretching, the stiffness of their cross-links tends to increase, and therefore the shearing constraint is affected as well [152,154].

The Limbert model initially requires the identification of 23 physical parameters. The authors point out that the parameter set can be reduced by pre-injecting some of these parameters *ab initio* from structural measurements and microscale experimental characterizations. It is the approach that was chosen by Limbert [110] to validate the model, using data from biaxial tests of rabbit skin by Lanir and Fung [42], as shown in Figure 1.31. The fiber families are considered to be aligned with both tensile directions (parallel and perpendicular to the Langer lines), and parameter identification is possible because no inter-laminar shearing is taken into account. The compressive behavior was neglected, both fiber families were considered to have the same elastic properties, and parameters $(n_{0i}, a_i, b_i, \bar{\lambda}_i^c)$ were initially injected, either from the literature or by adjusting the sigmoid function to the J-curve region shifts. This data, as well as other calculated parameters, are reported in Table 1.3.

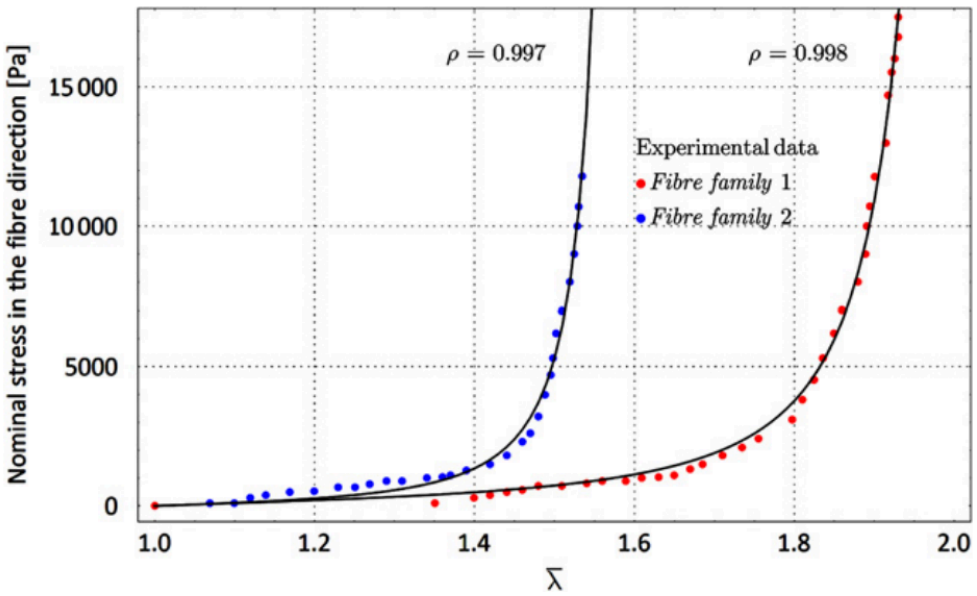

Figure 1.31. Simulations using the Limbert model to match experimental data from biaxial tests on rabbit skin, performed in directions perpendicular (fiber family 1) and parallel (fiber family 2) to the Langer lines, reported by Lanir and Fung [42]. High correlation coefficients are found for both orientations. From Limbert [110].

Table 1.3. Values identified with the Limbert model applied on the biaxial tests on rabbit skin reported by Lanir and Fung [42]. Fiber family 1 is aligned across the Langer lines, and family 2 is aligned along the Langer lines. Values that were computed are highlighted in grey.

Parameter		**Value**
Bulk modulus of the matrix	κ	$50\ kPa$
Sigmoid function parameter 1	a	50
Sigmoid function parameter 2	b	20
Sigmoid function locking stretch for fiber family 1	$\bar{\lambda}_1^c$	1.15
Sigmoid function locking stretch for fiber family 2	$\bar{\lambda}_2^c$	1.40
Chain density	n_{0i}	$7 \cdot 10^{21}\ m^{-3}$
Tropocollagen (Type I) contour length	L_i	$309\ nm$
Transverse shear modulus	μ_{i1}	$150.123\ Pa$
Fiber-fiber/fiber-matrix shear modulus	μ_{i2}	$9.981\ Pa$
Collagen persistence length for fiber family 1	L_{p1}	$22\ nm$
Initial length of crimped collagen for fiber family 1	r_{01}	$155\ nm$
Collagen persistence length for fiber family 2	L_{p2}	$65\ nm$
Initial length of crimped collagen for fiber family 2	r_{02}	$198\ nm$

The constitutive framework proposed by Limbert et al. results in a notoriously large number of parameters, and although the authors suggest that it can be reduced by pre-setting some of them based on prior knowledge of the structural arrangement, physical properties of the components, or adjustments with respect to the experimental J-curve, several problems can arise. First, convexity of the strain-energy potential must be addressed with care [141,155]; with such a large parameter range, uniqueness of a solution that minimizes the optimization problem cannot be guaranteed. This can be attenuated by restricting each parameter to a value within a physically realistic range; however, this may not be sufficient, as our current knowledge of the structure-mechanics relationship of the constituents of skin is rather limited, and different initial guesses on the parameter values may easily lead to different solutions. This statement is also relevant to other structural models with a large parameter set to identify. Secondly, the model

presupposes that the family of fibers are aligned with both tensile directions from Lanir and Fung's experiment, attributing transitions in the tensile J-curve solely to the fiber straightening process. Fiber reorientation is not considered as a participating process in the nonlinear response of the tissue. Moreover, the worm-like chain model is essentially phenomenological, thus relating the parameters of the model with physical quantities reported elsewhere may offer limited perspectives. The other calculated moduli are also difficult to relate with any physical entity of the structure, or a microstructurally based interaction. Further analyses, such as molecular dynamics of interacting collagen chains, *in situ* microscopic characterization, and a better knowledge of the structural arrangement of the building components of skin, could be conducted to inform the model. Nonetheless, an equivalent Young's modulus was identified for collagen fibers, using $E_{ci} = 4L_{pi}k_B\,\theta/(\pi R^4)$ and assuming that the chain is contained within a cylindrical volume of radius R. Using calculated parameters for fiber families 1 and 2 (see Table 3.1), one can find 293 MPa and 865 MPa, respectively, which falls within an acceptable range.

The semi-structural models of skin presented above commonly consist of a superposition of the contributions of the ground substance and the fiber families, oriented along a discrete, limited number of directions. Tissue anisotropy is therefore attributed to the arrangement of collagen fiber families, and structural parameters, such as fiber crimp, can be implemented to describe the nonlinear elastic response of skin. Still, the distinct models that are used to represent each component remain phenomenological, and they do not necessarily provide an accurate description of the microscale processes occurring in the tissue. Fiber alignment is often limited to two or three principal directions, and the out-of-plane component is often neglected, except in the anisotropic eight-chain model. A structurally-based model of fibrous tissue yields

physically relevant parameters only if the description of the fiber network is well informed with structural data [114], which is generally obtained from microscopy imaging. For skin, this implies that fiber splay and the tridimensional interweaving of the collagen network should be included in the constitutive framework.

1.3.4. Distributed Fiber Models of Skin with Fiber Dispersion

Fiber orientations in skin are distributed along preferred directions, described by the Langer lines [13,70]; however, some degree of dispersion around these principal orientations is observed [140,156]. After application of tensile loads (Figure 1.17.b-c.), this configuration is replaced by straightened fibers aligned closer to the tensile direction. The fibrils show a waviness with a reduced wavelength which is thought to be due to shrinking after fracture. It has been the goal of physically-based constitutive models of skin to incorporate these processes, namely gradual realignment of fibers and straightening. It is the coupled contribution of these processes that results in the nonlinear response of the material [41]. We present here the two main approaches used to incorporate fiber dispersion in the constitutive modeling of skin: angular integration (AI) and via generalized structural tensors (GST). The Lanir model and the Gasser-Ogden-Holzapfel model are introduced as examples for each approach. A more detailed classification of dispersed fiber models of soft collagenous tissues is reported by Holzapfel et al. [157].

1.3.4.1. An Example of the Angular Integration Approach: the Lanir Model

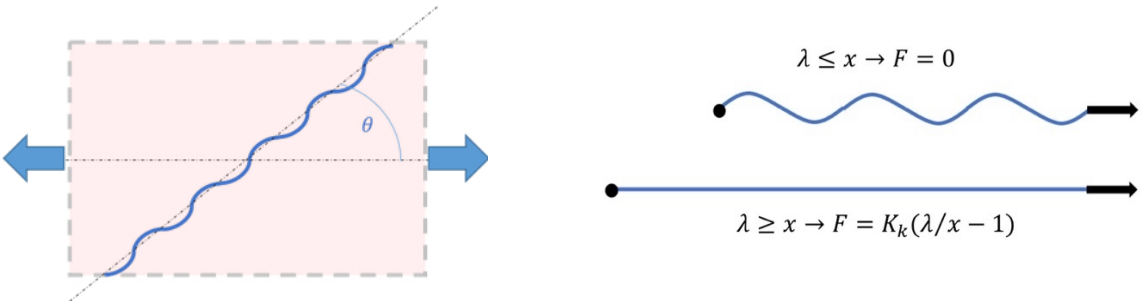

Figure 1.32. Left: Schematic illustration of a crimped collagen fiber in a rectangular RVE, oriented by an angle θ with the principal direction. In the Lanir model, fiber orientations follow a $R_k(\theta)$ distribution. Right: Illustration of the straightening model of a collagen fiber. When the stretch is below a locking value x, no load is needed to straighten it. When fully uncrimped, the fiber follows a linear elastic law.

Perhaps the first structurally-based constitutive model for soft collagenous tissues, the model introduced by Lanir in 1983 [158] is also one of the few that takes into account the contribution of elastin to the total deformation of the tissue. The model is based on a Representative Volume Element (RVE) consisting of an isotropic ground substance, modeled by a neo-Hookean function, a fraction ϕ_c of collagen and ϕ_e of elastin:

$$W_{Lanir} = (1 - \phi_c - \phi_e)\frac{\mu}{2}(I_1 - 3) + \phi_c W_c(\lambda) + \phi_e W_e(\lambda) \qquad (1.33)$$

Each fiber is oriented at an angle θ with a chosen principal direction and these orientations follow a statistical distribution $R_k(\theta)$; $(k = \{c, e\})$. The schematic illustrations in Figure 1.32 describe the corresponding RVE and the straightening process. It is assumed that collagen fibers are crimped and follow a one-dimensional linear elastic behavior only when unfolded; they buckle under compressive loads and no load is required to fully straighten them. The strain in the fiber is purely uniaxial. Elastin is already straight and linear elastic as well.

For collagen, the locking stretch x also follows a probability distribution function $D_c(x)$, implying that not all fibers follow the same geometry and curvature, and therefore a different

stretch is required to fully straighten them. The energy density function of a given fiber type is then defined by integration of the elastic energy over the angular and locking distributions:

$$W_c(\lambda) = \int_0^{\pi} \mathcal{R}_c(\theta) \int_1^{\lambda(\theta)} D_c(x) \frac{K_c}{2} \left(\frac{\lambda(\theta)}{x} - 1 \right)^2 dx d\theta$$
$$W_e(\lambda) = \int_0^{\pi} \mathcal{R}_e(\theta) \frac{K_e}{2} (\lambda(\theta) - 1)^2 d\theta \tag{1.34}$$

where K_k is the stiffness of fiber type k and $\lambda(\theta)$ is the stretch in the direction of the fiber. Thus, numerical integration is required in the Lanir model. In its early formulation, Lanir [158] opted for normally distributed orientations restricted to a two-dimensional plane, and locking stretches for collagen, and a uniform distribution for straight elastin fibers. In an extended version of the same model proposed by Lokshin and Lanir [159] for uniaxial tests on rat skin, it was considered that solely fibers aligned parallel to the tensile direction contribute to the deformation process. Fiber realignment was neglected, and the influence of the matrix hydrostatic pressure on fiber rotation as well. Hence, fibers that are not aligned with the tensile direction are either undergoing compression or are not fully stretched, and therefore withstand no load. For fiber uncrimping, a beta distribution was chosen for the locking stretch, because it can be integrated over a finite interval and it can be asymmetric. Their nonlinear elastic formulation was paired with a Quasi-Linear Viscoelastic (QLV) model to study time-dependent processes, which will be described in the next section.

Table 1.4. Parameters of the Lanir model applied for skin in the works of Meijer et al. [160] and Jor et al. [161]. Values in grey indicate parameters that were identified by Finite Element Analysis (FEA) while other values were implemented *ab initio*, from data in the literature. N.A.: Not Applicable.

Reference	**Meijer et al.** [160]		**Jor et al.** [161]	
Experimental Method	*In vivo* uniaxial stretching of human skin + Image tracking + FEA		*Ex vivo* biaxial stretching of porcine skin + Image tracking + FEA	
Matrix Stiffness $\boldsymbol{\mu}$	None		$2.5 - 15.9\ KPa$	
Collagen Volume Fraction $\boldsymbol{\phi_c}$	0.3 [162]		0.3 [162]	
Elastin Volume Fraction $\boldsymbol{\phi_e}$	0.02 [162]		None	
Collagen Orientation $\boldsymbol{R_c(\theta)}$	$1/\pi + C_1(\cos^4(\theta - C_2) - 0.375)$		π-periodic Von Mises Distribution $(\mu_\theta, \kappa_\theta)$	
Elastin Orientation $\boldsymbol{R_e(\theta)}$	Uniform Distribution $1/\pi$		N.A.	
Collagen Undulation $\boldsymbol{D(x)}$	Normal Distribution	$\mu_x = 1.418 - 1.433$ $\sigma_x = 0.2$ [162]	Gaussian Distribution	$\mu_x = 1.04 - 1.34$ $\sigma_x = 0.2$ [162]
Collagen Stiffness $\boldsymbol{K_c}$	$50.9 - 85.7\ MPa$		$48 - 366\ MPa$	
Elastin Stiffness $\boldsymbol{K_e}$	$1\ MPa$		N.A.	

Modeling of skin's elasticity with the Lanir approach can be encountered in the works of Jor et al. [161] and Meijer et al. [160]. Their assumptions and findings are compared Table 1.4. In both studies, displacements on the surface of the skin were measured using image-based point tracking, and a Finite Element Analysis mesh grid was superposed to identify a set of parameters for the Lanir model. In order to limit the number of parameters to identify, and consequently save computational time, quantitative data from the literature is pre-injected into the model. Characterizations of the structural arrangements of collagen and elastin can indeed be useful to estimate their volume fraction, distribution, splay, and undulation. Jor et al. [161] chose to neglect the contribution of the elastin network, focusing primarily on the response at high strains of skin, while Meijer et al. [160] considered that the contribution of the matrix only

takes place through hydrostatic pressure. Thus, parameter identification mainly focuses on collagen stiffness and mean undulation in each case.

Studies with experimental measurements on isolated collagen fibers report values from 30 MPa up to 1570 MPa for fiber stiffness [10] and of 1.2-1.6 for mean undulation (i.e. locking stretch) [162], which is in agreement with identified ranges in both studies. Computed collagen stiffness seems to fall closer to the lower bound of the experimental values, which could be attributed to the fact that, in the Lanir model, fiber-fiber and matrix-matrix sliding are ignored, although they might be a cause for tissue failure rather than failure of collagen itself. Moreover, these shearing interactions contribute also to the aggregation and realignment of fibers in the tensile direction.

Other models using the angular integration approach can be also encountered in the works of Tonge et al. [163] for skin, Freed et al. [164] and Driessen et al. [165] for cardiovascular tissues, and Federico and Gasser [166] for articular cartilage. Notable changes in the methods include two-dimensional or three-dimensional distributions, and different probability density functions (Gaussian [158,165], Beta [167], and Von Mises distributions [163,166], for example).

The angular integration approach accounts for fiber splay by introducing a probability density function as a continuous weighting factor for angular orientation [164]. Assuming an accurate estimation of collagen dispersion in the dermis, it is a rather elegant approach that introduces a relatively small number of additional parameters. A significant limitation of the AI approach is the considerable added computational cost, due to the fact that the integration needs to be performed for each point over the unit sphere [157,168].

1.3.4.2. The Gasser-Ogden-Holzapfel Model: a GST Approach

The Gasser-Ogden-Holzapfel (GOH) model [169] was first introduced to capture the deformation process of the arterial wall, an orthotropic soft tissue. Two main fiber families are considered, aligned with the material plane. For each fiber family, a generalized structure tensor $\boldsymbol{H_{0i}}$, is defined:

$$\boldsymbol{H_{0i}} = \kappa_i \boldsymbol{I} + (1 - 3\kappa_i)\boldsymbol{B_{0i}} \tag{1.35}$$

in which κ_i is the three-dimensional dispersion factor of family i, an integral of the probability distribution function of fiber orientations around the average direction over a unit sphere:

$$\kappa_i = \frac{1}{4}\int_0^{\pi} \rho_i(\theta) \sin^3\theta \; d\theta \tag{1.36}$$

Where $\rho_i(\theta)$ is the assumed distribution of fiber family i. $\kappa_i = 0$ corresponds to a fiber family where all the fibers are perfectly aligned in the same direction, whereas for $\kappa_i = 1/3$ all directions are equiprobable (isotropic). Note also that non-symmetric or bimodal fiber distributions can be incorporated, which yields a slightly more complex form of $\boldsymbol{H_i}$ [114,157]. A planar dispersion can also be assumed, in which case:

$$\boldsymbol{H_{0i}} = \kappa_{i2D} \boldsymbol{I_2} + (1 - 2\kappa_{i2D})\boldsymbol{B_{0i}} \tag{1.37}$$

Where $\boldsymbol{I_2}$ is the two-dimensional identity tensor, in the plane of fiber alignment, and κ_{i2D} is the planar dispersion of fiber family i [157,163]. The energy density function was defined as follows:

$$W_{GOH} = \frac{\mu}{2}(I_1 - 3) + \sum_{i=1}^{2} \frac{k_{i1}}{2k_{i2}} [exp(k_{i2}(\boldsymbol{H_{0i}}: \boldsymbol{C} - 1)^2) - 1] \tag{1.38}$$

One can observe that the first term of Equation 1.38 is the neo-Hookean behavior applied to describe the matrix, with shear modulus μ, while fiber stretching is described with exponential

terms. k_{i1} and k_{i2} are material parameters proper to each fiber family. With dispersion factors κ_i; $i = (1,2)$ and assuming a perpendicular arrangement of fiber families, this potentially results in eight parameters that need to be identified.

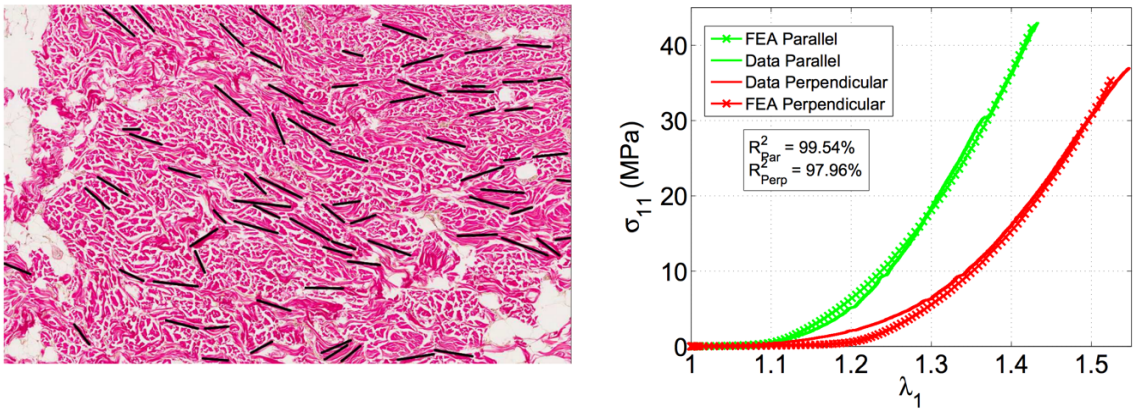

Figure 1.33. Left: Manual segmentation of collagen from histology image. Elongated fibers are marked by black lines, their orientation is then measured manually to estimate the main orientation and the dispersion factor. Right: Comparison of experimental data from uniaxial tensile tests with simulations based on the GOH model for samples parallel (green) and perpendicular (red) to the Langer lines. From Ní Annaidh et al. [70].

In the context of skin mechanics, Ní Annaidh et al. [70] implemented the GOH model with uniaxial tests of human samples. They used histological cross-sections of slides taken parallel to the epidermis and estimated the distribution of orientations of the collagen fibers. Straight collagen fiber segments were identified and are marked by black lines in Figure 1.33. These lines tend to align with the horizontal direction. To simplify the approach and reduce the number of parameters, it was assumed that the two main fiber families are oriented symmetrically to the tensile direction and possess the same material properties. An orientation angle γ and the dispersion factor κ were determined and injected into the model. Thus, it is the first model introduced here where parameters are determined based on structural observations, instead of phenomenological ones. Very good agreement between experimental results and Finite Element Analysis calculations based on the GOH description were found, for tests performed along and across the Langer lines (see Figure 1.33, right).

In a comparative analysis of models to simulate full field bulge tests on skin, Tonge et al. [163] compared a 3-D GOH, a 2-D GOH, and a fully integrated fiber (AI) models to match their experimental results. Their transversely isotropic 3D-GOH model assumes the existence of only one fiber family, with a three-dimensional dispersion vector, whereas for the 2D-GOH model the out-of-plane direction is restricted, which affects the structural tensor $\boldsymbol{H}$, as described in equation 1.37. The fully integrated (AI) model uses a Von Mises distribution and assumes a planar arrangement of fibers. In their conclusions, the authors observed that a three-dimensional distribution does not seem appropriate to represent the actual collagen fiber distribution in skin, and that both formulations of the GOH model have difficulties reflecting the anisotropy of the material, which was much more successful with the FI model. An advantage of the former formulation is that the energy density function presents a closed-form expression whereas the latter necessitates numerical integration. It is also relevant to point out that better results have been obtained with two fiber families instead of one, and that these observations are specific to the bulge tests reported in their study.

Buganza-Tepole et al. [170] used the GOH model for simulations of tissue expansion methods to identify the one that would minimize the concentration of stresses, which they associated with the likelihood of tissue necrosis. Their study is a remarkable illustration of the application of structural models to predict tissue behavior and consequently improve medical techniques.

The GST approach differs from the AI method mainly by the fact that the distribution of fiber orientations is directly averaged and incorporated into the structural tensors $\boldsymbol{H}_i$. This results in a superior computational efficiency, compared to AI, as the angular integration is only performed once [168]. However, a resulting limitation of this averaging method is that

selectively attributing a different behavior for fibers undergoing compression or straightening is no longer possible, which does not reflect the real behavior of the tissue [114]. This is in agreement with the observations made by Tonge et al. [163] in their comparative analysis. Methods attempting to exclude compressed fibers in the generalized structure tensor, by either reducing the integration interval in the dispersion parameter, or introducing a Heaviside function in the strain-energy of the fibers, were reviewed by Holzapfel et al. in [114]. It is also not possible to consider a distributed fiber undulation, as it can be in the AI method.

Dispersed fiber models present an improvement in the representation of the collagen network, and the angular distribution of fibers can be quite accurately captured by a selected probability density function, with a reduced amount of added constitutive parameters. This implies that some prior information on fiber dispersion in the material is needed, whether it is assumed from general observations of the skin microstructure, or if it is directly measured on the tested sample. With higher structural accuracy, the deformation processes in the structure are more likely to reflect reality and the obtained parameters gain in physical relevance. Variations in these parameters can be then attributed to differences in tissue anisotropy (i.e. dispersion), fiber concentration, or crimp. However, these models do not take into account fiber-fiber interactions, such as the influence of inter-fiber cross-linking, which may play a role in fiber recruitment, tissue stiffening, or delamination before failure. The improved structural accuracy is also hindered by the added computational cost of angular integration. A compromise to this shortcoming was proposed by Flynn et al. [171], who suggested the use of a discretized weighted fiber distribution for collagen (with 6 principal fiber directions). A closed-form solution of the strain-energy function becomes possible, and distributed fiber undulation can be considered, as well as potential fiber-fiber interactions. Nonetheless, material anisotropy and

continuous fiber realignment are less accurately captured with this approach, and the stress-stretch curve shows more pronounced transitions as fiber families get recruited.

Another aspect of skin mechanics that needs to be taken into consideration is viscoelasticity, as the nonlinear elastic formulations described so far do not include the influence time-dependent processes.

1.1 Modeling Viscoelasticity

In tests such as stress-relaxation and creep, the viscoelastic behavior of skin is revealed and characterized by a response that changes with time and loading history. In loading-unloading tests, the hysteresis of the stress-strain curve also indicates a dissipative viscoelastic behavior. The strain rate sensitivity of the tissue is another example of this behavior. Hence, for a more complete description of the mechanical response of skin under different types of loads, it is important to consider the effect of time-dependent processes occurring in the material. In the case of soft fibrous tissues, viscoelastic effects are often decoupled from the elastic contribution, and the total response of the material is obtained by superposition of the elastic and time-dependent processes.

1.3.4.3. Quasi-Linear Viscoelastic Theory (QLV)

Fung [125] first proposed in 1967 to describe the stress-strain relationship of soft biological materials by linear decomposition of stresses into an elastic part and a history-dependent part, i.e. a viscoelastic component, in an integral form:

$$\sigma(t) = \int_0^t g(t-\tau)\frac{\partial \sigma_{el}(\tau)}{\partial \tau} d\tau \tag{1.39}$$

where $g(t)$ is the reduced relaxation function, and σ_{el} is the instantaneous elastic nominal stress. The elastic stress can be any nonlinear function chosen to describe tissue deformation.

Equation 1.39 contains a history-dependent component via the time integral and is essentially a convolution between the reduced relaxation $g(t)$ and the time derivative of the elastic component of the stress. Different forms for $g(t)$ can be encountered, including Prony series [11,67], exponential functions [73,133,159,172], logarithmic functions [173], and power law functions [174]. The QLV model generally offers good flexibility with a tunable quantity of descriptive parameters. Liu and Yeung [133] implemented an exponential stress-strain relationship and a sum of three decreasing exponentials for the relaxation function. Relaxation of swine skin, taken at different relaxation strains, was very well captured (see Figure 1.34). Bischoff et al. [172] modeled porcine skin with QLV by coupling an orthotropic worm-like chain model and an exponential integral relaxation function, and found very satisfying results with only seven parameters. Stress relaxation and cyclic loading were well captured by the model. However, researchers highlight the lack of consistency of this approach, with different parameters identified for different loading conditions [172], and an inability to capture short-term viscoelastic phenomena, such as preconditioning or strain rate sensitivity [67].

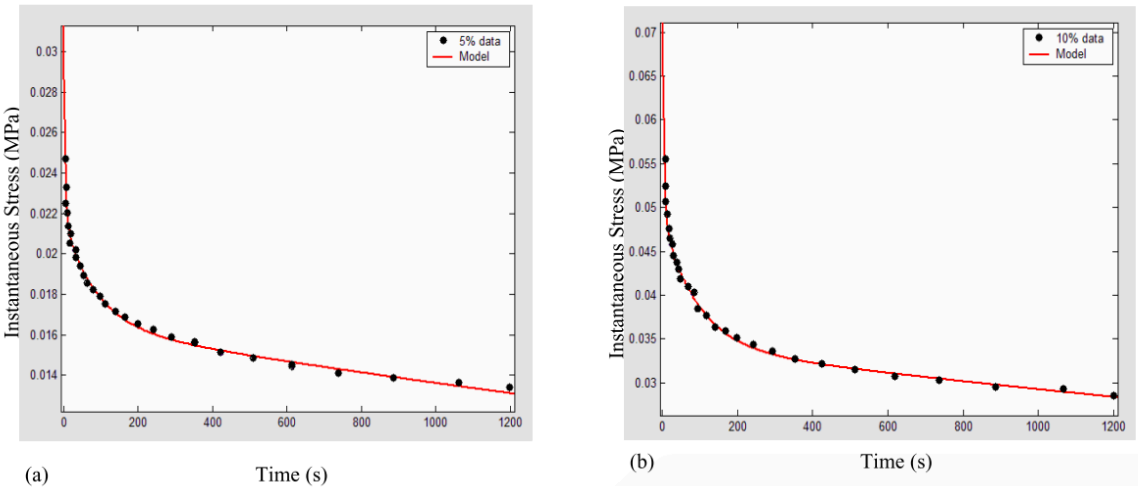

Figure 1.34. Stress relaxation tests on swine skin, initiated at different strains (black dots). Because it encompasses the loading history, the QLV theory (red lines) fits very well both for cases. Adapted from Liu and Yeung [133].

1.3.4.4. Differential Viscoelastic Models

According to the *principle of fading memory* [9,175], recent deformations have a greater influence on the stress-state than those that happened in a distant past. Thus, one apparent limitation of the QLV approach is that the integral form captures the entire deformation history without any emphasis on recent events, an important consideration at high deformation speeds. Following this observation, Pioletti et al. [56] proposed a differential viscoelastic law for soft biological materials, based on the Clausius-Duhem inequality under isothermal conditions [176]:

$$\left(\boldsymbol{S} - 2\rho_0 \frac{\partial W_e}{\partial \boldsymbol{C}}\right) : \frac{\dot{\boldsymbol{C}}}{2} \geq 0 \tag{1.40}$$

where $\boldsymbol{S}$ is the second Piola-Kirchhoff stress tensor, $\boldsymbol{C}$ the right Cauchy-Green deformation tensor, $\dot{\boldsymbol{C}}$ its first time derivative, ρ_0 the initial material density, and W_e the elastic potential. For a viscoelastic material subject to energy dissipation, one can assume the existence of a viscoelastic potential W_v [56], such that:

$$\boldsymbol{S} = 2\rho_0 \frac{\partial W_e}{\partial \boldsymbol{C}} + 2\frac{\partial W_v}{\partial \dot{\boldsymbol{C}}} \tag{1.41}$$

The formulation detailed in Equation 1.41 takes into account rate-dependency and enables the modeling of nonlinear viscoelastic materials via the introduction of suitable elastic and viscoelastic potentials. Pioletti and al. [56] successfully modeled the strain-rate sensitivity of tendon and ligament using a Veronda and Westmann elastic potential [126] and the following viscous potential:

$$W_v = \frac{\eta}{4} tr\dot{\boldsymbol{C}}^2 (tr\boldsymbol{C} - 3) \tag{1.42}$$

with η as a viscosity factor. Very good consistency is obtained with a reduced number of parameters, although the assumption of an isotropic material is disputable. Limbert and Middleton [177] further extended this framework to transverse isotropy using tensors, and found as well good agreement with their experimental results.

1.3.4.5. Generalized Maxwell Models and Nonlinear Extensions

A Generalized Maxwell Model is an arrangement in series or in parallel of viscous and elastic components, usually mimicking the microscale arrangement of constituents within the material. There are three common representations: the Maxwell, the Kelvin-Voigt, and the Standard models. Other Generalized Maxwell viscoelastic models can be formed by assembling, in series or in parallel, these three classic formulations, such as the Burgers model for example. At higher levels of complexity, it becomes more difficult to analytically solve governing stress-strain equations, and numerical solving needs to be performed. Each building block of the model can be used to represent a sub-unit or constituent of the tissue at a given hierarchical level. For example, Puxkandl et al. [178] proposed a model for collagen fibers in tendons consisting of two Kelvin-Voigt cells in series: one block to describe fibrils, and the other block for the surrounding proteoglycan matrix. This formulation was used to quantify effects of strain rate on the apparent viscosity of tendons. It is however less common to encounter Generalized Maxwell models used to represent the viscoelasticity of skin. The structural arrangement is more complex than in the case of tendons, where collagen fibers are mainly aligned with the direction of tension [172,178], and the standardized elastic block cannot capture the nonlinear behavior of skin in tension. Instead, linear strain and stress decomposition can be extended to nonlinear constitutive laws, both for the elastic components as well as the inelastic (viscous) ones. For example, Yang et al. [41] introduced a modified Maxwell model

for skin using a polynomial function for the elastic constitutive equation between the external stress and elastic strain, to take into account the nonlinearity of the tissue. Another formulation for viscoelasticity, based on the Standard model, was proposed by Bergstrom and Boyce [179], and is presented in the following section.

1.3.4.6. Bergstrom-Boyce Model

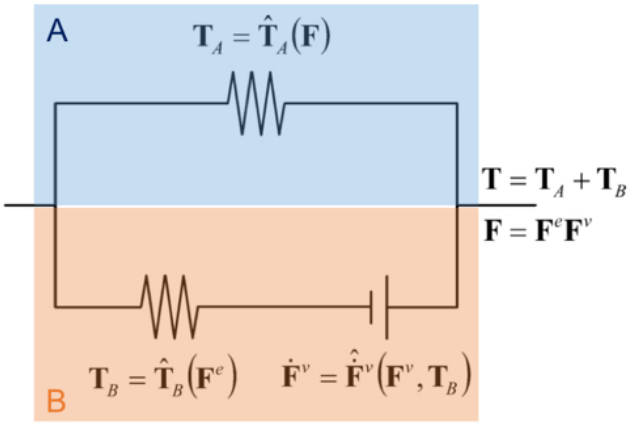

Figure 1.35. Schematic description of the rheological model based on the Standard Maxwell model using the Bergstrom-Boyce formulation of viscoelasticity, implemented by Bischoff et al. [147] to capture the mechanical behavior of skin. Component A is purely elastic, component B contains a viscous part.

Bischoff et al. [147] implemented the Bergstrom-Boyce model for their modified rheological model of skin. Initially intended for the characterization of the viscoelastic properties of rubber-like elastomers, Bergstrom and Boyce's constitutive law [179] is based on the proposition that an elastomer can be modeled as two interacting networks of polymers, the first one capturing the elastic (or equilibrium) response of the material and the other one the time-dependent deviation from equilibrium, as earlier suggested by Roland [180]. This can be represented by a modified Standard Maxwell element (see Figure 1.35). In this representation the total true stress is obtained by summation of the stress state in both components $T = T_A + T_B$. The deformation gradient in the same in both networks: $\boldsymbol{F} = \boldsymbol{F}_A = \boldsymbol{F}_B$. The purely elastic

component A follows an orthotropic Arruda-Boyce model. For the sake of simplicity, it is described here for the isotropic case:

$$W_A = n_A k_B \Theta \left[\lambda_{lock_A} \lambda_{chain_A} \beta - \lambda_{lock_A}^2 \, ln\left(\frac{sinh\,\beta}{\beta}\right)\right] \tag{1.43}$$

The true stress-stretch relationship $T_A(\lambda_{chain_A})$ is then obtained by derivation, where $\lambda_{chain_A} = \sqrt{tr(\boldsymbol{B}^*)/3}$ is the effective distortional stretch of chain A, and $\boldsymbol{B}^* = J^{-2/3}\boldsymbol{F}\boldsymbol{F}^{\boldsymbol{T}}$. For component B, the transformation gradient is decomposed into purely elastic and viscous components: $\boldsymbol{F_B} = \boldsymbol{F_B^{el}}\boldsymbol{F_B^{v}}$. The elastic block of component B is also described by the Arruda-Boyce model. The effective distortional elastic stretch in network B can be obtained by isolating the elastic contribution of the transformation gradient: $\lambda_{chain_B}^{el} = \sqrt{tr\left(\boldsymbol{B}_B^{el^*}\right)/3}$, with $\boldsymbol{B}_B^{el^*} = J_B^{el^{-2/3}} \boldsymbol{F_B^{el}} \boldsymbol{F_B^{el^T}}$, and $J_B^{el} = \det\left(\boldsymbol{F_B^{el}}\right)$.

The velocity gradient of the viscous network is also defined $\boldsymbol{L_B^{v}} = \boldsymbol{\dot{F}_B^{v}}\,\boldsymbol{F_B^{v^{-1}}}$ where the first term corresponds to the time derivative of the viscous deformation gradient tensor. In the absence of plastic spin [179], the velocity gradient becomes equal to the viscous rate of change $\boldsymbol{D_B^{v}}$, which, in the Bergstrom-Boyce framework, is constitutively prescribed by:

$$\boldsymbol{D_B^{v}} = \dot{\gamma}_v \, \frac{dev(\boldsymbol{T_B})}{\|\boldsymbol{T}_B\|} \tag{1.44}$$

where $\dot{\gamma}_v$ is the effective deformation rate (or reptation coefficient), and $dev(\boldsymbol{T_B})/\|\boldsymbol{T_B}\| = \boldsymbol{N_v}$ is a vector defining the direction of the stress driving the viscous deformation. The expression of $\dot{\gamma}_v$ is then based on the theory of reptation [147]:

$$\dot{\gamma}_B = \dot{\gamma}_0 (\lambda_B^v - 1)^C \left(\frac{\|\boldsymbol{T}_B\|}{\tau}\right)^m \tag{1.45}$$

and $\dot{\gamma}_0$, C, τ, and m are material parameters, and $\lambda_B^v = \sqrt{tr\left(\boldsymbol{F_B^v F_B^{v\,T}}\right)/3}$. Hence, a relationship between $\boldsymbol{F_B^v}$ and the nominal stress tensor $\boldsymbol{T_B}$ can be obtained. By numerical integration, the total stress-stretch relationship can then be solved. Bischoff et al. [147] employed the orthotropic formulation of this method to fit the stress-relaxation and the loading-unloading curves from Lanir and Fung [42], performed biaxially in the two main orientations. Their results, reproduced in Figure 1.36, show that the model can capture time-dependent processes quite well, with a consistent set of parameters. Inaccuracies could stem from the lack of knowledge of the tissue's real orientation, rather than from the model itself. A drawback of the Bergstrom-Boyce model is that, in order to capture viscoelasticity, 10 additional material parameters are involved. Moreover, the description developed in this constitutive framework does not take into consideration the real structure of the tissue, and the parameters involved are purely phenomenological. The freely-jointed chain model, used to describe fiber stretch, is not defined for values of λ above λ_{lock}, meaning that the fiber cannot stretch more than its maximal extended length. This poses substantial problems in terms of representation of the deformation sequence of collagen fibers in the dermis [41].

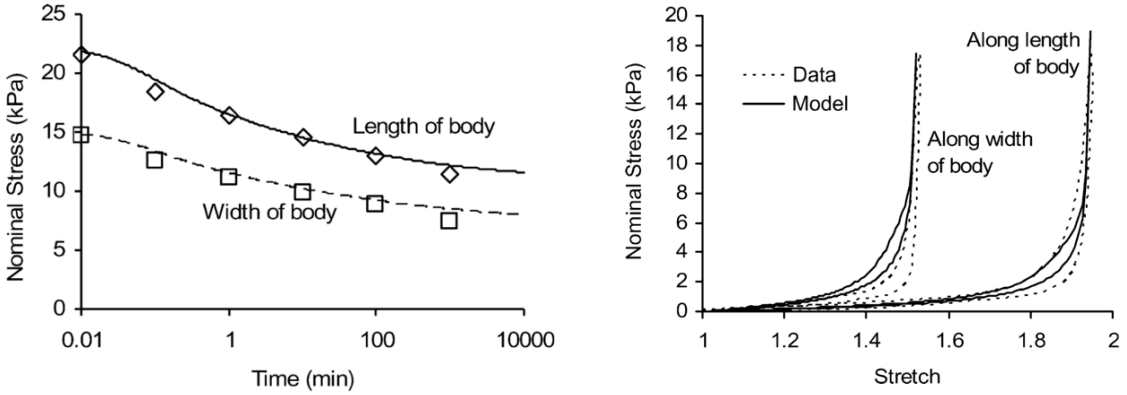

Figure 1.36. Experimental data from planar biaxial tests on rabbit skin by Lanir and Fung [42], captured by the Bergstrom-Boyce model. Left: Stress relaxation done along the length and the width of the body (experiments – symbols; simulations - lines). Right: Loading/unloading tests conducted along the length and the width of the body (experiments – dashed lines; simulations – lines). From Bischoff et al. [147].

In order to provide a better description of the tissue structure, the approach used by Bischoff et al. [147] can adapted to a rheological framework with a matrix component and a fiber component in parallel, as suggested by Limbert [9]. The method described in the section above can then be applied to each component, where separate elastic and viscoelastic sub-components are introduced for each network. Note that for the elastic components, other models than the eight-chain function can be implemented.

The decomposition of the total deformation in an elastic and a viscoelastic component offers flexibility in terms of selecting separate constitutive behaviors for each contribution, including the ones listed above. Models for the viscoelastic component are generally simple and phenomenological, mainly to reduce the set of added parameters, but also because the physical time-dependent processes occurring in the tissue, such as internal reorganization of the microstructure, fluid flow, fiber sliding, and intrinsic component viscoelasticity, are still not fully understood and lack experimental characterization. Furthermore, said processes are believed to be the cause of other dissipative and loading history-dependent features of the

mechanical behavior of skin, which should be taken into consideration and are developed in the next section.

1.3.5. Modeling the Dissipative Behavior of Skin

In his book on the Mechanical Properties of Living Tissues, Fung [181] listed several physical features characteristic of soft biological tissues under uniaxial tension:

- The stress-strain relationship of the material is nonlinear,
- A hysteresis loop can be observed during loading-unloading tests,
- Stress relaxation occurs at constant strain,
- Preconditioning: with repeated loading cycles, the tissue reaches a steady-state, and the hysteresis loop reduces in width with each cycle,
- The stress relaxation at a fixed stress level reduces with repeated cycles,
- The hysteresis response is nearly independent of strain rate.

A number of these features are illustrated for skin in Section 2.4. To the authors' knowledge, experimental data on skin is lacking on the effect of strain rate on the hysteresis loop. Nonlinear elasticity is a well-known property of skin, and has been developed in detail in this review. Stress relaxation and hysteresis, to which creep and strain rate sensitivity can be added, reflect the viscoelastic behavior of the material, as discussed in the previous section. However, nonlinear elasticity and viscoelasticity are not sufficient to explain the last three material properties identified by Fung [181]. The preconditioning behavior, the displayed Mullins effect (see Section 2.4.9), and the existence of remnant strains after each loading-unloading cycle (see Figure 1.26a.) are clearly indicative that the loading history has an influence on the material response. This suggests that irreversible changes in the tissue have occurred, and that a new equilibrium state is being reached. These changes are believed to be caused by rearrangements

of the microstructure during loading, and a redistribution of the internal fluids [135,182]. Interfibrillar cross-links may break and reform, affecting the resting configuration of the material. At larger strains, more pronounced irreversible processes take place: fiber sliding, delamination, and finally tissue failure are observed [41]. This is translated by a softening response of the material prior to failure.

The aforementioned phenomena are often neglected in constitutive models of skin, generally because the reference experiments are taken before failure and are limited to single uniaxial tests, one loading-unloading cycle, or normalized stress relaxation. Some models that incorporate these dissipative inelastic properties are presented in this section, with either a phenomenological approach or a semi-structural description of the processes at stake.

1.3.5.1. The Rubin-Bodner Model

Rubin and Bodner [182] described in 2002 a formulation to model the dissipative response of soft tissue, based on phenomenological elastic-viscoplastic constitutive equations. Their objective was to fully address the physical features of soft biological tissues identified by Fung [181], with a three-dimensional model capturing material anisotropy. In the elastic-viscoplastic theory, history dependent state-variables are introduced and determined by evolution equations [182,183].

The current configuration of the material is taken at time t. The velocity gradient tensor $\boldsymbol{L}$ is introduced as time derivative operator of the deformation gradient $\boldsymbol{F}$:

$$\dot{\boldsymbol{F}} = \boldsymbol{L}\boldsymbol{F} \tag{1.46}$$

The rate of deformation tensor $\boldsymbol{D}$ is then expressed as the symmetric part of the velocity gradient:

$$\boldsymbol{D} = \frac{1}{2}(\boldsymbol{L} + \boldsymbol{L}^{\boldsymbol{T}}) \tag{1.47}$$

In the presented continuum description, $\boldsymbol{D}$ effectively serves as a measure of the evolution of the deformation. It is convenient to separate the total deformation tensor $\boldsymbol{b}$ ($\boldsymbol{b} = \boldsymbol{F}\boldsymbol{F}^{\boldsymbol{T}}$), into the dilatation $J = \det \boldsymbol{b}$ and a unimodular distortional component $\boldsymbol{b}^* = J^{-2/3}\boldsymbol{b}$. Since $\det \boldsymbol{b}^* = 1$, two independent invariants of $\boldsymbol{b}^*$ can be introduced:

$$\begin{aligned} \beta_1 &= \boldsymbol{b}^* : \boldsymbol{I} \\ \beta_2 &= \boldsymbol{b}^* : \boldsymbol{b}^* \end{aligned} \tag{1.48}$$

The time derivatives of J, $\boldsymbol{b}^*$, β_1, and β_2 are expressed via the evolution equations:

$$\begin{aligned} \dot{J} &= J\boldsymbol{D} \cdot \boldsymbol{I} \\ \dot{\boldsymbol{b}^*} &= \boldsymbol{L}\boldsymbol{b}^* + \boldsymbol{b}^*\boldsymbol{L}^{\boldsymbol{T}} - 2/3\,(\boldsymbol{D} : \boldsymbol{I})\boldsymbol{b}^* \\ \dot{\beta}_1 &= 2[\boldsymbol{b}^* - 1/3\,(\boldsymbol{b}^* : \boldsymbol{I})\boldsymbol{I}] : \boldsymbol{D} \\ \dot{\beta}_2 &= 4[\boldsymbol{b}^{*2} - 1/3\,(\boldsymbol{b}^{*2} : \boldsymbol{I})\boldsymbol{I}] : \boldsymbol{D} \end{aligned} \tag{1.49}$$

Following the work of Rubin and Attia [184], a distortional tensor for the elastic part of the dissipative component is defined, by integration of the evolution equation:

$$\dot{\boldsymbol{b}}^*_{\boldsymbol{de}} = \boldsymbol{L}\boldsymbol{b}^*_{\boldsymbol{de}} + \boldsymbol{b}^*_{\boldsymbol{de}}\boldsymbol{L}^{\boldsymbol{T}} - 2/3\,(\boldsymbol{D} : \boldsymbol{I})\boldsymbol{b}^*_{\boldsymbol{de}} - \Gamma \boldsymbol{A}_{\boldsymbol{d}} \tag{1.50}$$

in which $\Gamma\boldsymbol{A}_{\boldsymbol{d}}$ is a measure of the rate of inelastic deformation, with:

$$\boldsymbol{A}_{\boldsymbol{d}} = \boldsymbol{b}^*_{\boldsymbol{de}} - \left(\frac{3}{\boldsymbol{b}^{*\,-1}_{\boldsymbol{de}} : \boldsymbol{I}}\right)\boldsymbol{I} \tag{1.51}$$

where Γ is a non-negative scalar function to be defined. Similarly, two independent invariants associated with the inelastic component can be introduced:

$$\begin{aligned} \alpha_1 &= \boldsymbol{b}^*_{\boldsymbol{de}} : \boldsymbol{I} \\ \alpha_2 &= \boldsymbol{b}^*_{\boldsymbol{de}} : \boldsymbol{b}^*_{\boldsymbol{de}} \end{aligned} \tag{1.52}$$

their corresponding time derivatives are:

$$\begin{aligned}\dot{\alpha_1} &= 2[\boldsymbol{b}^*_{\boldsymbol{de}} - 1/3\,(\boldsymbol{b}^*_{\boldsymbol{de}}\!:\boldsymbol{I})\boldsymbol{I}]\!:\boldsymbol{D} - \Gamma\boldsymbol{A_d}\!:\boldsymbol{I} \\ \dot{\alpha_2} &= 4[\boldsymbol{b}^{*2}_{\boldsymbol{de}} - 1/3\,(\boldsymbol{b}^{*2}_{\boldsymbol{de}}\!:\boldsymbol{I})\boldsymbol{I}]\!:\boldsymbol{D} - \Gamma\boldsymbol{A_d}\!:\boldsymbol{b}^*_{\boldsymbol{de}}\end{aligned} \tag{1.53}$$

The Rubin-Bodner model also includes a set of N fiber families, with a given orientation $\boldsymbol{n_{ti}}$ in the current configuration ($i = 1,2,\dots N$). The stretch of a fiber family is measured by λ_i. Their evolution equations are expressed as follows:

$$\dot{\lambda}_\iota = \frac{1}{\lambda_i}(\boldsymbol{n_{ti}}\otimes\boldsymbol{n_{ti}})\!:\boldsymbol{D} \tag{1.54}$$

The strain-energy function of the material can therefore be defined as a function of the invariants: $W = W(J, \beta_1, \beta_2, \alpha_1, \alpha_2, \lambda_1, \dots, \lambda_N)$.

The rate of material dissipation $\mathcal{D}$, based on the balance of entropy [182,184,185], is defined by:

$$\mathcal{D} = \boldsymbol{\sigma}\!:\boldsymbol{D} - \rho_0\dot{W} \geq 0 \tag{1.55}$$

and is always zero or positive. Note that the equation above is equivalent to the Clausius-Duhem inequality introduced in Equation 1.40. By decomposing the Cauchy stress into deviatoric and hydrostatic terms: $\boldsymbol{\sigma} = \boldsymbol{\sigma_{dev}} - p\boldsymbol{I}$, Equation 1.55 becomes:

$$\begin{aligned}&\boldsymbol{\sigma_{dev}}\!:\boldsymbol{D} - p\boldsymbol{I}\!:\boldsymbol{D} \\ &-\rho\left(\frac{\partial W}{\partial J}J\boldsymbol{D}\!:\boldsymbol{I} + \frac{\partial W}{\partial \beta_1}\dot{\beta}_1 + \frac{\partial W}{\partial \beta_2}\dot{\beta}_2 + \frac{\partial W}{\partial \alpha_1}\dot{\alpha}_1 + \frac{\partial W}{\partial \alpha_2}\dot{\alpha}_2 + \sum_{i=1}^{N}\frac{\partial W}{\partial \lambda_i}\dot{\lambda}_\iota\right) \geq 0\end{aligned} \tag{1.56}$$

Terms with the factors $\boldsymbol{D}$ and $\boldsymbol{I}\cdot\boldsymbol{D}$ (deviatoric and distortional terms) correspond to purely elastic equilibrium and get canceled out. The dissipative terms remain:

$$\mathcal{D} = \frac{\partial W}{\partial \alpha_1}\Gamma\boldsymbol{A_d}\!:\boldsymbol{I} + \frac{\partial W}{\partial \alpha_2}\Gamma\boldsymbol{A_d}\!:\boldsymbol{b}^*_{\boldsymbol{de}} \geq 0 \tag{1.57}$$

A hyperelastic model for W, as well as a suitable function for Γ, need to be defined. For the latter, positivity of the dissipation needs to be ensured, and the following function is generally used:

$$\Gamma = (\Gamma_1 + \Gamma_2 \|\boldsymbol{D}\|) \exp\left(-\frac{1}{2}\left(\frac{Z}{\|\boldsymbol{b}^*_{\boldsymbol{de}}\|}\right)^{2n}\right) \tag{1.58}$$

where Z is the effective hardening associated with fluid flow, Γ_1, Γ_2, n are material parameters and $\|\boldsymbol{X}\| = \sqrt{2/3\, \boldsymbol{X}_{\boldsymbol{dev}} : \boldsymbol{X}_{\boldsymbol{dev}}}$ is a specific tensorial norm, analogous to the definition of the Von Mises stress, the subscript dev referring to the deviatoric part of tensor $\boldsymbol{X}$, i.e. $\boldsymbol{X}_{\boldsymbol{dev}} = \boldsymbol{X} - 1/3(\boldsymbol{X}:\boldsymbol{I})\boldsymbol{I}$. Z is determined by the evolution equation:

$$\dot{Z} = \left(\frac{r_1 r_3 + r_2 \|\boldsymbol{D}\|}{r_3 + \|\boldsymbol{D}\|}\right) \Gamma \|\boldsymbol{b}^*_{\boldsymbol{de}}\| - r_4 Z^{r_5} \tag{1.59}$$

and $(r_1, \dots, r_5)$ are additional material constants. Note that $\|\boldsymbol{D}\|$ corresponds to the effective total distortional deformation rate $\dot{\varepsilon}$.

The Rubin-Bodner model incorporates hyperelasticity, tissue anisotropy with the introduction of fiber families, and a dissipative component represented here as a consequence of temporary structural rearrangements and fluid flow in the material. The observed changes in volume during deformation, as described in Section 2.4.10, can be therefore explained by the outflow of the water content and quantified in the model. In essence, the constitutive framework is akin to a Maxwell model with an elastic component and a dissipative/viscoplastic component in parallel. Although the general form of the Rubin-Bodner model is quite complex, several simplifications are often made. Rubin and Bodner [182] chose an exponential hyperelastic function that neglects the influence of β_2 and α_2, and only one fiber family was considered, without dispersion and no resistance to compression. The experimental dataset on excised facial

skin, taken from the work of Har-Shai et al. [186], is not sufficient to fully determine the 14 constitutive parameters of the proposed model. The authors suggested to reduce the parameter set to 7 material constants, by pre-setting the value of the 7 others, based on expected physical features of the tissue. It was also assumed that the volumetric deformation is characterized by the volumetric response of the internal fluid, assimilated here to water. The proposed formulation has proven to be a very good descriptor for cyclic loading and stress relaxation of facial skin, and captures all the physical features identified by Fung [181].

The same constitutive framework was implemented into a finite element model of facial skin and subcutaneous layers by Mazza et al. [183] to simulate the long term effects of aging. No fibers were incorporated; instead, a layered model was described and an aging parameter was introduced, to model loss of tissue stiffness with time. Although the simulations are based on very simplistic assumptions of the tissue behavior, their results suggest that the short-term response of facial tissue is not affected over large periods of time, and that the long-term response is dominated by the gradual reduction in elastic stiffness, which has interesting ramifications for the study of aging mechanisms. Additional experimental data on *in vivo* facial skin were later gathered by Barbarino et al. [187] to improve the accuracy of the layered model.

Flynn and Rubin [185] applied a similar approach with a discretized fiber distribution model [171] coupled with a dissipative component, described following Hollenstein et al. [188]. Although their model successfully matches the biaxial loading-unloading and stress relaxation tests of rabbit skin reported by Lanir and Fung [42], the large parameter set (21 material constants) poses substantial problems in terms of uniqueness of the identified solution. The authors indicate this set can be reduced by pre-determining some of the structural quantities, e.g. the orientation distribution of collagen fibers, yet a notable limitation is that the model

parameters are for the most part phenomenological. The dissipative features, as well as fiber uncrimping, are not described by physical processes of the tissue structure. The model also shows limited success at larger strains, where more irreversible processes start taking place.

1.3.5.2. Breakage and Rearrangement of Interfibrillar Bridges

In a soft collagenous tissue, the collagen fibrils within a same fiber are interconnected via peripheral cross-links that bridge them together. With the assumption of discontinuous fibrils, these cross-links, besides providing structural integrity to the fiber, also enable force transfer, something that has been modeled earlier by Puxkandl [178] for collagen in tendon. Upon stretching, mechanisms of rupture, slippage, and reformation of these junctions can therefore ensue. Thus, irreversible deformation happens when ruptured bonds can no longer (or do not have the time to) reform and slippage reaches a critical level. Ciarletta and Ben Amar [189] addressed this aspect with a dissipative constitutive model, intended for ligaments and tendons in their case, but which could be extended to skin as well. The model considers a set of collagen fiber families (fj) embedded in an isotropic matrix (m). For the sake of simplicity index $i = \{m, fj\}$ is used to refer to each constituent, unless the equation differs. During deformation, one can consider that a certain fraction of mass of constituent i, $N_i(t,\tau)$ has rearranged before an intermediate time τ, such that $0 \leq \tau \leq t$. $N_i(t,0)$ is therefore the current concentration of constituent that has not rearranged yet. Relative rates of reformation $\gamma_i(\tau)$ [190] are defined by:

$$\gamma_i(\tau) = \frac{1}{N_i(0,0)}\left[\frac{\partial N_i(t,\tau)}{\partial \tau}\right]_{\boldsymbol{t=\tau}} \tag{1.60}$$

These occur at random times. Similarly, rates of breakage of the constituents can be introduced:

$$\Gamma_i(t,0) = -\frac{1}{N_i(t,0)}\frac{\partial N_i(t,0)}{\partial t} \tag{1.61}$$

$$\Lambda_i(t,\tau) = -\left[\frac{\partial N_i(t,\tau)}{\partial \tau}\right]^{-1} \frac{\partial^2 N_i(t,\tau)}{\partial t \partial \tau}$$

where $\Gamma_i(t,0)$ is the rate of breakage of units that have not rearranged, while $\Lambda_i(t,\tau)$ is the rate of breakage of units rearranged before time τ. Integration of Equations 1.60 and 1.61 leads to the following expressions:

$$\begin{aligned} N_i(t,0) &= N_i(0,0)\exp\left(-\int_0^t \Gamma_i(s,0)ds\right) \\ \frac{\partial N_i(t,\tau)}{\partial \tau} &= N_i(0,0)\gamma_i(\tau)\exp\left(-\int_\tau^t \Lambda_i(s,\tau)ds\right) \end{aligned} \tag{1.62}$$

By decoupling the behavior of rearranged and broken units in the energy density function, a dissipative component of the mechanical response can be isolated, capturing history-dependent processes. Functions $\gamma_i(\tau)$ and $\Lambda_i(t,\tau)$ are fully determined by the thermally activated processes that govern the kinetics of breakage and rearrangement, as well as by the loading conditions. In their models of tendon and ligament, Ciarletta and Ben Amar [189] chose to represent the matrix using a Mooney-Rivlin description, and implemented a modified GOH model for the collagen fibers. The rates of breakage in the matrix and at the interfibrillar level were defined via the Eyring theory of thermally activated processes [191] and the Wagner phenomenological relationship [192]:

$$\Gamma_i(t,0) = \Gamma_i^0 \exp(\kappa_i\sqrt{N_i(0,0)W_i(t,0)}) \tag{1.63}$$

where Γ_i^0 is the constant rate of breakage of component i,and κ_i is a material parameter. Breakage and rearrangement occur at the interfibrillar level and in the matrix, allowing for a representation of both damage and viscoelasticity, which can be particularly suited for cyclical

or dynamic testing of collagenous tissues, and has proven to give accurate results with a considerably reduced number of parameters (see Figure 1.37).

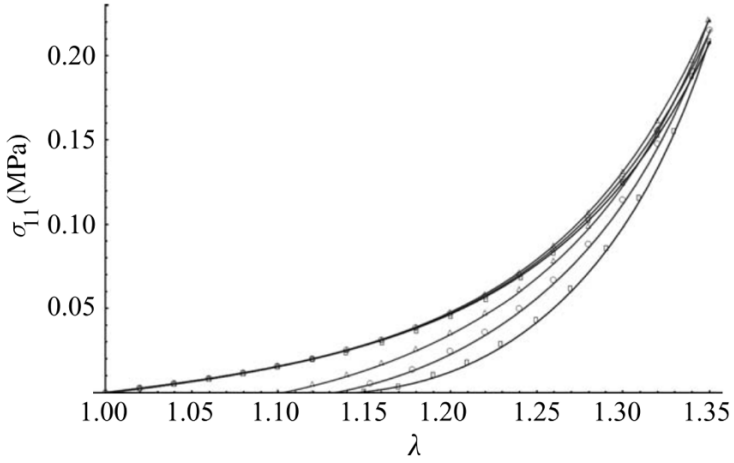

Figure 1.37. The dissipative constitutive model proposed by Ciarletta and Ben Amar [189] shows remarkable agreement with experimental results from strain-dependent tensile loading and unloading tests in periodontal ligaments, performed by Natali et al. [193]. From [189].

1.3.5.3. Volokh's Model

Volokh [194] proposed a phenomenological model for the damage-induced behavior of soft anisotropic materials, by introducing energy limiters. When failure is initiated, the global stress in the material decreases and the behavior can no longer follow the strain energy function of the intact material. The following formulation for the strain energy ψ was suggested:

$$\psi(\phi, m, W) = \frac{\phi}{m}\left[\Gamma\left(\frac{1}{m}, 0\right) - \Gamma\left(\frac{1}{m}, \frac{W^m}{\phi^m}\right)\right] \tag{1.64}$$

where ϕ is the energy limiter, m describes the sharpness of the failure transition, W is the strain energy function of the intact material, and Γ is the upper-incomplete gamma function $\Gamma(s, x) = \int_x^\infty t^{s-1}\, e^{-t}\, dt$. It can be noted that for $\phi = \infty$, then $\psi = W^m$, which corresponds to a material without failure, otherwise the energy is always limited by the value of ϕ.

Volokh [194] suggested that an extended GOH model with two fiber families f_i and a neo-Hookean matrix M would be particularly suited to simulate the damage-induced behavior of arterial walls:

$$\psi(\phi_i, m_i, W_i) = W_M\,(\phi_M, m_M, W_{NH}) + \sum_{i=1}^{2} W_{fi}(\phi_{f_i}, W_{GOH}) \tag{1.65}$$

Li and Luo [195] implemented the Volokh framework to model uniaxial deformation of skin from different species, for which the data was accessible from the literature. The model reproduced very well the softening behavior at high strains with a relatively low number of additional parameters, although some of them need to be pre-set in the case of uniaxial tensile tests, where information on the anisotropy of the material is lacking. Some results showing the performance of the model on human skin [140] and swine belly skin [47] are presented Figure 1.38. The authors report that the mean fiber angle β and the dispersion factor κ of the GOH model are the parameters that have the highest influence on the damage model, suggesting that it is preferable to determine them initially.

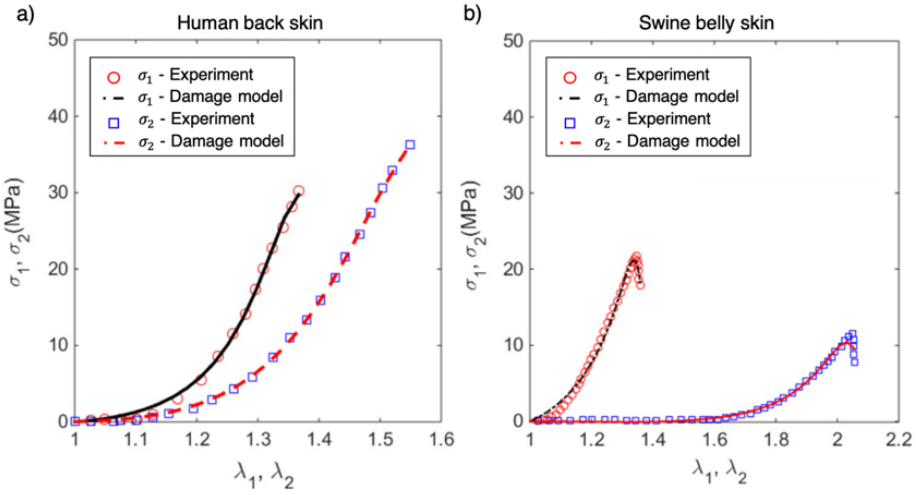

Figure 1.38. Computed and measured stress-stretch curves of uniaxial tests in perpendicular orientations on (a) human back skin [140] and (b) swine belly skin [47]. Li and Luo [195] implemented a Volokh damage model with a GOH nonlinear elastic model to capture the softening behavior of skin prior to sample failure. Adapted from [195].

1.3.5.4. Shear-Lag Model

It is generally believed that mechanisms of shear play a critical role in the viscoelastic and dissipative behavior of skin, mostly at high strains [7,41,178]. Interfibrillar and fiber-matrix shear interactions occur during the straightening process of fibers (or fibrils), and most importantly when they start sliding past each other. The shear-lag model takes these processes into consideration by estimating the relative displacement between fibers during deformation. It was initially introduced by Cox in 1952 [196] for fiber reinforced composites, and later on adapted to biological tissues [150,197–199].

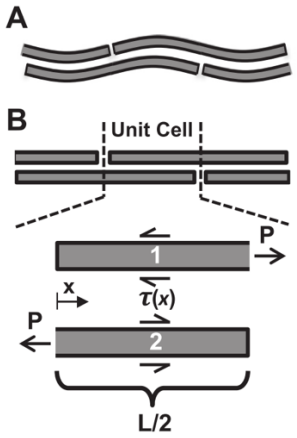

Figure 1.39. Microstructural shear-lag model described by Szczesny and Elliot [150]. A simplified representation of discontinuous fibers consists of a unit cell with two fibers embedded in a matrix. In the initial configuration, fibers are crimped (A), and bear loads only when fully straightened (B). The applied tensile loads are transferred to the matrix via shear stresses τ.

In the model, a unit representative cell consists of two discontinuous elastic fibrils embedded in a viscous matrix. When a tensile load is applied at the edges of the cell, the two fibrils move in opposing directions, thus generating shear in the matrix interface. Szczesny and Elliot [150] also incorporated fiber crimp in their shear-lag model of tendon, but assumed that only fully straightened fibers bear load and transfer shear stresses. Following the representation in Figure 1.39, we consider that a tensile load is applied in the x-direction, +P for fiber 1 and –

P for fiber 2. Fibers are of initial length L (such that the unit cell is of length L/2) and of radius r, and are significantly stiffer than the viscoelastic matrix. In this case, the stresses in each fiber σ_i must equilibrate with circumferential shear stresses τ:

$$\frac{\partial \sigma_1(x,t)}{\partial x} = -\frac{\partial \sigma_2(x,t)}{\partial x} = \frac{2\tau(x,t)}{r} \tag{1.66}$$

Additionally, the force balance on the unit cell gives the following relationship:

$$P(x,t) = \pi r^2\big(\sigma_1(x,t) + \sigma_2(x,t)\big) \tag{1.67}$$

Shear stresses lead to relative sliding δ between fibers 1 and 2, with:

$$\delta(x,t) = u_1(x,t) - u_2(x,t) \tag{1.68}$$

The constitutive relationship in each fiber yields:

$$\sigma_i(x,t) = E_f \varepsilon_i(x,t) = E_f \frac{\partial u_i(x,t)}{\partial x} \tag{1.69}$$

where E_f is the Young's modulus of the fibrils. Equations 1.67, 1.68, and 1.69 can be rearranged such that:

$$\begin{aligned} \sigma_1(x,t) &= \frac{E_f}{2}\frac{\partial \delta(x,t)}{\partial x} + \frac{P(x,t)}{2\pi r^2} \\ \sigma_2(x,t) &= -\frac{E_f}{2}\frac{\partial \delta(x,t)}{\partial x} + \frac{P(x,t)}{2\pi r^2} \end{aligned} \tag{1.70}$$

Lastly, the interfibrillar matrix shear strain $\gamma(x,t)$ is expressed as:

$$\gamma(x,t) = \frac{\delta(x,t)}{h} \tag{1.71}$$

where h is the vertical spacing between fibers. By rearranging equations 1.66, 1.70 and 1.71, we find that:

$$\frac{rhE_f}{4}\frac{\partial^2 \gamma(x,t)}{\partial x^2} = \tau(\gamma) \tag{1.72}$$

So the evolution of γ depends on the constitutive law between the shear stress τ and the shear strain γ.

In their shear-lag model of tendon fascicle, Szczesny and Elliot [150] compared elastic, plastic, and combined elastoplastic models for the constitutive relationship of the interfibrillar shear stress. According to their analysis, the plastic model represents more accurately the deformation process of a fascicle than the elastic model, because it predicts the observed tissue softening behavior (Figure 1.40). The combined elastoplastic model, which introduces an additional parameter, slightly improves the total prediction, but stays very close to the plastic model.

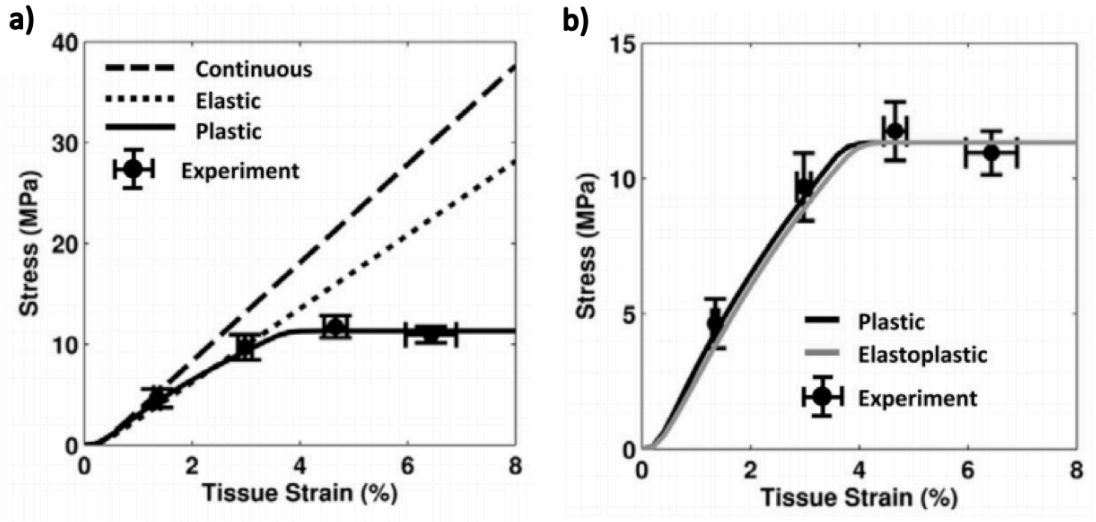

Figure 1.40. Performance of the shear lag model in predicting the tensile behavior of tendon fascicle, with different constitutive laws for the shear behavior of the matrix: (a) – continuous (no shear lag), elastic, plastic; (b) – plastic and combined elastoplastic. Even though the elastic shear lag model gives a better representation of the macroscopic stiffness of the fascicle, it is unable to simulate the softening behavior at higher strains, unlike the plastic and elastoplastic models. From [150].

More recently, Wu et al. [197] implemented a Kelvin-Voigt model for the shear behavior of the matrix, to account for viscoelastic processes occurring in the structure. This requires complex solving of a nonhomogeneous PDE. Although the model encompasses the dynamic

behavior of the tissue, it still cannot represent the softening response captured by the plastic model.

It should also be pointed out that shear-lag models of collagenous tissue are principally representing interactions at the fibril level. Although relative sliding at the fiber level probably plays a non-negligible role in the dissipative behavior of skin, some key points need to be addressed to include these processes into a structural model of the dermis. First, the description of the unit representative cell in the shear-lag model entails fiber discontinuity, and little is known about the extended length of collagen fibers in the dermis, or on how fibers are connected at their ends. Second, fiber dispersion in skin makes it challenging to provide a global representation of the shear interaction, compared to the proposed parallel arrangement.

1.4. Advantages and Limitations of Semi-Structural Modeling

The present review details a broad range of models that have been (or could be) implemented to describe the mechanical behavior of skin, including nonlinear elasticity, anisotropy, viscoelasticity, evolution of damage, or other dissipative processes. Although phenomenological isotropic models are sometimes preferred for their simplicity and ease of implementation, they are generally limited by the lack of physical significance of the parameters at play. Moreover, because soft collagenous tissues like skin exhibit high anisotropy, isotropic models do not appear as an appropriate choice. In contrast, semi-structural models attempt to bridge the structure-property gap by taking into account the contribution of distinct constituents and, to some degree, their structural arrangement. In the case of skin, the material is generally represented as the assembly of the collagenous network, the ground substance, and more rarely the elastin fibers. This decomposition enables the decoupling of strain-energy functions, usually phenomenological, associated with the behavior of each component. With this approach,

specific physical features of the material can be attributed to the properties of separate constituents: tissue anisotropy can be related to collagen fiber splay, or viscoelasticity can be taken a property of the ground substance, for example. For the collagen fiber network, additional structural accuracy is reached by incorporating the dispersion in orientation of fibers.

With a more detailed description, models increase in complexity, and more constitutive parameters are generally introduced. Concurrently, the representation of the structure is more accurate, and the parameters gain in physical relevance. The macroscopic deformation of the tissue can be associated with processes occurring in the microstructure, and the model can be informed by previously determined structural data on the material, thus potentially reducing the number of constitutive parameters that need to be identified. However, the predetermination of material constants should be addressed with care: this approach is only appropriate if the proposed structural arrangement and the associated mechanical processes provide a reasonable approximation of reality.

A considerable amount of research has been conducted to fully characterize the mechanical properties of the main components of skin [12,200,201]. Main difficulties that remain to be overcome to improve semi-structural models are to identify the correct structural arrangement of each of these components, and how they interact with each other. Current knowledge on the actual distribution of collagen fibers in the dermis is still quite limited, especially given that it varies substantially according to species, region of the body, age, and other factors.

Studies that involve microscopic imaging of skin are essentially restricted to two-dimensional visualization of the dermis, and understanding the out-of-plane arrangement can still be challenging. Li [202] reviewed some existing hypotheses for the distribution of collagen fibers in skin, essentially centered around idealized two-dimensional fiber networks with

varying degrees of freedom [203–205]. Sherman et al. [12], based on Transmission Electron Micrographs of rabbit skin, proposed that the dermis consists of plane layers of imbricated collagen fibers, also with varying angular distributions, supporting the hypothesis of a planar arrangement as well. Yet, some other studies, including the work of Jor et al. [13] for pig skin and Ferdman and Yannas [206] for human skin, report a three-dimensional organization of collagen, with preferred angular alignments close to $\pm 45°$ in the cross-section and a high degree of interweaving, far from planar models for which this angle stays at 0°, and where fibers do not cross. Models extending to three-dimensional networks, or with braided structures, have seldom been explored at this point.

Fiber crimp plays an important role in the nonlinear behavior of skin. The tensile response of wavy collagen fibers is marked by a transition from the straightening process, requiring little elastic energy, followed by a purely tensile state. In semi-structural models, this process is incorporated by defining piecewise phenomenological functions for collagen fibers, depending on the stretch state, or nonlinear functions that approximate this transition, such as exponential functions for example. In a number of representations, it is also frequently assumed that collagen fibers bear no load in compression. This distinction in elastic behavior participates to the anisotropy and the nonlinear elasticity of the material, and is therefore an important mathematical consideration for constitutive models. Models can be informed by direct measurements of the undulation of collagen fibers in their resting state, which provides an estimate of the transition from crimped to fully taught configurations. To incorporate fiber curvature, beam-like representations of collagen fibers can also be encountered in the literature, most of which were reviewed by Sherman et al. [10] (see Figure 1.41). Planar representations include rigid corner [207,208], sequential loading [209], sinusoidal [151,210,211], and semi-

circular [12,41] models. The helical model [212] is the only representation with a three-dimensional fiber configuration, forming a spring-like coil. While it is probably more suitable to describe a tridimensional, interwoven arrangement of the collagen network, the determination of an undulation parameter is more challenging. An advantage of beam-like descriptions is that such models can be adjusted to reproduce the microscale deformation of collagen fibers, and the framework can be extended to a macroscale model of the dermis, based on representative elements [148,151,213]. Microscopic imaging of the collagen network and micromechanical testing on isolated fibers provide information that can serve to tune the model. Important questions remain concerning fiber characteristic length, and the nature of their attachment with other fibers and their surroundings, which need to be addressed to define appropriate loading and boundary conditions.

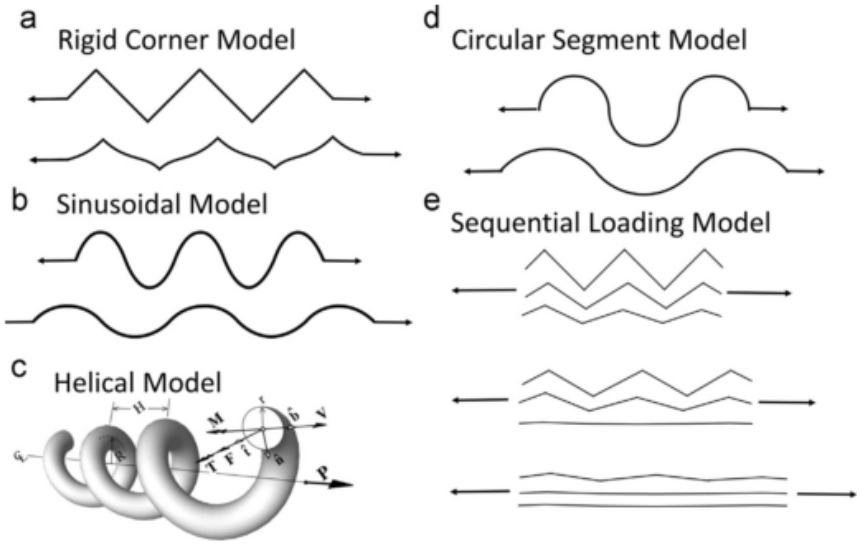

Figure 1.41. Beam-like models of collagen fibers. (a) The rigid corner model (Diamant et al. [207]) assumes that straight oblique beams are rigidly jointed together, adding rigidity to the structure and limiting the straightening process. (e) The sequential loading model (Kastelic et al. [209]) assumes free rotation at the joints, implying that the beam bears load only when fully straightened, as in most elastic models presented in this review. The (b) sinusoidal (Comminou and Yannas [210], Lanir [174], Gao et al. [151]) and (d) circular segment (Sherman et al. [12]) models attempt to replicate the smooth curvy shape of collagen in the dermis. (c) The helical model (Freed and Doehring [212]) extends the structure in three dimensions, to account for the out-of-plane configuration of the fibers. Reprinted from Sherman et al. [10].

Significantly less information is available on elastin. Weinstein and Boucek [214], but also Brown [68], and Belkoff and Haut [145], question its contribution in the deformation process, mainly because of its low weight percentage in the dermis and its high extensibility. This justification is often provided when the influence of the elastin network is neglected in constitutive models, or absorbed into the contribution of the ground substance. Yet, Lanir [174], Oxlund et al. [215], as well as others [57,159,161], argue that elastin is mainly responsible for the quick recoil of skin at low strains, which studies on skin with denatured elastin seem to confirm [215].

1.5. An Application of Skin Mechanics: Synthetic Skin

Current signs of progress in bioengineering are gradually broadening the possibilities in terms of mimicking the behavior of biological materials. Important breakthroughs involve the development of functional and biocompatible synthetic materials with matching structure and mechanical properties. In the clinical context, applications with synthetic skin grafts can offer great perspectives for patients with deep and/or large burns, or large tissue excisions for example. Various products are already commercially available, ranging from synthetic sheets [216–218] to 3D printed tissue [33,219,220]. However, an ongoing challenge is to match as closely as possible the mechanical properties of the skin, in order to maximize conformity between the graft and the tissue, in the affected region. Difficulties arise from the fact that these properties can vary according to region of the body, age, gender, and health condition. It is therefore essential to have a complete understanding of the mechanics of the material prior to replicating it, both from macrostructural and microstructural standpoints. Experimental results supply a large database of expected responses, while models can provide objectives in terms of

mechanical parameters to match. By referring to them, the choice of fabrication materials is simplified.

Common existing solutions consist of a polymer sheet that provides a scaffold for new skin to grow. This process can be facilitated by pre-growing in a bioreactor some of the patients' fibroblasts and keratinocytes from their healthy skin into the scaffold. The cells are expected to produce a suitable extracellular matrix, compliant with the properties of the skin. During the regeneration process, the mechanical properties change, due to densification of collagen and keratin (at the epidermis level). Sander *et al.* [221] reported these changes from collagenous scaffold grafted on mice, presented in Figure 1.42. Their study shows that engineered synthetic skin, initially quasilinear elastic, starts stiffening and eventually behaves more nonlinearly, after infiltration of cells and grafting. Six weeks after surgery, synthetic skin replicates quite well the J-curve behavior in tension, although the regenerated tissue is still too stiff to fully comply with healthy skin. Similar observations are also made with autografts or scarred tissue. The authors point out that cell concentration, polymer properties, infiltration and post-grafting times are important parameters that will affect the response of the material, and should be investigated in the future. To palliate problems with densification, and to better control the regeneration of the tissue, other approaches intend to directly create a scaffold mimicking the collagen fiber arrangement, and therefore matching the mechanical properties of skin. This can be achieved by electrospinning, where fiber geometry, orientation, and mechanics can be tuned. Such methods have been reviewed in detail by Dias *et al.* [222]. 3D printed truss-lattice microstructures are another interesting direction that has been adopted for wearable devices [148,223], and could be potentially extended to synthetic grafts.

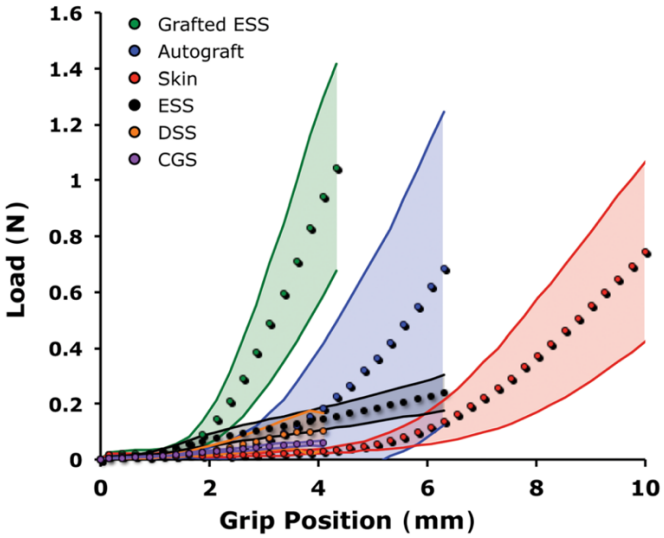

Figure 1.42. Tensile response of engineered synthetic skin grafts at different stages of cell infiltration and post-surgery. Healthy skin and autografted skin are also added for comparison. CGS: Collagenous Scaffold; DSS: CGS infiltrated with fibroblasts; ESS: DSS seeded with keratinocytes on the top surface. Results six-weeks after surgery (Grafted ESS) show that the grafted synthetic skin starts replicating the nonlinear behavior of healthy and autografted skin, but the material is stiffer and less stretchable. Reprinted from Sander et al. [221].

1.6. Conclusions and Future Challenges

In order to fulfill a broad range of vital functions throughout life, it is essential for skin to maintain a certain level of structural integrity, and to have the ability to undergo large deformations caused by motion, impact, and other external factors. The present review focuses on the tensile properties of skin, mostly attributed to the response of the dermis. Understanding, characterizing, and predicting the mechanical response of this complex anisotropic structure to various loads is of valuable importance in many fields of engineering.

The variety of experimental protocols, most of which are reviewed here, and the lack of standardized testing methods for skin yield results that often cannot be directly compared. For example, the estimation of a tangent modulus for the linear portion of skin depends on the testing conditions, the experimental protocol, or the tested species. It shows values that can differ by up to four orders of magnitude (cf. Table 1.2). This indicates that particular attention needs to be paid to the specifics of the experimental methods, and to the approach used to obtain

representative parameters. With a consistent experimental framework, some qualitative and sometimes quantitative results can be observed, highlighting the influence of factors such as tested organ, age, gender, species, external temperature, hydration, and dynamics and loading history. Constitutive modeling is a valuable tool to extract quantitative information from the database of experimental results, via the identification of material constants.

However, in a number of studies, the experimental characterization and constitutive modeling are often conducted independently from each other. Experimental results are taken from a previous study, or the protocol is designed without accounting for the amount of information that is required by the model to adequately determine the material constants. As pointed out by Rubin and Bodner [182] and by Holzapfel et al. [114], there is a need to develop experimental methods in concert with model development, so that sufficient information is available, and the three-dimensional mechanical response of skin can be fully characterized.

Constitutive models of skin vary in complexity, with a tradeoff between the number of parameters and the ability of the model to reflect the material's structural arrangement, as well as the mechanical processes taking place at the microstructure scale. While it can be preferable to maintain a certain level of simplicity to reduce the computational cost and increase the robustness of a model, more accurate and consistent parameters can be obtained with a more realistic description of the tissue structure. Ideally, a good constitutive model should not only be descriptive, and match the mechanical response for a fixed number of experimental results, but also predictive, meaning that it should also be able to predict the behavior of the material for given loading conditions that differ from the reference test set. This is one of the fundamental limitations encountered with isotropic hyperelastic models, despite the fact that they have been extensively used to characterize the tensile response of skin. In contrast,

structurally-based descriptions of the dermis enable the incorporation of effects of anisotropy, with physically relevant constitutive parameters, under the condition that the assumptions of the model are in close agreement with reality.

It is also important to consider the experimental results that are available to inform the model: for example, a dissipative component has limited interest if the dissipative response of the tissue is not observed. *In vivo* or *ex vivo* testing conditions yield notable differences in edge effects, surrounding tissues, and potentially compressibility, which need to be considered in the selected model. Uniaxial tensile testing does not provide sufficient information to fully characterize skin anisotropy, therefore the identified material constants may not be unique or reflect reality if a complex anisotropic model with dispersed fibers is chosen. Moreover, if no structural data are available on the tested sample, then the representation of fiber distribution is merely an assumption of the model, based on available statistical analyses on fiber dispersion. With significant inter-sample variability, pre-setting the associated constitutive parameters increases the likelihood of inaccurately describing the material. Hence, there is a need to develop multi-scale modeling frameworks coupled with experimental techniques that inform the model at different levels of scale, such as *in situ* microscopy imaging, as well as more general testing protocols that characterize the three-dimensional response of skin [9,114,155] and provide additional insight into the interactions between the constitutive elements.

The structural arrangement of the constituents of the dermis can be investigated using microscopy imaging techniques, such as scanning electron microscopy (SEM), transmission electron microscopy (TEM), or multiphoton microscopy. With large inter-sample variations, it is an arduous task to reach a general level of representation of the tissue structure. Semi-structural models with angular integration or generalized structure tensors opt for a statistical

description of the collagen network, offering a reasonable compromise between structural representativity and model complexity. With recent developments in computational modeling, discrete network modeling with stochastic fiber distributions are also an interesting direction to pursue.

SEM, multiphoton microscopy, or small angle x-ray scattering, can be coupled with mechanical testing devices to observe the deformation *in situ*, adding the possibility to study time-dependent and dissipative processes at the microscale level. These approaches involve the development of advanced testing platforms, and are complicated by several factors. It is challenging to apply them in the *in vivo* configuration, and the testing conditions *ex vivo* often require vacuum, water immersion, lengthy sample preparation (and potential deterioration), which is far from physiological conditions.

Replicating the structure and the mechanical behavior of skin can yield important outcomes in fields such as tissue engineering, interventional surgery, or cosmetics, where conformity of the material is essential. Developing fabrication methods that generate synthetic tissues that match the features of skin is another challenging task. The following are some unresolved problems that, in our opinion, would benefit from concentrated research efforts:

- What is the role of elastin in the mechanical response of the skin? Although elastin represents only a small volume fraction, some researchers attribute a significant effect on the mechanical response. There are varied comments about its role, some dealing with the reversible deformation. Nevertheless, there is little quantification of its effect.
- What are the processes associated with changes in volume during the deformation of skin? A reduction in volume is often associated with internal fluid outflow, but this process has not been quantified in detail. On the other hand, increases in volume are

attributed to the auxetic nature of the fiber network, although there is very little evidence of structural features that support these claims at the moment.

- The fracture toughness and tear resistance of skin have been studied to a limited extent. Conventional tear opening tests for Mode I with a conventional tensile geometry presents problems such as the warping of the specimen out of the plane. The trouser test for Mode III is sometimes preferred for elastomers, but this yields a parameter in the out-of-plane direction, which might not be the principal mode of tear propagation in skin. The application of the J-integral approach to the fracture toughness of skin could also reveal many important structure-property features.
- Mechanical response of scar tissue. Scars affect the distribution of tension in skin, as shown for example by Wong et al. [26], and cause stress concentration at the interface with healthy tissue. How do these stresses vary with distance from the scar? Some analogies with the process of tear propagation and toughness could be drawn, and lead to improved surgical procedures and minimally invasive surgery.
- Dynamic response of skin. Little has been done, other than compressive tests (with strain rates up to 4000 s^{-1}) by Shergold et al. [45] on porcine skin, and tensile testing by Ottenio et al. [132] (up to 167 s^{-1}) on human skin. This has important potential applications in the study of trauma and blast injury in skin.
- Correlation between mechanical extension and structural evolution. Although there are preliminary results, a one-to-one quantitative correlation is lacking. Advanced *in situ characterization* techniques such as small angle X-ray scattering or confocal microscopy can provide answers.

The following chapters present a synthesis of our efforts directed at addressing some of these questions. In particular, we extend the experimental characterization of the tensile properties of porcine skin, with an emphasis on time-dependent and dissipative processes, conducted in a systematic approach. Using several of the microscopy tools available at our disposal, we further investigate on the microstructural arrangement of collagen in the dermis, at different stages of deformation. From our observations, we propose a semi-structural model that accounts for some specificities of this arrangement, and aims to provide microstructural explanations to some of the physical features that the skin exhibits. Finally, as a continuation of our experimental approach, we implement a quantitative analysis of the tear resistance of skin, coupled with additional microstructural characterization. The purpose is to provide accurate numerical estimates that describe the likelihood of tissue failure following extensive deformation.

1.7. Acknowledgements

Chapter 1, in full, has been submitted for publication of the material as it may appear in Progress in Materials Science, and is authored by A. Pissarenko and M.A. Meyers. The dissertation author was the primary investigator and author of this paper.

We acknowledge Prof. Eduard Arzt, Prof. Vlado Lubarda, Prof. Limbert, Ní Annaidh, Destrade, Holzapfel, and Mazza for their kind comments and constructive discussions.

CHAPTER 2. TENSILE BEHAVIOR AND STRUCTURAL CHARACTERIZATION OF PIG DERMIS

2.1. Introduction

The mechanical performance of skin is essential in ensuring that it can maintain its integrity throughout life, and therefore satisfy its primary functions of protection, sensing regulation via fluids, and heat exchange. It is the largest organ of the body of mammals, and its structure is a composite of three distinct layers that fulfill different functions [11]: the epidermis (~50-150 μm for humans [3,224]), is a hard keratinized layer at the surface of the tissue, lying on top of the dermis (~0.15-4 mm thickness [7,8]), the load-bearing component of skin formed by a complex arrangement of collagen (~70% of the dry weight of skin) and elastin (~2-4% of the dry weight of skin) fibers [7,8,225]; the hypodermis is the inner layer, mostly consisting of fat lobules that provide shock absorption and minimize friction with the internal organs of the body [7,8]. Thus, tensile properties are mostly provided by the dermis, and understanding the processes at play during deformation can be useful in a wide range of applications such as surgery, biomedical engineering, dermal armor, wearable devices, and biomimetics.

As extensively developed in the previous chapter, a significant amount of research on the mechanical behavior of the skin has shown that it is an anisotropic, non-linear elastic material that exhibits viscoelasticity and loading history dependence [7,42,134,187,225]. These properties can be attributed to the structure of the dermis, and the arrangement of its constitutive elements as well of their respective mechanical properties. Collagen fibrils, ~50-500 nm in diameter, are characterized by a d-period of 67 nm, due to the staggered arrangement of tropocollagen molecules, which have a length of ~ 300 nm and a diameter of ~ 1.5 nm. Bundled fibrils form collagen fibers, with diameters ranging 2-7 μm in skin [10,12]. In the dermis, these

collagen fibers are organized into a complex three-dimensional network, an arrangement that is not fully understood yet. Depending on the location on the body, collagen fibers follow preferred orientations in planes parallel to the outer surface, an alignment that can be related to pre-existing lines of tension in skin, i.e. the Langer lines [12,21–24], and therefore the material's anisotropy. Jor et al. [13] measured angular distributions of collagen fibers from confocal imaging of cross-sections of pig skin, and reported that the fibers tend to be oriented at ±45° with the normal direction to the outer surface, showing an important out-of-plane component in the undeformed configuration as well. Collagen fibers are initially crimped [12,212,226], and progressively straighten under tensile loading, explaining the non-linear elasticity of the tissue. At higher levels of strain, straight fibers slide past each other, and eventually delaminate, until failure occurs [41]. During this process, interfibrillar shearing is an additional factor of influence on non-linearity, but also on viscoelasticity and energy dissipation in skin. The surrounding ground substance (comprised of proteoglycans) also highly contributes to skin's viscoelasticity. The contribution of elastin in the overall mechanical behavior of skin is often discussed [68,145,161,214], mainly due to its low weight percentage and relatively little influence at high strains, and some researchers claim that it plays an important role in the recoil of skin at low stresses [57,174,215,226]. Thus, it is important to understand and measure changes in the structural configuration of the constitutive elements of skin during the deformation process in order to associate the macroscopic behavior with microscale phenomena.

Various experimental techniques have been applied to characterize skin's mechanical properties, involving torsion [58,89–91], suction [62,94,97,98,115], indentation [53,64,66,67], uniaxial [46–48,51,132,227], biaxial [109,112], and multiaxial [59] tests, which can be

conducted either *in vivo* or *ex vivo*. For a full characterization, *ex vivo* testing is preferred, so that the material can be tested until failure, or with irreversible damage. Under such conditions, uniaxial tensile tests are generally favored for their ease of implementation and standardized methods, and consequently a broad range of reported data in the literature enable comparison. Although biaxial testing is more suitable to assess tissue anisotropy, the method also comes with additional complications and restrictions that can compromise the accuracy, as well as the completeness of experimental results (sample gripping and slipping, inability to reach failure). Anisotropy can be partially quantified by testing different tissue orientations. The typical J-shaped stress-strain curve of skin can then be used to extract information on failure strain, failure stress, tangent moduli, deformation energy, and anisotropy [48,132,227]. Experimental setups are sometimes coupled with imaging techniques, such as Optical Coherence Tomography [5,120], or Digital Image Correlation (DIC) [62,227], mainly for increased accuracy of the measured deformation, and quantification of sample anisotropy via the measurement of lateral strains. Nonetheless, the obtained data is seldom used to evaluate the Poisson ratio, which can yield additional insight into the deformation process within the material. Lees et al. [228] reported values of the Poisson ratio for cow teat skin ranging from -0.8 to 2.0, with variations mainly caused by differences in sample geometry, loading conditions, and strain state, which is also encountered in knitted fabrics. Such large values are far from classic incompressible materials, such as rubber and silicone (0.4-0.5), to which skin is often compared.

Monitoring microstructural changes during the process of deformation is a more challenging task, and has been conducted *ex situ* using Scanning Electron Microscopy (SEM) [41,68], and *in situ* with Small Angle X-Ray Scattering (SAXS) [41] or Small Angle Light

Scattering (SALS) [167], and Second Harmonic Generation (SHG) microscopy [123]. The straightening and realignment process of collagen fibers in the direction of applied tension is evident, and sliding and delamination are also observed at high strains. However, it remains unclear whether a certain degree of entanglement between fibers exist, which would generate additional shearing constraints, irreversible damages, and out-of-plane effects. It is also important to note that such observations are mostly done parallel to the surface of the skin, implying that processes occurring out-of-plane are rarely reported.

The work presented in this chapter aims to expand our understanding on the mechanical behavior of skin, from uniaxial tensile tests conducted on freshly excised porcine skin. The same testing method is applied for all loading cases and samples to maintain consistency of results. We connect the change in collagen configuration, obtained by *ex situ* TEM, to the evolution of damage. This is conducted on three perpendicular planes for the initial, undeformed, configuration as well as after failure. Particular attention is given to the processes of rearrangement occurring within the structure, both at a macroscopic level with assessments of irreversibility of the deformation and changes in the Poisson ratio, and at the microscale via a quantitative analysis of the realignment of collagen in the dermis. Pig skin was chosen for this study because of its similarity with human skin and because it is relatively easy to obtain fresh samples.

2.2. Methods and Materials

2.2.1. Sample Preparation

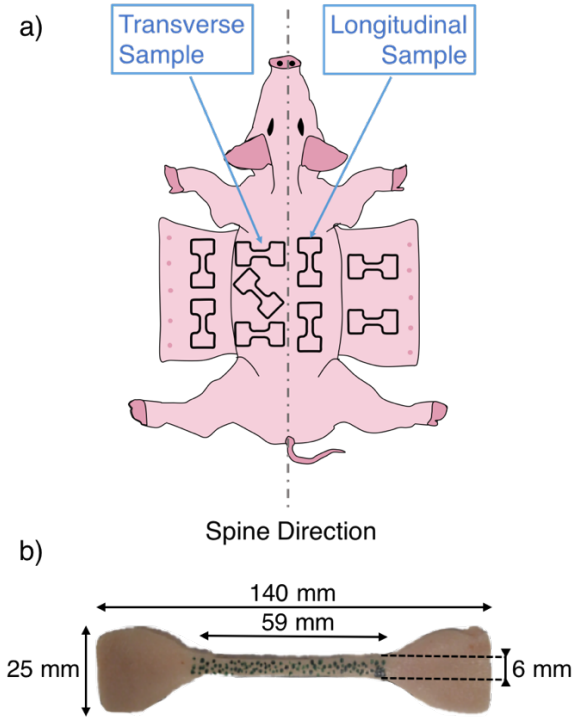

Figure 2.1. (a) Tensile specimens extracted from dorsal and ventral pig skin with orientations marked. (b) Dimensions of tensile specimens cut according to the ASTMD-412-B standard for testing rubbers and elastomers [229]; reduced gage length 59mm.

Porcine skin from two sources was used in the present investigation. The Veterinary School at the University of Cambridge (UK) provided two nine-week old pigs whose skin was excised shortly after being sacrificed. The excess fat on the hypodermis was cut down. The orientations of the obtained specimens are shown in Figure 2.1a. Both transverse (perpendicular to the direction of the spine) and longitudinal (parallel to the direction of the spine) hourglass-shaped specimens were removed using a cutting die, following the geometry described by the ASTM D412 Type B standard [229] for testing of rubbers and elastomers (Figure 2.1b.). To account for sample shrinkage or expansion due to pre-existing tension *in vivo*, dimensions were also

measured after excision. The skin was subsequently wrapped in cellophane and stored in a cold room at 4˚C to preserve freshness. Samples were left at room temperature a few hours prior to testing, and occasionally sprinkled with water to avoid excessive drying. Testing was conducted within 3 days after the pigs were sacrificed. In California, skin was obtained already excised from a local farm (Winfield Farm, Buellton, CA, USA), and shipped overnight. Samples were prepared following the same procedure. A significant difference is that the age of the pigs was much higher (~1 year-old), a factor that is known to cause differences in mechanical properties.

2.2.2. Tensile Setup and Loading Configurations

A special gripping method was used to prevent slipping of the specimen ends during testing. The assembly consists of perforated steel plates with sharp wedges, glued to wooden pads used for mounting on the testing machine. Samples were tested by using an HTE Hounsfield universal testing machine at the U. of Cambridge, and an Instron 3300 single column testing machine at UCSD. Strain-rate change, stress relaxation, and loading/unloading tests were conducted to extract fundamental parameters of deformation. No sample preconditioning was performed, to avoid generating irreversible damages to the tissue prior to actual testing.

2.2.2.1. Strain Rate Changes

A total of 30 samples were tested: 17 taken parallel to the direction of the spine (longitudinal samples), among which 14 were tested in Cambridge and 3 were tested in California, and 13 taken perpendicular to it (transverse samples), with 2 samples tested in Cambridge and 11 samples tested in California. Different crosshead speeds were imposed, resulting in strain rates of 10^{-4} s^{-1} (1 longitudinal sample), 10^{-3} s^{-1} (3 longitudinal and 2 transverse samples), 10^{-2} s^{-1} (6 longitudinal and 3 transverse samples), 10^{-1} s^{-1} (3 longitudinal

and 4 transverse samples), and 0.5 s^{-1} (4 longitudinal and 4 transverse samples). To further establish the influence of the strain rate on the mechanical response of skin, the crosshead speed changed in the course of a single test, increasing from 10^{-3} s^{-1}, to $5 \cdot 10^{-3}$ s^{-1}, and to 10^{-2} s^{-1} for one transverse sample, and decreasing from 10^{-2} s^{-1}, to 10^{-3} s^{-1}, and to 10^{-4} s^{-1} for another.

2.2.2.2. Stress Relaxation

The viscoelastic response of skin was observed by stretching 12 samples by given increments of strain: 0.1 increments - 2 transverse and 2 longitudinal samples; 0.2 increments - 3 transverse and 3 longitudinal samples; 0.5 increments - 1 transverse and 1 longitudinal sample.

The skin was left to relax for 30 seconds between each relaxation cycle, and the strain was incrementally raised until failure.

The obtained stress over time relaxation curves were normalized to facilitate comparison, and were then fit with a three-term Prony series, using the curve fitting tool in MATLAB:

$$\frac{\sigma(t)}{\sigma_0} = a + be^{-t/\tau_1} + ce^{-t/\tau_2} \tag{2.1}$$

where σ_0 is the stress at the onset of relaxation, a, b and c are material parameters, and τ_1 and τ_2 are time constants, associated with processes occurring at different time scales. Short relaxation times were preferred so that environmental conditions such as sample dehydration, inherent to *ex vivo* testing, could not affect the viscoelastic response of the material after several cycles. As a result, longer relaxation constants (>1000 s) were not measured.

2.2.2.3. Loading/Unloading Tests

Loading/Unloading tests of 8 longitudinal samples were conducted, with initial loading interrupted at strains ε_c of 15% (2 samples) and 35% (6 samples). After one cycle, the samples were reloaded until failure.

2.2.3. Digital Image Correlation

2.2.3.1. 2-D Mapping of the Deformation on the Outer Surface

Digital Image Correlation (DIC) was used for an accurate estimation of strain values. The deformation process was captured using a Phantom V120 high speed camera (resolution:512x512; frame rates: 10fps, 20fps, 80fps). The surface of the samples was speckled with dots, randomly placed using a permanent marker; a typical specimen is shown Figure 2.1b. The Poisson ratio of some recorded tests (5 transverse samples, 4 longitudinal) was calculated using the MATLAB DIC software Ncorr 2.1 [230], which was also used to evaluate sample slippage. The post-processing algorithm of the software provides average estimates of the Lagrange strains in the longitudinal/tensile direction E_{yy}, and in the lateral direction E_{xx}, over time. Using these parameters, the evolution of the Poisson ratio ν can be calculated:

$$\nu = -\frac{\ln(\lambda_{xx})}{\ln(\lambda_{yy})} \tag{2.2}$$

where ln (λ_{ii}) corresponds to the Hencky strain, for which the Poisson ratio remains constant for incompressible materials [231]. The stretch ratios λ_{ii} are obtained from the Lagrange strains via the following relationship:

$$\lambda_{ii} = \sqrt{1 + 2E_{ii}} \tag{2.3}$$

2.2.3.2. Coupling with Measurements of the Changes in Thickness

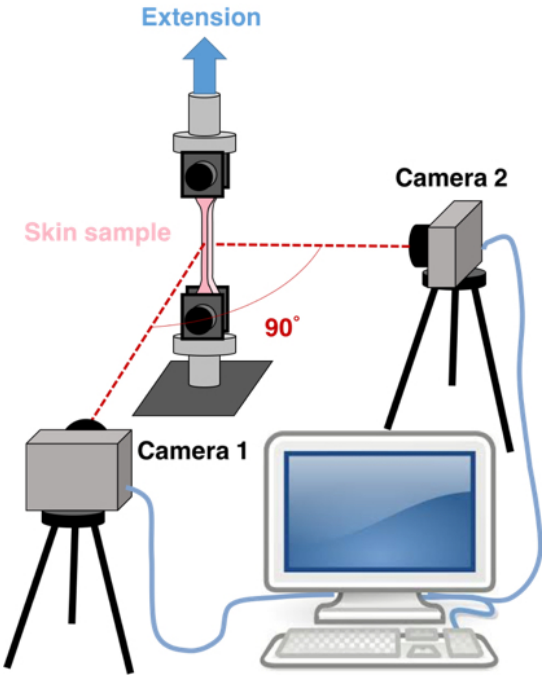

Figure 2.2. Schematic description of the experimental method to estimate sample deformation in the lateral and in the thickness directions compared to the deformation in the tensile direction, using two identical cameras focused along perpendicular axes. Camera 1 monitors the deformation on the outer surface of the sample, and Camera 2 records the deformation in the thickness direction.

The same setup as the one presented above was implemented for three longitudinal pig skin samples from California, except that this time two Logitech C920 high definition webcams were used to record the deformation in the lateral direction (similarly to what was done previously) and in the thickness direction. Both cameras were mounted on flexible tripods, and a laser alignment tool was used to ensure that each objective was well aligned with the observed surface of the sample (i.e. the outer surface and the thickness section of the sample) and that they are both perpendicular to each other. A schematic illustration of the setup is presented in Figure 2.2. The tested samples were mounted on the Instron 3300 and tested under tension at a strain rate of $0.01s^{-1}$, until sample failure. Samples were speckled on both sections, and the deformations were recorded synchronously via the proprietary software. Different colors were

used for speckling, to facilitate the observation of out-of-plane deformations (sample flattening or curving, twisting, etc.).

From recordings obtained on both sections of the sample, all three principal stretches λ_{xx}, λ_{yy}, and λ_{zz} could be obtained. Note that both sections provide a measurement of λ_{yy}, the stretch in the tensile direction. Thus, results were considered satisfying when the error between both measurements is below 2%. From these measurements, one can also estimate the rate of volume change, given by:

$$\frac{\Delta V}{V_0} = \lambda_{xx}\lambda_{yy}\lambda_{zz} \tag{2.4}$$

where ΔV indicates the change in volume and V_0 is the initial volume of the sample.

2.2.4. Imaging Techniques

Scanning and transmission electron microscopy were used to establish the structure prior to and after mechanical testing (until failure). Particular attention was placed on the configuration of collagen fibers in the dermis. For enhanced tridimensional visualization of collagen in fresh skin, second harmonic imaging microscopy was also used.

2.2.4.1. Scanning Electron Microscopy

The structure of skin was fixed in a 2% glutaraldehyde solution, immediately after excision or after testing. Samples were dehydrated by consecutive immersion in 50%, 70%, 90%, and 100% ethanol solutions. Strips of skin were cut in the cross-section and parallel to the surface of the dermis using a surgical blade. The samples were then dried in a critical point dryer (Tousimis Auto Samdri 815A), and the surfaces were sputter coated with iridium (Emitech K575X). A FEI SFEG ultra-high-resolution SEM was used to visualize the arrangement of the constitutive elements of skin.

2.2.4.2. Transmission Electron Microscopy

The skin was cut using a scalpel into 5 mm x 2 mm strips. Fixation was done by immersing the strips in 2.5% paraformaldehyde, 2.5% glutaraldehyde, 0.1M cacodylate buffer for 2 hours, and subsequently in 1% osmium tetroxide in 0.15M cacodylate buffer for 12 hours. The specimens were then stained in 1% uranyl acetate for 12 hours and dehydrated with 50%, 70%, 90% and 100% ethanol solutions followed by a 1:1 ratio of 100% ethanol and 100% acetone, and 100% acetone (20 minutes immersion each time). Samples were then embedded in low-viscosity resin, starting with a 1:1 ratio of 100% acetone and resin (40 minutes), and finally only resin, subsequently polymerized at 48 ˚C for 48 h. Sections 70-100 nm thick, in all three directions of the tissue, were sliced using a Leica Ultracut UCT ultramicrotome and a Diatome diamond, and placed on copper grids for TEM observation. Post-staining with Sato lead for 1 min was performed.

2.2.4.3. Second Harmonic Imaging Microscopy

A small piece (~10 mm x 5 mm x 5mm) of fresh pig skin was placed in a dish and immersed in water, prior to mounting it on the stage of a Leica SP5 confocal microscope. Collagen emits second harmonic generation fluorescence [232] and can therefore be observed using the appropriate contrasting method with the microscope. Using a 20x water objective, the cross section of the dermis region was observed, and perpendicular slices of the sample were acquired through the depth of the tissue, with a thickness of 129.36 μm and a spatial resolution of 1.47 μm. The volume rendering of the structure allows one to gain a better visualization of the tridimensional collagenous network.

2.2.5. Model Experiments

Human virgin black hair was purchased from an online vendor (www.s-noilite.com) and triple braids of bundles of hair of similar diameter (~4-5 mm) were made, in an attempt to represent the deformation process in interwoven collagen fibers. Portions of ~ 5cm were cut out, and both ends were glued to sandpaper sheets with epoxy. The samples were then placed in an Instron 3300 single column testing machine for loading/unloading tests, with loading cycles interrupted at 100, 150, and 200 N.

2.2.6. Statistical Analysis

In order to make a distinction between the effects of testing conditions and intrinsic parameters such as pig age and sample orientation, a backward stepwise multiple regression analysis was implemented, using the Minitab 17 Statistical Software (State College, PA: Minitab, Inc). Regression models are fit to a given response parameter, using results from all tests, and a p-value is associated to each parameter, as well as a global p-value and an adjusted R-square value. For each iteration of the model, the variable with the highest p-value in the previous regression is removed. The adjusted R-square is used to assess the ability of the model to predict the expected response, and the global p-value determines whether the model should be rejected or not, using an alpha of 5%.

2.3. Results and Discussion

The mechanical response of skin in tension is characterized by an increasing slope of the stress-strain curve; this is commonly referred to as the J-curve type of behavior, which can be encountered in many biological tissues such as tendon, arteries, and skin [10,124,125,211,213]. Figure 2.3a shows the four characteristic stages of this curve, which are well known in the literature: the toe corresponds an initial extension of the tissue, at relatively low loads, followed

by a hardening response with an increasing slope in the heel region, and a linear region characterized by a quasi-constant slope, which decreases at higher strains due to permanent damage, preceding failure. Some specific parameters of this tensile response, indicated on Figure 2.3a, are used in this study to quantify changes with different strain rates.

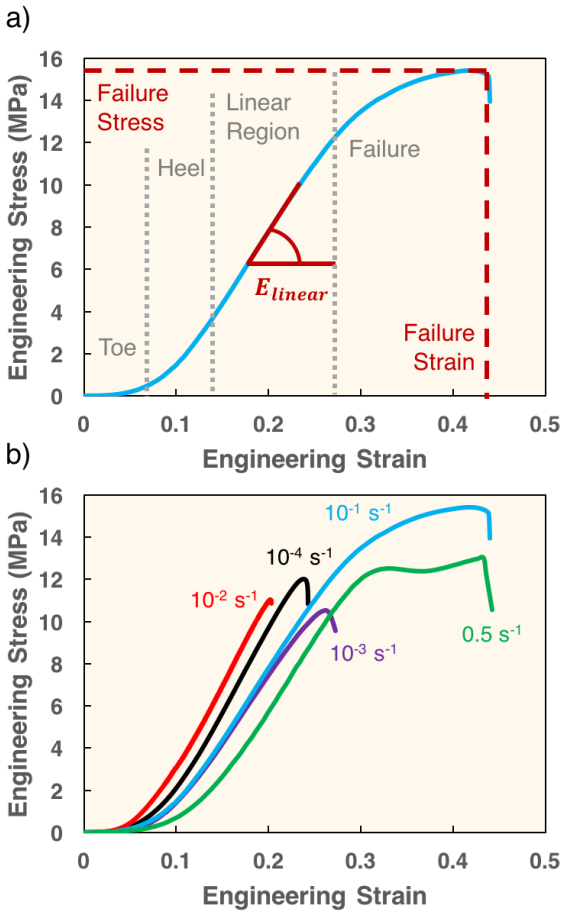

Figure 2.3.(a) Four characteristic stages of the tensile response of skin: toe, heel, and linear regions, succeeded by failure of the tissue. The slope of the linear region, i.e. the tangent modulus E_{linear}, is indicated as well. (b) Effect of strain rate on tensile response of skin (characteristic curves).

2.3.1. Strain Rate Sensitivity

2.3.1.1. Inter-Sample Variations

Figure 2.3b shows characteristic stress-strain curves of skin at five strain rates: $10^{-4}s^{-1}$, $10^{-3}s^{-1}$, $10^{-2}s^{-1}$, $10^{-1}s^{-1}$, and 0.5 s^{-1}. The variation between individual specimens is significant, and larger than the effect of the strain rate. Thus, it is difficult to directly observe the strain-rate sensitivity of skin from separate tests. It will be later shown that strain-rate change tests on a single specimen are more appropriate. To ease comparison between individual specimens, four parameters were extracted from the stress-strain curves to compare the effect of strain rate, as well as the effect of sample orientation; namely the failure strain, the failure stress, the modulus of the linear region (sometimes referred to high strain modulus or 'Young's' modulus in the literature), as well as the stress at the transition between the heel and the linear regions (see Figure 2.3a). The latter was determined by estimating the stress at which the derivative of the stress-strain curve transitions into a horizontal plateau region. The results are plotted in the bar charts of Figure 2.4. Red columns represent transverse sample orientation (perpendicular to spine direction), and blue columns correspond to the longitudinal orientation (parallel to spine direction). Moreover, because of the different sources of tested samples, the combined influence of orientation, strain rate, and pig age on all four parameters was studied in more detail by conducting a stepwise multiple regression (see section 2.6 of this chapter). Results are presented in Table 2.1.

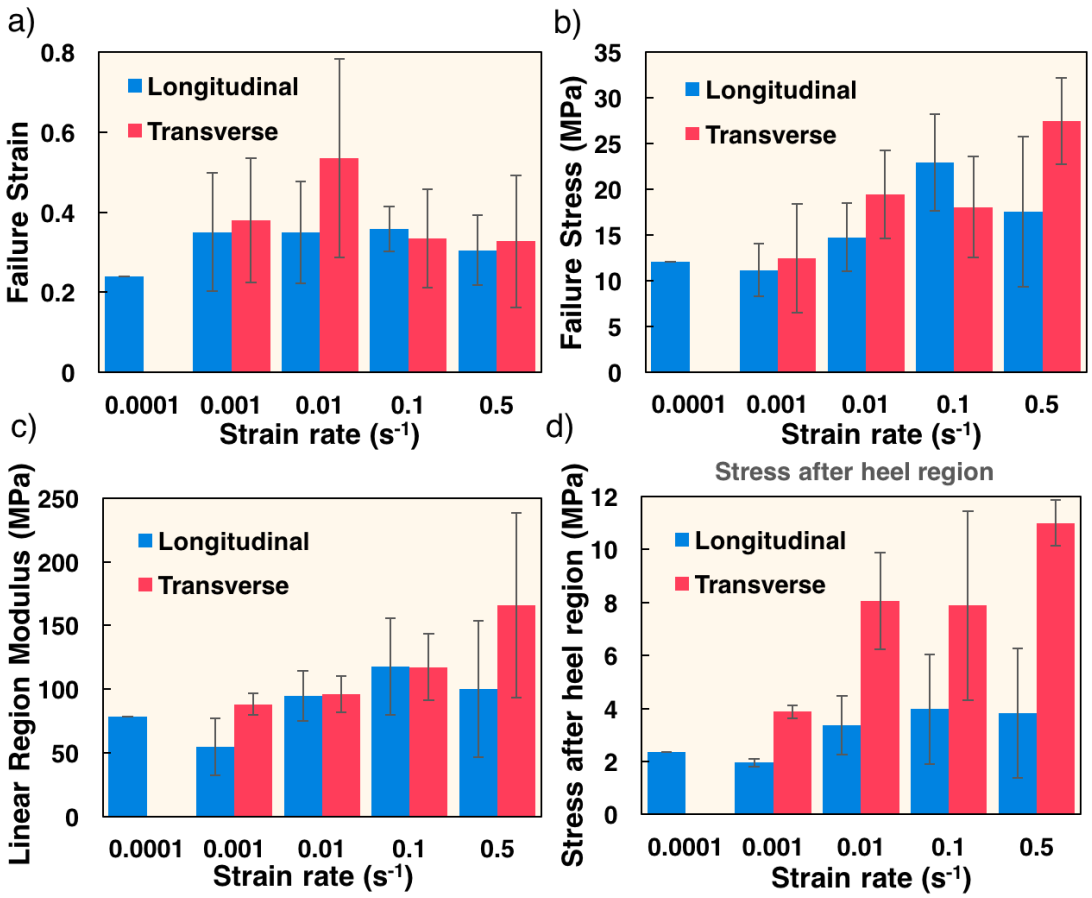

Figure 2.4. Tensile response parameters in longitudinal and transverse specimens removed from dorsal region, parallel and perpendicular to the direction of the spine. While failure strain (a) is not affected by strain rate, the failure stress (b), the tangent modulus in the linear region (c), and the stress level after the heel region (d) (beginning of linear region) increase with strain rate. Differences between longitudinal and transverse samples are not very significant in the dorsal region, but a generally higher level of stress after the heel region is observed for transverse samples.

There is no significant effect of either orientation, strain rate, or age on the failure strain, which nonetheless shows a wide variability, and no model is able to accurately predict it based on these parameters and the obtained results. Ankersen et al. [47] showed that for dorsal pig skin, the level of anisotropy is significantly lower than in the belly region, where stretches in the transverse direction can go up to 1.8, vs. ~1.3 in the longitudinal direction. The failure stress and the tangent modulus both are strongly influenced by sample orientation (with respective p-values of 0.04 and 0.02 for orientation in the best regression models). The

influence of strain-rate is less evident, with p-values of 0.062 for failure stress and 0.132 for the linear region modulus, slightly above the 5% limit of rejection, however neglecting their effect considerably reduces the accuracy of the prediction, as shown by the adjusted R-square values. Age does not appear to have a notable impact on these variables. These results corroborate the findings of Ottenio et al. [132] on the strain-rate sensitivity of dorsal human skin, where similar trends were reported for three strain rates. The stress at the onset of the linear region appears to be highly related with the age of the pig, with p-values below 0.001 for this parameter. The effect of orientation was rejected, however including the influence of the strain rate results in a slightly better prediction (a higher adjusted R-square), an effect that is also observable on the histograms in Figure 2.4d, suggesting that strain rate impacts viscoelastic and rearrangement processes.

Table 2.1. Multiple regression analysis of the influence of sample orientation, strain rate, and pig age on failure strain, failure stress, linear region modulus, and stress at the transition between the heel and the linear region. For each multi-parameter stepwise model, the global p-value, the p-value of each individual variable, and the adjusted R-square are provided. The asterisk (*) corresponds to a parameter that is omitted in the model. The best model for each response is highlighted in grey.

Parameter	p-value				Adjusted R-square
	Model	Orientation	Strain-rate	Age	
Failure strain	0.153	0.209	0.445	0.060	8.58%
	0.093	0.130	*	0.031	9.92%
	0.116	*	*	0.116	8.57%
Failure stress	0.046	0.135	0.077	0.994	17.62%
	0.017	0.040	0.062	*	20.67%
	0.030	0.030	*	*	15.73%
Linear region modulus	0.040	0.185	0.114	0.563	18.55%
	0.017	0.020	0.132	*	20.54%
	0.015	0.015	*	*	16.53%
Stress at heel	0.002	0.220	0.167	0.048	36.69%
	0.001	*	0.083	<0.001	35.33%
	0.001	*	*	0.001	32.57%

2.3.1.2. Intra-Sample Strain Rate Changes

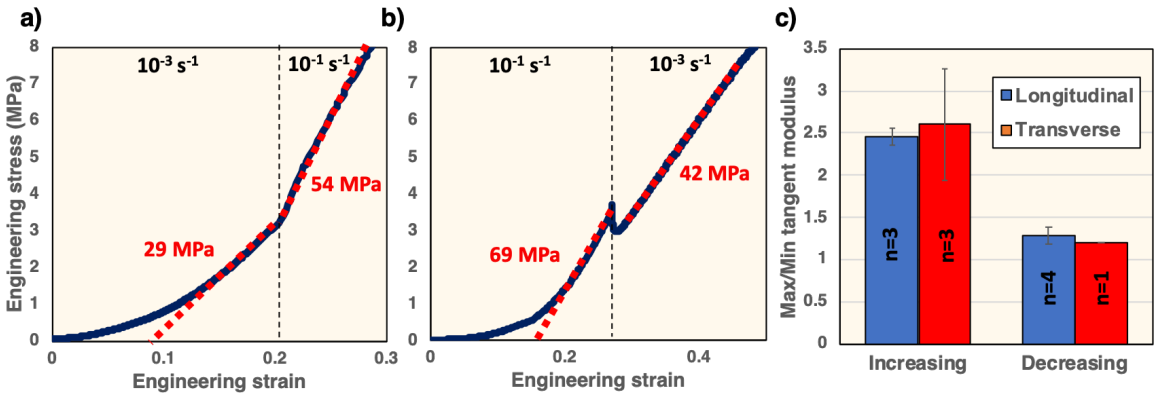

Figure 2.5. Effects of changes in strain rate applied to skin samples during tensile testing, around the middle of the linear region. Changes in linear slope can be measured, thus further providing evidence of the strain rate sensitivity of the material. a) Representative sample for an increase in applied strain rate, from 10^{-3} s^{-1} to 10^{-1} s^{-1}, showing an increase in tangent modulus. b) Representative sample for a decrease in applied strain rate, from 10^{-1} s^{-1} to 10^{-3} s^{-1}, with this time a decrease in tangent modulus. c) The ratio between the high strain rate moduli and the lower strain rate moduli is compared for increasing vs. decreasing strain rate, showing effects of the loading history on the response of the material.

Strain-rate change tests were conducted for individual specimens, by both increasing or decreasing the crosshead speed in the linear region of the J-curve according to the following sequences: 10^{-3}s^{-1} to 10^{-1}s^{-1} (3 longitudinal and 3 transverse sample) and 10^{-1}s^{-1} to 10^{-3}s^{-1} (4 longitudinal and 1 transverse sample). There is no clear jump in the stress when the strain rate is increased by a factor of ~10^2 (Figure 2.5a); this is different from the response of metals [233], in which an instantaneous increase in stress is observed by virtue of the dependence of dislocation velocity on stress, as expressed by the Orowan equation. However, an increase in the tangent modulus can be observed in the linear region, with values rising from 29 MPa, to 54 MPa for the representative sample in Figure 2.5a. For the decrease in strain rate, a small drop was observed (Figure 2.5b): there is relaxation in the specimen due to lower dynamics of the deformation, and the decrease in modulus is less pronounced, with measured values of 60 MPa to 42 MPa for the sample in Figure 2.5b. This change in slope and stress drop with

decreasing strain rate are viscosity effects, dictated by microscale time-dependent phenomena such as interfibrillar shear and the intrinsic viscosity of the ground substance. Interestingly, this effect of change in modulus with applied strain rate is not symmetric: the comparison of the high strain rate modulus with the low strain rate modulus in Figure 2.5c shows that the difference is more pronounced if the applied strain rate goes in the increasing direction, with an increase in modulus by a factor of ~2.5, compared to a ratio of ~1.3 for a decrease in strain rate. No significant influence of orientation was observed. This indicates that not only time-dependent effects have an influence on the behavior of skin, but that there is also an important dependence of the loading history of the material. This could also be related to early stage processes occurring before the linear region is reached in the loading curve.

2.3.2. Evolution of the Poisson Ratio and Influence of Sample Orientation

Some steps of the method to calculate the Poisson are presented Fig. 2.6a-d, and the evolution of the Poisson ratios with the applied stress is plotted Fig. 2.6e. During tension, the Poisson ratio of skin is not constant, and stays mostly outside of the range of traditional isotropic incompressible materials (where it is limited by 0.5). Figure 2.6c shows that, for a longitudinal sample, a rough estimation of the ratio between lateral expansion and tensile stretch can reach approximately 1: $(6.46/5.86)/(16.77/15.62) \approx 1.03$. This would result in a Poisson ratio around -1.4, which is close to the lowest values displayed in Figure 2.6e. An interesting observation is that the initial evolution of the parameters is dictated by sample orientation: longitudinal samples start with negative values at low stresses, mostly around [-1; -0.5], and gradually increase, converging towards 0.5, the limit of incompressibility of isotropic rubber-like elastomers. Inversely, transverse samples have their initial Poisson ratio around 1 or above, as in the work of Lees et al. [228], and decrease towards 0.5 with increasing tensile stress. This

effect of skin anisotropy on the Poisson ratio is reported herein for the first time, to our knowledge. It is likely that differences in the process of rearrangement of collagen fibers, with different initial orientations, affects lateral contraction of the samples, and therefore the Poisson ratio. The significant differences in values at low stresses can be related to different levels of anisotropy for each sample, which were taken from different regions of the body.

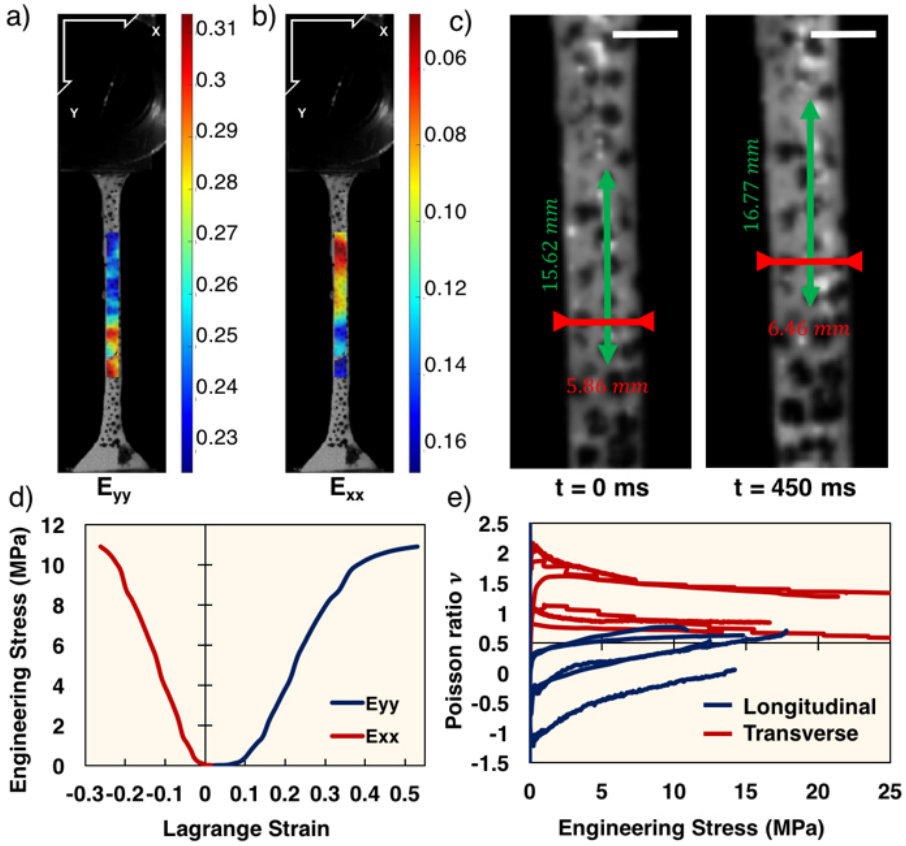

Figure 2.6. Post processing of recorded experiments by Digital Image Correlation (DIC). Local Lagrange strain maps in the vertical/tensile direction (a) and in the horizontal/lateral direction (b). (c) Manual measurements of two-point distances in the lateral and tensile direction in the initial configuration (t=0 ms) and during deformation (t=450 ms) at 0.5 s^{-1} of a longitudinal sample show that lateral expansion is almost equivalent to the tensile stretch (white scale bars = 5mm). (d) Local strains can be averaged to obtain the macroscopic deformation, and thus stress/strain curves in both directions. (e) Calculated Poisson ratio using post-processed DIC of 5 longitudinal samples and 6 transverse samples, plotted against applied stress. Results show a different evolution according to sample orientation, symmetric around 0.5, which is the incompressibility limit.

Data from measurements in both directions, as described in section 2.3.2 of this chapter, can be useful to estimate the other Poisson ratio in the thickness direction (ν_{yz}), volume

changes, and sample distortion. Experimental results are summarized in Figure 2.7. Figs. 2.7a-b show the 2D strain maps from which the average stretches are obtained. It can be observed that deformations in the thickness direction appear more heterogeneous, although the obtained average in the tensile direction is roughly the same. No torsion, flattening, or curving is observed during deformation. The region of interest of the DIC processing stays within the observed section of the sample. Note that each sample (1,2,3) was taken with the same orientation, but each time further away from the spine. A direct consequence is that a change in tissue anisotropy due to body region is directly observable in the experimental results, as seen on the stress-strain curves Fig 2.7c. Trends of the Poisson ratio in the lateral direction ν_{yx} (Fig. 2.7d) are slightly affected as well, but most importantly the initial offset of the evolution curve is different and decreases the closer one gets to the belly region, which is where most of the previous samples where tested. This time, the Poisson ratio in the thickness direction ν_{yz} can be observed as well (Fig. 2.7e): the opposing trend is seen for the initial offset, with values increasing as one gets further from the spine. Sample 1 shows an initial coefficient close to -0.8, indicating that negative Poisson ratios are also found in this direction. Interestingly, sample 2 starts from 0.5 but decreases towards negative values, reaching a final coefficient around -0.15, suggesting that these are not strictly limited to the reference state. This also implies that after a certain applied stress, the sample starts swelling in the thickness direction: this evolution is further detailed in Appendix A. As a matter of fact, considerable swelling can be observed for sample 1 (up to 5%) and sample 2 (up to 15%), as reflected by the evolution of $\Delta V/V_0$ (Fig 2.7f). Sample 3, which does not show a negative Poisson ratio, has a more stable evolution of the volume ratio, with a slight initial drop (<5%), suggesting some loss of volume.

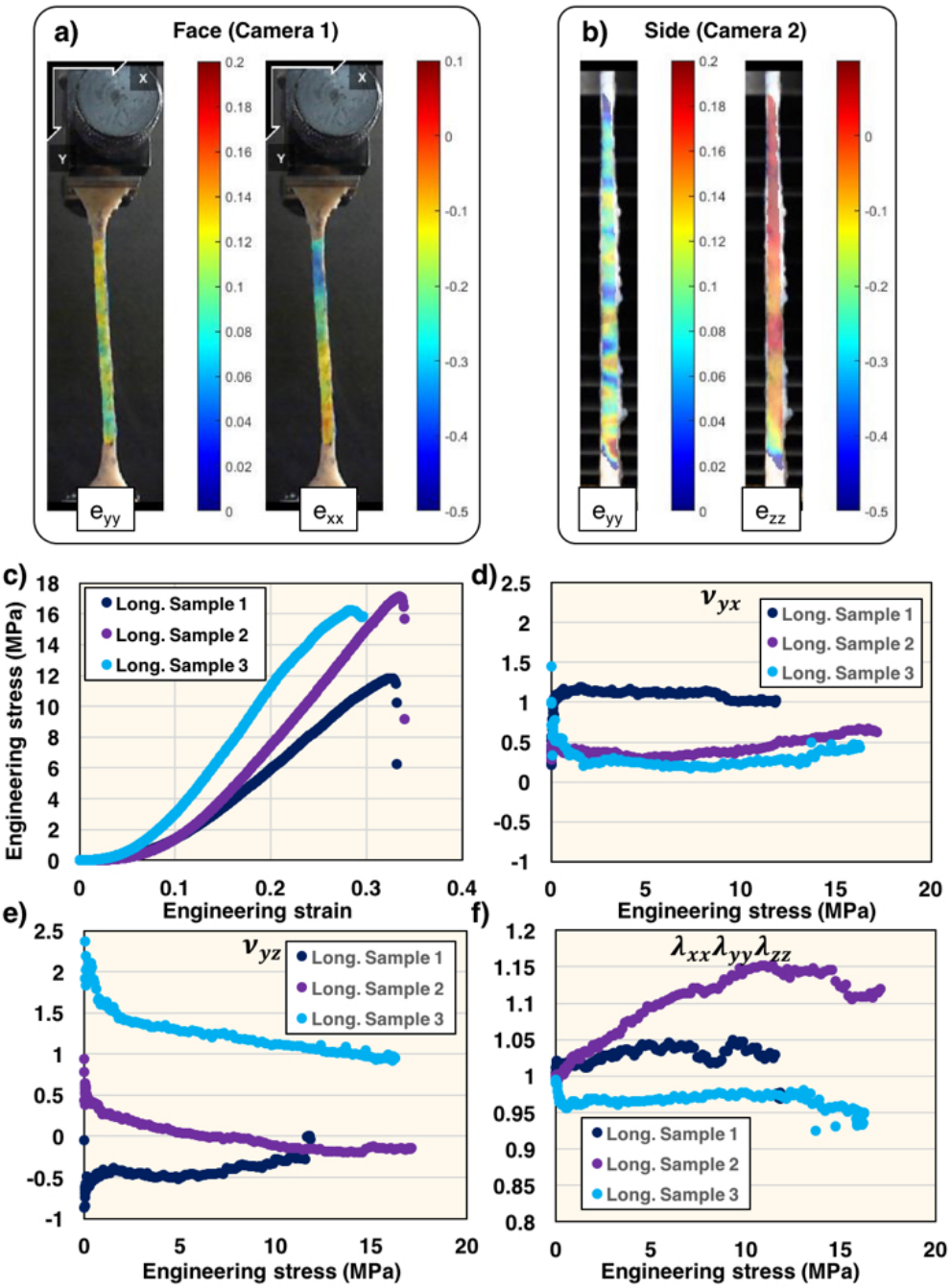

Figure 2.7. DIC post-processing from recordings of the face and the side of the tested sample. (a) Euler-Almansi strain maps from DIC post-processing in the tensile (yy) and lateral (xx) directions at a macroscopic stress level of 2.3 MPa for a pig skin sample. (b) Euler-Almansi strain maps in the tensile (yy) and thickness (zz) directions at the same stress level for the same sample. (c-d) Evolution of the Poisson ratios ν_{yx} (b) and ν_{yz} (c) with applied tensile stress for the three longitudinal skin samples that were tested. Results show large variations and high tissue anisotropy, with values spanning approximately -0.5 to 2. (e) Rate of volume change with applied stress. Trends indicate significant changes in volume depending of the region from which the sample was taken.

In order to test the accuracy of the method, we conducted similar tests with samples of layered thermoplastic rubber, for which the mechanical properties are more consistent. Results are available in Appendix B. From these tests, we conclude that some inaccuracies are inherent to the method itself, due to limitations in resolution, especially at low strains. However, good reproducibility and accuracy at larger stresses are reached in general.

Moreover, a uniaxial tensile setup is not sufficient to fully characterize the anisotropic deformation of the tissue [113,174]. Some complimentary Poisson ratios cannot be measured with this method, and additional degrees of freedom limit the precision of the indirect measurements. No influence of the strain rate on the Poisson ratio has been observed from our measurements.

2.3.3. Stress-Relaxation

Three normalized relaxation cycles of a longitudinal and a transverse skin sample are presented Fig. 2.8a-b. For each cycle and orientation, similar values of the stress before relaxation were isolated to facilitate comparison, namely approximately 1 MPa, 4 MPa, and 6 MPa. Prony series least-squares fit are also plotted, and generally show a high R-square coefficient, above 0.99. With increasing applied stress, the elasticity modulus at the end of the relaxation period increases, which is expected for a non-linear material with a J-shaped stress-strain curve, and thus an increasing tangent modulus. The moduli are higher for the transverse samples, as observed previously for strain-rate sensitivity tests. Further details on the relaxation times can be extracted from the evolution of the Prony series parameters with applied stress, presented Fig. 2.8c-f for the two samples that were selected. The time constant τ_1 (Fig. 2.8c) remains within the order of magnitude of 10 s. Rather similar trends are observed between longitudinal and transverse samples: the relaxation constant increases with tensile stress,

stabilizes near the linear region of the sample, and decreases at the onset of damage, close to failure. The smaller time constant τ_2 (Fig. 2.8d) is in the range of ~1 s, and follows a similar trend. Values for both constants are slightly higher for the transverse sample than for longitudinal one. The difference between the two time constants could come from the existence of mesoscale constituents with different viscosity and elasticity, in which case the soft viscous matrix would have a smaller relaxation time constant. Another possibility, suggested by Emile et al. [234] for spider dragline silk and by Yu et al. [235] for hair, is that each time constant corresponds to a different hierarchical level of the structure (nested model). We can hypothesize that the relaxation constants are due sliding processes occurring at the fiber level (τ_1) and at fibril level (τ_2), and longer time constants, associated with slower mechanisms in the tissue, can be identified with longer relaxation times. This would require the expansion of the Prony series to additional terms, and would modify also the previous values. Nonetheless, the consistency between experiments was favored, with similar relaxation times and function parameters, so that a compatible analysis can be performed. Parameters of the fitting function were limited to 5 to ease the comparison, and also because with a relaxation of 30 s and a time resolution of ~ 1 ms, identifiable time constants are constrained within this range. A notable difference between the transverse and the longitudinal reduced modulus a is seen Fig. 2.8e, which could also be expected from the difference in elastic modulus reported earlier. Parameters b and c are within the same range, and decrease with applied stress, with this time higher values for the longitudinal sample. This trend is explained by the fact that for any applied stress $\sigma(0)/\sigma_0 = a + b + c = 1$, and with the increasing trend of a.

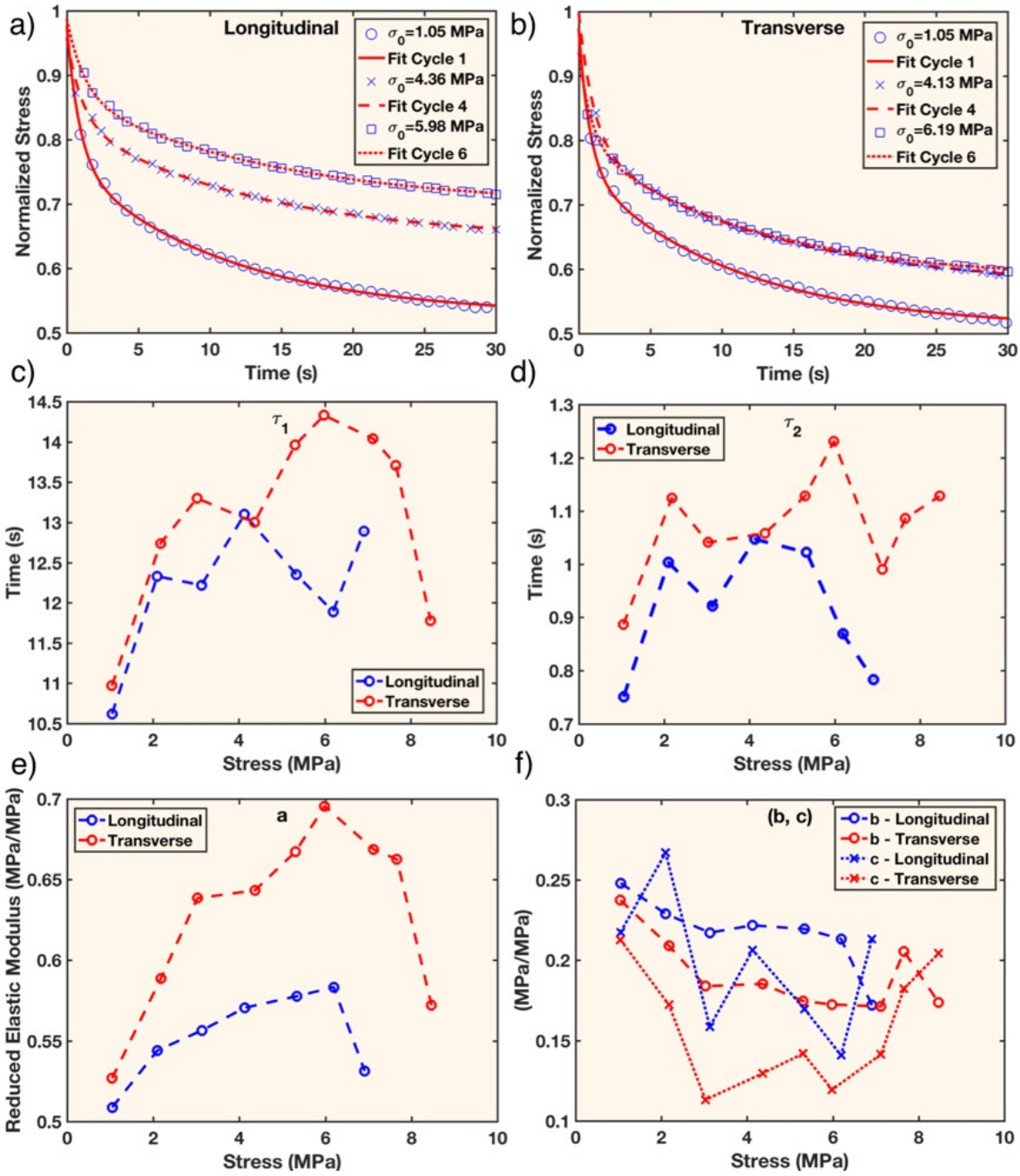

Figure 2.8. Normalized stress relaxation curves of (a) a longitudinal sample and (b) a transverse sample of pig skin, and Prony series fits.Experimental results are in blue, and red lines correspond to Prony series fits. Relaxation rounds were taken for samples tested around the same stresses to facilitate comparison. (c-f) Parameters of the Prony series relaxation function: time constants (c) τ_1 and (d) τ_2, (e) normalized elastic modulus a, and (f) material parameters b and c. The longitudinal and the transverse samples show similar evolutions of the material parameters, with a notable difference of the modulus a, as the first curves suggested.

Table 2.2 provides values of all the Prony series parameters taken for all the relaxation tests that were conducted. Only parameters taken from the stable region, the linear region of the J-curve, were used in the calculation of the average, to reduce data scattering. As a result, very consistent parameters were obtained, with small standard deviations, regardless of inter-sample and intra-sample variations. The p-value between transverse and longitudinal samples for each parameter was determined with a paired t-test, and show very significant differences for a, b, and τ_1, similarly to what was found in the comparison of the first two samples. The p-value of parameter c is slightly above 1% (p-value = 0.018), and no significant difference can be inferred on the values of the associated time constant τ_2. This suggests that there is a subset of constituents of the material, with low viscosity, that is less influenced by tissue anisotropy. However, all calculated average values are very close to each other, implying a rather low influence of sample orientation on the relaxation response of skin.

Table 2.2. Average values of the Prony series parameters compared between longitudinal and transverse sample orientations, with standard deviations. For each orientation, parameters are averaged regardless of inter-sample and intra-sample variations, for initial relaxation stresses between 2 MPa and 10 MPa. The p-value between longitudinal and transverse samples is also reported, (*) indicates a significant variation between parameters ($p<0.05$) and (**) corresponds to a very significant variation ($p<0.01$).

	Longitudinal (N=16)	**Transverse (N=22)**	**p-value**
a	0.580±0.042	0.618±0.041	0.009 (**)
b	0.223±0.017	0.204±0.023	0.0087 (**)
c	0.173±0.037	0.145±0.030	0.018 (*)
$\boldsymbol{\tau_1}$	12.102±0.925	13.784±1.670	0.0009(**)
$\boldsymbol{\tau_2}$	1.057±0.148	1.052±0.114	0.91

2.3.4. Cyclic Testing and Damage Evolution

Viscoelasticity of skin is also demonstrated by the hysteresis stress-strain curve followed during sequential loading and unloading of skin samples in tension, as can be seen in some results presented Fig. 2.9a. The existence of remnant strains after unloading shows the

establishment of a new equilibrium position, a result of irreversible changes occurring in the structure [51,236,237]. Experimental observations [134] have also shown that upon reloading, skin follows the same path as the unloading curve, a phenomenon called the Mullins effect (not presented here).

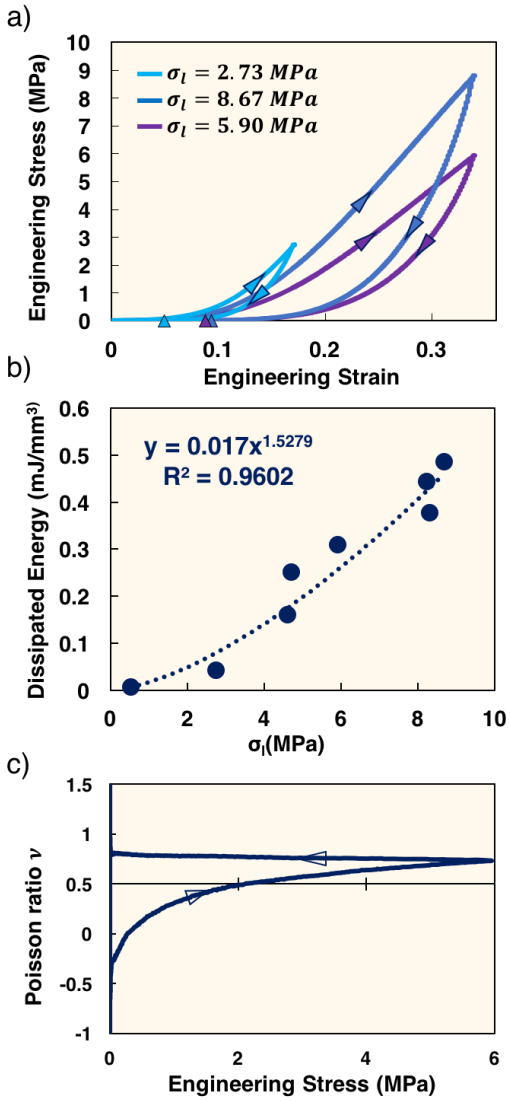

Figure 2.9. Irreversible changes occurring during loading/unloading tests. (a) Loading/unloading tests of pig skin interrupted at different stresses σ_l. Arrows indicate the remnant strain ε_r for each test. The integral of the hysteresis curve, i.e. its area, is equal to the dissipated viscoelastic energy. When plotted against σ_l (b), it appears to follow a power law trend with an exponent close to 3/2, as shown by the least-squares fit on the graph, with an R-square coefficient of 0.96. (c) The Poisson ratio, calculated using the DIC post-processing method, also follows a different path during loading and unloading of the sample. Arrows indicate the evolution of the coefficient. During unloading, it remains constant around 0.78, suggesting a constant lateral expansion, above the limit of incompressibility.

The area contained inside the hysteresis curve, equal to the viscoelastic dissipated energy E_d, was calculated. When compared to the stress at the end of the loading cycle for each sample (Fig. 2.9b), the energy appears to follow very closely a power law; the least-square function that was found is $E_d = 0.017\sigma_l^{1.5279}$, with a high R-square coefficient of 0.96. This implies that the dissipated energy is fully determined by the stress at the end of loading (for the longitudinal orientation), and that a stress-based criterion can facilitate inter-sample comparison, for which the data is usually scattered due to large variations in biological samples. Further analyses of the cyclical behavior at different strain rates indicated a slight decrease in dissipated energy, but with a level of significance below the dominating effects of sample orientation, inter-sample orientation, and tissue preconditioning. The effect of cyclical loading was also observed for the comparison of the Poisson ratio (see Figure 2.6d). Figure 2.9c shows the evolution of the Poisson ratio of one sample during one loading/unloading cycle: the loading evolution is typical of longitudinal samples, with an initial coefficient starting at -0.5, increasing and converging towards 0.7 at the end of tension. Interestingly, the value of the Poisson ratio at unloading follows a different path, and stagnates around 0.7 all the way until the new equilibrium position. A more complete description of this evolution is provided in Appendix C, showing that the coefficient can also go back to, or reach negative values for some samples prior to reloading, a trend that has also been found in fiber reinforced composites [238]. This evolution is another indication of the irreversibility of the deformation, and of an internal rearrangement of the constitutive elements of skin. More detailed insight into the process of realignment of collagen in the dermis during tension is presented in the following sections.

2.3.5. *Ex Situ* Imaging of Collagen Fiber Rearrangement

The principal method of characterization used was transmission electron microscopy, which was supplemented by scanning electron microscopy and second harmonic generation microscopy. These combined techniques enable a complete tridimensional picture of the collagen arrangement and its evolution prior to testing and after sample failure.

2.3.5.1. Initial Structure

The initial structure was imaged along three orientations: longitudinal, transverse, and in-plane. These are shown in Figure 2.10. The three planes form an orthogonal set and enable visualization of the principal features. One observation that is of high relevance is that the wavy pattern characteristic of collagen is observed in all three sections. Thus, the fibers (with an average diameter of ~3 μm) are not constrained to one plane, but form a tridimensional pattern. These fibers are seen in the longitudinal (Fig. 2.10a), transverse (Fig. 2.10b) and in-plane (Fig. 2.10c) sections. Each collagen fiber is composed of fibrils with diameters of ~ 80 nm, bundled together. Ground substance (proteoglycans) fills the gap. Detailed images of the collagen fibrils are shown in the out-of-plane direction in Fig. 2.10d and in the in-plane direction in Fig. 2.10e-f. The characteristic band pattern of 67 nm of collagen is observed [10]. Fig. 2.10f. shows in detail the change of orientation at the fibrillar level; where collagen in-plane fibrils transition from semi-circles into ellipses, as their angle with the viewing plane increases, until reaching 90˚ at which orientation the cross-section becomes circular, as in Fig. 2.10d.

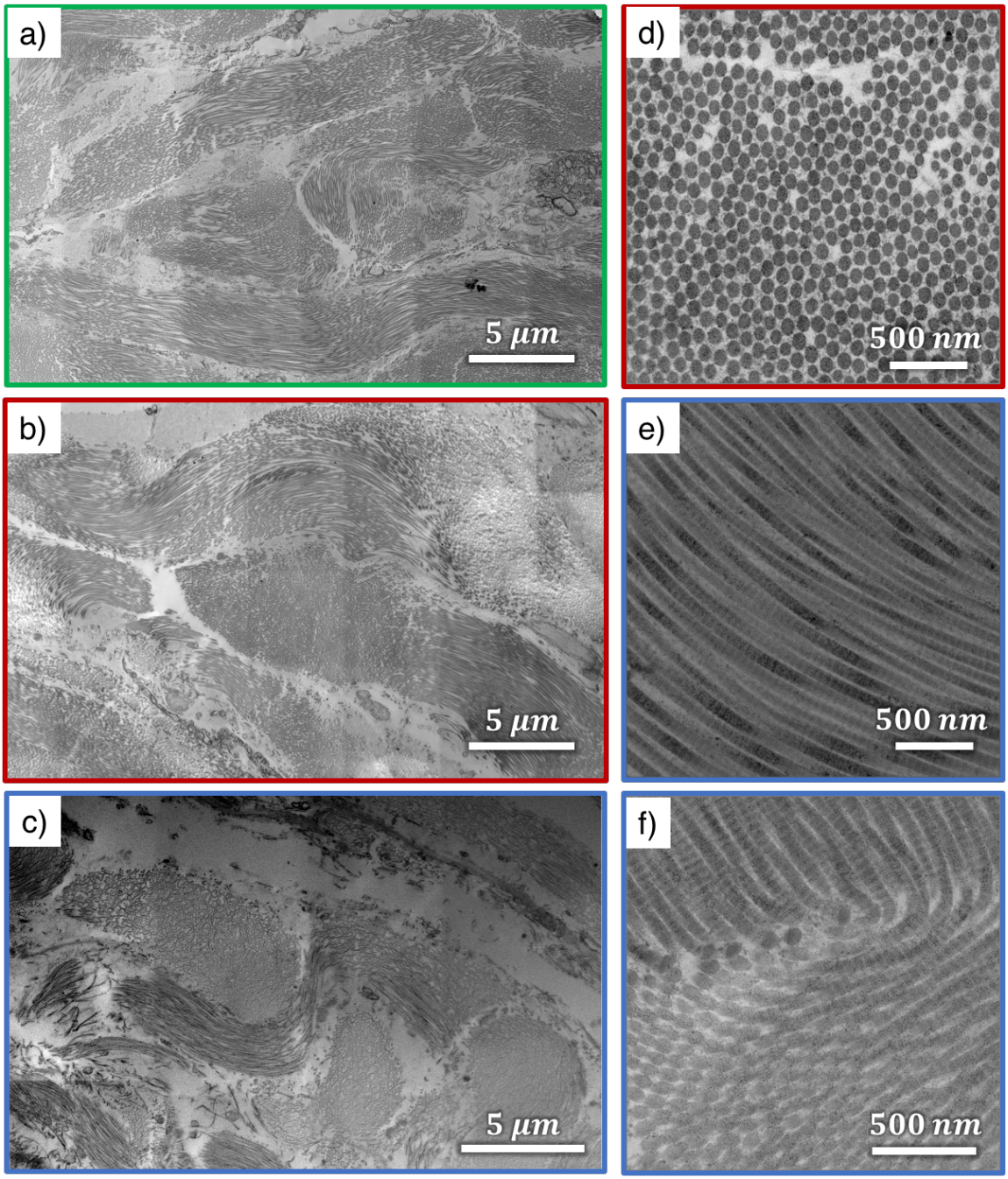

Figure 2.10. Transmission electron micrographs showing the configuration of collagen in untested skin viewed in three orientations; (a) longitudinal, (b) transverse, and (c) horizontal (parallel to the outer surface) sections. Note the tridimensional weave pattern of collagen fibers. (d) High magnification transverse section of the dermis, showing collagen fibrils bundled in a fiber, going out of plane. Fibril diameter and area fraction can be estimated here. (e,f) High magnification horizontal sections of the dermis showing characteristic 67 nm d-bands of collagen fibrils, bundled together in fibers. Fibers come in and out of plane, as seen here by changes in the cross-section of collagen fibrils, from circular, to elliptical, to in-plane.

The diameters, areal fraction, and fibril density were measured and the quantified results are shown in Figure 2.11. There is some variation, but the average numbers represent fairly well the distribution of sizes. Figure 2.11a shows the cross-section of one prominent fiber, which was isolated and binarized as shown in Figure 2.11b, to enable quantification. The fiber thickness was estimated by assimilating the cross-sectional area of a fiber to the one of a circle, and data was complemented by direct in-plane measurements of fiber thickness, from other micrographs. Very similar distributions were obtained, converging to a mean value of 2.2 μm (Fig. 2.11c). The distribution of the areal fraction of fibrils inside a fiber is provided in Fig. 2.11d, and was measured by calculating the area of black pixels (fibril) divided by the total cross-sectional area of the fiber; the rest (white pixels) is ground substance. The mean value is 0.69, compared to a theoretical maximal value of 0.85, if one assumes a close packed arrangement of cylinders inside a circle. The fibril diameter (Fig. 2.11f) shows some variation (see also Fig 2.10d), the mean being 82 nm, consistent with previous observations of collagen in other mammals [10] (see also Chapter 1).

Notable by its absence is elastin. It is known that it comprises a much lower fraction of the dermis (2-4%) than collagen (~70%). It is possible that the osmium tetroxide staining does not reveal it, but it is still puzzling that it does not seem to play a significant role in the architecture of the dermis, although it is often reported as essential to the ability of skin to reversibly recoil under low strains [215]. Confocal microscopy seems to be a more appropriate tool to reveal the arrangement of elastin in the dermis, with nonetheless very low volume fractions [18].

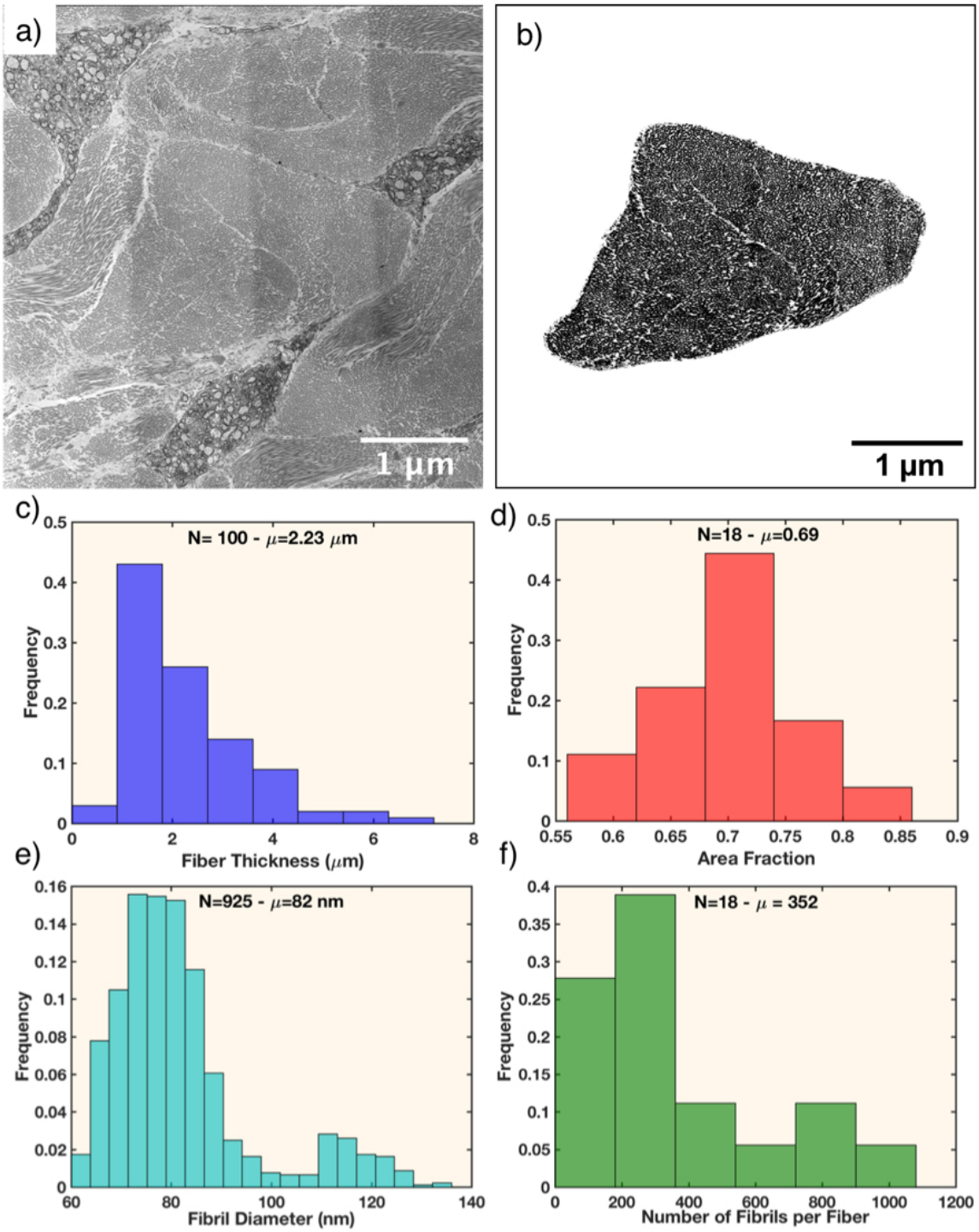

Figure 2.11. Estimation of collagen fiber and fibril dimensions. (a-b) Out-of-plane collagen fibers are cropped out, and a threshold is applied to the region to isolate fibrils from the surrounding ground substance, allowing for the calculation of dimensions and area fractions. (c) Distribution of collagen fiber thickness. (d) Distribution of the area fraction of collagen fibrils contained in a fiber, centered around 0.69, below the theoretical maximum value of 0.85. (e) Distribution of collagen fibril diameters. (f) Estimation of the number of collagen fibrils per fiber. N indicates the number of elements that were used for each calculation, μ is the mean value of the distribution.

2.3.5.2. Structure After Failure

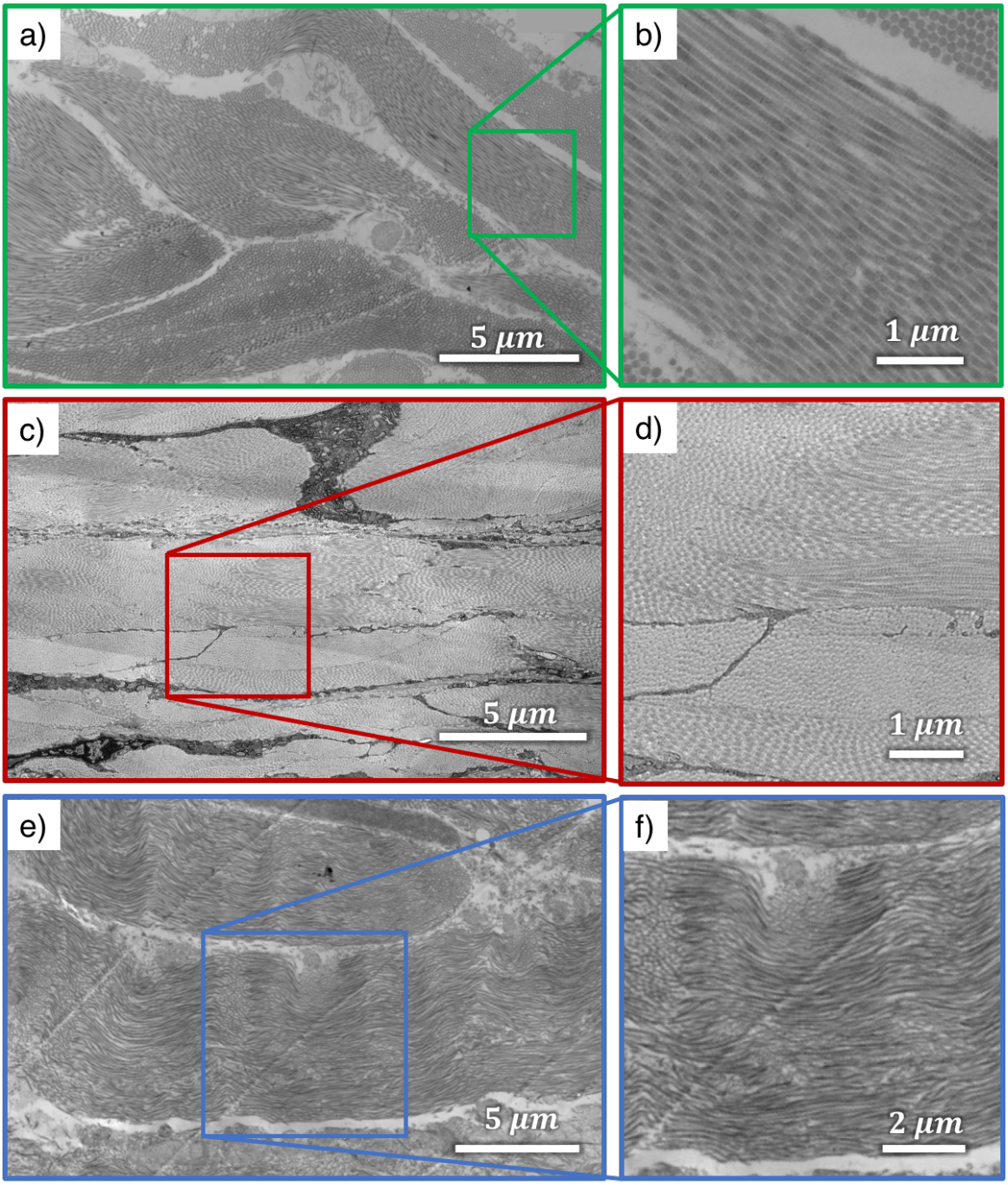

Figure 2.12. Configuration of collagen in deformed (to failure) skin in three orientations; (a-b) longitudinal, (c-d) transverse, and (e-f) horizontal (parallel to the outer surface) sections, visualized by transmission electron microscopy. Collagen fibers were straightened during the deformation process, and appear to be more confined in the horizontal plane. In the transverse orientation, fibers mostly appear to be going out of plane. Square inserts in (a,c,e) indicate the location of the magnified images in (b,d,f).

Extension of skin in tension to failure changes the configuration of collagen fibers significantly [7,41]. In the same way as for Fig. 2.10, TEM was used to image the three sections (longitudinal, transverse, and in-plane). Figure 2.12 shows low and high magnification views where the decrease in the curvature of the fibers is evident. The presence of interwoven fibers aligned with the three planes, is again observed. An increased alignment of the fibers with the tensile direction is seen as well, with a higher proportion of fibers confined in-plane (Fig. 2.12a-b), and the transverse section showing mostly out-of-plane fibers (Fig 2.12c-d). Fig. 2.12e-f show fibers with a much smaller wavelength than in the original state; this is thought to be due to the recoil of the sample after tensile failure. Quantitative measurements of the fiber alignment, which for the longitudinal and in-plane sections corresponds to the angle between the principal axis of a fiber and the tensile direction, and is the angle between the principal axis of a fiber and the direction orthogonal to the surface of the skin in the transverse direction, are reported before testing and after sample failure in Fig. 2.13. Fig. 2.13a describes the three principal directions previously defined with respect to the tensile direction (OX_2), which coincides here with the direction of the Langer lines, and the angles (α, β, γ) used to determine the main orientation of fibers. Namely, the plane (X_1, X_2) defines the dermis surface, (X_1, X_3) defines the transverse plane (perpendicular to the tensile load and to the Langer lines), and (X_2, X_3) is the longitudinal plane. The statistical data before testing and after failure are presented in Figs. 2.13b-d. After failure, an increased alignment of the fibers with the tensile direction (0˚) is seen, notably with a narrower distribution peak, for the dermis surface section. The same effect is observed in the longitudinal section, as collagen fibers are recruited into the tensile direction, with a decreased value of γ. In the transverse section the migration of fibers occurs

towards β= ±90˚ (Fig. 2.13c); this implies an increased in-plane confinement, as already observed Fig 2.12c-d.

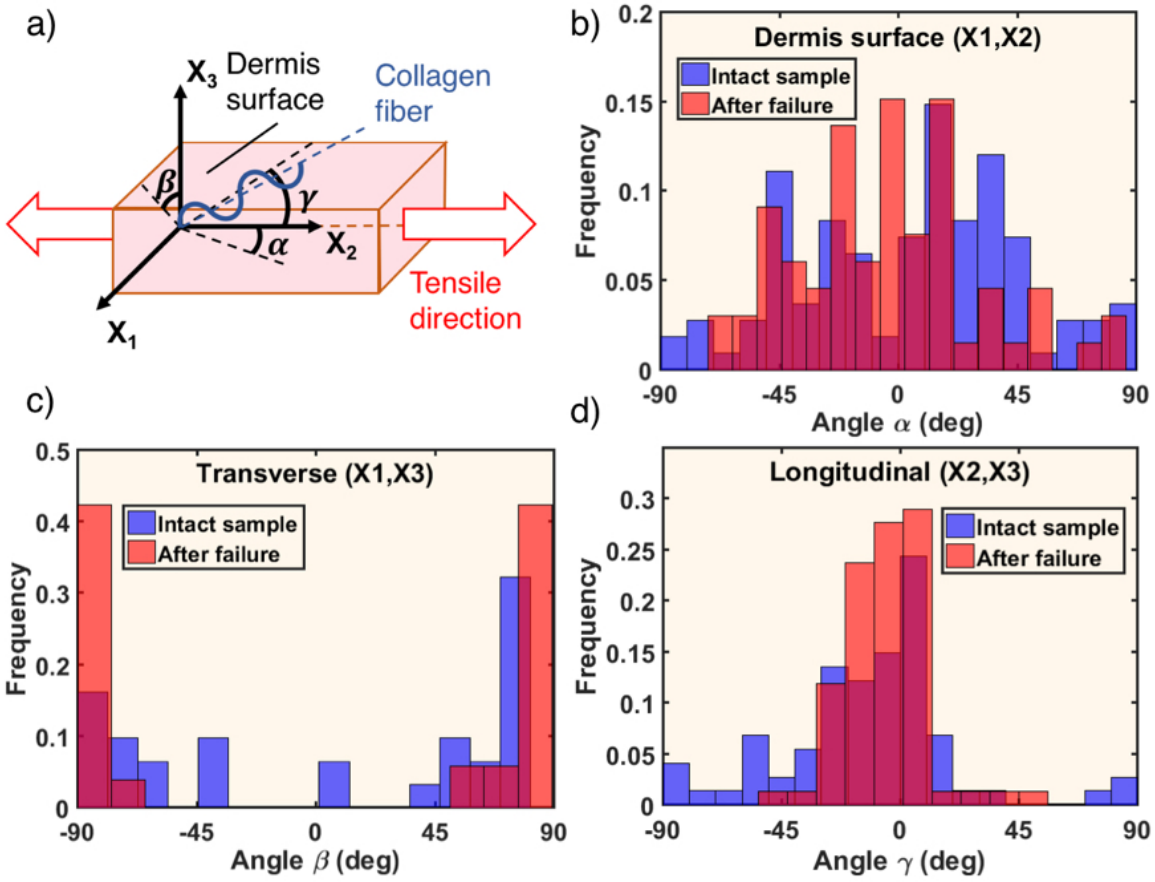

Figure 2.13. Distribution of orientations of collagen fibers measured by angles (α, β, γ) of diametral lines with the tensile direction in intact samples and after failure. Planes of observation and corresponding angles are illustrated in (a), the tensile direction coinciding with the direction of the Langer lines. Note an increase in concentrations close to 0˚ with the tensile direction in the (b) horizontal and (d) longitudinal planes, and consequently a realignment close to ±90˚ in the (c) transverse direction in the failed sample.

2.3.5.3. Collagen Deformation

The radii of curvature r and the opening angles, based on a semi-circular one-dimensional model of wavy collagen fibers previously proposed by Yang et al. [41], were measured to quantify the expected straightening of collagen fibers after failure. This is shown in Fig. 2.14a. Statistical data for both parameters (r and ω), measured before testing and after failure, is

reported Figs. 2.14b-c. It is expected that during deformation, the radius of curvature of every fiber increases, while the opening angle decreases with fiber straightening. The case of a fully taut fiber corresponds to an infinite radius and an opening angle of 0˚. Statistical distributions of r and ω show the opposite trend: the radius of curvature significantly decreases, while the opening angle increases. This result can be explained by fiber recoil after sample failure or extraction, as previously observed in Fig. 2.12. Moreover, even though electron micrographs show more straightened fibers, measuring a radius close to infinity is not straightforward, while second order crimps are easier to quantify. A configuration with some interweaving, or braid-like structure can also explain this post-failure recoil, with neighboring fibers being less subjected to confinement between each other.

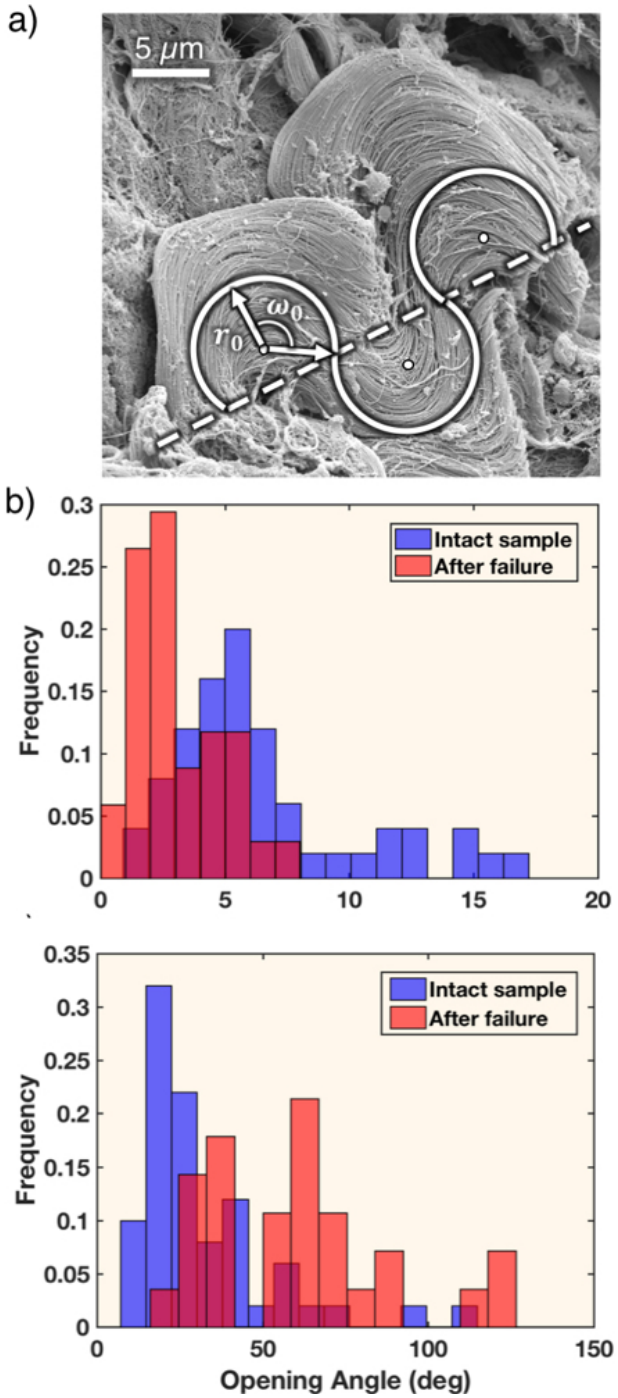

Figure 2.14. Configuration and radii of curvature of collagen fibers in intact sample and after failure. (a) Scanning electron micrograph of a collagen fiber in the dermis of pig skin, superposed by a simplified representation of the wavy collagen fibers. Semi-circular segments with radius of curvature r_0 and opening angle ω_0 (in the initial configuration) describe the neutral axis of a fiber. Distribution of (b) radii of curvature r and (c) opening angle ω in intact (N=50) and deformed (N=33) collagen fibers.

2.3.6. Interweaving of Collagen Fibers

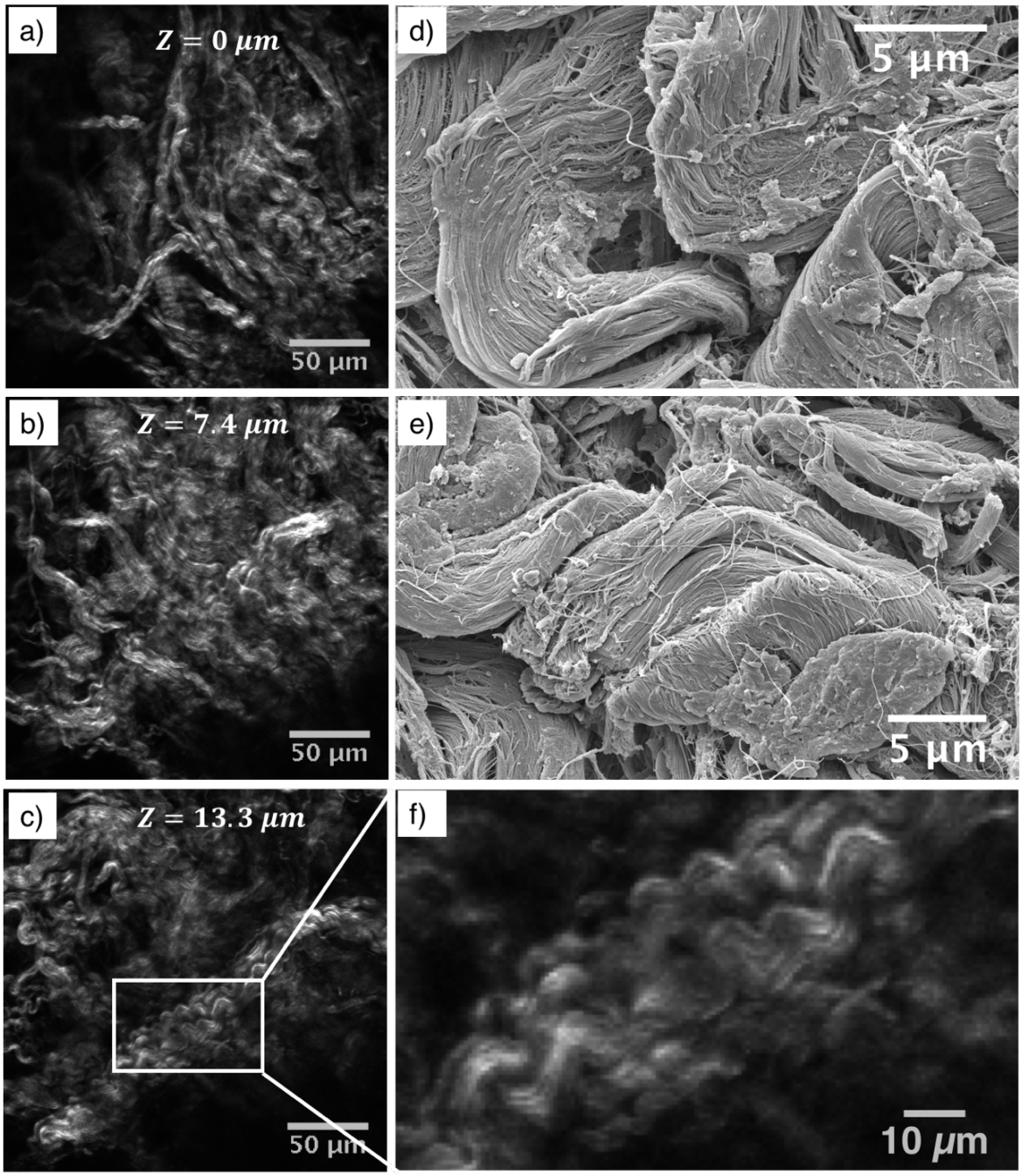

Figure 2.15. Cross section views of pig skin dermis, showing the tridimensional arrangement of the collagen fiber network, and a certain degree of entanglement. (a-c) Confocal images with second harmonic generation fluorescence of collagen, captured at different intervals of depth. Oblique, wavy, perpendicular, fibers are superposed at different locations throughout the depth of the tissue, suggesting an interwoven pattern. (d-e) Scanning electron micrographs of collagen fibers, with folds and braid-like arrangements demonstrating the non-planar configuration. (f) Close up view of (c) showing collagen crimp and entanglement.

The tridimensional nature of the collagen fiber configuration was evaluated by confocal and scanning electron microscopy. Observation on planes perpendicular to the dermis surface enable a look at this structure that has only been quantitatively characterized before by Nesbitt el al. [123]. Confocal microscopy conducted at three depth intervals of the cross section of the dermis is shown in Figs. 2.15a-c and Fig. 2.15f. It is clear that the collagen fibers are not arranged in layers parallel to the skin surface. Sherman et al. [12] observed a simpler arrangement for rabbit dermis and were able to peel layers parallel to the surface. Sections at 0 μm, 7.4 μm, and 13.3 μm show the waviness of the collagen with a radius of approximately 5 μm, as described in Figure 2.14. The fibers are oriented at different angles but there seems to be two main perpendicular directions, as quantified earlier by Jor et al. [13]. The same configuration with higher magnification is shown in the SEM micrographs of Figs. 2.15d-e, where twisted braid-like structures can be discerned.

The tridimensional character of the fiber arrangement is clearly demonstrated. Indeed, this tridimensional arrangement can generate a mechanical response that is unique because the straightening of the fibers in tension is constrained by the neighboring bundles. This configuration is akin to the one in braided filamentary structures. In order to test the hypothesis of constitutive dependence of the mechanical response on the arrangement of fiber bundles, a simple model experiment was performed using hair bundles. Straight hair was organized into three bundles and braided into a tress (Fig. 2.16a). Each bundle had approximately 2,000 hairs. The simplified schematic in Fig. 2.16b shows that, on top of the applied tensile load Fx_2, contact forces from neighboring hair bundles (or collagen fibers in the case of skin) oppose the straightening mechanism. We hypothesize that this can be approximated by a distributed force

$Fx_1(X_2, \varepsilon)$ applied on the concave surface of the bundle and depending on the proximity to the neutral axis as well as the deformation state. The tensile response was determined and is shown in Fig. 2.16c, together for a single hair. The difference is dramatic and the J-curve behavior exhibited by the braid is strongly reminiscent of skin. This response of the braid is produced by the interaction among the hair bundles and not by their permanent deformation, which has its onset at 150 MPa for human hair [239]. The hysteresis exhibited upon unloading is also present, in a manner similar to skin. The onset of the linear regime occurs at a lower strain than for skin, but this is a parameter that can be manipulated by varying the tightness of the hair braiding. This model experiment demonstrates that the mechanical response of the dermis is influenced by the tridimensional organization of the collagen fibers.

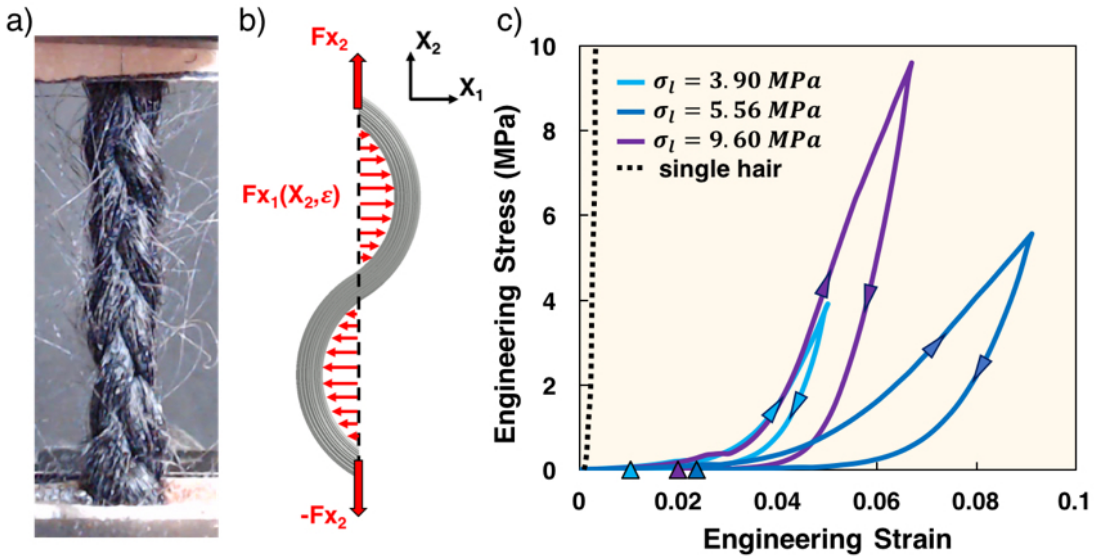

Figure 2.16. Analogy between the loading/unloading behavior of a hair braid with collagen structures in skin.

a) Mechanical test on a triple braid of hair. b) Simplified two-dimensional representation of the forces acting on one bundle of hair/fibrils under a tensile load Fx_2. The neighboring bundles apply contact forces, modeled here as a distributed load Fx_1, which depends on the position X_2 and the deformation state ε. c) Loading/unloading tests of different hair braids, with loading cycle stopped at different stresses. A hysteresis can be observed for each case, and remnant strains are present at unloading, indicated by arrows. Note also the J-shaped loading curve.

2.4. Conclusions

The present study provides a complete experimental characterization of the uniaxial tensile behavior of skin, showing that it is a non-linear elastic material exhibiting sensitivity to time dependent and loading history dependent processes, i.e. strain rate, relaxation, and cyclic loading. Cross sample and intra-sample variations are both reported and quantified. An important finding is that viscoelastic processes are mainly determined by the level of applied stress, while a strain-based comparison results in very dispersed data due to large variations in terms of toe width and failure strain. Sample orientation has only little influence on the viscoelasticity of the tissue.

The evolution of the Poisson ratio during deformation is presented here for the first time, to our knowledge. The different trends observed for transverse and longitudinal samples are of particular interest, and are indicators of different rearrangement processes occurring within the microstructure of the dermis. Other measurements indicate that this evolution, and particularly the initial offset of the Poisson ratio, is also dependent of the region of the body where the sample is taken. Loading/unloading tests show that this process is irreversible, with the Poisson ratio at unloading following a different path than during the loading cycle, similarly to the Mullins effect for the tangent modulus [134]. The particularly extreme values of the coefficient (from -1.2 to 0 for longitudinal samples and from 1 to 2.5 for transverse samples), as well as the global convergence towards values above 0.5 could be caused by a significant variation of local tissue anisotropy, and raise an interesting question regarding tissue incompressibility. Synchronous measurements in the lateral and in the thickness direction show that swelling occurs, and is initiated early in the deformation for some samples. Lees et al. [228] pointed out that comparable values can be observed for knitted fabrics, where the presence of voids affects

the apparent volume of the material. Van Paepegem et al. [238] demonstrated that fiber reinforced composites can have negative Poisson ratios after repeated loading/unloading cycles, reflecting an increase of microstructural damages. We have shown that for skin, damage initiates very early in the deformation process. Note also that the measurement of the Poisson ratios used here is a linearized ratio of the strain in the transverse directions over the strain in the tensile direction, and thus directly depend on the reference configuration of the material. A factor of considerable importance in the method implemented in this study is that skin samples are tested *ex vivo*, meaning that in they are not in their natural configuration when loaded on the uniaxial tensile setup. Post excision, samples can contract or expand in different ways based on their orientation and the region of the body they are taken from. It is therefore important to complement these results in the future to better identify the correlation between orientation and body region (for which the distribution of the collagen network vary), tissue contraction, and the evolution of the mechanical parameters with deformation.

To understand the macroscopic deformation, it is equally important to characterize the microscopic rearrangement processes occurring in the dermis. We provide quantitative data describing the straightening, but also the reorientation of collagen fibers before testing and after tensile failure, as well as their dimensions and properties. We observe that fibers converge towards the direction of applied tension, with initially a bimodal distribution of fiber orientation around the tensile axis in the surface plane changing to a narrower distribution with a single peak. This is similar to results reported by Yang et al. [41] by Small Angle X-Ray Scattering and *ex situ* Scanning Electron Microscopy, by Nesbitt et al. [123] by *in situ* Second Harmonic Generation Imaging, and earlier by Brown et al. [68] via *ex situ* Scanning Electron Microscopy, except that measurements are expanded to three dimensions in this work. Unexpectedly, we

measure an increase of the curvature and of the opening angle of collagen, incompatible with fiber straightening, although qualitatively visualized by Transmission Electron Microscopy. We hypothesize that tissue failure causes the collagen fibers to recoil, with therefore smaller radii of curvature. *In situ* measurements or *ex situ* characterization at lower levels of strain can help expanding our understanding of the mechanism. Finally, the three-dimensional configuration of collagen fibers is evidenced in pig skin. Earlier descriptions of the dermis [12] mention a layered disposition of adjacent collagen fibers, parallel to the surface of the dermis, or a non-interacting collagenous network [174,225]. A consequence of this representation is that fiber-fiber interactions are clearly neglected, and most structurally-based constitutive models, such as the Gasser-Ogden-Holzapfel model [169], the Lanir model [174], or the Weiss model [38], ignore this contribution. The contribution of elastin to the mechanical response and the collagen network interconnectivity is not evidenced here. Imaging of the dermis in this work also shows an interwoven network of collagen fibers, with the presence of some twisted and braid-like structures. Our model experiment with a triple braided tress of hair demonstrates the influence of such a configuration on the mechanical response when compared to a single hair, with non-linear elasticity and energy dissipation. Fundamental constituents in skin, such as hair follicles, nerve endings, and glands, are likely to be better protected during tensile deformation with the surrounding collagenous scaffold is not only restricted to one plane [123].

The next chapter focuses on the development of a semi-structural model, based on observations that were gathered in the present experimental characterization. In particular, effects of fiber braiding, and inter-fibrillar sliding during deformations are described, as well as effects of fiber distribution. The experimental curves obtained in this work are used as a database to evaluate the performance of the proposed model.

2.5. Acknowledgements

Chapter 2, in full, is published in Acta Biomaterialia and is authored by A. Pissarenko, W. Yang. H. Quan, K.A. Brown, A. Williams, W.G. Proud, M.A. Meyers. The dissertation author was the primary investigator and author of this paper.

K.A.B and W.G.P. acknowledge the Royal British Legion for its support of the Centre for Blast Injury Studies at Imperial College London. W.G.P. also acknowledges support from AWE and Imperial College London. K.A.B. acknowledges additional support from the Isaac Newton Trust and the Global Alliance at the University of Cambridge, and the European Office of Aerospace Research and Development (grant no. AFOSR-FA9550-17-1-0214). The authors thank Dr. Dan Tucker from the Department of Veterinary Medicine, University of Cambridge, for sample provision, Dr. Benjamin Butler from the Department of Physics, Cavendish Laboratory, University of Cambridge for provision of resources and assistance during experiments, as well as Mr. Andrew Rayment from the Mechanical Testing Laboratory, Department of Materials Science & Metallurgy, University of Cambridge for instructions on tensile measurements. Their help was crucial to the successful conduct of this project. The authors greatly benefited from the advice given by Dr. Vincent Sherman and by and Dr. Aisling Ní Annaidh, whose respective experiences with working on skin led to important adaptations to the methods. We also acknowledge the use of the UCSD Cryo-Electron Microscopy Facility, supported by NIH grants to Dr. Timothy S. Baker and a gift from the Agouron Institute to UCSD. We finally thank Mason Mackey at the National Center for Microscopy and Imaging Research at UCSD, whose instructions on TEM sample preparation were indispensable.

CHAPTER 3. CONSTITUTIVE DESCRIPTION OF SKIN DERMIS: ANALYTICAL CONTINUUM AND COARSE-GRAINED APPROACHES FOR MULTI-SCALE UNDERSTANDING

3.1. Introduction: Constitutive Modeling of the Skin

Constitutive modeling is essential in representing the physical behavior of materials, and accordingly enables their characterization, classification, and comparison. The selection of an appropriate formulation that accurately and consistently tracks the mechanical behavior of a given material is therefore of fundamental importance. For a soft tissue like skin, with anisotropy, non-linear elasticity, viscoelasticity, and dissipative behavior, this choice can become complex, and as a result a variety of models have been proposed and compared [7,49,137,195,225], as we have discussed in Chapter 1. The physical parameters of a model can be used to identify processes occurring in the microstructure; they can help differentiating between healthy and diseased tissue, or generate ideas for applications for example in biomimicry with synthetic grafts, wearable sensors, and dermal armors.

3.2. Structure of the Dermis and Deformation Process

The tensile properties of skin are to a large extent dictated by the dermis [17], the principal structural component of skin. As previously mentioned, the dermis is comprised of a dense network of curved collagen fibers (~70% of dry weight [7,8], or 30% volume ratio [160,162,240] in the hydrated state) with diameters ranging 2-10 μm [17,241]. These are formed by dense bundles of parallel fibrils (~50-120 nm in diameter, as shown in Chapter 2). These fibers are embedded in a viscoelastic matrix often called the “ground substance”, and a transverse network of elastin fibers, comprising 1-4% of the dry weight [7] (or 2-10% of the

volume ratio [160,162,240]) of the dermis. Figure 3.1 shows scanning electron and transmission electron micrographs of a longitudinal cross-section (i.e. along the Langer lines) of the dermis of pig skin. The fibers can be clearly seen and the bundles of fibrils that compose them show a characteristic d-banding in the transmission electron micrograph, which is caused by the 67 nm band pattern of collagen. The collagen fibers have, for pig skin, a wavelength of ~ 10 μm (see Results from Chapter 2, and Figure 2.14).

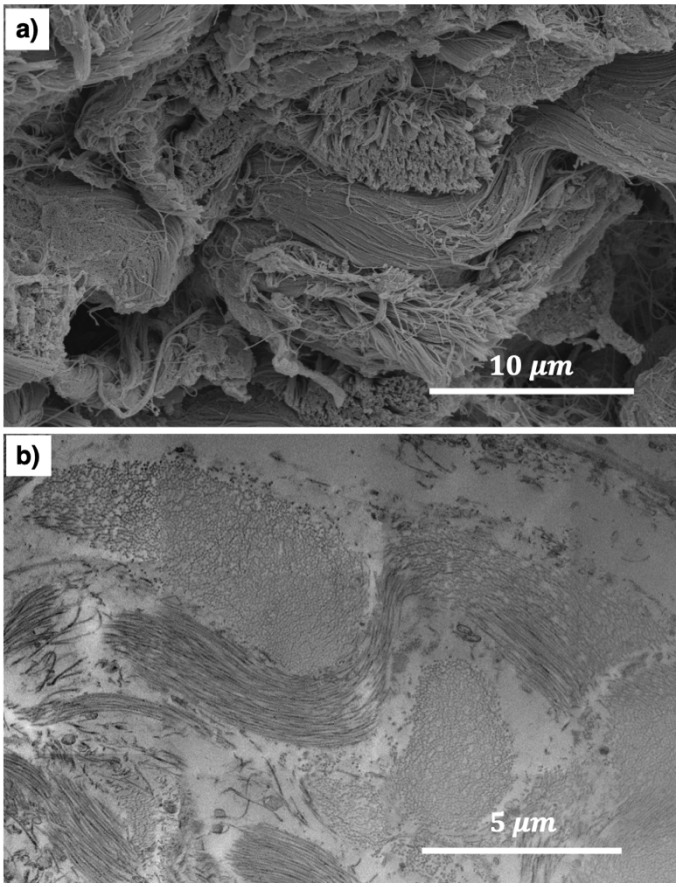

Figure 3.1. a) Scanning electron micrograph of a longitudinal cross-section of pig dermis showing a highly entangled network of wavy collagen fibers, formed by bundles of collagen fibrils. b) Transmission electron micrograph of a longitudinal section, showing similarities in entanglement and fiber crimp.

As the skin is stretched in tension, the structure undergoes a number of changes, which were classified by Yang et al. [41] into rotation, straightening, inter-fiber and intra-fiber sliding,

followed by fracture. Indeed, the non-linear elasticity of skin, and generally of soft collagenous tissues, can be attributed to two concurrent mechanical processes:

- The alignment of the loaded collagen fibers in the principal direction of tension by rotation.
- The straightening of the curved collagen fibers, which is marked by the transition from a tensile behavior mainly dictated by the bending stiffness of the fibers to a behavior imposed by their tensile stiffness, which is in general at least an order of magnitude higher for slender structures.

Several structurally-based formulations have attempted to represent fiber crimp by introducing rigid corners, sinusoidal, helicoidal, and more recently semi-circular descriptions of collagen fiber geometry, as reviewed by Sherman et al. [10]. The semi-circular, or horseshoe patterns were introduced by Sherman et al. [241] and by Ma et al. [148] independently, but were resolved using different approaches. A considerable advantage of this description is that it follows quite well the observed curvature of collagen fibers in the dermis with a reduced number of descriptive parameters, assuming that the fiber is confined in a plane.

Another important feature of the arrangement of collagen in skin is the tridimensional nature of the organization of fibers. It is well known that, in planes parallel to the outer surface of the skin, collagen fibers follow preferred orientations, defined by the so-called Langer lines. These correspond to directions of pre-existing tension in the tissue, which directly affect the anisotropy of the material. Ni Annaidh et al. [70] reported that the orientation of collagen fibers in the dermis of human skin follows a bimodal distribution. Jor et al. [13] measured orientations of collagen fibers in the thickness (out-of-plane) direction of the dermis of porcine skin, with different cross-sectional angles, taken with respect to the axis of the spine. Interestingly, they

also find a bimodal distribution of orientations (centered around the out-of-plane axis), with principal angles and standard deviations that vary according to cross-section and location on the body. Such fiber distributions, in planes that are perpendicular to each other, are in direct contradiction with a layered model, where collagen fibers would be confined to parallel planes.

Only a few representations of the structure of the dermis can follow this type of arrangement. The Gasser-Ogden-Holzapfel (GOH) model [169] has been widely used for skin [70,163,170] as well as other soft collagenous tissues, and accounts for tridimensional fiber dispersion (planar dispersion is also possible assuming the fibers are confined in plane). However, in such a model, fibers deform independently, interactions are neglected, and the focal point of each fiber family does not play any physical role.

Another example of a model including a tridimensional arrangement is the orthotropic eight-chain model that was used by Kuhl et al. [111] and by Bischoff et al. [147] to simulate tensile tests on rabbit skin that were reported earlier by Lanir and Fung [42], as discussed in Section 1.2.2.2. However, distribution in angular orientation of collagen fibers in these models is reduced to two pairs of angles, symmetric about the directions of local orthotropy. Moreover, the worm-like chain model that was used to describe fiber deformation is purely phenomenological, meaning that the constitutive parameters cannot be associated with intrinsic properties of collagen fibers.

The results of scanning electron microscopy (SEM), transmission electron microscopy (TEM), and second harmonic generation imaging (SHG) presented in the previous Chapter indicate that a certain degree of fiber entanglement or braiding should be considered in the deformation process, adding resistive forces and a dissipative component. We propose here a new constitutive description incorporating the lateral constraints imposed by the neighboring

fibers, as well as the inter-fibrillar shear occurring during fiber straightening. A coarse-grained molecular dynamics model of a deforming collagen fiber is also presented, providing additional insight into the interactions between fibrils and the forces at stake during this process.

3.3. Experimental Observations

3.3.1. Analogy with Braided Structures

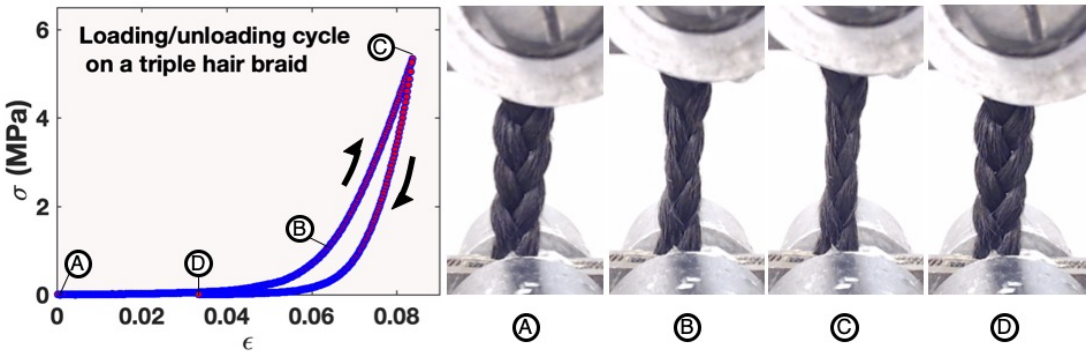

Figure 3.2. Illustration of the nonlinear elastic and dissipative behavior of a braided fibrillar structure, exemplified here with the loading/unloading cycle of a triple braid of human hair. In the initial configuration (snapshot A), the structure is loosely entangled, such that when loading is initiated, little applied stress is required to stretch the braid. With further extension, the fibers become more tightly packed (snapshot B), and each fiber interferes with the straightening process of the others by transverse resistance. The structure then reaches a linear regime, dominated by pure tension (snapshot C). After unloading, the braid reaches a new equilibrium position in the absence of applied stress (snapshot D), indicating the occurrence of irreversible processes.

Figure 3.2 shows a model experiment conducted on a triple hair braid, similar to the analogy developed in Section 2.2.5. Although this model is quite simple, it captures some of the important physical phenomena involved in the stretching of entangled structures, as the ones that can be encountered in the dermis. One important aspect is the loading/unloading response, exhibiting the nonlinear elastic (from position A to C along path B in Figure 3.2) and the dissipative behaviors of the structure, characterized by a hysteresis J-curve and the presence of remnant strains after unloading (position D), caused by frictional losses. After unloading, a new equilibrium configuration is reached, is illustrated by the sequence in Figure 3.2. This is an

insightful representation of the irreversible processes occurring during the deformation of skin, induced by the arrangement of collagen fibers. These interactions are introduced in a multi-scale description of the collagen network developed here.

3.3.2. Structure and Geometry of Collagen Fibers

In the reference state, collagen fibers in the dermis are wavy and follow different orientations in all three directions. Using a semi-circular approximation, as shown Figure 3.3a-b, an average radius of curvature r_n^0, opening angle ω_n^0, and thickness of the fibers H can be obtained (see also Figures 2.11 and 2.14). As shown in the previous Chapter, fibril diameter d_f and fibril density per fiber D_f were estimated from SEM and TEM characterization, as well as the orientation of the neutral axis of the fibers with respect to the Langer lines. The latter shows that fibers follow a bimodal distribution, centered around the axis of the Langer line, which was also reported by Ni Annaidh et al. [70]. Similar distributions are found for the planes perpendicular to the surface, as Jor et al. [13] have shown. The average values and spread of some of these parameters are reported in Table 3.1. These values are used as a reference for the model-based parameter estimation implemented in this study.

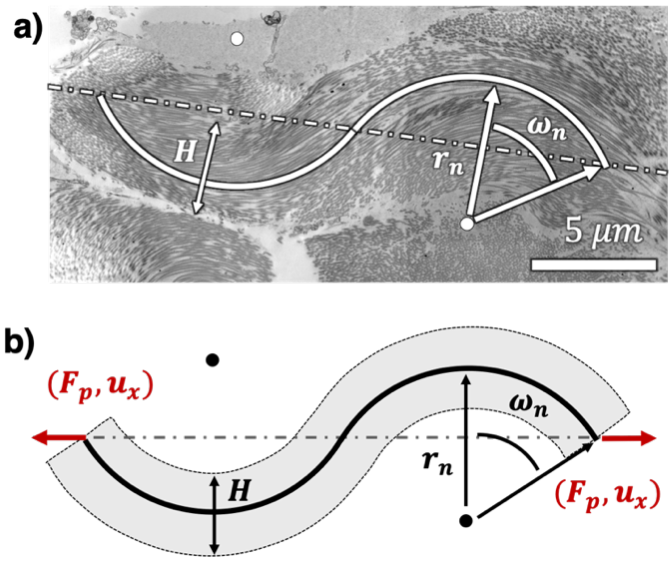

Figure 3.3. One dimensional S-shaped model of wavy collagen fibers. (a) Transmission electron micrograph of a section of pig dermis parallel to the skin surface, reproduced from [17], showing that the neutral axis of a wavy collagen fiber of thickness H can be approximated by semi-circular segments with radius of curvature r_n and opening angle ω_n. (b) One-dimensional approximation of the loading configuration, where a tensile load F_p (or reciprocally a displacement u_x) is applied along the principal axis of the fiber.

Table 3.1. Structural features of collagen fibers and fibrils, summarized from Chapter 2, for the untested pig dermis. Mean values and standard deviation (SD) are reported. Collagen orientation corresponds to the measured direction of the neutral axis of the fibers on a given section plane, with respect to the Langer line or the direction orthogonal to the tissue plane.* Indicates that the values provided were obtained from a fit with a symmetric bimodal normal distribution.

Parameter	**Mean value ± SD**
Fiber radius of curvature r_n^0	$6.56\ \mu m\ \pm\ 3.83\ \mu m$
Fiber opening angle ω_n^0	$32.1^\circ\ \pm 21.11^\circ$
Fiber thickness H	$2.23\ \mu m\ \pm 0.96\ \mu m$
Fibril density per fiber D_f	$0.69\ \pm 0.06$
Fibril diameter d_f	$82\ nm\ \pm 14.36\ nm$
Collagen orientation/Langer line (plane // dermis surface)*	$33.8^\circ\ \pm 25.0^\circ$
Collagen orientation/Langer line (plane ⊥ dermis surface – along Langer line)*	$7.8^\circ\ \pm 29.4^\circ$
Collagen orientation/normal to tissue (plane ⊥ to Langer line)*	$64.9^\circ\ \pm 19.4^\circ$

3.4. Numerical Methods: Constitutive Model and Coarse-Grained Simulations

3.4.1. Representative Cell of the Constitutive Model

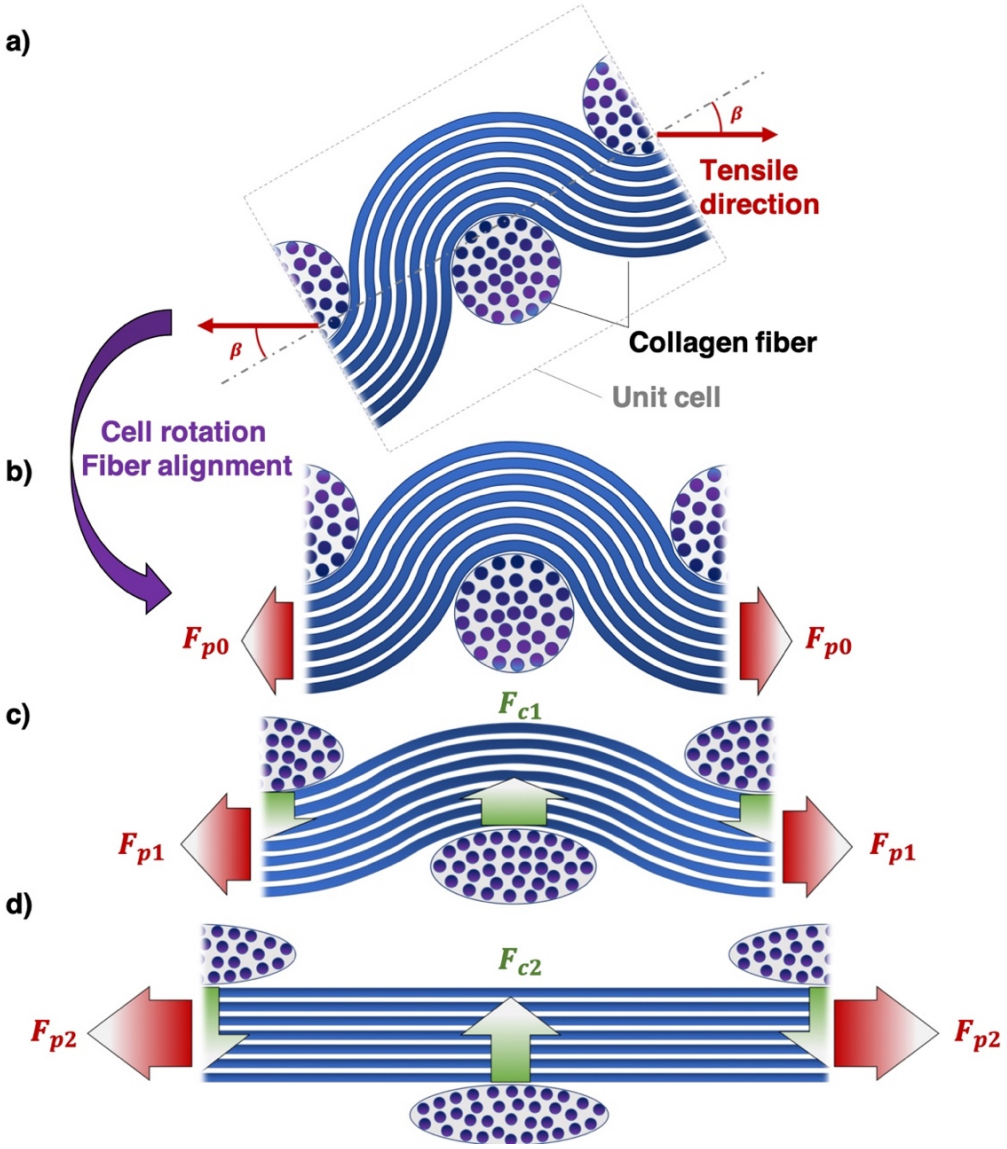

Figure 3.4. Schematic description of the process of collagen fiber realignment and straightening, with a transverse resistance due to perpendicular fibers. a) Periodic unit cell, composed of an S-shaped collagen fiber embedded in the ground substance, surrounded by perpendicular fibers lodged in the concave portions. The cell is initially oriented with an angle β with respect to the tensile direction. b) A first step of the deformation process is the rotation of the unit cell in the direction of the applied load. This occurs only at the expense of the ground substance. c) As the fiber straightens, the other transverse fibers resist to this process and deform, conforming to the change in curvature of the pulled fiber. They apply a force with a resultant perpendicular to the neutral axis of the unit cell. d) Configuration with a fully taught fiber.

Figure 3.4 describes the representative element of the dermis that is used in the present constitutive framework. A semi-circular collagen fiber, formed of a bundle of parallel collagen fibrils, has a neutral axis that follows the principal direction of the cell. The cell is oriented with an angle β with respect to the loading direction where $\beta \in [-\pi/2\,;\,\pi/2]$. In this description, it is assumed that loaded fibers can freely rotate, such that the realignment process does not require any added elastic energy. The load is mostly carried by the surrounding matrix in the realignment phase. As the tensile load increases, the fiber starts to straighten. One can therefore introduce an offset str*etch* λ_r after which the fiber becomes eventually aligned with the loading direction, and the straightening process is initiated:

$$\lambda_{\mathrm{r}} = \frac{1}{\cos\beta} \tag{3.1}$$

Such that:

$$\sigma(\lambda) = \begin{cases} 0 \text{ if } \lambda < \lambda_{\mathrm{r}} \\ \int_{1}^{\lambda_f} \mathrm{E_{app}}(\lambda)\mathrm{d}\lambda \text{ if } \lambda \geq \lambda_{\mathrm{r}} \end{cases} \tag{3.2}$$

Where $\lambda_f = 1 + \lambda - \lambda_r$ is the effective stretch of the fiber, and $E_{app}(\lambda)$ is the apparent modulus of the fiber structure, which needs to be determined as a function of the deformation state.

The entanglement (or braiding) of fibers is represented here with the addition of transverse fibers, lodged in the concavities of the collagen fiber that is being pulled. This generates resisting forces, that oppose the uncrimping of collagen, thus increasing the stiffness and adding potential dissipative mechanisms. The contact is maintained throughout the deformation, and displacement of the transverse elements is allowed. This effect is represented in the schematic

sequence of Figure 3.4. A simplified model of this interaction is proposed in the following sections.

3.4.2. 2D Model of Fiber Bundles

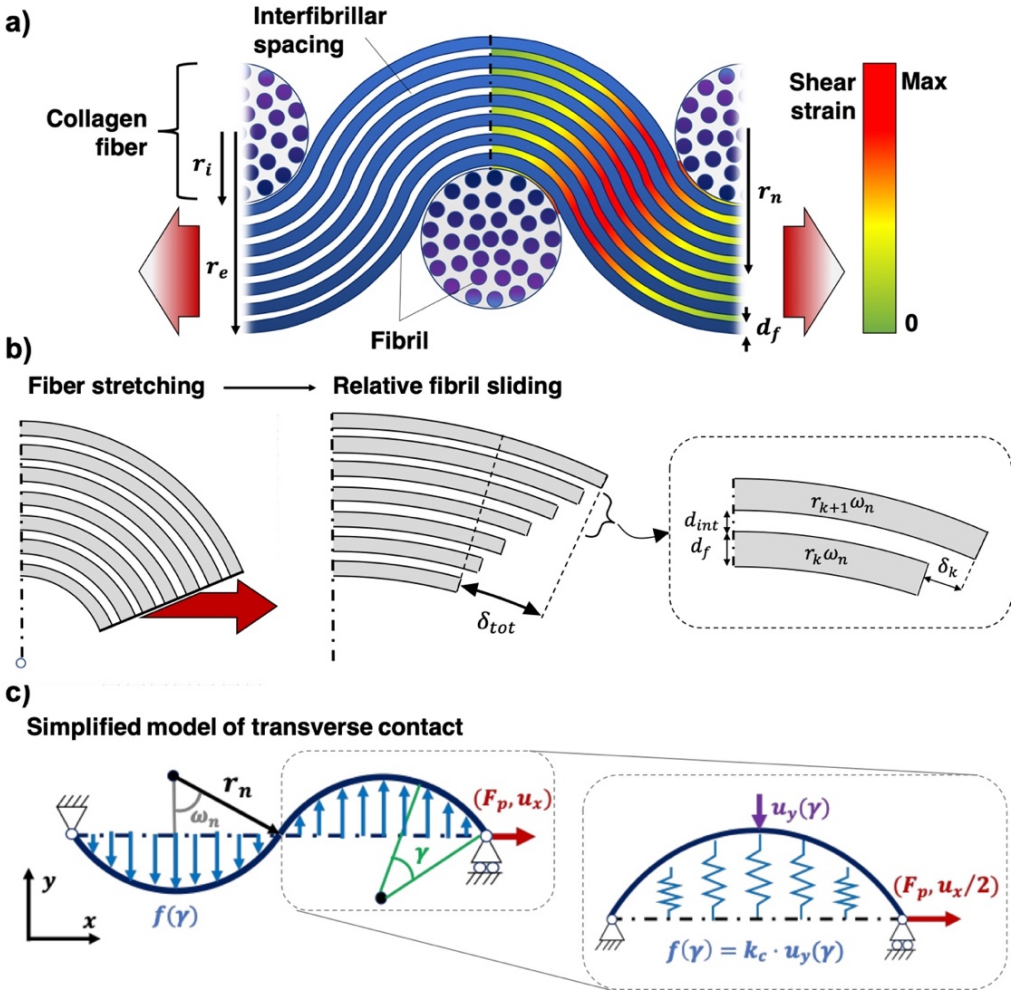

Figure 3.5. Mechanical models describing interfibrillar shear and transverse forces. a) Schematic representation of a fiber being under tension. Due to relative sliding of the fibrils during straightening, shear strain appears in the interfibrillar regions. It is null at the point of inflexion of the fiber and reaches its maximum at ω_n. b) Sequence illustrating relative sliding between fibrils during fiber stretching. From a portion of fiber spanning 0 to ω_n, it is clear that each fibril portion has a different arc length, defined by $r_k\omega_n$. When stretched, the fibrils do not align along the same opening angle anymore; this mismatch in alignment can be quantified as the relative sliding δ_k. c) Simplified one-dimensional representation of transverse forces applied on the fiber during stretching. The transverse force is linearly distributed along the concave portion of the fiber, and this force is proportional to the vertical displacement of each contact point, multiplied by a stiffness parameter k_c.

For the determination of the apparent modulus of the collagen fiber structure, it is considered that the fiber is already aligned with the tensile direction, as in the configuration in Fig 3.5a. Collagen fibers are represented as bundles of n_f parallel fibrils in a two-dimensional array, joined by an interstitial matrix. The neutral axis of the fiber can be approximated by a semi-circular wire, described by its initial radius of curvature r_n^0 and opening angle ω_n^0 (as described in Figure 3.5b). With an applied load F_p (or an applied displacement u_x) at its extremities, the fiber straightens and unfolds, before undergoing pure tension. In order to facilitate the resolution of the stress-stretch response of the proposed model, the following hypotheses are made:

- H1 – The k-th fibril away from the neutral wire is formed by two segments with radii of curvature r_k^+ and r_k^-, such that:

$$r_k^{\pm} = r_n \pm k\left(d_f + d_{int}\right) \tag{3.3}$$

  Where d_f is the cross-sectional diameter of a fibril, and d_{int} is the interspacing distance between two consecutive fibrils. Note that $d_{int} = H(1 - D_f)/(n_f - 1)$, with $n_f = [HD_f/d_f]$ the number of fibrils per fiber (and $[x]$ is the integer part of x). The radius r_k^+ describes the portion of the fibril that lies on top of the convex part of the neutral wire, and the radius r_k^- corresponds to the portion lodged in the concave part. An entire fibril is the assembly of two segments with radii r_k^+ and r_k^-, connected at the angle ω_n^0. For the sake of simplicity, it is assumed that the distance between successive fibrils does not change during deformation.

- H2 – The matrix in the interstice between fibrils is much softer compared to the collagen fibrils. It is assumed that the shear stress τ is the only significant component of stress acting during deformation, and it is linearly related to the shear strain γ via the shear modulus G_m. Shear strain can be quantified by evaluating the relative sliding occurring between adjacent fibrils during straightening, as illustrated in Figs. 3.5a-b.
- H3 – During the straightening phase, the effective length of the collagen fibrils does not change. This implies that in this phase, the deformation of the fibrils is bending-dominated, in the absence of normal strain. Consequently, the effective fiber length L_f can be expressed as a product of the radius of curvature r_n and the opening angle ω_n of the neutral fibril, at any stage of the deformation before the fiber is fully straightened:

$$L_f/4 = r_n^0 \omega_n^0 = r_n^t \omega_n^t \tag{3.4}$$

  The superscripts 0 and t denote the initial and current configurations, respectively. Consequently, for an applied displacement u, the configuration of the neutral fibril can be fully resolved if the initial configuration is known:

$$u/4 = r_n^t \sin\left(\frac{L_f}{4r_n^t}\right) - r_n^0 \sin\left(\frac{L_f}{4r_n^0}\right) \tag{3.5}$$

  Following (H1), the configuration of the other fibrils can be determined as well.
- H4 – The deformation of the fiber is described using a piecewise function, with a distinction between the straightening phase, and the phase where the fiber is fully taut and undergoes tension. The behavior of the fiber switches from bending-dominated to

purely tensile. The transition stretch λ_c can be simply estimated as the ratio between the effective length and the projected initial length on the tensile axis:

$$\lambda_c = \frac{\omega_n^0}{\sin\ \omega_n^0} \tag{3.6}$$

- H5 – The action of the transverse fibers acting of the loaded fiber is represented by a linearly distributed force, acting on a delimited linear portion of the fiber, where contact initially occurs. Friction is neglected. A simplified model is presented on Fig. 3.5c. The force is modeled by a set of idealized linear springs distributed over the contact surface, and is proportional to the transverse displacement of points of contact on the neutral wire. For the sake of simplicity, it is assumed that this force does not compress the fibers, but only acts against the straightening process.

The shear energy associated with the shear interaction assumed in (H2) is simpler to express as a function of shear strain via the relative fibril displacement. On the other hand, the contact force discussed in (H5) is a consequence of the transverse displacement of the fiber, and the effects on the bending energy of the system are more easily expressed using internal moments. For the complete system, the formulation of an energy-based approach can thus become problematic. Moreover, the assumptions of (H5) are more appropriate for a single equivalent fiber. In order to address these difficulties, the problem is treated in two separate steps. First, the straightening process of the fibrils coupled with the shearing interaction of the interstitial matrix is resolved in the absence of transverse fibers, using a strain-based approach in the expression for the internal energy of the system. The obtained solution yields an equivalent bending modulus, which can be attributed to an equivalent fiber. Next, the problem with

transverse contact forces is addressed by replacing the fibrils/matrix structure by the above defined equivalent fiber, using a stress-based approach in the expression of the internal energy. A stress-stretch relationship for the complete collagen structure is thus obtained, through application of energy theorems.

3.4.3. Equivalent Bending Stiffness

3.4.3.1. Bending Energy of the Semi-Circular Fibrils

It is considered that the deformation process of any fibril in the bundle is equivalent to the deformation of the neutral fibril, with an initial radius of curvature r_n^0 and opening angle ω_n^0. The contribution of all the fibrils is then obtained by summation of the bending energies. The study of the deformation of a single fibril can be further reduced to the analysis of one semi-circular portion of the S-shape, using a one-dimensional curved beam analogy. It is also convenient to introduce the fibril curvature $\rho_n = 1/r_n$.

Following the incremental approach of Gao et al. [151], we consider two successive deformation states, denoted by $t-1$ and t. The increment in bending energy of the fibril ΔU_{Bf} is expressed as follows:

$$\Delta U_{Bf} = \frac{1}{2} \int_{-\omega_n^0}^{\omega_n^0} E_f I \, (\rho_n^t - \rho_n^{t-1})^2 r_n^0 d\theta_n^0 \tag{3.7}$$

The total internal energy of the structure is the sum of the bending energies of all the fibrils in the fiber, as well as the shearing energies between all interfaces, which need to be expressed.

3.4.3.2. Shearing Energy Due to Relative Fibril Sliding

As stated in (H2), relative displacements occur between fibrils during the straightening phase, resulting in shear strains in the matrix. This process is illustrated in Fig. 3.4a-b: for a

portion of the fiber delimited by [0, ω_n^{t-1}], the arc length of each fibril segment is conserved during fiber straightening (as imposed by (H3)), such that in the deformed configuration, associated with a decrease in curvature, there is relative sliding δ_k between the k-th and the $(k+1)$-th fiber, as Fig. 3.4b shows. The relative displacement of the k-th fibril with respect to the neutral fibril $\Delta\delta_{k/n}$ at an angle $\theta_n^{t-1} \leq \omega_n^{t-1}$ between the deformation states $t-1$ and t can be quantified by comparing the expected arc length at t with the unchanged effective length of the arc:

$$\Delta\delta_{k/n} = r_k^t \theta_n^t - r_k^{t-1}\theta_n^{t-1} \tag{3.8}$$

Thus, the relative sliding between two adjacent fibrils is the difference between their relative displacement with the neutral fibril:

$$\Delta\delta_k = \Delta\delta_{k+1/n} - \Delta\delta_{k/n} = (r_{k+1}^t - r_k^t)\theta_n^t - (r_{k+1}^{t-1} - r_k^{t-1})\theta_n^{t-1} \tag{3.9}$$

Since $r_{k+1} - r_k = d_f + d_{int}$ at all times (according to (H1)), and $r_n^t \theta_n^t = r_n^0 \theta_n^0$ the expression of $\Delta\delta_k$ can be further simplified as:

$$\Delta\delta_k = \frac{1}{4}\big(d_f + d_{int}\big) r_n^0 \theta_n^0 (\rho_n^t - \rho_n^{t-1}) \tag{3.10}$$

The increment of shear strain $\Delta\gamma_k$ between two successive fibrils is hence defined by:

$$\Delta\gamma_k(\theta_0, r_n) = \frac{\Delta\delta_k(\theta_0, r_n)}{4d_{int}} = \frac{\big(d_f + d_{int}\big)}{4d_{int}} r_n^0 \theta_n^0 (\rho_n^t - \rho_n^{t-1}) \tag{3.11}$$

The increment of shear energy Δu_{sh}^k between two successive fibrils k and $k+1$ is:

$$\Delta U_{sh}^k = \int_0^{\omega_n^0} G_m \Delta\gamma_k^2 \, r_n^0 d_f d_{int} \, d\theta_n^0 \tag{3.12}$$

Note that it is assumed that the shear interaction takes place over a cross-section delimited by $d_f d_{int}$. The total increment of shear energy is obtained by summation over the number of

interfaces between fibrils. With no dependence in k, this is simply calculated by multiplying ΔU_{sh}^{k} by $\left(n_f - 1\right)$.

3.4.3.3. Total Internal Energy of the System

The total change in internal energy ΔU between the states $t-1$ and t of the fiber structure is the sum of the bending energies of all the fibers, and the shear energies in every interstice:

$$\Delta U = n_f \Delta U_B^f + \left(n_f - 1\right)\Delta U_{sh}^{k} \tag{3.13}$$

For a virtual displacement δu_x on the fiber, a force ΔF_p is required, resulting in an external work $\delta W_e = \Delta F_p \cdot \delta u_x$ This is associated with variations in bending energy and shear energy, that need to be developed. First, we have:

$$\begin{aligned} \delta\left(\Delta \mathrm{U}_{\mathrm{B}}^{f}\right) &= \int_{-\omega_n^0}^{\omega_n^0} E_f I\ (\rho_n^t - \rho_n^{t-1})\delta\rho\ r_n^0 d\theta_n^0 \\ &= \frac{1}{2} E_f I L_f (\rho_n^t - \rho_n^{t-1})\delta\rho \end{aligned} \tag{3.14}$$

Next, the variation in shear energy is expressed as follows:

$$\delta\left(\Delta U_{sh}^{k}\right) = 2\int_0^{\omega_n^0} G_m \Delta\gamma_{\mathrm{k}} \delta\gamma_{\mathrm{k}}\ r_n^0 d_f d_{int} d\theta_n^0 \tag{3.15}$$

By using the expression for $\Delta\gamma_k$, and with the following differentiation:

$$\delta\gamma_k = \frac{\left(d_f + d_{int}\right)}{4 d_{int}} r_n^0 \theta_n^0 \delta\rho \tag{3.16}$$

The variation in shear energy can obtained by integration:

$$\begin{aligned} \delta\left(\Delta U_{sh}^{k}\right) &= 2G_m {r_n^0}^3 \frac{d_f\left(d_f + d_{int}\right)^2}{4 d_{int}} \int_0^{\omega_n^0} (\rho_n^t - \rho_n^{t-1})\delta\rho\ {\theta_n^0}^2\ d\theta_n^0 \\ &= \frac{G_m L_f^3}{96} \frac{d_f\left(d_f + d_{int}\right)^2}{d_{int}} (\rho_n^t - \rho_n^{t-1})\delta\rho \end{aligned} \tag{3.17}$$

Hence, the variation in internal energy can be rewritten as:

$$\delta(\Delta U) = \left[\frac{1}{2} n_f E_f I L_f + \left(n_f - 1\right)\frac{G_m L_f^3}{96}\frac{d_f\left(d_f + d_{int}\right)^2}{d_{int}}\right](\rho_n^t - \rho_n^{t-1})\delta\rho \qquad (3.18)$$

Moreover, following Equation 3.5 in (H3), $\delta\rho$ can be expressed as a function of the virtual displacement δu_x:

$$\delta\rho = \frac{{\rho_n^t}^2}{4(\omega_n^t \cos(\omega_n^t) - \sin(\omega_n^t))}\delta u_x \qquad (3.19)$$

According to the principle of complementary virtual work, the variation in external work $\delta W_e = \Delta F_p \delta u_x$ is equal to the variation of the internal energy $\delta(\Delta U)$. Hence, the increment of force ΔF_p is obtained by isolating the factor in front of δu_x in the expression of $\delta(\Delta U)$:

$$\Delta F_p = \left[\frac{1}{2} n_f E_f I L_f + \left(n_f - 1\right)\frac{G_m L_f^3}{96}\frac{d_f\left(d_f + d_{int}\right)^2}{d_{int}}\right]\frac{{\rho_n^t}^2}{4(\omega_n^t \cos(\omega_n^t) - \sin(\omega_n^t))}(\rho_n^t - \rho_n^{t-1}) \qquad (3.20)$$

By introducing $\Delta\rho = \rho_n^t - \rho_n^{t-1}$, the apparent stiffness of the system between states $t-1$ and t can be defined:

$$\frac{\Delta F_p}{\Delta\rho} = \left[\frac{1}{2} n_f E_f I L_f + \left(n_f - 1\right)\frac{G_m L_f^3}{96}\frac{d_f\left(d_f + d_{int}\right)^2}{d_{int}}\right]\frac{{\rho_n^t}^2}{4(\omega_n^t \cos(\omega_n^t) - \sin(\omega_n^t))} \qquad (3.21)$$

We consider that the states $t-1$ and t are sufficiently close to assimilate the ratio above with the tangent stiffness of the system, i.e. $\Delta F_p/\Delta\rho \sim \partial F_p/\partial\rho$.

3.4.3.4. Equivalent Homogenous Fiber

It is now assumed that the fibril/matrix structure can be assimilated to an equivalent homogenous fiber, with bending modulus $(EI)_{eq}$, and the same effective length L_f. In this case, the deformation of the fiber is only dictated by the bending energy. By using a similar reasoning to the one developed above, it can be shown that:

$$\frac{\Delta F_p}{\Delta \rho} = \frac{1}{2}(EI)_{eq} L_f \frac{{\rho_n^t}^2}{4(\omega_n^t \cos(\omega_n^t) - \sin(\omega_n^t))} \tag{3.22}$$

By analogy with the fibril bundle structure, an equivalent bending modulus of the fiber is defined, from Equation 3.21 and Equation 3.22:

$$(EI)_{eq} = n_f E_f I + \left(n_f - 1\right)\frac{G_m L_f^2}{48}\,\frac{d_f\left(d_f + d_{int}\right)^2}{d_{int}} \tag{3.23}$$

The equivalent bending modulus thus defined can then be used in a stress-based approach to study the effect of the transverse force on the deformation process of the collagen structure.

3.4.4. Resistance to Straightening from Transverse Fibers

The problem is idealized using the simplified representation in Fig. 3.5c. A semi-circular fiber with initial radius of curvature r_n^0, opening angle ω_n^0, and bending modulus $(EI)_{eq}$ is subjected to an applied force F_p along its neutral axis. Hypotheses (H3), (H4), and (H5) still hold for the equivalent fiber. In particular, the effect of transverse fibers is represented here as a linear contact force, applied on the concave portion of the S-shape beam, as Fig. 3.4c illustrates. The maximum angle of the contact force ω_f^0 is limited by $\pi/2$, after which the contact does not constrain the fiber from straightening. Here again, we consider an increment of deformation between the states at $t-1$ and t, associated with curvatures ρ_n^{t-1} and ρ_n^t, such that $\Delta\rho = \rho_n^t - \rho_n^{t-1}$. We assume that $\Delta\rho/\rho_n^t \ll 1$.

The contact force is modeled by an idealized linear spring:

$$\Delta f_c(\gamma^t) = -k_c \Delta u_y(\gamma^t) \tag{3.24}$$

Where Δf_c is the increment in linear contact force, $\gamma^t \in [-\omega_f^t; \omega_f^t]$, and k_c is the contact stiffness. The vertical displacement $\Delta u_y(\gamma)$ of a point at an angle γ is the difference in vertical distance with the loading axis, between states $t-1$ and t:

$$\Delta u_y(\gamma^t) = \frac{1}{\rho_n^t}(\cos\gamma^t - \cos\omega_n^t) - \frac{1}{\rho_n^{t-1}}\left(\cos\left(\frac{\rho_n^{t-1}}{\rho_n^t}\gamma^t\right) - \cos\omega_n^{t-1}\right) \tag{3.25}$$

Which after further simplification becomes:

$$\Delta u_y(\gamma^t) \approx \frac{\Delta\rho}{{\rho_n^t}^2}(\cos\omega_n^t + \omega_n^t sin\omega_n^t - \gamma^t sin\gamma^t - cos\gamma^t) \tag{3.26}$$

As a consequence of the addition of the contact force, an additional force ΔF_r maintains the fiber along the loading axis during deformation, with:

$$\begin{aligned} \Delta F_r &= \int_{-\omega_f^t}^{\omega_f^t} \Delta f_c(\gamma) r_n^t d\gamma^t \\ \Delta F_r &= -\frac{2k_c\Delta\rho}{{\rho_n^t}^3}\left[\omega_f^t cos\omega_n^t + \omega_n^t\omega_f^t sin\omega_n^t - 2sin\omega_f^t + \omega_f^t cos\omega_f^t\right] \end{aligned} \tag{3.27}$$

The equilibrium of a portion of the fiber, limited by an angle θ_n^t, introduces a normal force ΔN and a moment ΔM, that can be decomposed into contributions from the increment of applied force ΔF_p, the constraining force ΔF_r, and the contact force Δf_c:

$$\begin{aligned} \Delta\mathrm{N} &= \Delta\mathrm{N}_p + \Delta\mathrm{N}_r + \Delta\mathrm{N}_c \\ \Delta M &= \Delta M_p + \Delta M_r + \Delta M_c \end{aligned} \tag{3.28}$$

With:

$$\begin{aligned} \Delta N_p &= -\Delta F_p \cos\theta_n^t \\ \Delta N_r &= -\Delta F_r \sin\theta_n^t \\ \Delta N_c &= sin\theta_n^t \int_{-\omega_f^t}^{\theta_n^t} f_c(\gamma^t) r_n^t d\gamma^t \end{aligned} \tag{3.29}$$

And:

$$\Delta M_p = -\Delta F_p r_n^t(\cos\theta_n^t - \cos\omega_n^t)$$

$$\Delta M_r = \Delta F_r r_n^t(sin\omega_n^t - \sin\theta_n^t) \tag{3.30}$$

$$\Delta M_c = \int_{-\omega_f^t}^{\theta_n^t} \Delta f_c(\gamma^t)(sin\gamma^t - sin\theta_n^t){r_n^t}^2 d\gamma^t$$

The increment in tensile elastic energy ΔU_T can be expressed as follows:

$$\Delta U_T = \int_{-\omega_n^t}^{\omega_n^t} \frac{\Delta N^2}{2E_f A_f} r_n^t d\theta_n^t \tag{3.31}$$

with $\Delta N^2 = \Delta N_p^2 + \Delta N_r^2 + \Delta N_c^2 + 2\Delta N_p \Delta N_r + 2\Delta N_p \Delta N_c + 2\Delta N_r \Delta N_c$.

Similarly, the change in bending energy ΔU_B of the fiber is expressed as follows:

$$\Delta U_B = \int_{-\omega_n^t}^{\omega_n^t} \frac{\Delta M^2}{2(EI)_{eq}} r_n^t d\theta_n^t \tag{3.32}$$

with $\Delta M^2 = \Delta M_p^2 + \Delta M_r^2 + \Delta M_c^2 + 2\Delta M_p \Delta M_r + 2\Delta M_p \Delta M_c + 2\Delta M_r \Delta M_c$.

Castigliano's second theorem states that the displacement Δu_x at the point of application of the force ΔF_p can be obtained by taking the derivative of the total elastic energy of the fiber by ΔF_p:

$$\Delta u_x/2 = \frac{\partial(\Delta U_T)}{\partial(\Delta F_p)} + \frac{\partial(\Delta U_B)}{\partial(\Delta F_p)} \tag{3.33}$$

Hence, this eliminates the terms that do not contain ΔF_p from Equation 3.33. It is also quite trivial to show that the term in $\Delta N_p \Delta N_r$ becomes zero after integration. The remaining terms

are therefore $\Delta N_p^2, 2\Delta N_p \Delta N_c$ in ΔU_T, and $\Delta M_p^2, 2\Delta M_p \Delta M_r, 2\Delta M_p \Delta M_c$ in ΔU_B. After several integration steps, Equation 3.33 can be rewritten:

$$\Delta u_x/2 = \Delta F_P \left(\frac{\varphi_T(\omega_n^t)}{E_f A \rho_n^t} + \frac{\varphi_P(\omega_n^t)}{(EI)_{eq} {\rho_n^t}^3} \right) - \frac{k_c \Delta\rho}{{\rho_n^t}^3} \left(\frac{\varphi_{TC}(\omega_n^t, \omega_f^t)}{E_f A \rho_n^t} + \frac{\left(\varphi_{BR}(\omega_n^t, \omega_f^t) + \varphi_{BC}(\omega_n^t, \omega_f^t)\right)}{(EI)_{eq} {\rho_n^t}^3} \right) \quad (3.34)$$

Where $\varphi_T(\omega_n^t)$, $\varphi_{TC}(\omega_n^t, \omega_f^t)$, $\varphi_P(\omega_n^t)$, $\varphi_{BR}(\omega_n^t, \omega_f^t)$, and $\varphi_{BC}(\omega_n^t, \omega_f^t)$ are functions resulting from the integration of energy terms associated with ΔN_p^2, $2\Delta N_p \Delta N_c$, ΔM_p^2, $2\Delta M_p \Delta M_r$, and $2\Delta M_p \Delta M_c$, respectively.

Next, assuming that $\Delta\rho \sim \partial\rho$, $\Delta u_x \sim \partial u_x$, and $\Delta F_P \sim \partial F_p$, and by using Equation 3.19, Equation 3.34 can be rearranged:

$$\left[\frac{\partial F_P}{\partial u_x}\right]_B = \left[\frac{\varphi_T}{E_f A \rho_n^t} + \frac{\varphi_P}{(EI)_{eq} {\rho_n^t}^3}\right]^{-1} \left[\frac{1}{2} + \frac{k_c}{4\rho_n^t(\omega_n^t cos\omega_n^t - sin\omega_n^t)} \left(\frac{\varphi_{TC}}{E_f A \rho_n^t} + \frac{(\varphi_{BR} + \varphi_{BC})}{(EI)_{eq} {\rho_n^t}^3}\right)\right] \quad (3.35)$$

The subscript B is introduced to specify that the expression of the tangent stiffness corresponds to the bending dominated regime, during fiber unfolding.

3.4.5. Tensile Regime of the Fibril Bundle

Once λ_c is reached (see Equation 3.6), the fiber is fully straightened, and the behavior of the structure is dominated by the tensile response of the fibrils in the bundle. The transverse fibers no longer have an effect on the deformation process, in the absence of transverse displacements. Due to the parallel arrangement of fibrils in the bundle, we have: $F_P = n_f F_f$, where F_f is the equidistributed force per fibril. Thus, for the whole fiber in tension:

$$\left[\frac{\partial F_p}{\partial u_x}\right]_T = n_f \left[\frac{\partial F_f}{\partial u_x}\right]_T = n_f \frac{A_f E_f}{L_f} \tag{3.36}$$

Where A_f is the cross-sectional area of a fibril, while the subscript T refers to the purely tensile state. By introducing $A = n_f A_f$ as the effective area of the fiber, it can be noted that Equation 3.35 converges to the same value for $\omega_n^t \to 0$.

3.4.6. Apparent Modulus of the Fiber Structure

The stress in the deforming fiber is approximated by $\sigma = F_p / A_e$, where $A_e = H d_f$ is the effective area of the fiber and H is its thickness. As stated in section 2.2 of this Chapter, the applied stretch is separated into two components, namely the stretch required to rotate the fiber in the tensile direction λ_r, which occurs without any applied force, and the stretch applied once the deformation of the fiber is initiated λ_f, with $d\lambda_f = du_x / (4 r_n^t sin\omega_n^t)$. Thus, the apparent modulus of the fiber structure E_{app} is expressed as:

$$E_{app}(\lambda_f) = \frac{\partial \sigma}{\partial \lambda_f} = \frac{4 r_n^t sin\omega_n^t}{H d_f} \frac{\partial F}{\partial u_x} \tag{3.37}$$

More particularly:

$$E_{app} = \begin{cases} \dfrac{4 r_n^t sin\omega_n^t}{H d_f} \left[\dfrac{\partial F_p}{\partial u_x}\right]_B, & if\ \lambda_f < \lambda_c \\ \dfrac{4 r_n^t sin\omega_n^t}{H d_f} n_f \dfrac{A_f E_f}{L_f}, & if\ \lambda_f \geq \lambda_c \end{cases} \tag{3.38}$$

The total stress-stretch relationship of the fiber structure is then obtained by numerical integration of Equation 3.2.

3.4.7. Constitutive Framework of the Tensile Behavior of the Dermis

3.4.7.1. Experimental Dataset

In the precedent Chapter, uniaxial tensile tests on *ex vivo* samples of porcine skin were conducted, with changes in applied strain rate. Samples were cut parallel (longitudinal) and perpendicular (transverse) to the direction of the spine. For the purpose of the present study, experimental results from 29 uniaxial tensile tests (17 longitudinal and 12 transverse samples), tested under four different strain rates (0.0001 s^{-1}, 0.001 s^{-1}, 0.01 s^{-1}, 0.1 s^{-1}) were extracted to test the ability of the proposed model to capture the nonlinear elastic behavior of skin and time-dependent effects.

3.4.7.2. Distribution of Collagen Fibers

As illustrated by the sequence Figure 3.4, it is assumed that a representative element lies with an angle β with respect to the tensile direction, where $\beta \in]-90^{\circ}; 90^{\circ}[$. In reality, collagen fibers in the dermis follow many different orientations, which have been often described using probability distribution functions, for which angles are either contained in planes parallel to the surface of the dermis [70,160,161,163], or span three dimensions [13,163,170]. In the present representation of fiber realignment by rotation, there is also no distinction between positive and negative orientations, as well as between in-plane and out-of-plane arrangement, so the range for β can be restrained to $[0\,;\,90^{\circ}[$. Based on the hypothesis formulated by Ridge and Wright [108], also adopted by Ni Annaidh et al. [70], it is assumed that the distribution of collagen fibers is symmetric about the tensile direction (0°), and that it follows a bimodal normal distribution. To reduce computational cost, angular distribution is discretized in increments of 2.5°, resulting in the following modified distribution function:

$$D(\beta|\beta_m,\sigma_f) = \frac{\exp\left(-\frac{(\beta-\beta_m)^2}{2\sigma_f^2}\right) + \exp\left(-\frac{(\beta+\beta_m)^2}{2\sigma_f^2}\right)}{\sum_{k=1}^{36}\exp\left(-\frac{(2.5\pi k/180-\beta_m)^2}{2\sigma_f^2}\right)} \tag{2.39}$$

Where β_m is the average angular orientation, and σ_f is the standard deviation.

3.4.7.3. Matrix Component

With the description of the collagen fiber component, the remainder of the representative element is occupied by the ground substance, described by the neo-Hookean behavior:

$$\sigma_m(\lambda) = \mu_m\left(\lambda^2 - \frac{1}{\lambda}\right) \tag{3.40}$$

Where σ_m is the component of the stress applied to the ground substance (or matrix). Note that the derived stress-stretch relationship corresponds specifically to uniaxial tension, which is the type of experiment that the constitutive model is compared to in this study. We assume that the contribution of the elastin network is captured by the matrix component. It is considered that the contributions of the fibers and the matrix in the unit cell can be taken in parallel.

3.4.7.4. Quasi-Linear Viscoelastic Component

As demonstrated in Sections 2.3.3. and 2.3.4, time-dependent effects in skin are exhibited by a change in tissue response with changes in strain rate (increase of the modulus of the linear region, higher failure stress) [17,55,132], and during stress relaxation [17,42,133]. It is also observed that the loading history of a sample has an impact on the time-dependent behavior. For example, Liu and Yeung [133] showed that the shape of the relaxation curve is affected by the level of strain at which relaxation is initiated. The quasilinear viscoelastic theory (QLV), first introduced by Fung [125], incorporates simultaneously time-dependent effects and loading

history-dependence by convolution of the purely elastic response $\sigma_{el}(t)$ with the time derivative of a reduced relaxation function $g(t)$:

$$\sigma(t) = \sigma_{el}(t) + \int_0^t \sigma_{el}(t-\tau)\frac{\partial g(\tau)}{\partial \tau}\, d\tau \tag{3.41}$$

Note that this definition of the stress in the QLV theory requires that the time derivatives of $\sigma_{el}(t)$ and $g(t)$ are continuous over the considered interval. In the present constitutive framework, the purely elastic response is obtained by resolution of the stress state for the unit cell, as derived above. A three-term Prony series is used for the reduced relaxation function:

$$g(t) = a + be^{-t/\tau_1} + ce^{-t/\tau_2} \tag{3.42}$$

Where (a, b, c) are Prony constants and (τ_1, τ_2) are the time constants of the material, and $g(0^+) = 1$. This is the same reduced relaxation function that was used to fit normalized relaxation plots in Section 2.2.2.2 (Equation 2.1), for which average values of the constants were reported in Table 2.2 and showed good consistency.

3.4.7.5. Constitutive Model and Parameter Identification

The entire constitutive model of the dermis consists of the assembly of the distributed collagen network, with a volume fraction ϕ_c, the neo-Hookean matrix, with a volume fraction $(1-\phi_c)$, and the QLV component, for which the time derivative of the reduced relaxation function is convoluted with the elastic response of the structure. This representation is illustrated in Fig. 3.6, showing the assembly in parallel of the constitutive elements.

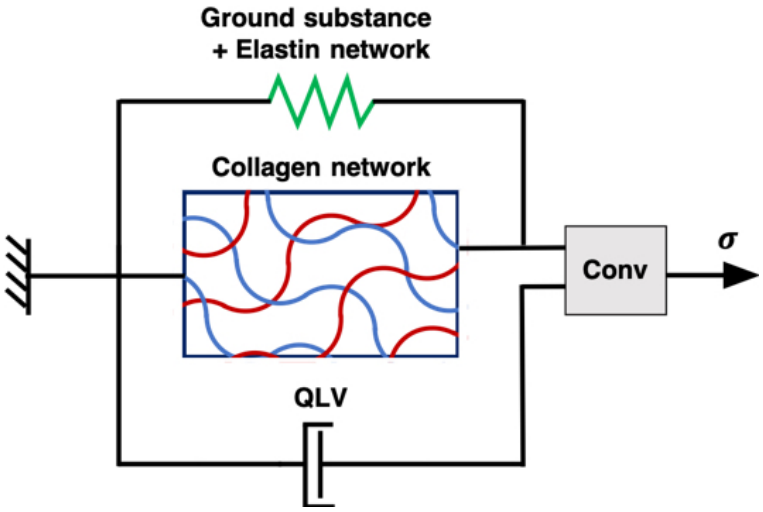

Figure 3.6. Schematic representation of the elements of the constitutive model of the dermis. The collagen network, formed by an assembly of distributed collagen fiber structures, is in parallel with the neo-Hookean ground substance, which also captures the contribution of the elastin network. The time-dependent behavior of the material is modeled by convolution of the elastic response with a reduced relaxation function, as defined by the QLV theory.

The complete resolution of the constitutive model is achieved by summation of the stresses for the elastic component, after numerical integration of Equation 3.2, and discrete convolution with the QLV component, equivalent to Equation 3.40. This is executed in MATLAB.

Table 3.2. Summary of the constitutive parameters used in the constitutive model of the dermis. Pre-injected parameters are highlighted in grey, other parameters were calculated with the provided ranges, taken from previous studies, except for G_m, which was roughly estimated based on a reasonable ratio between the straightening phase and the purely tensile regime.

Parameter	**Value**	**Set/Calculated**
Collagen volume fraction ϕ_c	0.3 [160,161]	Set
Fiber thickness H	2.5 μm (Chapter 2)	Set
Fibril diameter d_f	80 nm (Chapter 2)	Set
Fibril density D_f	0.7 (Chapter 2)	Set
Fiber initial curvature r_n^0	5 μm (Chapter 2)	Set
Matrix shear modulus μ_m	1 kPa [160]	Set
Prony constant a	0.6 (Chapter 2)	Set
Prony constant b	0.21 (Chapter 2)	Set
Time constant τ_1	12.9 s (Chapter 2)	Set
Time constant τ_2	1.05 s (Chapter 2)	Set
Collagen fibril stiffness E_f	30-1570 MPa [10]	Calculated
Fibril interspace shear modulus G_m	0-10 MPa	Calculated
Fiber initial crimp angle ω_n^0	0º-60º (Chapter 2)	Calculated
Fiber average orientation β_m	0º-90º	Calculated
Orientation standard deviation σ_f	0.01-1	Calculated
Transverse stiffness k_c	$0 - 0.1\ N/m^2$	Calculated

In total, there are 16 constitutive parameters that need to be identified. These are listed in Table 3.2, some of which were already listed in Table 3.1. With such a large parameter set, it becomes difficult to guarantee the uniqueness of a solution that minimizes the optimization problem. In order to facilitate this process, and reduce computational cost, some of these parameters were pre-set, using values that have been reported elsewhere in the literature. This

generally concerns parameters for which the reported values are quite consistent, or which have a relatively low influence on the behavior of the model. These are highlighted in grey in Table 2. For example, average values of the reduced relaxation function parameters $(a, b, c, \tau_1, \tau_2)$ were reported in Chapter 2 with good consistency and small standard deviations, without much influence due to sample orientation. For the identified parameters, a physically reasonable range of values is indicated, to assist the optimization algorithm and to reduce the field of search. These values are also indicated at the bottom of Table 3.2.

Identification of the six remaining parameters is executed using the Parameter Estimation tool in MATLAB, by minimization of the Sum Squared Error cost function with a nonlinear least-squares optimization method and a trust-region-reflective algorithm.

3.4.8. Coarse-Grained Model of Collagen Fibers

Molecular dynamics computations are a powerful tool and can capture essential aspects of the physical phenomena. In the present case a coarse-grained model, based on a simple elastic network [242–245] and inspired from studies of Arapaima fish scales by Yang et al. [246], was used to theoretically investigate the mechanisms of the deformation in a two-dimensional S-shape curved collagen fiber under uniaxial tension, equivalent to the continuum description developed in Section 4.3. In order to capture the essential physics at an acceptable scale, the collagen fiber consists of an array of adjacent collagen fibrils (see Figure 3.7), whereby each collagen fibril is modeled as a series of beads connected by harmonic springs. The initial inter-bead distance is r_0= 82 nm, which is the same as the average diameter of collagen fibrils d_f, as reported from electron microscopy images. Since the density of collagen is $1.34 \cdot 10^3\ kg/m^3$, the mass of each bead is equal to $5.8 \cdot 10^{-15}\ kg$. The total deformation energy of the simulation system is given by:

$$U_{total} = U_T + U_B + U_{weak} \tag{3.43}$$

where U_T, U_B and U_{weak} are the energies of all pair wise, three-body and weak inter-fibril interactions, respectively, such that:

$$\begin{aligned} U_T &= \sum_{pair} \varphi_T(r) \\ \varphi_T(r) &= K(r - r_0)^2 \\ K &= \frac{E_f A}{2r_0} \end{aligned} \tag{3.44}$$

K being the stiffness of the pair wise interaction spring between neighboring beads on the same fibril, e.g. beads $\big((j, i-1), (j, i)\big)$ as illustrated on Figure 3.7. K is estimated from the Young's modulus E_f and the cross-section area A of the collagen fibril. The triplet energy is expressed as:

$$\begin{aligned} U_B &= \sum_{triplets} \varphi_B(r) \\ \varphi_B(r) &= K_B(\theta - \theta_0)^2 \\ K_B &= \frac{7}{32} \frac{E_f \, \pi d_f^4}{r_0} \end{aligned} \tag{3.45}$$

K_B being the bending stiffness of the angular spring of the triplet of beads. Finally, the weak inter-bead energy is defined as:

$$\begin{aligned} U_{weak} &= \sum_{r<r_{cutoff}} \varphi_{weak}(r) \\ \varphi_{weak}(r) &= 4\epsilon[(\sigma/r)^{12} - (\sigma/r)^6] \end{aligned} \tag{3.46}$$

Where ϵ is the interaction energy between to inter-fibril beads that is given by $\epsilon = d_f r_0 \gamma$ where γ is the surface energy of the collagen fibrils, and $\sigma = d_e/\sqrt[6]{2}$, the equilibrium distance between two neighboring fibrils, so that $d_e = d_f + d_{int}$. To ensure that each collagen fibril only interacts with its nearest neighbors in adjacent fibrils $(j, j+1)$, the cutoff of the interaction is set as $r_{cutoff} = 1.1 d_e$.

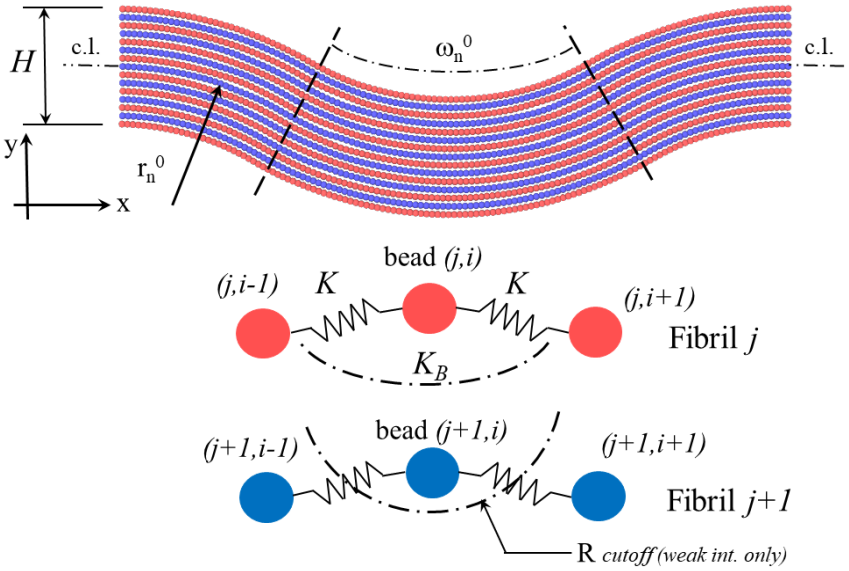

Figure 3.7. Initial configuration of the coarse-grained model. An array of collagen fibrils makes a collagen fiber. Each collagen fibril is alternatively colored red-blue-red-blue for visualization purposes.

For the sake of simplicity, the model is two-dimensional, and inspired by electron microscopy images (see Figure 3.1). In this concept-case study, the model fiber is made of 15 adjacent collagen fibrils with an inter-fibril separation of $d_e = d_f + d_{int} \approx 120\ nm$, for a total thickness of 1.8 μm. Periodic boundary conditions in the direction parallel to the principal axis of the fiber are defined, hence assuming fiber continuity. Prior to deformation, the fibril bundle was minimized and relaxed for 100,000 integration steps.

Uniaxial tensile strain was applied to the entire multi-fibrillar arrangement in a quasi-static manner. For every deformation increment, a uniaxial strain of 0.004 was applied to the model, carrying out energy minimization and equilibrium for 100000 integration steps. The stress-strain response of the structure during deformation was recorded. In order to visualize and quantify relative sliding of fibrils, the deformation of all the collagen fibrils during the entire loading process was monitored. Simulations were carried out with LAMMPS [247], and visualization was performed using OVITO [248].

3.5. Predictions of Models and Comparison with Experimental Results

3.5.1. Parameter Influence on the Fiber Structure Model

Figure 3.8 shows the effect of different constitutive parameters on the stress-strain response of the two-dimensional fibril bundle structure, in the absence of the surrounding ground substance. As expected, the Young's modulus of the fibrils E_f mainly affects the stiffness in the purely tensile region, as shown in Fig. 3.8a. Because the combined stiffness of the fibrils is divided by the effective area of the fiber ($A_f = Hd_f$), the measured slope is smaller compared to the value of E_f. In contrast, the shear modulus of the interfibrillar matrix G_m mainly affects the stiffness of the structure in the straightening phase (Fig. 3.8b). The contact stiffness k_c caused by the structural entanglement has a comparable effect on the straightening phase, except that it also triggers an earlier activation of the purely tensile regime (Fig. 3.8c). This can be explained by the fact that for a certain threshold of the contact force, resistance to unfolding becomes too large and the tensile component dominates, which can be assimilated to the tightening effect that is seen in braided structures (see Fig. 3.2) The value of the initial radius of curvature r_n^0 of the neutral fibril has a similar effect on the stress-strain curve (Fig. 3.8d), because r_n^0 is mainly a scaling parameter of the fiber, as no notable effect of the fiber thickness

H was observed. With a fixed opening angle ω_n^0 (in this case $\omega_n^0 = 30^\circ$), a larger radius simply provides a larger contact length for the linearly distributed contact force f_c. This further justifies the pre-setting of r_n^0 and H is the parameter estimation, and to avoid coupled effects with the identification of k_c. On the other hand, a variation of the initial opening angle ω_n^0 directly impacts the undulation of the semicircular fiber and thus affects the transition from unfolding to tensile regime, as Equation 3.6 describes (Fig. 3.8e). As prescribed by Equations 3.1-3.2, the fiber alignment angle β simply offsets the initiation of the deformation process, as Fig. 3.8f shows. Hence, with distributed fibers (see Equation 3.39), the process of gradual fiber recruitment can be captured, which also affects the nonlinearity of the J-curve.

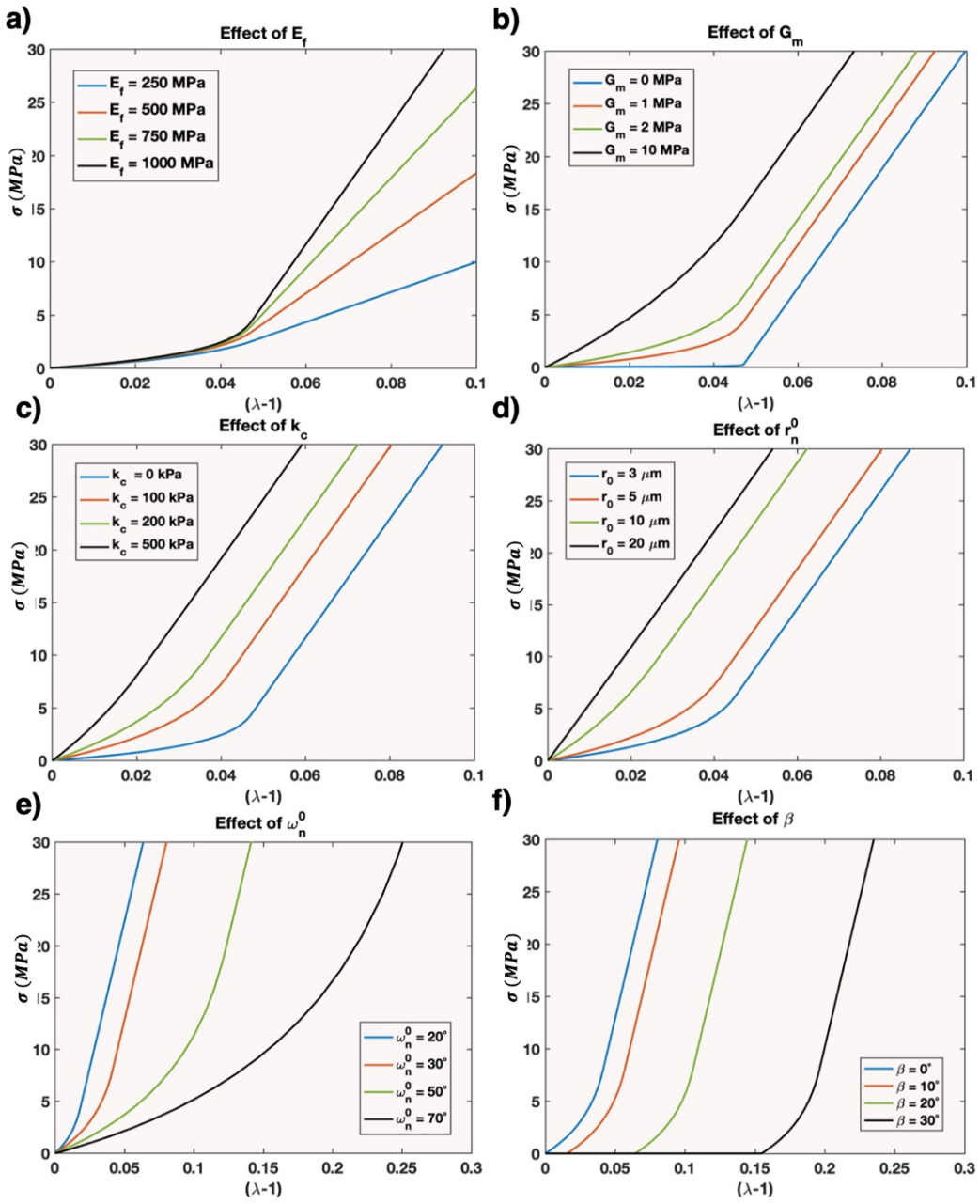

Figure 3.8. Effect of different parameters of the fiber structure model on the stress-strain response. Parameters $H = 3\ \mu m$; $d_f = 80\ nm$; $D_f = 0.7$; are maintained constant for all simulations. a) Effect of the collagen fibril Young's modulus E_f, for $G_m = 1\ MPa; k_c = 0\ kPa;\ r_n^0 = 5\ \mu m; \omega_n^0 = 30^\circ; \beta = 0^\circ$. b) Effect of the interfibrillar shear modulus G_m, for $E_f = 1\ GPa; k_c = 0\ kPa;\ r_n^0 = 5\ \mu m; \omega_n^0 = 30^\circ; \beta = 0^\circ$. c) Effect of the contact stiffness parameter k_c, for $E_f = 1\ GPa;\ G_m = 1\ MPa;\ r_n^0 = 5\ \mu m; \omega_n^0 = 30^\circ; \beta = 0^\circ$. d) Effect of the initial neutral radius of curvature r_n^0, for $E_f = 1\ GPa;\ G_m = 1\ MPa; k_c = 0.1\ MPa;\ \omega_n^0 = 30^\circ; \beta = 0^\circ$. e) Effect of the initial opening angle of the neutral fibril ω_n^0, for $E_f = 1\ GPa;\ G_m = 1\ MPa; k_c = 0.1\ MPa;\ r_n^0 = 5\ \mu m; \beta = 0^\circ$. Effect of the initial orientation between the principal axis of the fiber and the tensile direction, described by the angle β, for $E_f = 1\ GPa; G_m = 1\ MPa; k_c = 0.1\ MPa;\ r_n^0 = 5\ \mu m; \omega_n^0 = 30^\circ$.

3.5.2. Tensile Behavior of the Coarse-Grained Model

3.5.2.1. Deformation Sequence

For comparison purposes, a series of simulations was performed with different Young's moduli for the collagen fibrils, namely 0.5 GPa and 1.0 GPa, which is within the average estimates from collagen fibrils from both computational and experimental approaches [249]. The value of $1\ J/m^2$ was attributed to the surface energy of the inter-fibrillar weak interaction. Although it is expected that this energy depends on the degree of hydration, mineral composition and protein sequence, among other factors, the selected value is within the standard range that is found in the literature [10].

Using the present model, one might obtain a diversity of stress–strain curves by using different surface energies and elastic moduli, yet such a parametric study is beyond the scope of the present work. Instead, a first assessment of the model is proposed. As Figure 3.9 shows, the coarse-grained tensile responses follow a typical J-curve shape, with a first stage where the load slightly increases as the fiber unfolds from its most curved configuration ($0 < \varepsilon < 0.04$), with a bending dominated behavior through K_B. As the strain keeps increasing ($0.04 < \varepsilon < 0.07$, Stage II), the fiber not only continues straightening but stretching starts playing an important role, so the slope of the loading curve increases. Finally, in stage III ($\varepsilon > 0.07$), the fiber is fully taut and deformation is mostly dominated by the constant K of the pair-wise interaction. The rather wavy behavior of the loading curve for $0 < \varepsilon < 0.07$ can be understood by tracking the trajectory of the beads over time (strain), see Fig. 3.10.

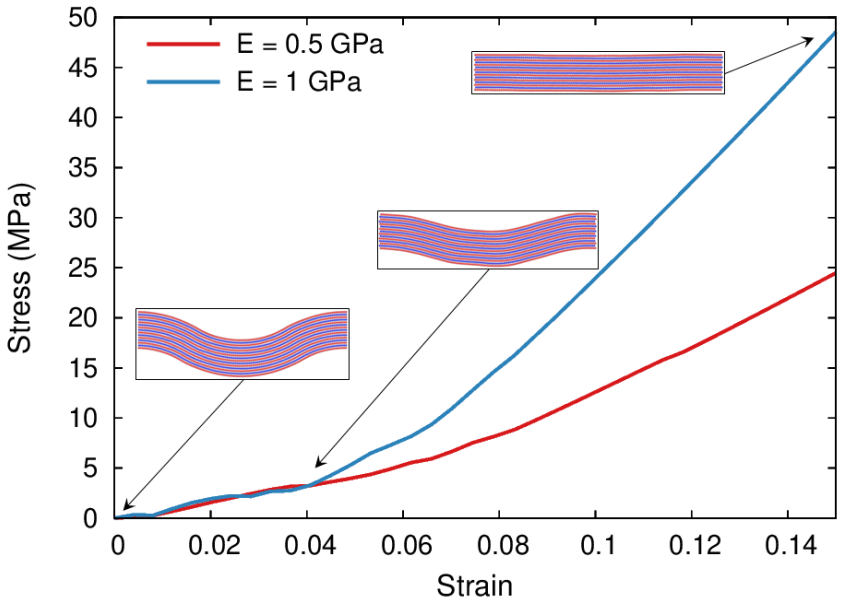

Figure 3.9. Loading curves showing the influence of Young's modulus. Visualization of the intermediate configuration for a strain of 0.04 shows what seems and uneven deformation state. Reasons explained in main text.

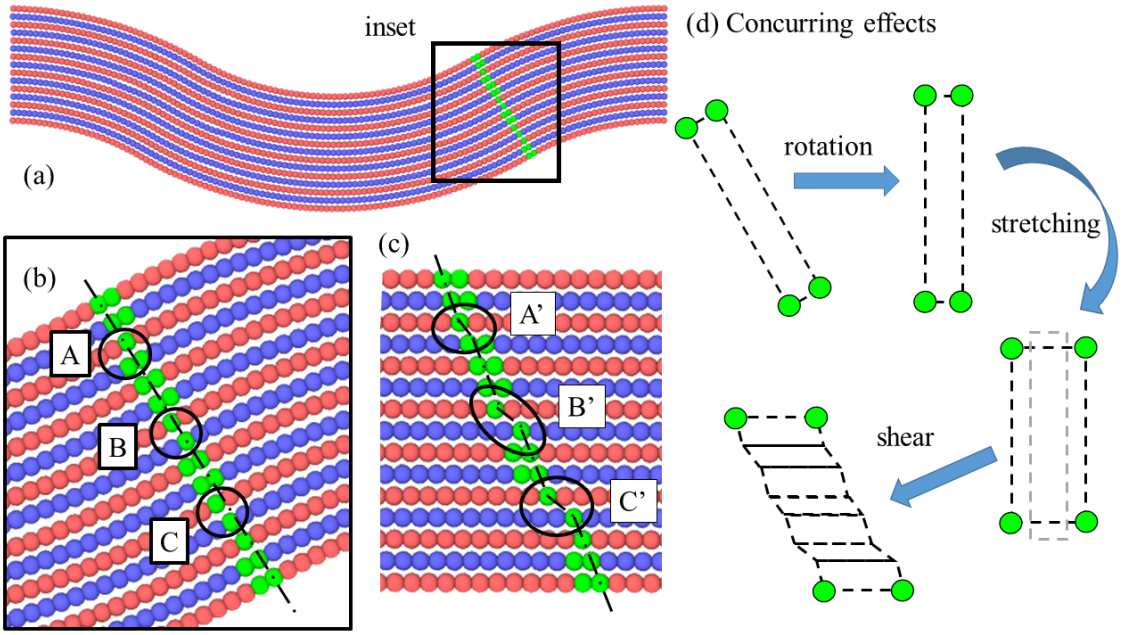

Figure 3.10. Relative bead displacement during deformation in the CG model. (a) The inflection section of the bi-curved fiber is identified and tracked during deformation. (b) and (c) present the initial configuration and its ε=0.14 counterpart, corresponding to a fully stretched state. Note the changes A-A', B-B' and C-C'. The deformation can be interpreted as the result of three concurring effects, rotation of the section, stretching and shear (d).

For the magnitude of strain attained in this simulations, the stresses on each fibril are within the experimental values of single fibril stress-strain experiments by Shen et al. [250]. By comparing the simulation snapshots shown in Fig. 3.10 and its accompanying schematics, one can better interpret the deformation process. Starting from the initial semicircular undeformed configuration, the application of subsequent strain steps is accommodated by three concurrent effects, in a manner similar to the analytical model: a) straightening of the fiber comprised of circular segments, producing the rotation of transverse sections; b) chain extension through separation of neighboring beads due to the tensile strain (stretching); c) sliding between neighboring fibrils (shearing), as suggested by the description of relative sliding (Figs. 3.5a-b). The latter effect is not homogeneously distributed across the entire section, but rather takes place as discrete bursts, which are quite marked for tags B-B', C-C' and, to a lesser extent, A-A'. There are other parts e.g. above A' or below C', where shear is homogeneously distributed. The total displacement between the left-topmost and the right-bottommost green beads is of the order of 0.9 μm for an applied strain of $\varepsilon = 0.14$, past the complete unfolding of the fiber. From the value of the initial parameters used for this simulation, the analytical description of shear, described in Section 4.3.2 of this Chapter, predicts a final cumulative relative sliding displacement of ~0.89 μm, which is in excellent agreement with the measured value.

3.5.2.2. Comparison with the Analytical Description

The tensile response of the above described coarse-grained fiber for $E_f = 1\ GPa$ is compared with the response of the continuum representation, resolved in the absence of resistive forces due to transverse fibers ($k_c = 0\ MPa$) in Figure 3.11. For the same initial conditions, i.e. $E_f = 1\ GPa;\ r_n^0 = 5\ \mu m; \omega_n^0 = 30^\circ; H = 1.8\ \mu m; d_f = 82\ nm; D_f = 0.7$, the analytical model (grey dotted line in Figure 3.11) shows an earlier transition from the unfolding

phase to the tensile regime, and a stiffer linear behavior compared to the atomistic simulation (blue circles). The former can be explained by the fact that in the coarse-grained simulation, initial equilibration (minimization and relaxation) of the structure slightly affects the geometry of the S-shape, and thus the opening angle. Estimates show that the opening angle of the semi-circular portion after relaxation is closer to 37˚ (see Appendix D). Thus, the value of ω_n^0 in the continuum (analytical) model was modified accordingly, and as a result the red curve in Figure 3.11 more accurately captures the unfolding-stretching transition of the coarse-grained model. The value of the fibril Young's modulus was adjusted to $E_f = 0.92\ GPa$ to better fit the linear regime. In the coarse-grained model, the tensile modulus is slightly below the prediction, presumably due to effects of the weak interaction (Eq. 3.46), when the bead-to-bead distance increases (i.e. while the pairwise interaction is dictated by a harmonic spring, the weak interaction obeys a Lennard-Jones potential law with a different power law to that of a spring. It is reasonable to expect a slight deviation from the theoretical value associated to the pairwise spring). Notwithstanding these adjustments, Figure 3.11 shows that a very good agreement is obtained between the responses of the atomistic model and of the adjusted continuum representation, for an interfibrillar shear modulus of $G_m = 5\ MPa$.

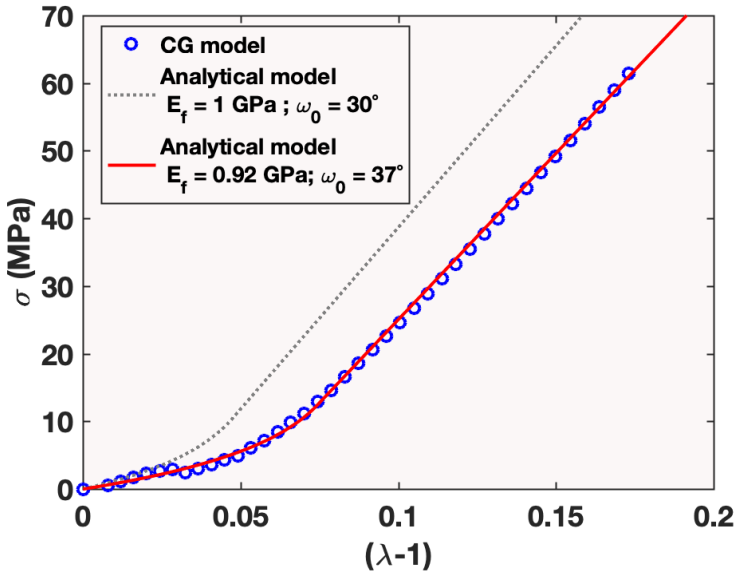

Figure 3.11. Comparison of the stress-strain curves obtained for the coarse grained (CG) atomistic model, and the analytical model with equivalent initial values (grey dotted curve), and with adjusted parameters (red curve), showing a better agreement between both descriptions. The optimal value of 5 MPa was used for G_m.

3.5.3. Parameter Identification from the Constitutive Framework

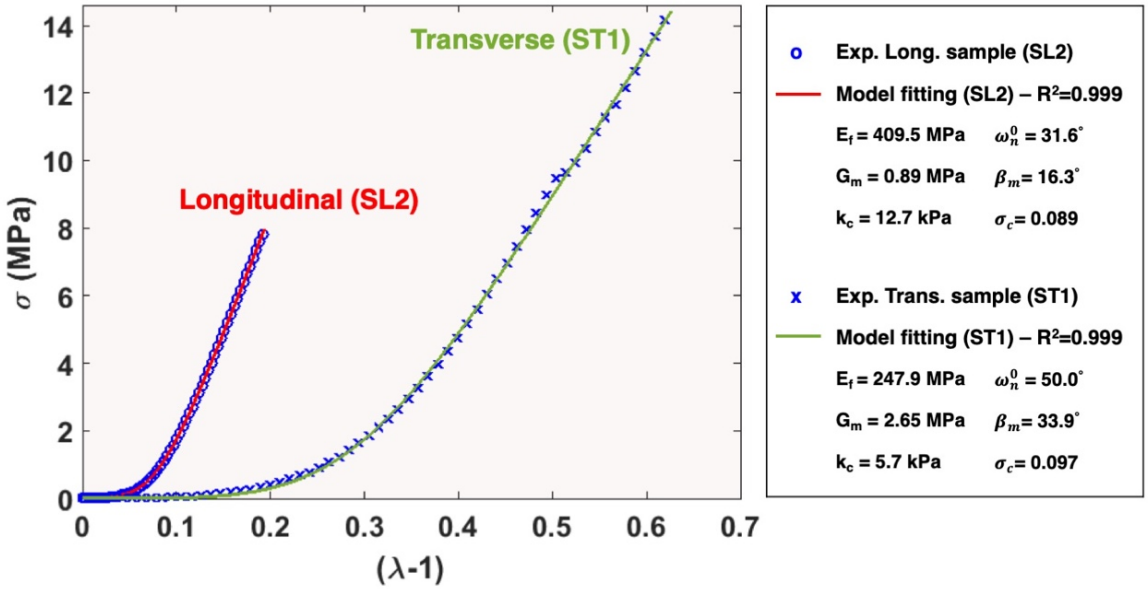

Figure 3.12. Perfomance of the model with two selected experimental (Exp.) curves, a longitudinal sample (SL2), and a transverse sample (ST1), both tested at a strain rate of $10^{-3}s^{-1}$. Fitted curves display the good ability of the model to capture the nonlinear elastic behavior of skin for two perpendicular orientations. The legend on the side of the graph also indicates the identified values of the constitutive parameters.

The Parameter Estimation tool in MATLAB determines the optimal values for the set of parameters listed in Table 3.2, for each given experimental curve. Examples for one longitudinal sample and one transverse sample, tested at a strain rate of 10^{-3} s^{-1}, are shown in Figure 3.12. The constitutive model matches very well the different deformation stages of the J-curve of skin, with coefficients of determination R^2 above 0.99. This is in majority due to the combined contribution of the gradual realignment of collagen fibers and the straightening process which the model captures.

Table 3.3. Average values ± S.D. of the constitutive parameters after curve fitting of experimental results, sorted by sample orientation (17 longitudinal samples and 12 transverse).

	Longitudinal (Mean ± S.D.)	Transverse (Mean ± S.D.)	Total (Mean ± S.D.)
E_f	$420.4 \pm 138.1\ MPa$	$435.0 \pm 165.2\ MPa$	$426.5 \pm 147.2\ MPa$
G_m	$1.31 \pm 0.87\ MPa$	$2.02 \pm 1.84\ MPa$	$1.61 \pm 1.37\ MPa$
k_c	$14.1 \pm 11.4\ kPa$	$47.0 \pm 56.2\ kPa$	$27.7 \pm 39.9\ kPa$
ω_n^0	$36.7^\circ \pm 5.3^\circ$	$39.5^\circ \pm 8.4^\circ$	$37.9^\circ \pm 6.8^\circ$
β_m	$20.5^\circ \pm 4.94^\circ$	$29.6^\circ \pm 10.1^\circ$	$24.2^\circ \pm 8.6^\circ$
σ_f	0.084 ± 0.040	0.244 ± 0.318	0.150 ± 0.217

The complete dataset of identified parameters is provided in Appendix E. For the sake of conciseness, only average values and standard deviations for transverse and longitudinal sample orientations are presented in Table 3.3. Additionally, a Spearman rho correlation analysis was conducted in order to identify potential correlations between the constitutive parameters, as well as the experimental conditions, i.e. sample orientation and applied strain rate (see Table 3.4), and a parameter sensitivity analysis is also detailed in Appendix F, identifying the parameters with the highest influence on the response of the model. At first glance, it is interesting to point out that the applied strain rate does not correlate with any of the estimated parameters, suggesting that the QLV component adequately captures the time-dependent behavior of the tissue.

Table 3.4. Spearman correlation analysis of the six identified constitutive parameters, also compared to the applied strain rate and sample orientation. The spearman rho coefficient (in **bold**) indicates the strength and the direction of the correlation, while the p-value (in *italic*) provides the significance (*=p-value<5%).

	E_f	G_m	k_c	ω_n^0	β_m	σ_c
G_m	**-0.342** *0.069*					
k_c	**0.275** *0.148*	**0.120** *0.536*				
ω_n^0	**-0.321** *0.090*	**0.440** *0.017**	**-0.178** *0.355*			
β_m	**-0.259** *0.175*	**0.261** *0.171*	**0.105** *0.586*	**0.493** *0.007**		
σ_c	**0.071** *0.715*	**0.139** *0.471*	**0.009** *0.962*	**-0.057** *0.769*	**0.291** *0.126*	
Strain rate	**0.155** *0.422*	**-0.113** *0.560*	**0.057** *0.770*	**0.015** *0.939*	**0.181** *0.348*	**0.039** *0.842*
Orientation	**0.008** *0.966*	**0.209** *0.276*	**0.209** *0.276*	**0.071** *0.714*	**0.427** *0.021**	**0.393** *0.035**

An average Young's modulus of $426.5 \pm 147\ MPa$ was found for collagen fibrils, which falls in the lower range of experimentally reported values [10]. Intrinsic phenomena such as fiber and fibril sliding can contribute in decreasing the apparent stiffness of collagen. Nonetheless, the estimated stiffness is in reasonable agreement with the values found by Jor et al. [161] (~360 MPa) and Meijer et al. [160] ($360\ MPa - 518\ MPa$) with the Lanir model. No significant effect of orientation was found, indicating that material anisotropy is dictated by other constitutive parameters. The inter-fibril shear modulus G_m displays rather large variations ($1.61 \pm 1.37\ MPa$ in total), especially for transverse samples ($2.02 \pm 1.84\ MPa$), but the average values are about two orders of magnitude below the fibril modulus, as expected from the estimations with the coarse-grained model.

The average curvature of collagen fibers ($\omega_n^0 = 37.9^\circ \pm 6.8^\circ$) is consistent with the measured values for a radius of curvature of $r_n^0 = 5\ \mu m$, and does not show any dependence on

orientation. An increase in opening angle is significantly correlated with an increase in G_m (p-value = 0.017). This can be interpreted by the effect of a more curved initial state, but also by the notion that with a fixed radius of curvature a larger opening angle increases the effective length of the fiber L_f, and therefore the contact area with the interfibrillar matrix is increased, which could affect the effect shear in a nonlinear fashion.

The calculated average orientation of collagen β_m, $\beta_m^L = 20.5^\circ \pm 4.9^\circ$ for longitudinal samples and $\beta_m^T = 29.6^\circ \pm 10.1^\circ$ for transverse samples, shows a significant correlation (p-value = 0.021) between the initial alignment of collagen fibers and the orientation of the tested sample. However, the difference between both orientations is well below the expected trend, as perpendicular orientations should yield average alignments approximately 90° apart. This observation highlights two limitations of the present representation: a) an increase of the angle β substantially delays the onset of fiber deformation (cf. Fig. 3.8b), and the gap in response between two subsequent angular increments becomes more pronounced, which yields a more discontinuous response for a higher value of β_m; b) the proposed fiber distribution imposes symmetry around the loading axis, which may not be a realistic assumption. These shortcomings also explain the highly significant correlation (p-value = 0.007) between β_m and ω_n^0, which should not be observed, as one is an effect of the loading configuration and the latter is an intrinsic property of the collagen fibers. Still, as both parameters have an effect on the transition of the J-curve, it is understandable that the model finds a correlation between their distinct influences. As mentioned earlier, fiber unfolding and realignment are concurrent processes in skin [41]. It is therefore preferable that one of them would be determined *a priori* in the model, which is also reflected by the sensitivity analysis (see Appendix F) which indicates that both parameters have a high influence on the model response.

The standard deviation in fiber distribution σ_c is also an intrinsic property of the sample, and should not be influenced by sample orientation, which is in this case confirmed by a weak correlation between the two. As a direct measure of tissue anisotropy, the standard deviation would probably be more affected by the region of the body from which the sample is extracted, which was not systematically reported for this experimental dataset. As a matter of fact, most skin samples were extracted close to the spine, which is generally less anisotropic compared to other regions [47,108]. In fact, the identified average of $\sigma_c = 0.15 \pm 0.22$ yields an estimated fiber dispersion coefficient [169] that is at least one order of magnitude below other reported values for skin [70,163]. This is another consequence of the strong effect of the initial alignment of fibers in the model. A wider distribution effectively reduces the fraction of collagen fibers that contribute to the deformation process, which is in contradiction with the consistency of the measured stiffness. With a maximum strain of ~0.6 prior to failure, following Equation 3.1, the maximum angle for which a fiber participates in the response of the tissue is approximately 52˚, hence directly eliminating the contribution of fibers with a higher alignment angle. This further indicates that the representation of realignment needs to be refined, and that σ_c should preferably be predetermined, as also suggested by the sensitivity analysis (Appendix F).

Finally, the estimated contact stiffness from transverse fibers k_c ($27.7 \pm 39.9\ kPa$ in total; $14.1 \pm 11.4\ kPa$ for longitudinal samples; $47.0 \pm 56.2\ kPa$ for transverse samples) appears to be slightly affected by sample orientation, however the correlation analysis rejects this hypothesis. It is however possible that a larger cell rotation is more likely to result in highly entangled structures. Current lack of knowledge on the interactions resulting from fiber entanglement in collagenous tissues, and on the transverse stiffness of collagen fibril bundles renders the interpretation of the obtained data more complicated.

3.6. Conclusions

The present constitutive model of skin proposes a new approach to the mechanical behavior of the dermis, based on observations of the arrangement of the collagenous network. In particular, two microscale characteristics were incorporated:

a) The effect of fiber braiding, following recent observations which suggest a certain level of inter-fiber entanglement (see also Figure 3.1). Coincidentally, uniaxial tensile tests on braided structures reveal physical features, such as nonlinear elasticity and dissipative behavior, that are reminiscent of some aspects of the tensile behavior of skin;

b) The effect of shear at the interface between adjacent fibrils in a fiber bundle, as a result of fiber undulation. This process is prominent in the bending-dominated straightening phase of the fiber.

These characteristics are implemented in the model within a representative element, comprising a two-dimensional semicircular bundle of collagen fibrils, transverse fibers that generate interaction forces opposing to the straightening process, and a surrounding hyperelastic ground substance. The effects of shear are described in the interstitial matrix between the fibrils. The geometry of the unit cell is dictated by the average dimensions of the collagen fiber: fiber thickness $H \approx 2.5\,\mu m$, fiber neutral radius of curvature $r_n^0 = 5\,\mu m$, opening angle of the circular segment $\omega_n^0 \approx 37.8^\circ \pm 6.8^\circ$, and a fibril diameter $d_f \approx 82\,nm$. The following are the principal results of this investigation:

- Predictions are in reasonable agreement with tensile response that has been reported elsewhere, either experimentally or with comparable modeling approaches. However, some large variations in the estimated values of some parameters or unexpected trends reveal some limitations of the constitutive framework.

- In the present description, the rotation process of the fibers does not require the application of any force; instead an "alignment" stretch dictates the onset of fiber deformation. During the realignment phase, the ground substance mainly bears the load. This representation is analogous to a fiber network where all fibers are connected by ball-and-socket joints [251]. However, results of the parameter estimation point out that this representation yields unrealistic effects, where only a reduced portion of the fibers is recruited, or highly concentrated fiber alignments are found. Experiments using *in situ* small angle x-ray scattering (SAXS) or multiphoton imaging with a tensile setup generally show that a significantly larger population of fibers gets recruited during tensile deformation [41,123,252]. Notwithstanding, still little is known on the actual arrangement of collagen fibers in the dermis, most particularly on the persistence length of the fibers, their respective interactions, and the nature/type of the connection between them. Future work on the topic would provide clues that could inform further improvements of the constitutive model. Moreover, a better knowledge of the arrangement of collagen and its evolution will remove uncertainties in the model caused by fiber orientation and dispersion (or standard deviation), as the results of the sensitivity analysis suggest.
- The time-dependent behavior of the material is described by the quasilinear viscoelastic theory (QLV) theory, with a three-term Prony series relaxation function. Changes in the parameters of the QLV component were not considered in this study, as the approach mainly focuses on the elastic contribution. A notable interest in implementing viscoelasticity was to observe whether the effect of applied strain rate can be entirely captured by this component, without affecting the other structural and elastic

parameters. This was then correctly established in the correlation analysis. Besides the fact that some limitations of the QLV theory have been reported for skin [67,172], future developments of the model should aim to replace this component with structural features that incorporate time-dependence and the dissipative behavior of skin. Indeed, the definitions of the interfibrillar shear interaction and of the contact between entangled fibers can be expanded to include viscoelasticity, dissipative behavior, irreversible damages, and friction. Fibril discontinuity should be further studied to account for effects of shear-lag [150]. Lastly, relative sliding between fibers, which could explain the low values that were found for the Young's modulus E_c, were not directly investigated here.

- The proposed coarse-grained model has the potential to allow for a systematic investigation of how different geometric and mechanical characteristics influence the response of fibers to loading, e.g. radius of curvature, fiber thickness, number of fibrils, spanned angle, inter-fibril interaction strength and the stiffness of a single collagen fibril. Moreover, further iterations of the model could incorporate features such as a post-elastic behavior (damage) [253], or irreversible deformations caused by relative displacements of beads, which could be evidenced under cyclical loads.

3.7. Acknowledgements

Chapter 3, in full, has been submitted for publication of the material as it may appear in Acta Biomaterialia, and was authord by A. Pissarenko, C.J. Ruestes, and M.A. Meyers. The dissertation author was the primary investigator and author of this paper.

We thank Prof. K. A. Brown, Prof. A. Williams, and Dr. Ben Butler for their contributions to the experiments conducted on porcine tissue at Cambridge University.

CHAPTER 4. THE TOUGHNESS OF PORCINE SKIN: QUANTITATIVE MEASUREMENTS AND MICROSTRUCTURAL CHARACTERIZATION

4.1. Introduction

As the outermost layer of the body, and consequently the first protective barrier against external aggressions, it is important for the skin to maintain its structural integrity throughout life. Injuries can result in tears or scratches that easily become sites with an increased risk of infection. Moreover, it is crucial that these damaged areas do not expand or grow to a critical extent following movement, which would considerably affect the efficiency of the healing process. Surgical interventions often require that external tissues are incised, in order to facilitate access to the regions to treat. Considerable efforts have been made to reduce the size of incision, for cosmetic purposes, but also to minimize exposure and the formation of excessive scar tissue. Repeated access through the area of intervention generates load concentration around the incised region, potentially causing tear propagation. In skin, this process is mitigated thanks to its remarkable resistance to tearing, a property that has recently been characterized by Yang et al. [41] for rabbit. Collagen fibers in the dermis realign in the direction of tension and help alleviate the stresses which concentrate around the tear. This process of realignment was observed and quantified by small angle X-ray scattering (SAXS), and can be seen macroscopically as the region around the tear starts blunting, replacing sharp crack tips which are regions of stress concentration. This process was also evidenced for thinner collagenous tissues using multiphoton imaging [254]. Nonetheless, although some light has been shed on the mechanisms at stake during tear propagation, quantitative information on the toughness of skin is incomplete. Such knowledge is of considerable interest in designing better strategies for

surgical pre-planning, or minimizing scar tissue formation by improving healing techniques, for example.

Wegst and Ashby [255] compiled a modulus-toughness plot for many biological materials, including skin. It reports that skin exhibits amongst the highest values of J_c with a rather low elasticity modulus. They point out that according to a criterion where the material must support a given displacement without failure, reflected by the parameter $M_{12} = (J_c/E)^{1/2}$, skin performs particularly well. It is interesting to observe that in an earlier publication, Ashby et al. [256] had a plot with a much wider range in moduli and in toughness for skin, namely $E \approx 2 \cdot 10^{-3} - 1.5 \cdot 10^{-1}\ GPa$ and $J_c \approx 1 - 20\ kJ/m^2$, while the updated plot shows $E \approx 0.01 - 0.07\ GPa$ and $J_c \approx 6 - 30\ GPa$, suggesting that our understanding of these measures is becoming more accurate. The compiled values come from tests conducted on different species, for which the variation can be quite broad [Pissarenko and Meyers, unpublished], and from different methods used to measure a given material property influencing the final result. Since skin is a nonlinear elastic material, the estimation of a single modulus of elasticity is also questionable [257]. For toughness, it appears that the results by Bauer et al. [258] on lizard skin, by Purslow [259] on rat skin, and by Vincent [260] on rabbit skin were used as a reference in the Ashby plots. The methods for the estimation of toughness differed: Bauer et al. [258] calculated the area under the stress-strain curve, while Purslow [259] used the trouser test. It is likely that the results on lizard skin were ultimately removed in the latest versions of the Ashby plots [255]. The data used to estimate the toughness of skin are therefore rather limited and suffer from large variations due to the influence of species and of the testing method.

More recently, Comley and Fleck [261] calculated a toughness of $J_c = 17 \pm 4\ kJ/m^2$ for pig skin from trouser tests, which is in good agreement with the previously mentioned range.

Note that for trouser tests, the pulling direction is out-of-plane, implying that the fracture occurs in Mode III. The calculated toughness thus corresponds to this specific shear mode, which is not necessarily the principal mode of tear propagation in skin.

In-plane tension, which has been studied extensively over the past few years [17,41,47,132,227], is probably the principal mode of deformation in skin. On the other hand, for the study of toughness, conventional in-plane methods can be limited by the fact that it is difficult to maintain a skin sample flat during the test. This difficulty can be overcome with shear tests. For pure shear, where the width has to be 6 to 10 times larger than the gage length [262], the area to grip becomes considerably large and can become problematic. Hollenstein et al. [263] proposed a solution by taking thin slices of the dermis using a dermatome. This offers interesting perspectives for the testing of tear propagation in such conditions, although whether properties obtained for a thin slice can be transferred to the properties of a full section of skin has not been addressed.

In a recent study on the toughness of arapaima scales [264], an experimental setup was developed to conduct crack opening tests (mode I). The sample geometry is quite similar to the one for trouser tests, except this time both legs are pulled apart from each other along the surface plane. The grips are free to rotate in the out-of-plane direction, facilitating the opening motion. Plexiglass sheets are used to contain the unstretched portion of the sample to prevent it from folding or buckling. This is particularly appropriate for the testing of thin biological materials and soft tissues.

Other possible in-plane methods are the single edge notch tension (SENT) and the centrally cracked tension (CCT) tests. In each case, a tensile specimen is notched perpendicularly to the tensile direction with a sharp cut at mid-length, either on one side of the sample, or

symmetrically in its center. CCT tests can be preferred for the symmetry of the sample and the loading conditions, allowing for an easier observation of the tear ovalization in the case of skin [41], while SENT tests are more favorable if one wants to focus on the process of tear propagation, since it will only occur on one side. While this method is well implemented in the context of linear elastic fracture mechanics (LEFM), or elastic-plastic fracture mechanics, several assumptions on the mechanical behavior of the tissue as well as on the local stress distribution around the crack are necessary to analytically determine the toughness of soft tissues.

The use of digital image correlation (DIC) to measure the local deformation of skin during deformation has gained in popularity over the last few years, notably because it offers the possibility to correct errors in the evaluation of the macroscopic strain and to non-invasively map local strains [227,265,266]. More recently, DIC was also used for the estimation of a linearized Poisson ratio and to track volume changes with applied uniaxial tension [17,135]. However, to the authors knowledge, this technique has not yet been implemented to study the process of tear propagation in skin.

DIC can indeed be a useful tool to measure the toughness of materials via the direct calculation of the J-integral or other failure criteria. The theory is well established in the framework of LEFM, and a wide range of examples can be encountered, mainly for isotropic linear elastic materials [267–271], as well as some applications also covering anisotropy [272] and hyperelasticity [273–275]. In the context of skin mechanics, although such applications could yield interesting results, this venture is substantially complicated by the fact that the method requires the evaluation of local stresses, and therefore a constitutive behavior for the material must be established. Despite ongoing attempts to consistently and accurately describe

the mechanical response of skin, inter-sample variations are a source of important variations in behavior, meaning that a unique constitutive law is not suitable in this case. Added with the uncertainties inherent to the DIC method, the results can be highly inaccurate.

Nevertheless, the local strain maps that can be obtained from DIC provide valuable information on the distribution of strains, and especially their concentration near the tip of a crack, and the size of the processing zone (where a high strain gradient can be observed). Potentially, strain-based criteria for failure can be evaluated. Changes in shape of the tear opening can also be observed. Liu et al. [276] performed this analysis on a PVA dual-crosslink hydrogel, and observed a steady-state propagation of the crack, meaning that once initiated, the crack propagates in a self-similar manner if one follows the position of the crack tip. They also noted that prior to propagation, the strain levels in the static blunted crack is higher.

The present study aims to provide a quantitative analysis of the toughness of porcine skin, by adapting conventional testing techniques to the material, coupled with the use of digital image correlation. The strain profile from the crack tip is measured, with the intention to provide a strain-based failure criterion for skin. Moreover, microstructural effects associated with tear mitigation in skin are further characterized with a systematic microscopic analysis of the arrangement of collagen fibers: first *ex situ* with transmission electron microscopy (TEM), and finally *in situ* with environmental scanning electron microscopy (ESEM), coupled with a micromechanical tensile testing device.

4.2. Methods and Materials

4.2.1. Sample Extraction and Preparation

Pig skin samples were obtained from two juvenile (~9 weeks old) piglets, provided from the Veterinary School at the University of Cambridge, in the same way as it was done for the

study in Chapter 2. Removal of the skin was done within a few hours after sacrificing. To facilitate the tracking of displacements on the surface of the skin, the epidermis was depilated using a commercially available hair removal cream (Veet, Reckitt Benckiser Group plc, Slough, UK). Excess fat on the proximal side of the skin was removed with a surgical scalpel. Samples were extracted following two distinct orientations, i.e. parallel (longitudinal sample) and perpendicular (transverse sample) to the direction of the spine. For trouser and crack opening tests, rectangular sections of 80 mm x 25 mm and 60 mm x 50 mm were cut, respectively. For SENT tests, a dumbbell-shaped cutting die was used to extract the samples; the exact dimensions are further detailed below. Lastly, smaller rectangular sections of approximately 40 mm x 10 mm were isolated for *in situ* testing in the ESEM. Prior to testing, the dimensions of each sample, as well as the thickness, were remeasured to account for effects of tissue expansion or shrinkage. All samples were kept in mildly hydrated plastic bags and stored in a cold room at 4˚C. Mechanical testing was performed within 2 days post extraction.

4.2.2. Experimental Methods

4.2.2.1. Tensile Testing Setup

A conventional tensile testing machine (THE Hounsfield) was used to perform the mechanical tests. A crosshead speed of 0.1 mm/s^{-1} was applied, and the load-displacement curves were recorded. More specifications for each experiment are detailed in the sections below.

4.2.2.2. Trouser test samples

The trouser test, used for the skin by Purslow [259] and Comley and Fleck [261], is a well-established method used to determine the fracture toughness of elastomeric materials in tear mode [262]. A rectangular sample is cut centrally along its length so that two legs are formed.

The legs are pulled in opposite directions, and the force at which the cut starts growing is measured [277]. Figure 4.1a provides the trouser sample dimensions that were used for the present study. The hatched area designates the portion of the sample that is attached to the grips. Specifically designed grips were used, to reduce the likelihood of slippage during testing, as explained in Section 2.2.2. Samples are cut with a sharp razor blade in the middle along their length, forming legs with a length of 50 mm, which corresponds to an effective pre-crack length of 25 mm excluding the gripped parts. The intact portion of the sample, along which the crack propagates during the test, has a length of ~30 mm. Figure 4.1b shows a real trouser sample of pig skin, which is subsequently mounted on the testing machine, as shown in Figure 4.1c. During testing, the legs of the trouser sample are gradually pulled apart such that the tissue is undergoing Mode III shear. This was done until complete failure, i.e. the separation of both legs. Three longitudinal and three transverse samples were tested.

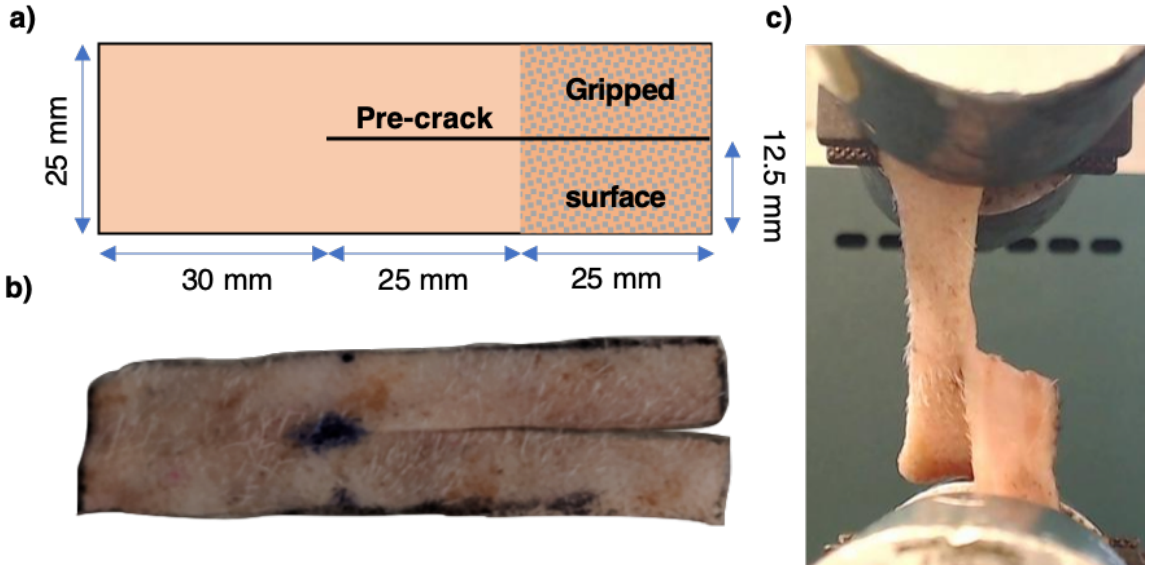

Figure 4.1. Trouser tests. a) Schematic description of the geometry of a sample. b) Pig skin sample prior to testing, following the given dimensions (picture scales with a)). c) The sample is mounted on the tensile testing machine; the separation of the grips leads to the propagation of the pre-crack.

4.2.2.3. Crack Opening Tests

As mentioned earlier, Yang et al. [264] designed a set of grips to perform Mode I crack opening tests on arapaima scales. The same methodology was applied here for pig skin, and the dimensions of the samples were adapted to fit the gripping area, indicated by the hatched region on Figure 4.2a. A pre-cut was made along the length of the sample, starting from the middle of one side, with a length of ~25 mm. Figure 4.2b shows a pig skin sample mounted on the testing machine. Note that each grip is connected to the testing machine via pins, enabling free rotation. The effective portion of the sample, along which the crack is meant to propagate during testing, was maintained between two plexiglass plates which ensured that the sample stays fairly flat and enabled the visualization of tear propagation. It was assumed that the effect of these plates on the deformation process is negligible. Here as well, both legs were gradually separated until complete failure of the skin sample. Three longitudinal and three transverse samples were tested.

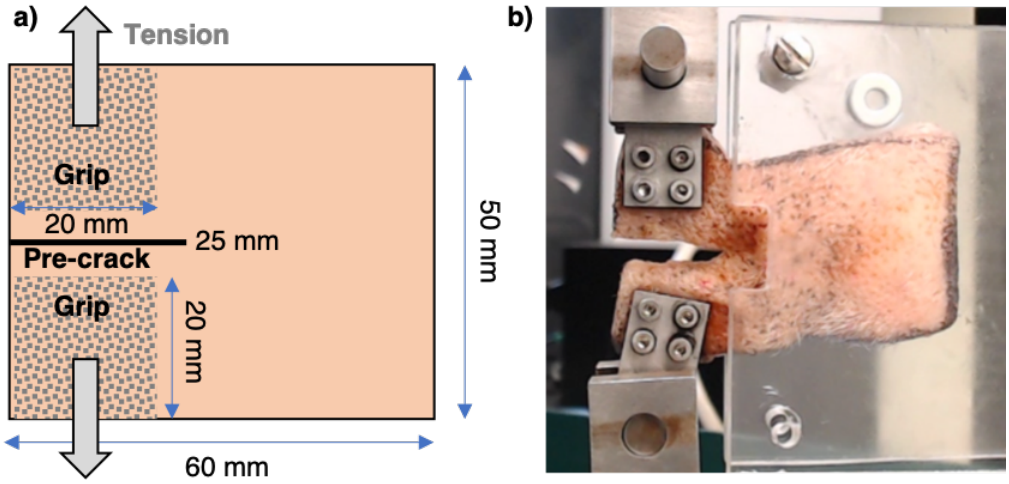

Figure 4.2. Sample preparation for crack opening tests. a) Schematic illustration with description of the principal dimensions and testing conditions. b) Pig skin sample prior to testing, mounted with the specific grip fixtures, which allow for the rotation of the grips during the opening of the legs. Two plexiglass sheets maintain the sample in-plane during the test, to facilitate image recording and monitor the tear opening process.

4.2.2.4. Single Edge Notch Tension (SENT) Tests

4.2.2.4.1. Sample Mounting and Mechanical Testing

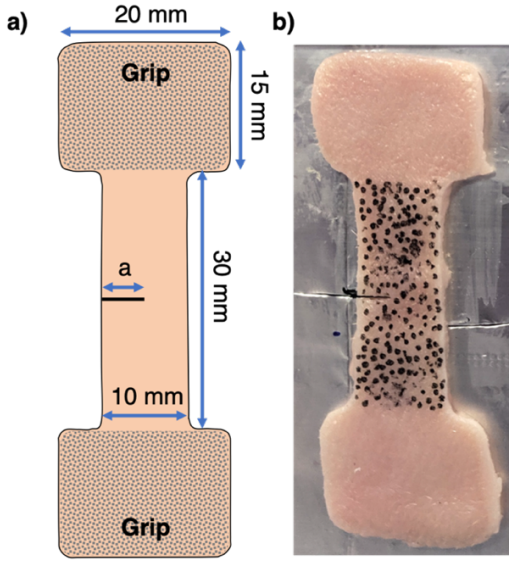

Figure 4.3. SENT sample. The specimen is extracted from the skin using a cutting die, with the indicated geometry. a) Schematic description of the sample, showing the notch on the side, made at mid-length in the gauge region, with length a. b) Pig skin sample, shown here for a/W=0.5. The dimensions of b) scale with a) so that the slight changes in size can be appreciated. The skin is speckled to facilitate post-processing with DIC.

Figure 4.3a provides the dimensions of the SENT samples that were obtained after extraction with the cutting die. The resulting gage dimensions are 30 mm x 10 mm. At mid-length of the sample, a pre-notch of length a was made on the side, such that $a/W = 0.25$ (for one longitudinal and three transverse samples), and $a/W = 0.5$ (for 3 longitudinal and 3 transverse samples), where a is the initial pre-crack length and W is the width of the sample. Figure 4.3b shows a real SENT sample of pig skin, presenting some slight changes in dimension following extraction. As a consequence, the value of a is adapted to the actual measured width of each sample. Specimens were mounted on the tensile testing machine using the same grips that were used for trouser tests, and uniaxial tension was applied until complete failure of the tissue. Figure 4.3b also shows that a random speckle pattern was applied to the surface of the

skin, which was done using a thin permanent marker. The speckle pattern facilitates the tracking of displacements for the DIC algorithm. Each SENT test was synchronously recorded using a high resolution camera (Logitech C920), placed in front of the speckled surface. A laser alignment tool was used to ensure that the camera was well aligned with the normal to the sample surface.

4.2.2.4.2. Digital Image Correlation Post-Processing

The recorded videos from SENT tests were post-treated using the open-source Matlab software NCorr 2.1 [230]. NCorr is particularly suited to track large deformations, as the DIC post-processing algorithm updates the reference image as the sample deforms, in a stepwise fashion. The software provides local measurements of vertical (y-direction) and horizontal (x-direction) displacements, and calculates the local eulerian strains e_{xx}, e_{xy}, e_{yy} in the plane of the image. The parameters of the DIC analysis were iteratively selected such that: a) the region of interest (ROI) accurately follows the geometry of the sample, in particular the shape of the notch; b) the obtained displacement and strain maps would provide a good compromise between accuracy (in terms of resolution/size of the subset radius), and consistency, as points near the crack tend to have a poor correlation if the subset radius is too small. The DIC post-processing algorithm is executed for each tested SENT sample.

4.2.3. *Ex Situ* Transmission Electron Microscopy

4.2.3.1. Sample Loading and Region-Specific Observations

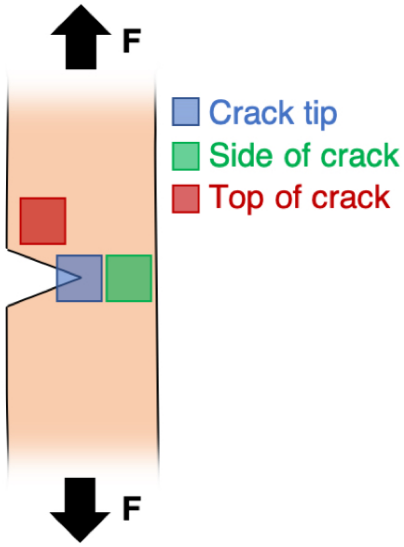

Figure 4.4. Schematic description of the extracted regions on SENT samples isolated for TEM observation, namely the tip of the crack (blue square), the region on its side, ahead of the crack tip (green square), and the region behind the crack (red square).

In order to gain a better understanding of the processes of microstructural rearrangement that occur in skin during a SENT test, three additional transverse specimens were isolated for *ex situ* characterization. All samples were initially pre-notched with $a/W = 0.5$. A first specimen was kept intact (untested); another one was loaded until initiation of the crack propagation is observed, and finally a last one was tested until complete failure. For each, strips located in specific regions with respect to the initial crack tip were extracted (~3mm x 3mm) , as described in Figure 4.4:

- A piece of skin containing the crack tip (blue square in Fig. 4.4), where a high concentration of stresses can be observed. For the failed sample, the areas immediately at the top and at the bottom of the initial crack tip were extracted;

- A piece in the area located on the side of the crack (green square in Fig. 4.4), which bears most of the uniaxial load during tensile deformation, after the tip of the crack. For the failed sample, this piece was taken slightly above the path of the propagated crack;
- A piece above the notch, well behind the tip of the crack (red square in Fig. 4.4). During deformation, this area bears almost no load.

4.2.3.2. Tissue Preparation and Microscopy Imaging

Immediately after extraction, the skin pieces were immersed in a solution containing 2.5% paraformaldehyde, 2.5% glutaraldehyde, and 0.1M cacodylate buffer. The staining and embedding protocol for TEM preparation is detailed in Section 2.2.4.2. The strips were embedded in low viscosity resin with the hypodermal surface facing the bottom surface of the block. This was done so that sectioning could be more easily performed starting from this side. After trimming ~0.5 mm off the surface of the block, ~70-100 nm thin sections of the dermis were sliced using a Leica Ultracut UCT microtome with a Diatome diamond blade, and subsequently placed on copper grids for TEM observation. A FEI Technai 12 spirit transmission electron microscope was used to visualize the nano-microstructure of skin. To increase the field of observation, grids of images were acquired in areas of interest, i.e. where collagen fibers were majorly found. The open-source software IMOD 4.9 (https://bio3d.colorado.edu/imod/) was used to stitch the images together and correct potential misalignments.

4.2.4. *In Situ* Scanning Electron Microscopy of Tear Propagation

While *ex situ* imaging with TEM provides high magnification visualization of areas of interest at different stages of deformation, *in situ* imaging enables real-time observation of the deformation process. Here, a micromechanical tensile testing device was mounted in the

chamber of an environmental scanning electron microscope (FEI XL30 ESEM). Two opposing steel pads are used to grip the skin specimen, and a remotely controlled actuator guides the distance between the grips, by setting into rotation a screw mechanism. As shown in Figure 4.5, the skin is mounted with the inner dermal layer facing the objective of the microscope, and the gage dimensions are ~20 mm in length and ~10 mm in width. A side notch of 5 mm is made at mid-length.

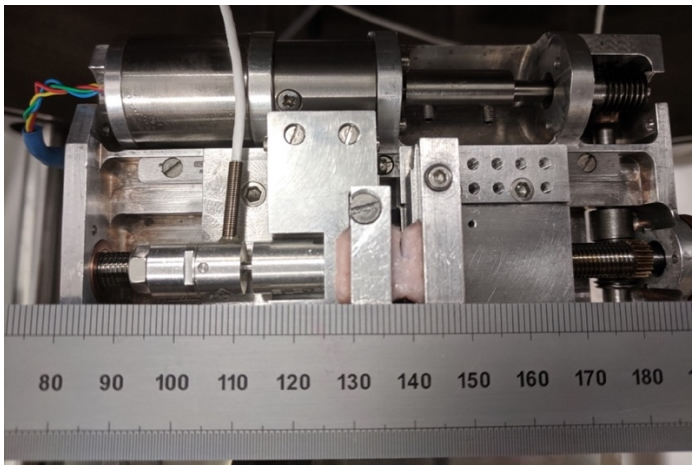

Figure 4.5. Experimental setup for *in situ* observation of tear propagation in an environmental scanning electron microscope. A remotely-controlled actuator extends the distance between the steel pads between which the skin is gripped, therefore pulling the skin sample in tension.

Once the skin specimen is mounted on the testing device, the pressure in the microscope chamber is decreased to a level of ~200 Pa. Tensile deformation is then initiated. Throughout the test, the field of view is adjusted to follow the position of the crack tip.

4.3. Results and Discussion

4.3.1. Force-Displacement Curves from Trouser and Crack Opening Tests

Figure 4.6 provides a summary of the force-displacement curves obtained from trouser and crack opening tests. Both results show similar trends: after an initial nonlinear loading phase, the curve reaches a force plateau, which coincides with crack propagation. Some relative

oscillations around the plateau value are observed, until both legs are completely torn apart; the latter corresponds to a sharp drop in applied force. The force plateau value is generally around ~15 N, and appears to be relatively higher for transverse samples, and in particular for crack opening tests. Note that differences in sample thickness are also likely to affect this result. It is also worth mentioning that the extension required to fully separate the legs after crack initiation, i.e. the width of the plateau region, is around ~80 mm, which is significantly larger than the initial propagation length of the samples (~30 mm for trouser tests; ~35 mm for crack opening tests), marking important elastic-plastic deformations occurring in the material during the tests. The difference between crack opening tests and trouser tests is not very pronounced.

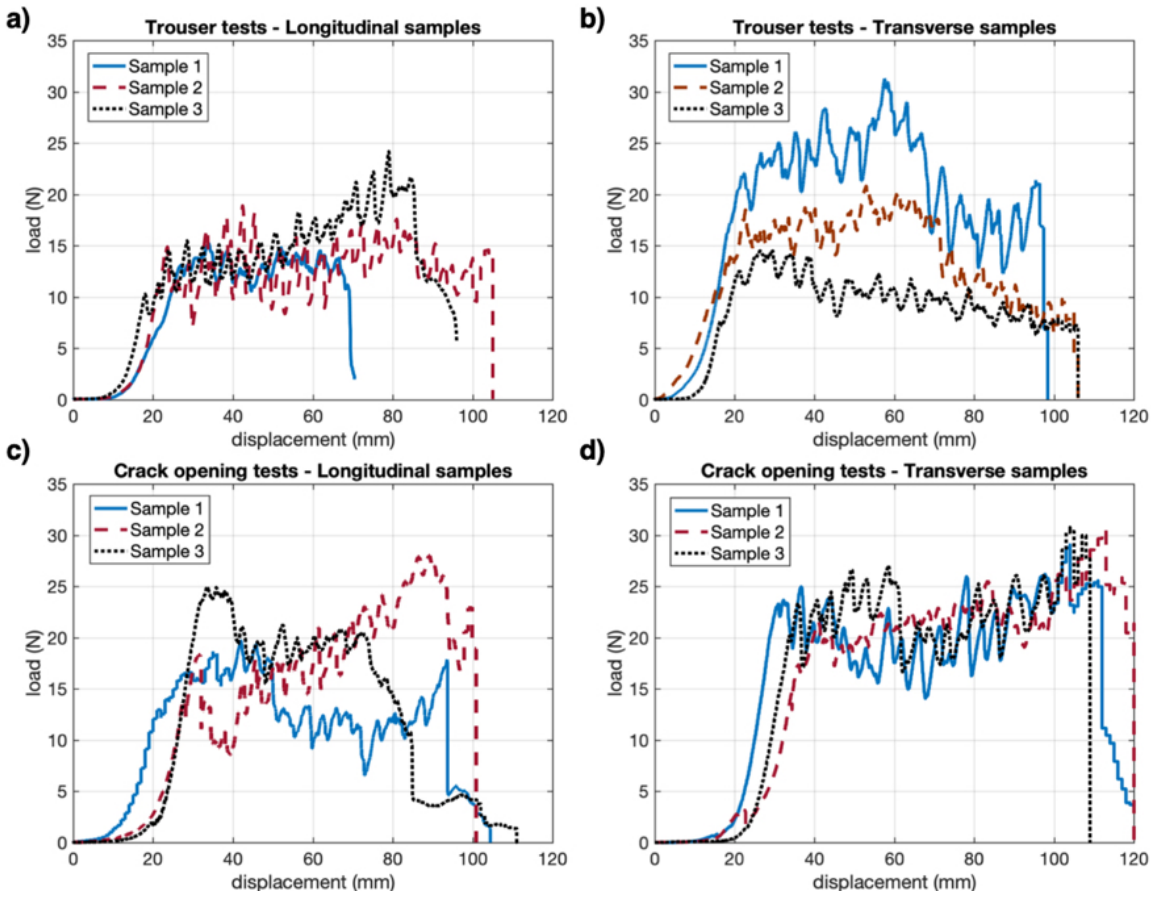

Figure 4.6. Load-displacement curves obtained from trouser tests in the a) longitudinal and b) transverse orientations, and from crack opening tests in the c) longitudinal and d) transverse orientations.

4.3.2. Estimation of J_c

Following the methodology of Comley and Fleck [261] and Purslow [259] for trouser tests on porcine skin, and earlier fundamental work by Rivlin and Thomas [262], the toughness J_c of the material is given by:

$$J_c = \frac{2\bar{F}}{t} \tag{4.1}$$

Where t is the sample thickness, and $\bar{F}$ is the average value of the applied force in the plateau region. The same assumptions are made for opening tests (Mode I). The obtained results for J_{IIIc} (from trouser tests) and J_{Ic} (crack opening tests) are reported in Table 4.1 for longitudinal and transverse orientations.

Table 4.1. Summary of the estimated toughness (mean values ± standard deviations) obtained from trouser tests (J_c^{III}) and for crack opening tests (J_c^{I}), measured for longitudinal and transverse samples, and total average.

Toughness	Longitudinal (n=3)	Transverse (n=3)	Total (n=6)
J_{IIIc}	$20.77 \pm 1.11\ kJ/m^2$	$20.42 \pm 3.19\ kJ/m^2$	$20.60 \pm 2.15\ kJ/m^2$
J_{Ic}	$26.00 \pm 4.41\ kJ/m^2$	$33.6 \pm +1.13\ kJ/m^2$	$30.38 \pm 4.90\ kJ/m^2$

Total averaged values for both types of tests indicate that the overall toughness is generally higher for opening Mode I, with an average of $J_{Ic} = 30.38 \pm 4.90\ kJ/m^2$, compared to $J_{IIIc} = 20.60 \pm 2.15\ kJ/m^2$. While differences in orientations are not found for shear Mode III ($J_{IIIc}^{long} = 20.77 \pm 1.11\ kJ/m^2$; $J_{IIIc}^{trans} = 20.42 \pm 3.19\ kJ/m^2$), more pronounced variations are reported for opening Mode I ($J_{Ic}^{long} = 26.00 \pm 4.41\ kJ/m^2$; $J_{Ic}^{trans} = 33.68 \pm 1.13\ kJ/m^2$). In the in-plane configuration, the effect of the alignment of collagen fibers (commonly described by the Langer lines) probably plays a more important role. In the transverse orientation, collagen fibers are more likely to be aligned perpendicular to the direction of the

crack, and thus more actively mitigate its propagation, reflected here by a higher value of toughness. Out-of-plane deformations probably cause different processes of damage to the collagen network, such as separation and early stage delamination.

Figure 4.7 shows the updated Wegst-Ashby modulus-toughness plot [255], with the addition of the values obtained from the present study, for Modes I and III. The average values of the elastic modulus for pig skin were taken from the tangent modulus of the linear region of the deformation curves reported in [17]. The results for trouser tests fall in the higher range of the previously reported values, and are in good agreement with the values found by Comley and Fleck [261]. On the other hand, the (in-plane) opening mode has a toughness clearly above the range for the skin in the Wegst-Ashby plot, thus extending the quantification of toughness.

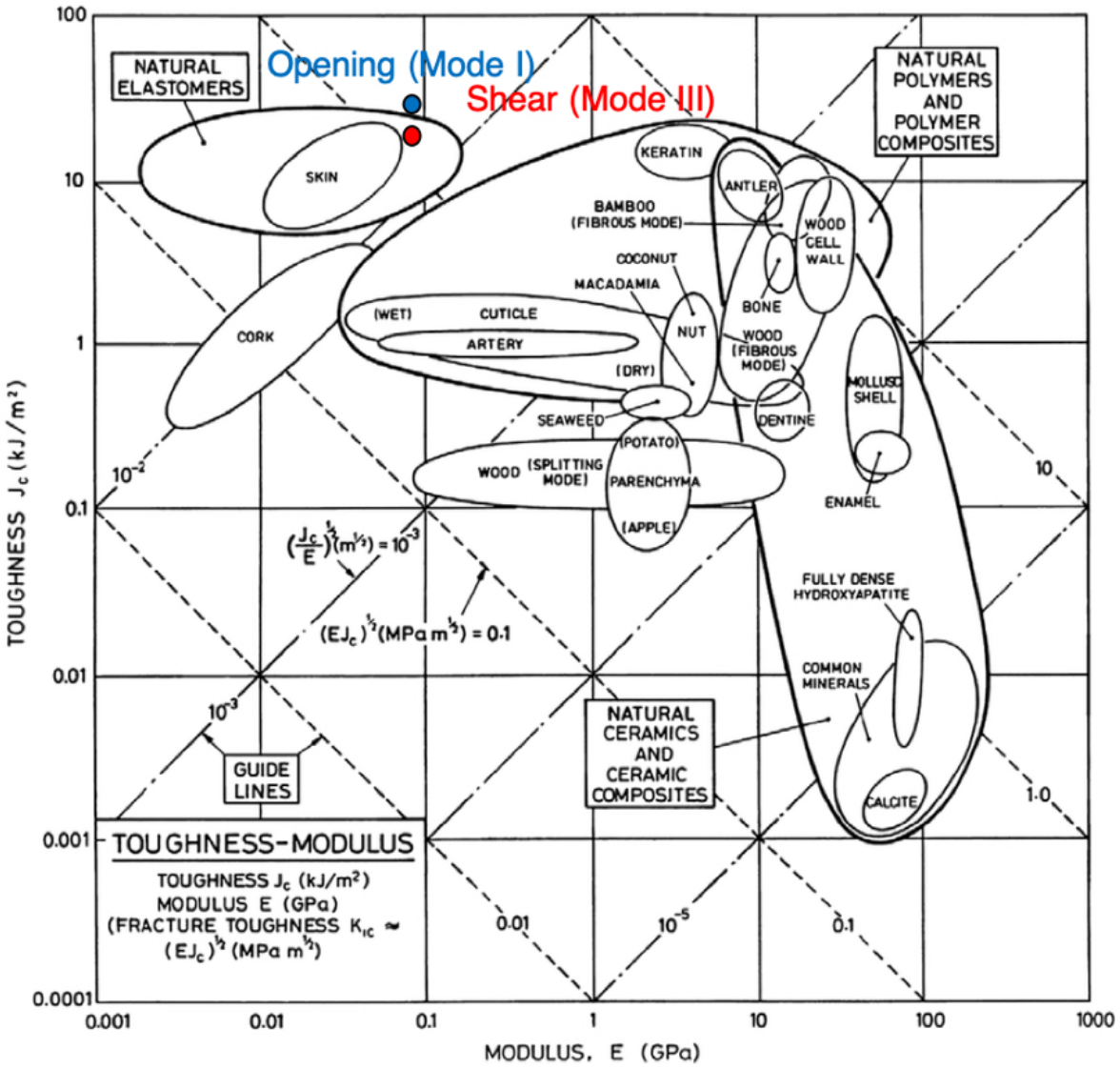

Figure 4.7. Updated Wegst-Ashby plot of modulus vs. toughness for several biological materials, including the total average values of J_c estimated in the present work, for trouser tests (red circle) and crack opening tests (blue circle). Circles do not scale with the calculated standard deviations. Reprinted from [255].

4.3.3. Strain Profiles Around the Crack Tip

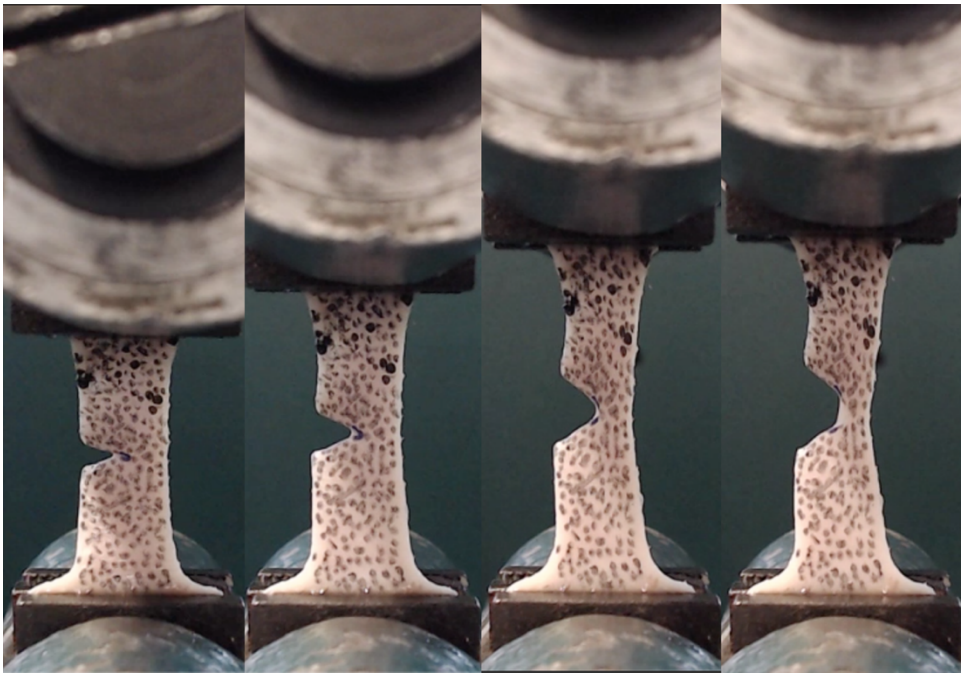

Figure 4.8. Time sequence of a SENT test ($a/W \approx 0.5$), shown here for a sample in the transverse orientation. Crack blunting can be observed, followed by tissue delamination shortly prior to failure.

The sequence of images in Figure 4.8 shows the typical deformation process of tear propagation in a SENT sample of pig skin. After an initial stage of tensile deformation, the tear starts to blunt and stabilizes until a critical deformation is reached in the material, after which the crack rapidly propagates. In the present analysis, particular emphasis is given to the strain state in the tissue shortly before the crack starts propagating.

An equivalent plastic strain e_{eq}, analogous to the Von Mises stress, was introduced to define a general parameter characterizing the overall strain state in the plane of the material, such that:

$$e_{eq} = \sqrt{\frac{2}{3}\bar{\bar{e}}_{dev} : \bar{\bar{e}}_{dev}} \tag{4.2}$$

Where $\bar{\bar{e}}_{dev} = \bar{\bar{e}} - 1/3\, tr(\bar{\bar{e}})\bar{\bar{1}}$ where $\bar{\bar{e}}$ is the eulerian strain tensor, and $\bar{\bar{1}}$ is the identity tensor. It is assumed that $e_{zz} = -\nu e_{yy}$, with ν~0.5.

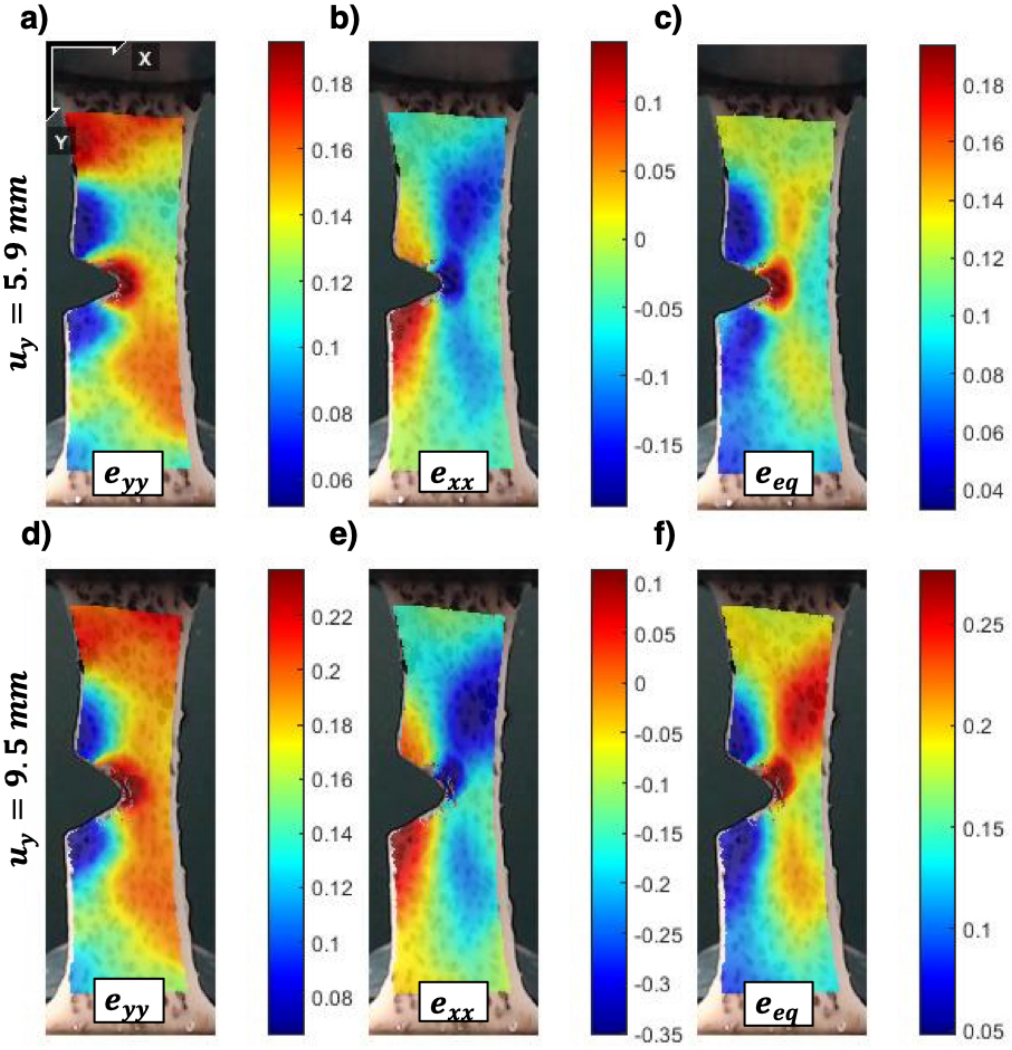

Figure 4.9. Strain maps on a transverse SENT sample, obtained from DIC, taken for an applied displacement of $u_y = 5.9\ mm$: a) e_{yy}, b) e_{xx}, c) e_{eq}; and for $u_y = 9.5\ mm$ *d*) e_{yy}, e) e_{xx}, f) e_{eq}; right before tear propagation. The first row shows that initially, maximum strain values concentrate in a quasi-circular manner around the crack tip. Right before crack propagation (second row), strain distribution appears to be more diffuse, the region on the side ahead of the crack taking up some of the deformation. This is particularly apparent for e_{eq}.

Figures 4.9a-f present typical 2D strain maps that were calculated from DIC on the same sample at two stages: the blunting phase (Figs. 4.9a-c) and right before crack propagation (Figs. 4.9e-f). These correspond to the second and the third images in the sequence Fig. 4.8. The maps

of e_{yy} (tensile direction, Figs. 4.9a and 4.9d) and e_{xx} (lateral direction, Figs. 4.9b and 4.9e), and e_{eq} (equivalent plastic strain, Figs. 4.9c and 4.9f) generally show that initially, strains localize around the tip of the crack, almost forming an almost quasi-circular "processing zone". Right before crack propagation, the strains on the surface of the sample become more diffusely distributed. This is particularly clear from the change in the distribution of e_{eq}. As expected, the region ahead of the crack path bears most of the tensile load (Figs. 4.9d), and the increased strain level helps alleviating strain concentration at the singularity, thus delaying the onset of failure at the crack tip. In contrast, the region behind of the crack, especially right above the notch, undergoes almost no deformation.

Using the strain maps calculated by DIC, one can also plot the strain profile along the crack path at different stages of deformation. Plots for the transverse sample from Figs. 4.8-4.9 and for a longitudinal SENT sample ($a/W = 0.5$) are presented in Figure 4.10, showing the strain profiles of e_{yy} (Fig. 4.10a-b) and e_{eq} (Fig. 4.10c-d) as the specimens are extended, until failure is initiated. Besides a difference in width, which is due to contraction or expansion of the specimen depending on its initial orientation, the strain profiles do not differ much based on orientation. Results were also not found to differ much based on the value of the a/W ratio, except the fact that it takes a higher applied extension u_y to completely break the sample. Interestingly, the strain in the tensile direction e_{yy} evolves with an almost self-similar profile. As expected, the maximum value is found at the tip, and the vertical strain progressively decreases until ~2.5mm, after which it remains at more stable values. This trend reflects the progressive contribution of the region ahead of the crack tip, which reduces effects of localization. The profiles of e_{eq} show a sharper decrease near the tip, which become more

pronounced as the sample is deformed, reflecting the combined effects of tension/compression near the singularity, yet also highlighting the progressive contribution of the region on the side of the crack.

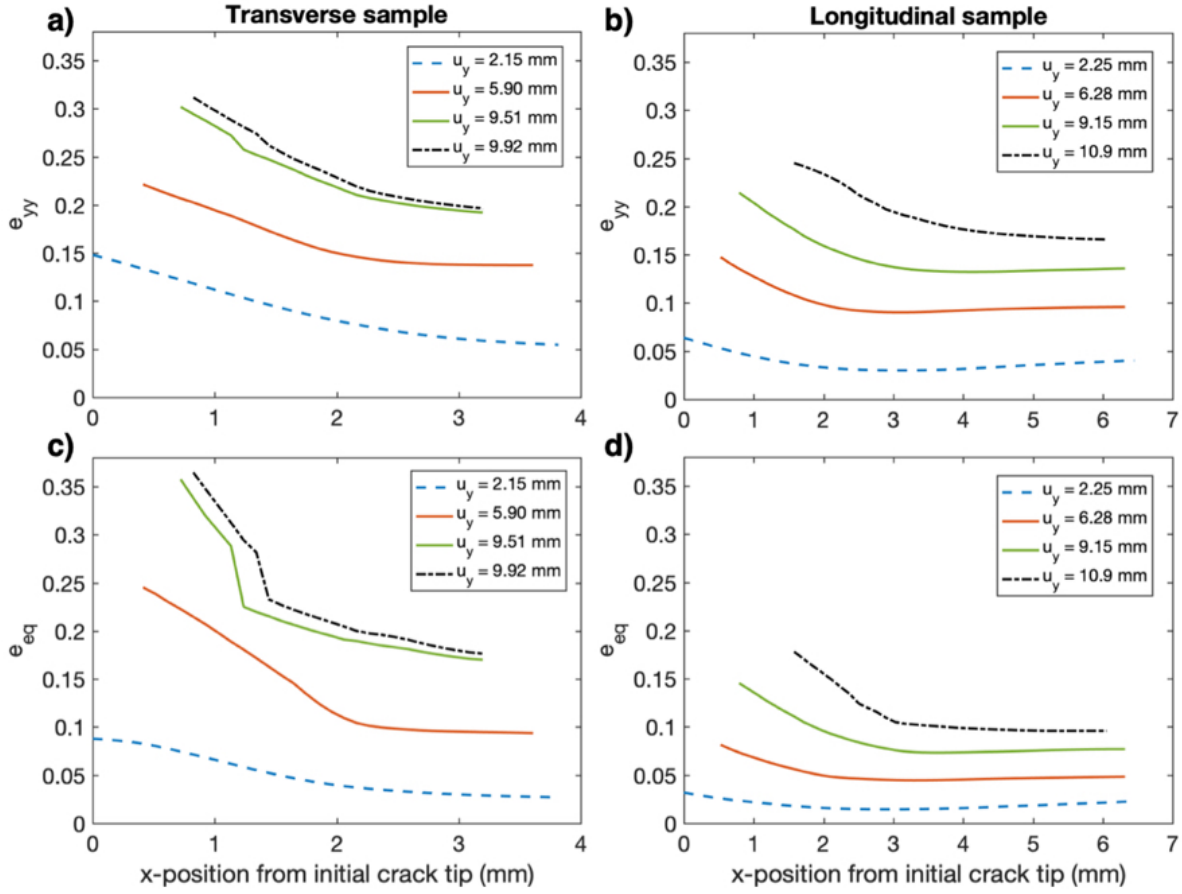

Figure 4.10. Strain profiles along the x-direction from the initial position of the crack tip. Plots of e_{yy} for a) a transverse sample and b) a longitudinal sample are provided at four similar deformation states, the last state (black dashed line) taking place right before propagation of the crack. The equivalent plastic strain e_{eq} for c) the transverse sample and d) the longitudinal sample is also plotted at the same deformation states, showing differences in strain concentration close to the crack tip.

It is also revealing to observe the evolution of the maximum strain values, found close to the tip of the crack, over the applied extension. These are plotted Figure 4.11a and 4.11b, for e_{yy} and e_{eq} respectively, for both presented samples. Here again, the evolution of the maximum strains is quite representative of what is found for the other specimens that were tested. More importantly, one can identify the strain level at which crack propagation is seen, thus

introducing strain-based criteria for tissue failure. The calculated strains at which the tear starts propagating (indicated by the black arrows in Figure 4.11) are compiled in Table 4.2 for all samples. No notable effect of the a/W ratio was found, but in the same way as for crack opening tests, the transverse orientation is tougher than the longitudinal one. Maximum strain values of $e_{yy}^{trans} \sim 0.30$ (and $e_{eq}^{trans} \sim 0.31$) are found on average for transverse samples, compared to $e_{yy}^{long} \sim 0.27$ (and $e_{eq}^{long} \sim 0.22$) for longitudinal samples. Note also that these values are in close agreement with the average failure strains that were reported in [17], and can therefore serve as a limiting criterion to estimate the onset of failure in the tissue. Moreover, since the crack propagates in a self-similar manner, these values can be compared to the applied global strain on the material, which can then be used to introduce limiting stretches that should be exerted on the tissue if failure needs to be avoided.

Table 4.2. Maximum values of e_{yy} and e_{eq} at the onset of crack propagation, for all the tested SENT samples of pig skin. Averages and standard deviations are also calculated for each orientation and for all samples.

Orientation	Sample	a/W	$\max(e_{yy})$	$\max(e_{eq})$
Longitudinal	1	0.5	0.2407	0.2169
	2	0.5	0.2592	0.2069
	3	0.5	0.3002	0.2305
	4	0.25	0.2677	0.2316
	Total (mean±S.D.)		0.2670±0.0249	0.2215±0.0118
Transverse	1	0.5	0.3035	0.3753
	2	0.5	0.2084	0.3020
	3	0.5	0.3599	0.3479
	4	0.25	0.3267	0.2173
	5	0.25	0.3381	0.32
	6	0.25	0.2726	0.3392
	Total (mean±S.D.)		0.3015±0.0546	0.3140±0.0514
Total (mean±S.D.)			0.2877±0.0467	0.2770±0.0616

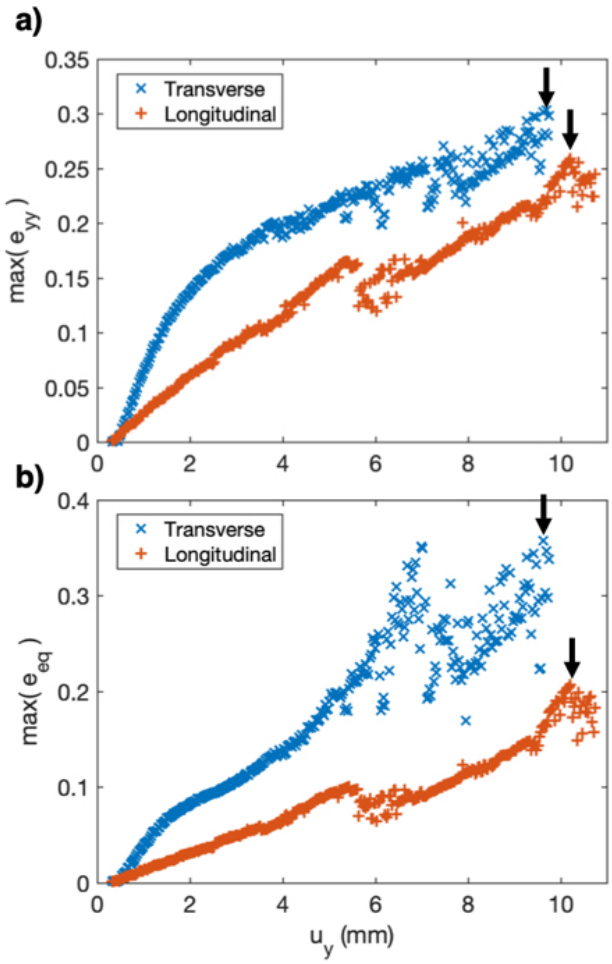

Figure 4.11. Evolution of the maximum values of a) the strain in the tensile direction e_{yy} and b) the equivalent plastic strain in the tissue e_{eq} as a function of applied extension, plotted for a transverse and a longitudinal sample. The black arrows indicate the onset of crack propagation in the tissue.

4.3.4. Structural Rearrangements of the Collagen Network

4.3.4.1. Transmission Electron Microscopy

A montage of the images acquired by *ex situ* TEM is presented in Figure 4.12. Each row corresponds to a specific region, as described in Section 4.2.3.1, and each column corresponds to a deformation state, i.e. untested, onset of crack propagation, failure. For the untested configuration, the characteristic tridimensional collagen network is seen. Fibers do not appear to follow any preferential arrangement, perhaps with the exception of the crack tip region,

where a certain degree of vertical alignment can be seen. This could either be due to sample or location-related differences, or a consequence of the pre-cut, causing fibers that are not perpendicularly aligned with the direction of the cut to recoil. At the onset of crack propagation, fibers around the tip of the crack are less organized and more compact, and principally lie in-plane. Given that the largest strains concentrate in this region, it is likely that the fiber distribution that is observed is the consequence of tissue relaxation, between the times the sample is unmounted from the testing machine and the time it is immersed in fixative, or of substantial damage. On the side of the crack, collagen is highly aligned in the tensile direction. Since the side of the crack is the only portion of the SENT sample that continuously extends from both grips, this region principally alleviates the load from the singularity at the tip of the notch, as seen from the strain maps (Fig. 4.9). As also expected from the observed distribution of strains, the structure of collagen at the top part behind the crack is unaltered. Lastly, the-post fracture structure of collagen is dramatically changed. In the vicinity of the crack path, loose, out of plane collagen fibrils are observed. This a consequence of the irreversible processes that are fiber sliding, delamination, and ultimately fracture. Right above the crack propagation path, after collagen fibers have undergone realignment and a high level of stretch, fractured collagen fibers recoiled, as seen by the rugged surface of the fibers, which is another indication of considerable damages that have taken place in the structure, except that a higher level of fiber integrity is maintained. Besides a slightly higher degree of fiber alignment, which could be specific to the observed section, no dramatic changes to the structure are seen behind the crack path.

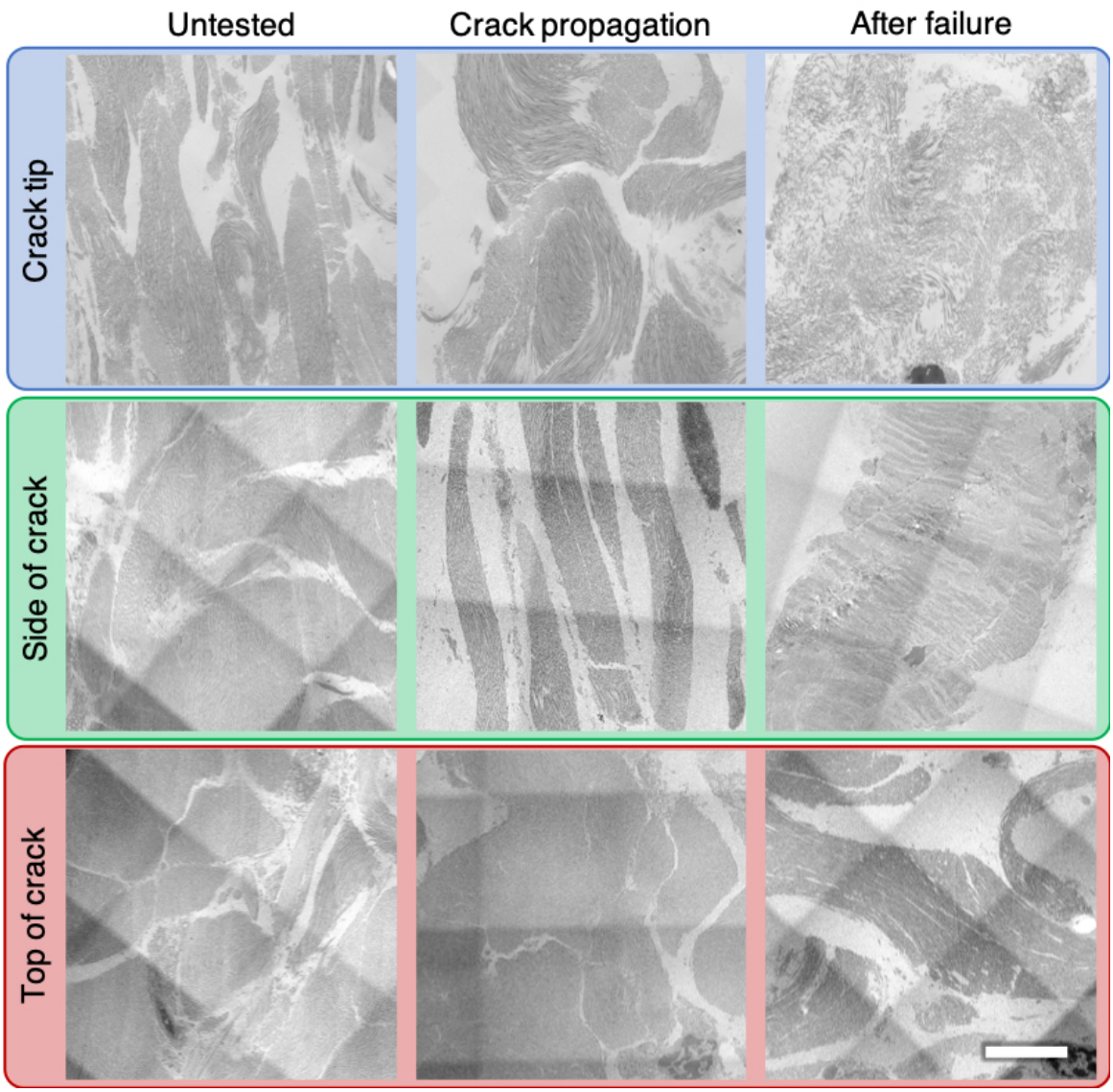

Figure 4.12. Stitched TEM images of the three isolated regions of SENT samples of pig skin (Crack tip, side, and top) at three different stages of deformation: untested (first column), loaded until onset of crack propagation (second column), and after tissue failure (third column). The microscopy reveals the arrangement of the collagen fibers for each deformation state, showing regions that underwent the most important changes. Square grids are the result of the stitching process. Scale bar in the bottom right corner = 5 μm (applies to all images).

4.3.4.2. *In Situ* Environmental SEM

A notable difficulty in observing the rearrangement of collagen fibers in the ESEM method implemented in this study resides in the fact that the inner layer that is observed still contains a fair amount of subcutaneous fat, and therefore poses a challenge for immediate observation of the collagen fibers in the dermis. Nonetheless, after a certain deformation level, tissue

delamination reveals the collagen fibers that contributed to tear mitigation. The sequence in Fig. 4.13 illustrates this effect, showing that as the sample is deformed, substantial delamination occurs, seen by the progressive appearance of collagen fibers and the erosion of superficial layers. Tear propagation is mitigated by highly aligned extended collagen fibers that bridge the crack, until they reach failure. This is also accompanied by gradual recruitment of the fibers on the side of the crack, which, as discussed above, helps alleviate the loads near the singularity. This process is illustrated in the schematic sequence Figure 4.14: the initially wavy distributed collagen fibers (Fig. 4.14a) are gradually recruited in the tensile direction and start straightening, an effect that is more pronounced closer to the crack tip. This leads to crack blunting (Fig. 4.14b). During crack propagation, straightened collagen fibers near the crack bridge the crack and progressively fail, as other aligned fibers ahead of the crack tip mitigate the propagation (Fig. 4.14c). The recoiled, post-failure structure of the collagen fibers is further manifested in the series of images in Figure 4.15.

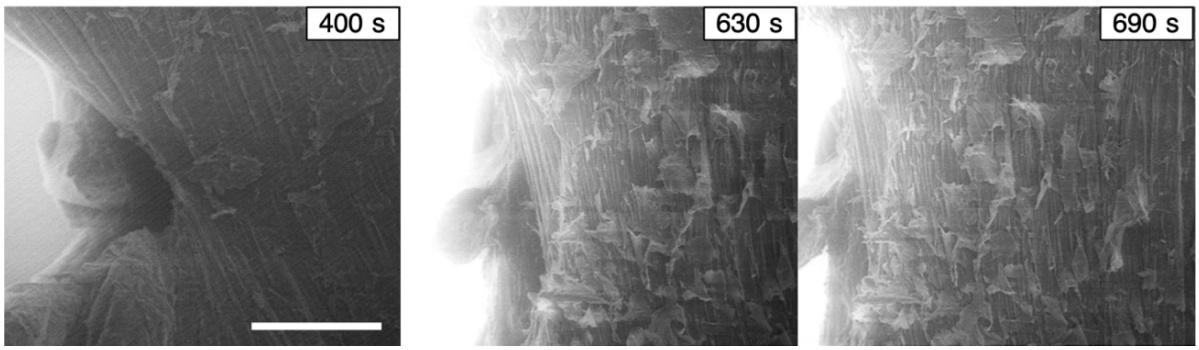

Figure 4.13. *In situ* environmental SEM sequence of a pre-notched sample undergoing tensile deformation. The highly extended collagen fibers that bridge the crack tip can be distinguished from the second image, and progressive layer delamination is also observed.

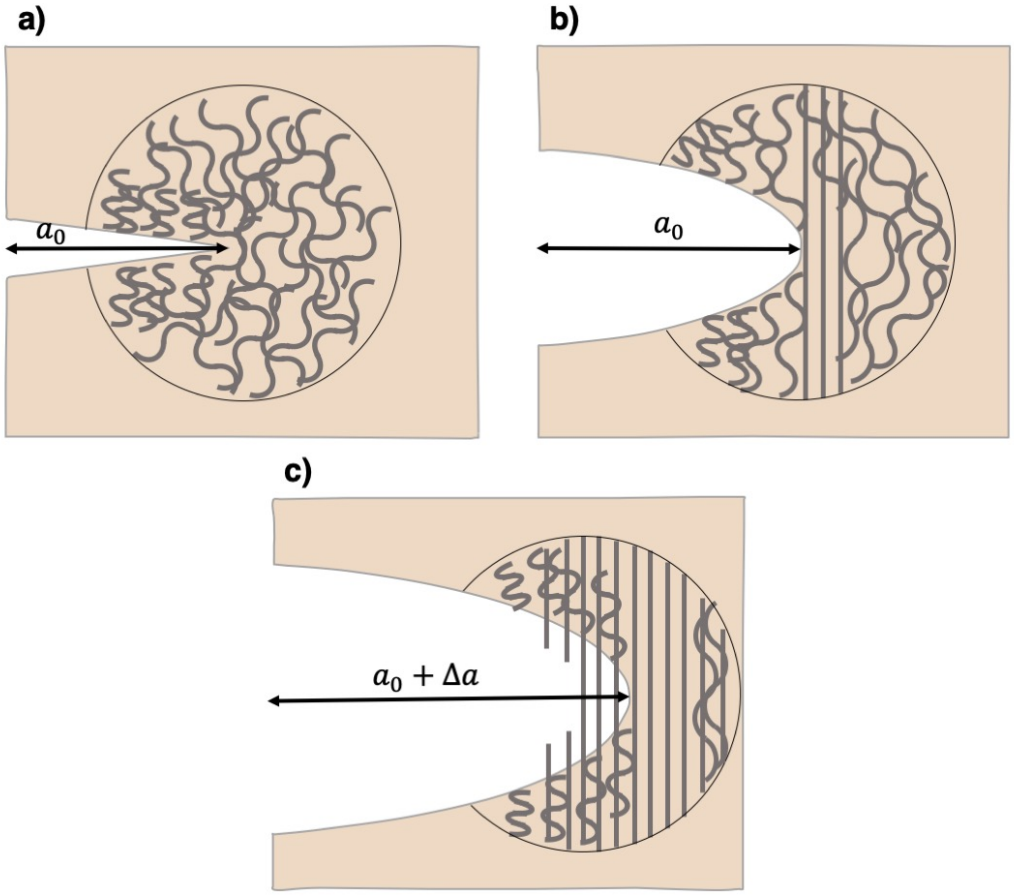

Figure 4.14. Schematic illustration of collagen reorganization during the deformation of a pre-notched sample of length a_0. a) In the initial configuration, collagen fibers are wavy and dispersed. Cut fibers near the notch recoil. b) During deformation, fibers gradually align in the direction of tension, causing the crack to blunt. Near the crack tip, fibers appear to be more highly stretched. c) When failure is initiated, straightened fibers bridge the crack until failure. Straight, aligned fibers ahead of the crack tip mitigate crack propagation by alleviating the concentration of stresses near the tip.

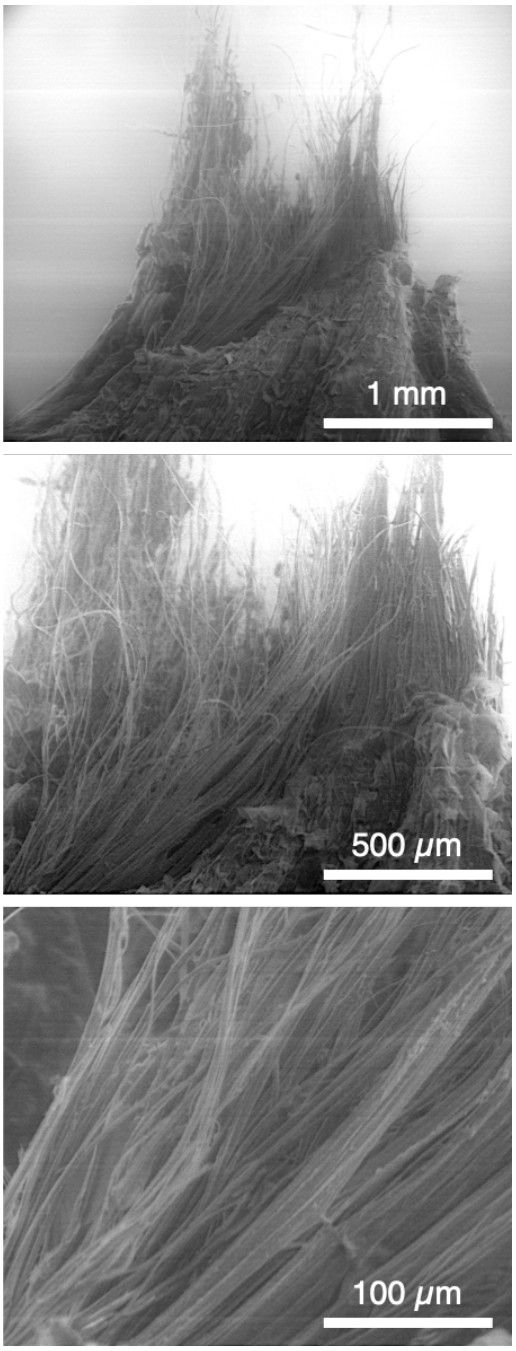

Figure 4.15. Post-failure microscopy of a pig skin sample tested in the environmental scanning electron microscope. Close-up visualization of the failed collagen fibers, for which internal damages caused a loss of cohesion, and some of the fibers that had realigned in the tensile direction have recoiled.

4.4. Conclusions

In the present work, the tear resistance of skin was studied using different approaches, with the aim to provide quantitative estimates that define limiting criteria for tissue failure, and to extend our understanding of the structural processes occurring in the porcine skin that participate to crack mitigation. The principal findings in this study are:

- The toughness was evaluated by conducting out-of-plane tear propagation (Mode III) and in-plane crack opening (Mode I). A value of $J_{Ic} \approx 30\ kJ/m^2$ was found in Mode I, with notable differences between the longitudinal orientation ($J_{Ic}^{long} \approx 26\ kJ/m^2$) and the transverse one ($J_{Ic}^{trans} \approx 34\ kJ/m^2$). For Mode III, $J_{IIIc} \approx 20\ kJ/m^2$ and does not show much dependence with orientation.
- During tensile deformation of a side edge notched sample, the strains initially localize around the tip of the notch. The region on the side of the crack reduces strain concentration by gradual recruitment of the collagen fibers.
- This effect is further exhibited by measuring the strain profiles during deformation, starting from the tip of the crack. Throughout the deformation, the strains gradually increase, but the profile maintains a fairly similar shape, meaning that the region ahead of the crack tip also contributes considerably to the deformation, and prevents the establishment of high strain gradients around the singularity.
- A Strain-based failure criterion is proposed for porcine skin, by reporting the maximum strain values at which fracture is initiated. Good consistency is obtained between the reported values of the strain in the tensile direction and an equivalent plastic strain, also indicating that the transverse orientation is tougher

than the longitudinal one. On average, strain values above ~0.27-0.3 are likely to cause tear propagation in the tissue.

- The strain values at the tip of propagating cracks agree closely with the average failure strains measured in smooth tensile porcine specimens reported earlier [17], which showed no significant dependence with applied strain rate.
- The contribution of the collagen network around the crack and ahead of the crack tip is characterized in more detail by *ex situ* TEM observations, showing that collagen fibers locally realign in the direction of principal tension. Post-failure, irreversible damages in the collagen fibers is clearly seen, with fibril delamination, loss of cohesion, and rugged, less regular structures. These processes contribute to mitigating the propagation of the crack.
- *In situ* environmental SEM provides real-time visualization of the gradual realignment of collagen fibers and provides additional insight into the processes that contribute to the exceptional tear resistance of skin, with crack bridging, progressive delamination, and eventually fracture of the fibers, which recoil after breakage.

The experimental methods presented in this study can serve as a basis to further establish failure criteria for skin, which, depending on the loading configuration, can find useful applications in domains such as tissue expansion, plastic surgery with reduction of scar zones, and other surgical methods. A relevant example would be the estimate of a critical tensile stretch around an incision of the skin that would not lead to the extension of the cut, in the context of invasive surgery. Results can also apply to the study of stretch marks in skin, which are a

consequence of extended stretching over long periods of times, where local delamination and fiber realignment are apparent, a behavior that is akin to crazing in polymers.

4.5. Acknowledgements

Chapter 4, in full, is currently being prepared for submission for publication of the material, and is authored by A. Pissarenko, W. Yang, H. Quan, B. Poyer, K.A. Brown, A. Williams, and M.A. Meyers. The dissertation author was the primary investigator and author of this paper.

We thank Andy Rayment and Dr. Ben Butler for the assistance they provided during sample preparation and mechanical testing. We thank Dr. Richard Langford, Jon J. Rickard, and Eric Tapley for helping with *in situ* microscopy, and Mason Mackey for valuable advice on TEM tissue preparation. Discussions with Prof. CT Lim and members of his group greatly helped improving the quality of the present work. We gratefully acknowledge the constructive comments and advice that stemmed from discussions with Prof. Cai.

CHAPTER 5. CONCLUSIONS AND FUTURE PERSPECTIVES

The topic of skin mechanics will undoubtedly continue to spark interest from the scientific community. First, the growth of cross-disciplinary research fields offers new perspectives and opportunities for the development of innovative solutions. As briefly discussed in this thesis, the implementation of standard methods from materials science and mechanical engineering can offer new insights to fields such as medicine and biology, for the development of engineered synthetic grafts, for example. Second, the continuous development of experimental methods and technologies extend the range of possibilities, with more tailored setups, higher resolution microscopy tools, and more computational power, which can help one gain a better understanding of the behavior of the material and its structure, with a higher level of accuracy.

The first Chapter of the present dissertation provides an extensive review of the state of the art on the materials science of skin, from experimental and structural characterization to constitutive modeling. The complex mechanical features of the skin, ranging from nonlinear elasticity, anisotropy, time-dependent and dissipative behavior, to region-specific behavior and sensitivity to external conditions, makes the development of methods enabling a complete characterization of the material quite challenging. Constitutive models that attempt to provide structurally-based explanations for some of these features encounter various difficulties, which stem from a compromise between model complexity and structural accuracy. Moreover, it appears that current knowledge on the structural arrangement of the constituents of skin is incomplete: in particular the arrangement of the collagen fibers, as well as the role of elastin, which is still being questioned.

From these observations, the research presented in the following chapters of this thesis provided an outlook of our contributions, aimed at addressing some of these limitations, and extending our understanding of skin mechanics.

5.1. Tensile Behavior of Skin

In our work on the experimental characterization of porcine dermis, we systematically implemented the use of uniaxial tensile testing (a simple, standard, *ex vivo* testing method) to study effects of time-dependent (through strain-rate sensitivity and stress relaxation tests) and cyclical loading processes on the tensile response of dermis. The use of freshly excised porcine skin provided a considerable advantage, reducing problems related with tissue preservation, despite the limited quantity of samples that could be tested and important variations depending on the tested location. Results show that the skin stiffens with an increase in applied strain rate, without significantly affecting the failure strain. The relaxation behavior is dependent of the loading state, and is quite consistent across samples, suggesting that the viscoelastic response is not related with an anisotropic component of the tissue. Loading/unloading curves show that the dissipated energy of the material depends on the loading stress state, and that with applied deformation, a new, irreversible equilibrium position is reached with the appearance of remnant strains, an effect which can be reduced with sample preconditioning. The use of digital image correlation proved to be a simple yet highly useful tool to reduce errors in measurement, and map local deformations. To our knowledge, the evolution of the linearized Poisson ratio of skin is reported for the first time, using this technique. Experimental results indicate that this evolution is dependent on sample orientation, and that it is also subject to irreversible changes (hysteresis in cyclic testing). Changes in volume during deformation were also quantified, showing a) a decrease in volume due to loss of water content for some samples b) a slight

increase in volume during tension, suggesting that some regions of the skin are auxetic, which was already suggested for elbow skin. It is not clear whether this effect also occurs *in vivo*, where the loading configuration of the tissue is different.

5.2. Tridimensional Aspect of the Collagen Network

Variations in the Poisson ratio, and the observed dissipative behavior of skin suggest that important structural changes occur during deformation, some of which are ultimately irreversible. Our structural analysis of the collagen network using transmission electron microscopy and scanning electron microscopy, before deformation and after tissue failure, reveal the important consequences of the mechanical processes taking place at the microstructural level: with fiber realignment, stretching, delamination, and ultimately failure. A comprehensive quantitative analysis of some structural features of collagen fibers was conducted, i.e. fiber dispersion, waviness, fiber and fibril diameter/thickness, and density. The obtained database was subsequently used for the implementation of a structurally based constitutive model.

An important observation from this microstructural characterization is the confirmation that collagen fibers in the dermis of pig skin form a complex tridimensional network. Three-dimensional imaging techniques, such as serial block face electron microscopy, could also extend our understanding of this aspect. Additionally, microscopy imaging shows the existence of sites where collagen fibers are somewhat entangled, in a braid-like fashion, a feature that potentially has notable consequences on the fiber-fiber interactions and on the dissipative behavior of skin, as our analogy with triple hair braids suggest. Micromechanical *in situ* testing techniques offer promising perspectives for real-time characterization of these effects on the mechanical response of the dermis.

5.3. Constitutive Modeling of the Collagen Network

Based on microstructural observations of the collagen network in the dermis, a structural model of entangled collagen fibers was proposed. The constitutive description includes effects of relative sliding between collagen fibrils, and resistance to straightening resulting from fiber entanglement. A coarse-grained model of the fibril bundle was developed in parallel to study in detail the effect of fiber deformation on interfibrillar interactions, and their relative displacements. While the model reproduces the tensile behavior of the skin with high accuracy, it has a limited ability to reflect fiber splay, which further highlights the need to precisely understand how the structural arrangement of collagen in the dermis has consequences on the mechanical behavior of skin. In particular, characterizing the effective length of fibers, their relative interactions, and the nature of their attachments can provide key answers in defining more structurally accurate multi-scale models.

Nonetheless, the proposed constitutive model is the first to explicitly address the effects of relative fibril sliding and fiber braiding, and further iterations could yield a more accurate description of the dissipative processes taking place during tissue deformation. Certainly, this requires that later improvements incorporate dissipative components in the interaction between the different constitutive elements of the model.

5.4. On the Toughness of the Skin

The experimental framework that was implemented for the tensile characterization of the skin was further extended to study the process of tear propagation in the tissue. Based on the knowledge that skin exhibits a remarkable ability to mitigate the propagation of tears, and thus delay catastrophic failure, our approach was to propose a quantitative analysis of the toughness of the skin, coupled with a microstructural analysis of collagen realignment in strategic regions

around the tip of a propagating crack. The toughness J_c of the skin was measured out-of-plane from trouser tests, and in-plane from opening tests. A significantly higher toughness is reported in-plane ($\sim 30\ kJ/m^2$), also with a higher sensitivity to sample orientation. This implies that previously reported values of skin toughness, mostly based on out-of-plane measurements ($\sim 6 - 20\ kJ/m^2$), underestimated the ability of the material to withstand in-plane deformations, where the alignment of collagen is more optimal. Digital image correlation was used with side edge notched samples to demonstrate that, despite the fact that strains mainly localize around the tip of the crack during deformation, the region ahead of the crack withstands an important part of the load and alleviates the concentration around the singularity, thus effectively delaying the onset of propagation. A strain-based criterion is introduced, with the purpose of providing an alternative way of estimating the likelihood of tissue failure, for a given state of local deformation. This can have important applications in fields such as reconstructive surgery.

The effect of fiber recruitment is further evidenced using *ex situ* transmission electron microscopy, and *in situ* environmental scanning electron microscopy. The notable contribution of the region ahead of the crack is clearly observed, with highly aligned and extended collagen fibers. The previously reported characteristics associated with tissue failure, i.e. delamination and fiber recoil, are confirmed.

Thus, it is clear that the collagen fiber network plays a fundamental role in the behavior of the skin, whether it is under purely tensile loading, or during tear propagation. Our contributions highlight this importance and provide new clues to unraveling our understanding of its complex structural arrangement. With a better understanding, not only more accurate predictions of the

behavior of skin can be obtained, but also synthetic materials that replicate this behavior more realistically can be developed.

APPENDIX A: EVIDENCE OF SKIN SWELLING IN THE THICKNESS DIRECTION DURING TENSION

The following series of images, presented in Figure A, demonstrate that the thickness of a skin sample (in this case Long. skin sample 2 presented in Fig. 2.7 of the manuscript) can increase considerably during tensile deformation, without showing any signs of twisting, realignment or curving.

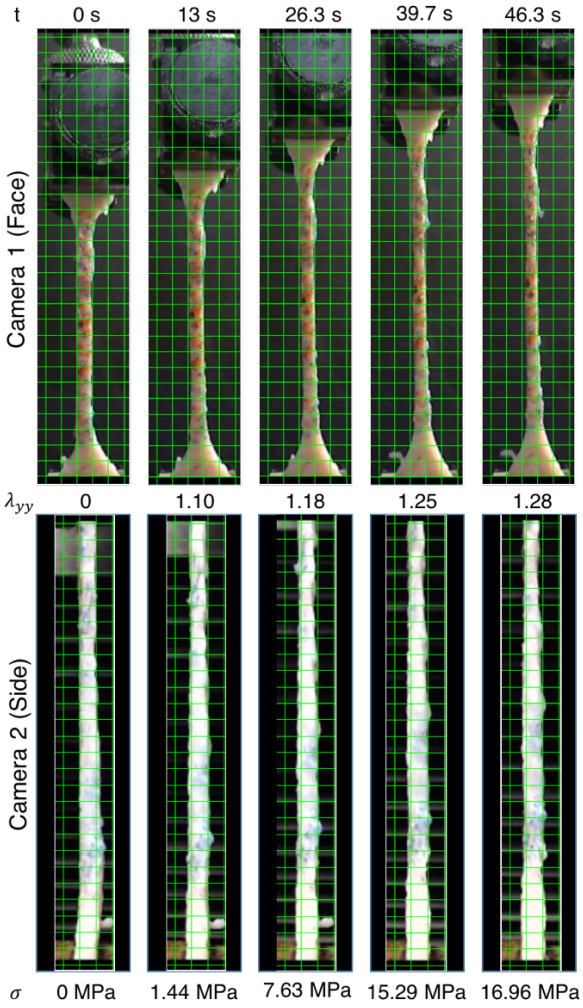

Figure A. Time series the deformation of a skin sample (Long. Sample 2 in the manuscript) captured by the two cameras synchronously. A grid is overlaid on the images to facilitate the observation of sample deformation. The tensile stretch and stress at each chosen increment of time is also indicated. The top row shows the outer surface (Camera 1) with a grid size of 6 mm, and the bottom row corresponds to the thickness plane (Camera 2), with a grid size of 2 mm. Camera 2 shows clearly that the average sample thickness increases over time.

APPENDIX B: TESTS WITH THERMOPLASTIC RUBBER (TPR)

In order to assess the accuracy of the method, three samples were extracted from a layered thermoplastic rubber sheet with a thickness of 1/8", which is comparable to the thickness of skin in some areas. Sheets were obtained from Roppe© (www.roppe.com). The same cutting die was used to maintain sample geometry (as described in Figure 2.1). The method detailed above was used to obtain the stress-stretch, Poisson ratios, and rate of volume change curves. Results are presented on Figure B. Strain maps on Fig. Ba-b, as well as the stress-stretch curves on Fig. Bc show that data obtained with TPR is generally very consistent, with slight variations at the onset of damage and shapes that are typical for hyperelastic rubbers. Changes in volume do not exceed 2% prior to damage, a variation that can be attributed to imprecisions in the experimental method, which at this level is acceptable. When damage is initiated, the volume increases (as the spacing between macromolecules is increased). Interestingly, significant variations are seen at low stresses for the Poisson ratios ν_{yx} and ν_{yz} (see Fig. Be-f), followed by a stable and consistent convergence towards ~0.33 in the lateral direction and ~0.67 in the thickness direction. Such oscillations can be attributed to the experimental and the strain averaging methods, for which local strain measurements directly depend on the reference configuration and the image resolution. A small deviation at low strains will have a higher impact on the calculation of the Poisson ratio than at large strains, where it represents a lower percentage of the calculated value.

Nonetheless, it can be noted that the calculated Poisson ratios always add up to 1 (within a 2% range), which contributes to the conservation of volume and respects the thermodynamic

limits for an incompressible material. Similar trends for the lateral Poisson ratio of soft polymers have been reported by Lee et al. [278].

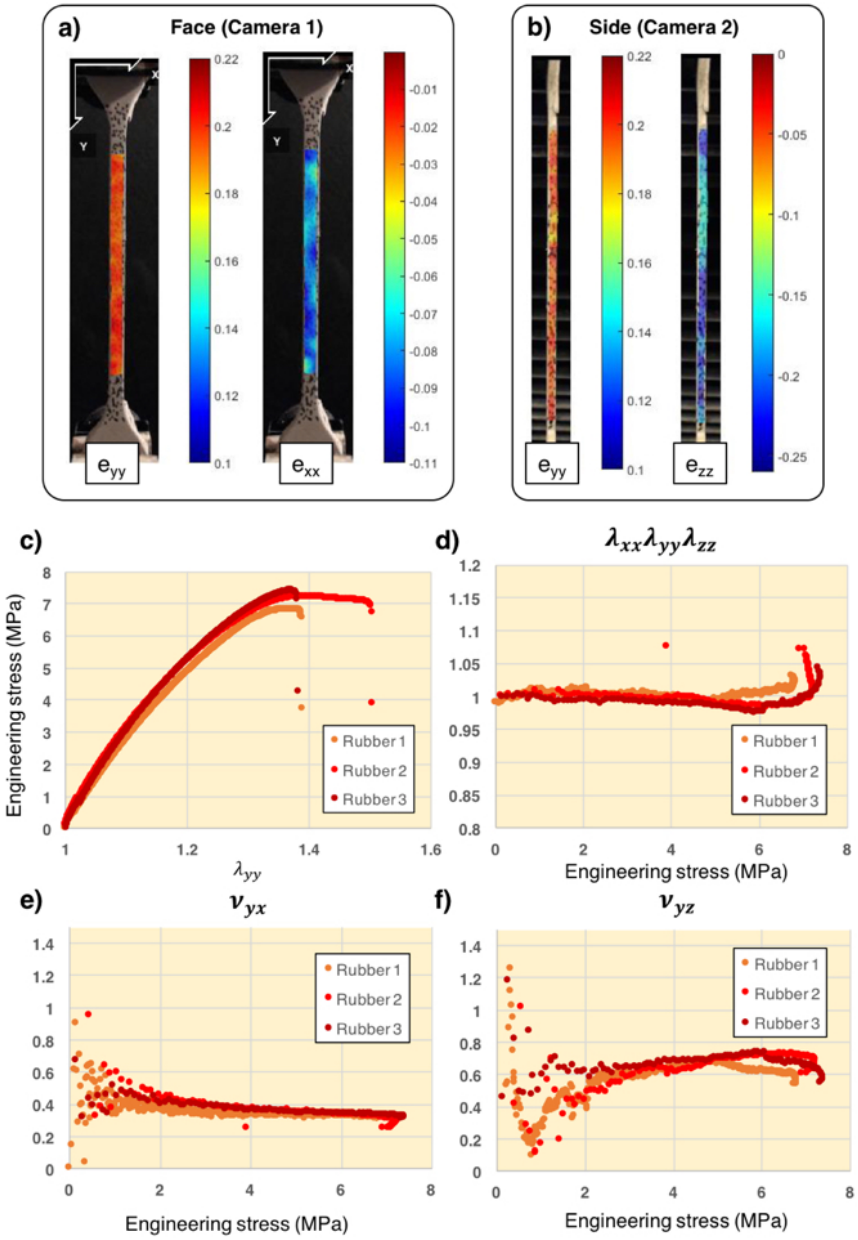

Figure B. DIC-based measurements from tests on thermoplastic rubber. (a-b) Euler-Almansi strain maps on the outer surface (a) and on the side (b) of the sample show a rather homogeneous distribution of the strains (e_{xx}, e_{yy}, e_{zz}), and results are consistent with the imposed deformation. (c) Engineering stress-stretch curves showing a typical rubber-like hyperelastic response, with very good repeatability. (d) The rate of volume change shows little variation and generally increases with higher stresses $(\sim 6\ MPa)$, at the onset of damage. (e-f) The evolution of the Poisson ratios ν_{yx} (e) and ν_{yz} (f) shows good repeatability, but large variations at low stresses.

APPENDIX C: EVOLUTION OF THE POISSON RATIO DURING LOADING/UNLOADING TESTS

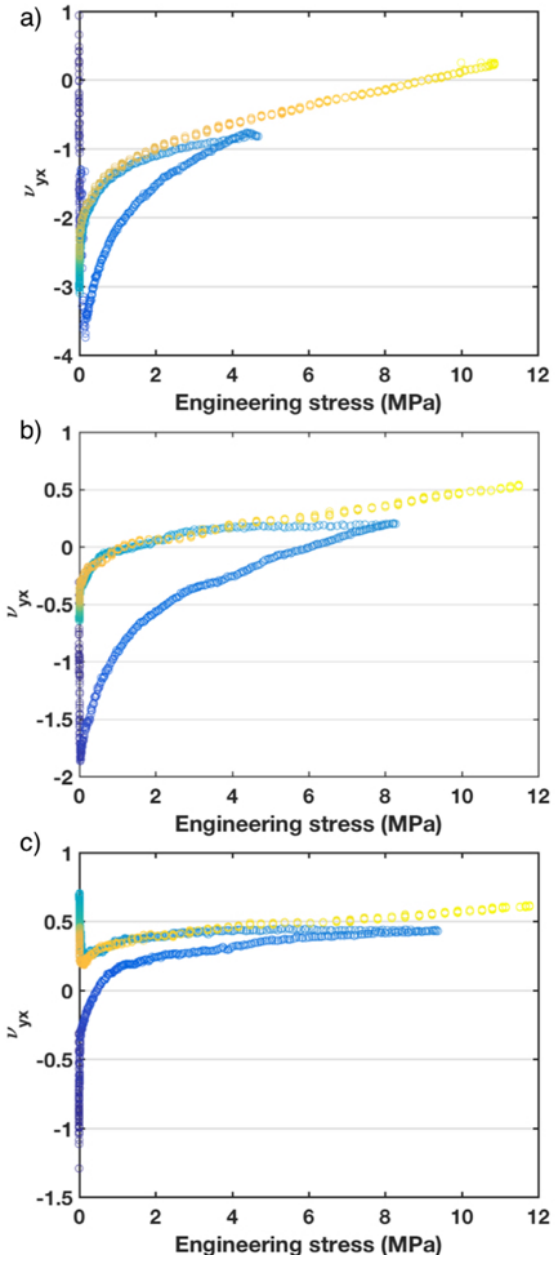

Figure C. Evolution of the Poisson ratio during loading/unloading tests of longitudinal pig skin samples for which the first loading round is interrupted at 4.68 MPa (a), 8.27 MPa (b), and 9.38 MPa (c). The color changes with loading history, starting from purple to yellow. Trends vary according to stress level, but also according to which region of the body the sample is taken from.

Results presented in Figure C show that, as in Fig. 2.9c of the manuscript, the unloading curve of the Poisson ratio does not follow the same curve as the loading one. Interestingly, depending the stress level and the sample type, unloading can also go back to negative values for the Poisson ratio, as it can be seen for Fig. Ca-b. The newly reached equilibrium value indicates dissipated viscoelastic energy and irreversible damages, and may explain some offset initial values for the reported data in this study. Nonetheless, the reloading curve always appears to follow closely the unloading one, in a trend similar to the Mullins effect that has been reported for the tangent modulus of skin [134].

APPENDIX D: INITIAL RELAXATION OF THE COARSE-GRAINED MODEL

Figure 3.10 shows that for a similar set of initial structural parameters, the response of the continuum description transitions from the unfolding phase to the purely tensile regime at a lower level of strain than for the coarse-grained model. Further analysis of the deformation sequence of the atomistic model shows that the initial equilibration of the structure slightly affects the geometry of the fiber, as Figure D shows. Thus, the actual initial opening angle of the semicircular fiber is in fact larger that the input value and was measured to be around 37˚. Adjustment of this value in the analytical model indeed shows a better match between both descriptions.

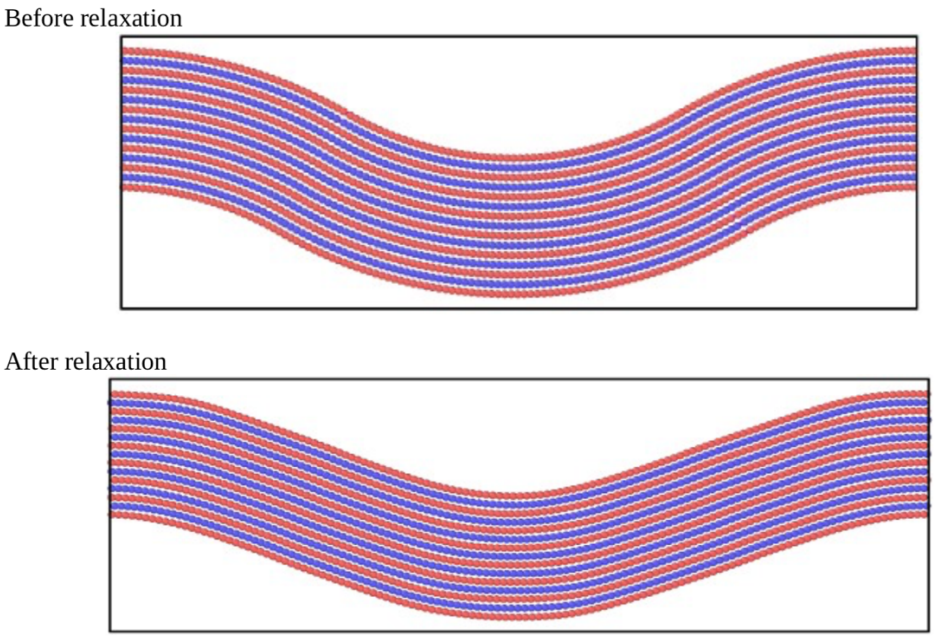

Figure D. Changes in fiber geometry following the initial equilibration of the structure, following 100000 integration steps. Before relaxation, the fiber follows the geometry imposed by the selected input parameters. After relaxation, the structure of the fiber is altered, in particular its curvature.

APPENDIX E: SUMMARY OF RESULTS FROM PARAMETER ESTIMATION

Table E provides a complete summary of the identified parameters obtained after running the parameter estimation algorithm in Matlab on 29 experimental curves. The values of the pre-set parameters and the guessing ranges are listed in Table 4.2 of the main text.

Table E. Summary of the constitutive parameters identified by parameter estimation, performed on 29 samples of porcine skin, (17 longitudinal, 12 transverse), tested at different strain rates (S.R.). 0˚ refers to the longitudinal orientation (Ori.), and 90˚corresponds to transverse samples. The coefficient of determination R-squared (R^2) and the adjusted R-squared ($R^2 - adj$) are also calculated.

Sample	E_f (MPa)	G_m (MPa)	k_c (kPa)	ω_n^0 (˚)	β_m (˚)	σ_c	S.R. (s^{-1})	Ori. (˚)	R^2	$R^2 - adj$
SL1	446.15	0.93	27.83	33.37	15.17	0.085	0.0001	0	0.99999957	0.99999957
SL2	409.45	0.89	12.66	31.61	16.34	0.089	0.001	0	0.99999974	0.99999974
SL3	519.38	2.71	31.51	35.87	16.86	0.071	0.001	0	0.99999992	0.99999992
SL4	207.6	1.66	3.39	44.33	18.53	0.065	0.001	0	0.99999496	0.99999495
SL5	593.96	0.00	29.56	28.86	14.73	0.194	0.01	0	0.99999965	0.99999965
SL6	557.71	0.78	15.82	38.15	22.66	0.032	0.01	0	0.99999925	0.99999925
SL7	440.59	0.89	5.16	31.96	20.82	0.089	0.01	0	0.99999967	0.99999967
SL8	343.9	1.16	1.71	37.66	23.24	0.059	0.01	0	0.99999875	0.99999875
SL9	722.42	0.88	15.92	31.65	30.60	0.108	0.01	0	0.99999959	0.99999959
SL10	335.46	1.26	2.42	33.68	14.78	0.111	0.01	0	0.99999978	0.99999978
SL11	218.36	1.73	11.94	37.48	21.43	0.050	0.01	0	0.99999763	0.99999762
SL12	421.24	3.68	7.36	50.00	31.42	0.125	0.01	0	0.99999691	0.99999682
SL13	253.58	1.15	10.71	37.58	22.94	0.113	0.01	0	0.99999977	0.99999977
SL14	387.89	2.12	22.89	37.80	20.12	0.048	0.1	0	0.9999994	0.99999939
SL15	491.12	0.79	1.73	32.78	17.40	0.054	0.5	0	0.99999817	0.99999798
SL16	499.35	1.01	3.28	37.69	18.25	0.094	0.5	0	0.99999816	0.99999799
SL17	299.09	0.70	35.29	43.07	22.88	0.039	0.5	0	0.99999683	0.9999965
ST1	247.88	2.65	5.70	50.00	33.94	0.098	0.001	90	0.99999777	0.99999776
ST2	294.94	1.77	0.00	49.95	30.07	0.879	0.001	90	0.9999618	0.99996152
ST3	337.72	2.23	26.64	50.00	36.14	0.105	0.01	90	0.99999838	0.99999834

ST4	193	2.91	152.79	30.49	42.78	0.119	0.01	90	0.99999617	0.9999961
ST5	696.9	0.59	41.04	31.63	18.01	0.057	0.1	90	0.99999966	0.99999965
ST6	552.47	6.42	142.20	50.00	32.74	0.213	0.1	90	0.99999788	0.99999782
ST7	456.4	0.00	41.15	33.13	30.71	0.955	0.1	90	0.99997806	0.99996892
ST8	390.51	1.32	26.31	36.95	36.38	0.090	0.1	90	0.99999848	0.999998
ST9	404.08	1.16	15.13	37.57	15.46	0.027	0.5	90	0.99996432	0.99995908
ST10	736.05	4.13	112.62	33.57	20.04	0.108	0.5	90	0.9999937	0.99999268
ST11	444.32	0.96	0.01	29.62	15.31	0.167	0.5	90	0.99997527	0.99997115
ST12	465.66	0.10	0.13	41.69	43.45	0.111	0.5	90	0.99999598	0.99999375

APPENDIX F: SENSITIVITY ANALYSIS

In order to evaluate how the parameters of the constitutive model influence the model output, a sensitivity analysis was performed in the Parameter Estimation environment with a randomly generated parameter set of 1000 samples and compared to a representative experimental curve. The analysis calculates the value of the cost function for each sample and plots it for each associated parameter value, as shown in the scatter plots Figure F1. The results can be a useful resource to assist the parameter estimation algorithm in finding the optimal values faster, and also inform on the parameters that should be identified in priority, so that the efficiency of the optimization is improved. The bars of the "tornado" plot in Figure F2 indicate the strength and direction of the different correlation coefficients (Linear, Spearman rho, Kendall, and partial correlations) with respect to the evaluated cost function. By most measures, the influence of the constitutive parameters ranks as follows: $E_f > \sigma_c > \omega_n^0 > \beta_m > r_n^0 > k_c > G_m > H > \mu_m$.

In their sensitivity analysis of a Volokh damage model coupled with the Gasser-Ogden-Holzapfel elasticity model, Li and Luo [195] point out that it is preferable, if possible, to initially pre-set the value of the parameters with a high sensitivity. In their case, without considering the damage-related parameters, fiber alignment and dispersion are the parameters with the highest influence on the model output. Their interpretation suggests that predetermining these values in priority would assist the parameter estimation, in spite of the fact that this information is generally difficult to access directly on the tested sample.

The analogous parameters β_m and σ_c in the model proposed in this work also display a high level of priority in the sensitivity analysis, and observations from the correlation analysis

(reported in Table 4 of the main text) already suggested that these constants should be identified in priority. This would also add the benefit of eliminating effects of parameter cross-correlation, between β_m and ω_n^0 for example. The case of the fibril Young's modulus E_f is somewhat different: since it is the most important parameter driving the deformation in the linear regime, its critical influence is easily explained. Its determination from the experimental curve is trivially achieved in the optimization algorithm, when a reasonable initial range is provided.

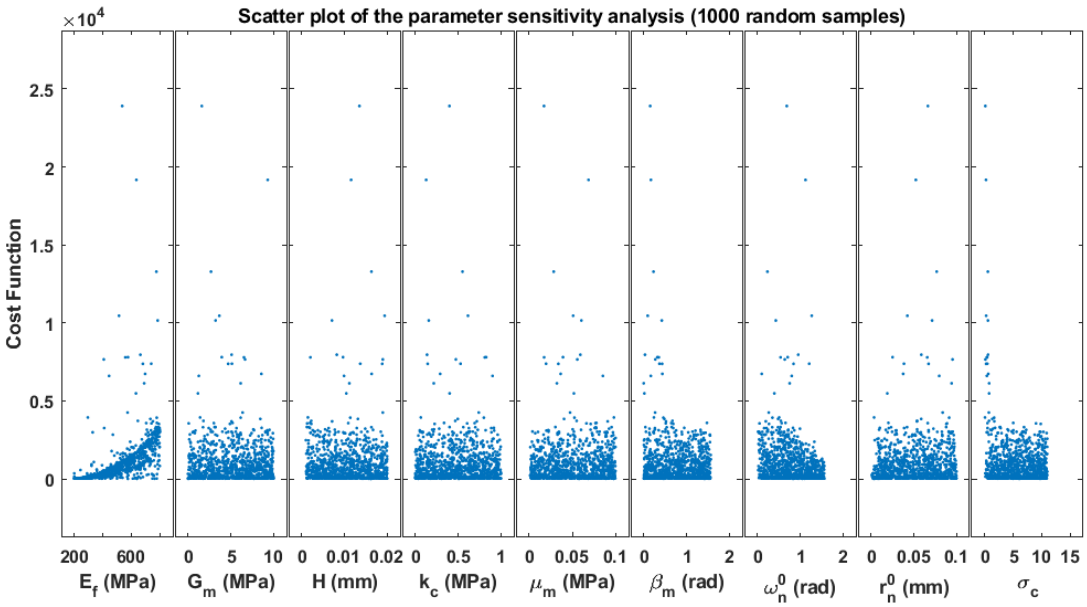

Figure F1. Scatter plot from the parameter sensitivity analysis of the constitutive model, based on 1000 randomly generated samples of parameter values. For each computed sample, the value of the cost function is plotted against each parameter. Trends show the influence of the parameter on the model output.

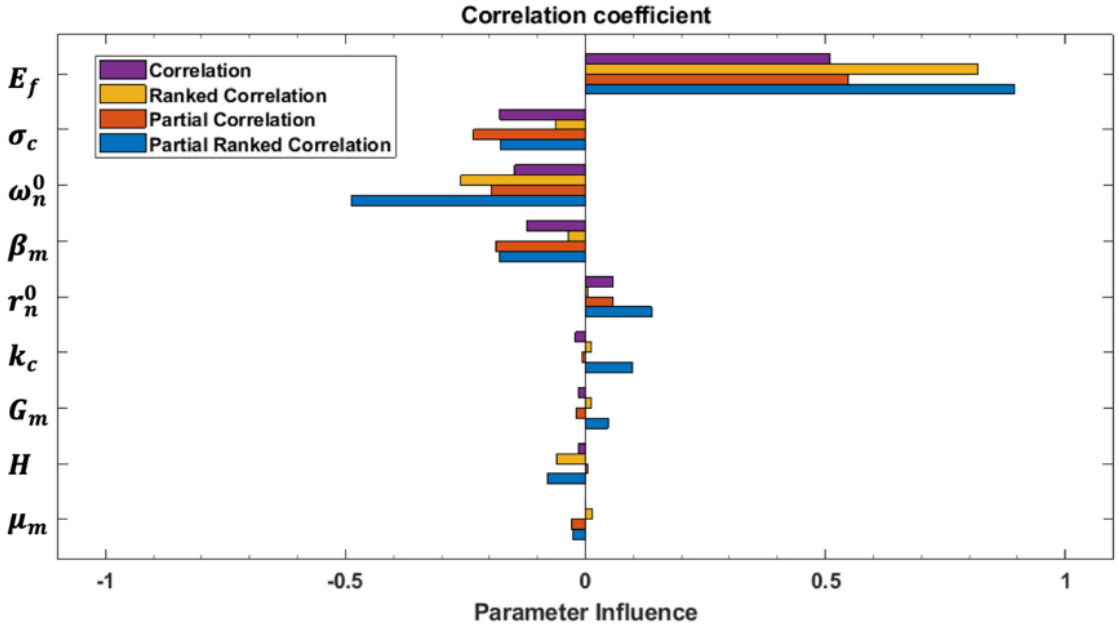

Figure F2. Tornado plot showing the influence of some constitutive parameters on the model output. Each bar indicates the strength and the direction of this effect, based on different correlation coefficients, i.e. Pearson (purple bars), ranked-Spearman (yellow bars), partial Pearson (red bars), and partial ranked-Spearman (blue bars) correlations. Parameters are thus ranked by order of influence on the model.

REFERENCES

[1] G.J. Tortora, B. Derrickson, Principles of Anatomy and Physiology, John Wiley and Sons, Inc., 2009.

[2] J.T. Whitton, J.D. Everall, The thickness of the epidermis, Br. J. Dermatol. 89 (1973) 467–476. doi:10.1111/j.1365-2133.1973.tb03007.x.

[3] M. Huzaira, F. Rius, M. Rajadhyaksha, R.R. Anderson, S. González, Topographic variations in normal skin, as viewed by in vivo reflectance confocal microscopy, J. Invest. Dermatol. 116 (2001) 846–852. doi:10.1046/j.0022-202X.2001.01337.x.

[4] J. Sandby-Møller, T. Poulsen, H.C. Wulf, Epidermal Thickness at Different Body Sites: Relationship to Age, Gender, Pigmentation, Blood Content, Skin Type and Smoking Habits, Acta Derm. Venereol. 83 (2003) 410–413. doi:10.1080/00015550310015419.

[5] F.M. Hendriks, D. Brokken, C.W.J. Oomens, D.L. Bader, F.P.T. Baaijens, The relative contributions of different skin layers to the mechanical behavior of human skin in vivo using suction experiments, 28 (2006) 259–266. doi:10.1016/j.medengphy.2005.07.001.

[6] M.F. Leyva-Mendivil, A. Page, N.W. Bressloff, G. Limbert, A mechanistic insight into the mechanical role of the stratum corneum during stretching and compression of the skin, J. Mech. Behav. Biomed. Mater. 49 (2015) 197–219. doi:10.1016/j.jmbbm.2015.05.010.

[7] J.W.Y. Jor, M.D. Parker, A.J. Taberner, M.P. Nash, P.M.F. Nielsen, Computational and experimental characterization of skin mechanics: Identifying current challenges and future directions, Wiley Interdiscip. Rev. Syst. Biol. Med. 5 (2013) 539–556. doi:10.1002/wsbm.1228.

[8] G.L. Wilkes, I.A. Brown, R.H. Wildnauer, The biomechanical properties of skin., CRC Crit. Rev. Bioeng. 1 (1973) 453–95. http://www.ncbi.nlm.nih.gov/pubmed/4581809.

[9] G. Limbert, Mathematical and computational modelling of skin biophysics: a review, Proc. R. Soc. A Math. Phys. Eng. Sci. 473 (2017) 20170257. doi:10.1098/rspa.2017.0257.

[10] V.R. Sherman, W. Yang, M.A. Meyers, The materials science of collagen, J. Mech. Behav. Biomed. Mater. 52 (2015) 22–50. doi:10.1016/j.jmbbm.2015.05.023.

[11] B.J. Butler, R.L. Boddy, C. Bo, H. Arora, A. Williams, W.G. Proud, K.A. Brown, Composite nature of fresh skin revealed during compression, Bioinspired, Biomim. Nanobiomaterials. 4 (2015) 133–139. doi:10.1680/bbn.14.00028.

[12] V.R. Sherman, Y. Tang, S. Zhao, W. Yang, M.A. Meyers, Structural characterization and viscoelastic constitutive modeling of skin, Acta Biomater. (2017). doi:10.1016/j.actbio.2017.02.011.

[13] J.W.Y. Jor, P.M.F. Nielsen, M.P. Nash, P.J. Hunter, Modelling collagen fibre orientation in porcine skin based upon confocal laser scanning microscopy, Ski. Res. Technol. (2011) 149–159. doi:10.1111/j.1600-0846.2010.00471.x.

[14] M. Zhou, N. Zhang, X. Liu, Tendon allograft sterilized by peracetic acid / ethanol combined with gamma irradiation, (2014). doi:10.1007/s00776-014-0556-9.

[15] G. Parent, N. Huppé, E. Langelier, Low stress tendon fatigue is a relatively rapid process in the context of overuse injuries, Ann. Biomed. Eng. 39 (2011) 1535–1545. doi:10.1007/s10439-011-0254-0.

[16] E.C. Schmidt, M. Chin, J.T. Aoyama, T.J. Ganley, K.G. Shea, M.W. Hast, Mechanical and Microstructural Properties of Pediatric Anterior Cruciate Ligaments and Autograft Tendons Used for Reconstruction, (2019) 1–12. doi:10.1177/2325967118821667.

[17] A. Pissarenko, W. Yang, H. Quan, K.A. Brown, A. Williams, W.G. Proud, M.A. Meyers, Tensile behavior and structural characterization of pig dermis, Acta Biomater. (2019). doi:10.1016/j.actbio.2019.01.023.

[18] N.J. Vardaxis, T.A. Brans, M.E. Boon, R.W. Kreis, L.M. Marres, Confocal laser scanning microscopy of porcine skin: implications for human wound healing studies, J. Anat. 190 (1997) 601–611. doi:10.1046/j.1469-7580.1997.19040601.x.

[19] J. Pittet, O. Freis, G. Périé, G. Pauly, Evaluation of Elastin/Collagen Content in Human Dermis in-Vivo by Multiphoton Tomography—Variation with Depth and Correlation with Aging, (2014) 211–221. doi:10.3390/cosmetics1030211.

[20] J.L. Powell, The Kerr Incision: John Martin Munro Kerr, J. Pelvic Surg. 7 (2001) 177–178.

[21] M.A. Meyers, P.-Y. Chen, Biological Materials Science, Cambridge University Press, 2014.

[22] K. Langer, On the anatomy and physiology of the skin, Br. J. Plast. Surg. 31 (1978) 3–8. doi:10.1016/0007-1226(78)90003-6.

[23] H.T. Cox, The cleavage lines of the skin, Br. J. Surg. 29 (1941) 234–240. doi:10.1002/bjs.18002911408.

[24] M. Kwak, D. Son, J. Kim, K. Han, Static Langer's line and wound contraction rates according to anatomical regions in a porcine model, Wound Repair Regen. 22 (2014) 678–682. doi:10.1111/wrr.12206.

[25] S.F. Swaim, R.A. Henderson, D. Fowler, Small Animal Wound Management, (2nd ed), Vet. Surg. 27 (2008) 158–158. doi:10.1111/j.1532-950x.1998.tb00113.x.

[26] V.W. Wong, K. Levi, S. Akaishi, G. Schultz, R.H. Dauskardt, Scar Zones, Plast. Reconstr. Surg. 129 (2012) 1272–1276. doi:10.1097/PRS.0b013e31824eca79.

[27] M. Topaz, N. Carmel, A. Silberman, The TopClosure ® 3S System , for skin stretching and a secure wound closure, (2012) 533–543. doi:10.1007/s00238-011-0671-1.

[28] G.C. Gurtner, R.H. Dauskardt, V.W. Wong, K.A. Bhatt, K. Wu, I.N. Vial, K. Padois, J.M. Korman, M.T. Longaker, Improving Cutaneous Scar Formation by Controlling the Mechanical Environment, Ann. Surg. 254 (2011) 217–225. doi:10.1097/SLA.0b013e318220b159.

[29] G.C. Gurtner, R.H. Dauskardt, M.T. Longaker, P. Yock, Skin treatment devices and methods with pre-stressed configurations, 2016. https://www.google.ch/patents/US20160213522.

[30] R.A. Kamel, J.F. Ong, E. Eriksson, J.P.E. Junker, E.J. Caterson, Tissue engineering of skin, J. Am. Coll. Surg. 217 (2013) 533–555. doi:10.1016/j.jamcollsurg.2013.03.027.

[31] S. MacNeil, Progress and opportunities for tissue-engineered skin, Nature. 445 (2007) 874–880. doi:10.1038/nature05664.

[32] D.M. Supp, S.T. Boyce, Engineered skin substitutes: Practices and potentials, Clin. Dermatol. 23 (2005) 403–412. doi:10.1016/j.clindermatol.2004.07.023.

[33] N. Cubo, M. Garcia, J.F. Cañizo, D. Velasco, J.L. Jorcano, J.F. del Cañizo, D. Velasco, J.L. Jorcano, 3D bioprinting of functional human skin: production and in vivo analysis, Biofabrication. 9 (2016) 15006. doi:10.1088/1758-5090/9/1/015006.

[34] G. Schwartz, B.C.K. Tee, J. Mei, A.L. Appleton, D.H. Kim, H. Wang, Z. Bao, Flexible polymer transistors with high pressure sensitivity for application in electronic skin and health monitoring, Nat. Commun. 4 (2013) 1858–1859. doi:10.1038/ncomms2832.

[35] X. Wang, Y. Gu, Z. Xiong, Z. Cui, T. Zhang, Silk-molded flexible, ultrasensitive, and highly stable electronic skin for monitoring human physiological signals, Adv. Mater. 26 (2014) 1336–1342. doi:10.1002/adma.201304248.

[36] L. Rodrigues, EEMCO Guidance to the in vivo Assessment of Tensile Functional Properties of the Skin, Skin Pharmacol. Physiol. 14 (2001) 52–67. doi:10.1159/000056334.

[37] Y.C. Fung, Biomechanics: Its Foundations and Objectives, 2nd ed, Prentice Hall Inc., 1972.

[38] R.B. Groves, S.A. Coulman, J.C. Birchall, S.L. Evans, An anisotropic, hyperelastic model for skin: Experimental measurements, finite element modelling and identification of parameters for human and murine skin, J. Mech. Behav. Biomed. Mater. 18 (2013) 167–180. doi:10.1016/j.jmbbm.2012.10.021.

[39] H.G. Vogel, W. Hilgner, The “step phenomenon” as observed in animal skin, J. Biomech. 12 (1979) 75–81. doi:10.1016/0021-9290(79)90011-3.

[40] R.C. Haut, The effects of orientation and location on the strength of dorsal rat skin in high and low speed tensile failure experiments, J. Biomech. Eng. 111 (1989) 136–140. doi:10.1115/1.3168354.

[41] W. Yang, V.R. Sherman, B. Gludovatz, E. Schaible, P. Stewart, R.O. Ritchie, M.A.

Meyers, On the tear resistance of skin., Nat. Commun. 6 (2015) 6649. doi:10.1038/ncomms7649.

[42] Y. Lanir, Y.C. Fung, Two-dimensional mechanical properties of rabbit skin—II. Experimental results, J. Biomech. 7 (1974) 171–182. doi:10.1016/0021-9290(74)90058-X.

[43] J. Lim, J. Hong, W.W. Chen, T. Weerasooriya, Mechanical response of pig skin under dynamic tensile loading, Int. J. Impact Eng. 38 (2011) 130–135. doi:10.1016/j.ijimpeng.2010.09.003.

[44] G. Uzer, A. Ho, R.A.F. Clark, F. Chiang, Mechanical Properties of Pig Skin, in: Proc. SEM Annu. Conf., 2009.

[45] O.A. Shergold, N.A. Fleck, D. Radford, The uniaxial stress versus strain response of pig skin and silicone rubber at low and high strain rates, Int. J. Impact Eng. 32 (2006) 1384–1402. doi:10.1016/j.ijimpeng.2004.11.010.

[46] K.H. Lim, C.M. Chew, P.C.Y. Chen, S. Jeyapalina, H.N. Ho, J.K. Rappel, B.H. Lim, New extensometer to measure in vivo uniaxial mechanical properties of human skin, J. Biomech. 41 (2008) 931–936. doi:10.1016/j.jbiomech.2008.01.004.

[47] J. Ankersen, a E. Birkbeck, R.D. Thomson, P. Vanezis, Puncture resistance and tensile strength of skin simulants., Proc. Inst. Mech. Eng. H. 213 (1999) 493–501. doi:10.1243/0954411991535103.

[48] B. Zhou, F. Xu, C. Chen, T. Lu, Strain rate sensitivity of skin tissue under thermomechanical loading., Philos. Trans. R. Soc. A Math. Phys. Eng. Sci. 368 (2010) 679–690. doi:10.1098/rsta.2009.0238.

[49] S.D. Łagan, A. Liber-Kneć, Experimental testing and constitutive modeling of the mechanical properties of the swine skin tissue, Acta Bioeng. Biomech. Orig. Pap. 19 (2017). doi:10.5277/ABB-00755-2016-02.

[50] A.S. Caro-bretelle, P.N. Gountsop, P. Ienny, R. Leger, S. Corn, I. Bazin, F. Bretelle, Effect of sample preservation on stress softening and permanent set of porcine skin, J. Biomech. 48 (2015) 3135–3141. doi:10.1016/j.jbiomech.2015.07.014.

[51] A.E. Ehret, M. Hollenstein, E. Mazza, M. Itskov, Porcine dermis in uniaxial cyclic loading: Sample preparation, experimental results and modeling, J. Mech. Mater. Struct. 6 (2011) 1125–1135. doi:10.2140/jomms.2011.6.1125.

[52] R.J. Lapeer, P.D. Gasson, V. Karri, Simulating plastic surgery: From human skin tensile tests, through hyperelastic finite element models to real-time haptics, Prog. Biophys. Mol. Biol. 103 (2010) 208–216. doi:10.1016/j.pbiomolbio.2010.09.013.

[53] C. Pailler-Mattei, S. Bec, H. Zahouani, In vivo measurements of the elastic mechanical properties of human skin by indentation tests, Med. Eng. Phys. 30 (2008) 599–606. doi:10.1016/j.medengphy.2007.06.011.

[54] P.G. Agache, C. Monneur, J.L. Leveque, J. de Rigal, Mechanical properties and Young's modulus of human skin in vivo., Arch. Dermatol. Res. 269 (1980) 221–232. doi:10.1007/BF00406415.

[55] A. Ni Annaidh, K. Bruyere, M. Destrade, M.D. Gilchrist, M. Ottenio, Characterization of the anisotropic mechanical properties of excised human skin, J. Mech. Behav. Biomed. Mater. 5 (2012) 139–148. doi:10.1016/j.jmbbm.2011.08.016.

[56] D.P. Pioletti, L.R. Rakotomanana, J.F. Benvenuti, P.F. Leyvraz, Viscoelastic constitutive law in large deformations: Application to human knee ligaments and tendons, J. Biomech. 31 (1998) 753–757. doi:10.1016/S0021-9290(98)00077-3.

[57] A.J. Gallagher, A. Ni Anniadh, K. Kruyere, M. Ottenio, H. Xie, M.D. Gilchrist, Dynamic tensile properties of human skin, 2012 IRCOBI Conf. (2012) 494–502. doi:Irc-12-59.

[58] B. Finlay, Dynamic mechanical testing of human skin "in vivo," J. Biomech. 3 (1970). doi:10.1016/0021-9290(70)90040-0.

[59] Y.A. Kvistedal, P.M.F. Nielsen, Estimating material parameters of human skin in vivo, Biomech. Model. Mechanobiol. 8 (2009) 1–8. doi:10.1007/s10237-007-0112-z.

[60] R. Meijer, L.F.A. Douven, C.W.J. Oomens, Characterisation of Anisotropic and Non-linear Behaviour of Human Skin In Vivo, 5842 (2017). doi:10.1080/10255849908907975.

[61] J.L. Leveque, J. de Rigal, P.G. Agache, C. Monneur, Influence of ageing on the in vivo extensibility of human skin at a low stress, Arch. Dermatol. Res. 269 (1980) 127–135. doi:10.1007/BF00406532.

[62] T.K. Tonge, L.S. Atlan, L.M. Voo, T.D. Nguyen, Full-field bulge test for planar anisotropic tissues: Part I-Experimental methods applied to human skin tissue, Acta Biomater. 9 (2013) 5913–5925. doi:10.1016/j.actbio.2012.11.035.

[63] R.O. Potts, D.A. Chrisman, E.M. Buras, The dynamic mechanical properties of human skin in vivo, J. Biomech. 16 (1983) 365–372. doi:10.1016/0021-9290(83)90070-2.

[64] G. Boyer, L. Laquièze, A. Le Bot, S. Laquièze, H. Zahouani, Dynamic indentation on human skin in vivo: Ageing effects, Ski. Res. Technol. 15 (2009) 55–67. doi:10.1111/j.1600-0846.2008.00324.x.

[65] R. Reihsner, B. Balogh, E.J. Menzel, Two-dimensional elastic properties of human skin in terms of an incremental model at the in vivo configuration, Med. Eng. Phys. 17 (1995) 304–313. doi:10.1016/1350-4533(95)90856-7.

[66] C. Flynn, A. Taberner, P. Nielsen, Measurement of the force-displacement response of in vivo human skin under a rich set of deformations, Med. Eng. Phys. 33 (2011) 610–619. doi:10.1016/j.medengphy.2010.12.017.

[67] C. Flynn, A. Taberner, P. Nielsen, Mechanical characterisation of in vivo human skin using a 3D force-sensitive micro-robot and finite element analysis, Biomech. Model. Mechanobiol. 10 (2011) 27–38. doi:10.1007/s10237-010-0216-8.

[68] I.A. Brown, A scanning electron microscope study of the effects of uniaxial tension on human skin, Br. J. Dermatol. 89 (1973) 383–393. doi:10.1111/j.1365-2133.1973.tb02993.x.

[69] C. Edwards, R. Marks, Evaluation of biomechanical properties of human skin, Clin. Dermatol. 13 (1995) 375–380. doi:10.1016/0738-081X(95)00078-T.

[70] A. Ni Annaidh, Karine Bruyere, M. Destrade, M.D. Gilchrist, C. Maurini, M. Ottenio, G. Saccomandi, Automated estimation of collagen fibre dispersion in the dermis and its contribution to the anisotropic behaviour of skin, Ann. Biomed. Eng. 40 (2012) 1666–1678. doi:10.1007/s10439-012-0542-3.

[71] A. Delalleau, G. Josse, J.-M. Lagarde, H. Zahouani, J.-M. Bergheau, Characterization of the mechanical properties of skin by inverse analysis combined with the indentation test, J. Biomech. 39 (2006) 1603–1610. doi:10.1016/j.jbiomech.2005.05.001.

[72] L.-C. Gerhardt, J. Schmidt, J.A. Sanz-Herrera, F.P.T. Baaijens, T. Ansari, G.W.M. Peters, C.W.. Oomens, A novel method for visualising and quantifying through-plane skin layer deformations, 2012. doi:10.1016/j.jmbbm.2012.05.014.

[73] C. Flynn, A.J. Taberner, P.M.F. Nielsen, S. Fels, Simulating the three-dimensional deformation of in vivo facial skin, J. Mech. Behav. Biomed. Mater. 28 (2013) 484–494. doi:10.1016/j.jmbbm.2013.03.004.

[74] J.M. Pereira, J.M. Mansour, B.R. Davis, The effects of layer properties on shear disturbance propagation in skin., J. Biomech. Eng. 113 (1991) 30–5. doi:10.1115/1.2894082.

[75] L.H. Jansen, P.B. Rottier, Some mechanical properties of human abdominal skin measured on excised strips: a study of their dependence on age and how they are influenced by the presence of striae., Dermatologica. 117 (1958) 65–83. http://www.ncbi.nlm.nih.gov/pubmed/13561736.

[76] H.L. Stark, Directional variations in the extensibility of human skin, Br. J. Plast. Surg. 30 (1977) 105–114. doi:10.1016/0007-1226(77)90001-7.

[77] H. Vogel, Age dependence of mechanical and biochemical properties of human skin, Bioeng. Ski. 3 (1987) 67–91.

[78] S. Diridollou, M. Berson, V. Vabre, D. Black, B. Karlsson, F. Auriol, J.M. Gregoire, C. Yvon, L. Vaillant, Y. Gall, F. Patat, An in vivo method for measuring the mechanical properties of the skin using ultrasound., Ultrasound Med. Biol. 24 (1998) 215–224. doi:10.1016/S0301-5629(97)00237-8.

[79] F.M. Hendriks, D. Brokken, J.T.W.M. van Eemeren, C.W.J. Oomens, F.P.T. Baaijens, J.B. a M. Horsten, A numerical-experimental method to characterize the non-linear mechanical behaviour of human skin., Ski. Res. Technol. 9 (2003) 274–283. doi:10.1034/j.1600-0846.2003.00019.x.

[80] F. Khatyr, C. Imberdis, P. Vescovo, D. Varchon, J.-M. Lagarde, Model of the viscoelastic behaviour of skin in vivo and study of anisotropy, Ski. Res. Technol. 10

(2004) 96–103. doi:10.1111/j.1600-0846.2004.00057.x.

[81] C. Jacquemoud, K. Bruyere-Garnier, M. Coret, Methodology to determine failure characteristics of planar soft tissues using a dynamic tensile test, J. Biomech. 40 (2007) 468–475. doi:10.1016/j.jbiomech.2005.12.010.

[82] J. Jachowicz, R. McMullen, D. Prettypaul, Indentometric analysis of in vivo skin and comparison with artificial skin models, Ski. Res. Technol. 13 (2007) 299–309. doi:10.1111/j.1600-0846.2007.00229.x.

[83] M. Ventre, M. Padovani, A.D. Covington, P.A. Netti, Composition, Structure and Physical Properties of Foetal Calf Skin, in: Proc. IULTCS-EUROCONGRESO, Istanbul, 2006: pp. 1–21.

[84] R.E. Shadwick, A.P. Russell, R.F. Lauff, The structure and mechanical design of rhinoceros dermal armour, Philos. Trans. R. Soc. London. Ser. B Biol. Sci. 337 (1992) 419–428. doi:10.1098/rstb.1992.0118.

[85] W.A. Sodeman, G.E. Burch, A direct method for the estimation of skin distensibility with its application to the study of vascular states, J. Clin. Invest. 17 (1938) 785–793. doi:10.1172/JCI101009.

[86] J.H. Evans, W.W. Siesennop, Controlled quasi-static testing of human skin in vivo, in: 7th Int. Conf. Med. Biol. Eng., 1967.

[87] R.W. Snyder, L.H.N. Lee, Experimental study of biological tissue subjected to pure shear, J. Biomech. 8 (1975) 415–419. doi:10.1016/0021-9290(75)90077-9.

[88] L. Coutts, J. Bamber, N. Miller, Multi-directional in vivo tensile skin stiffness measurement for the design of a reproducible tensile strain elastography protocol, Ski. Res. Technol. 19 (2013) 37–44. doi:10.1111/j.1600-0846.2011.00604.x.

[89] C. Escoffier, J. de Rigal, A. Rochefort, R. Vasselet, J.-L. Leveque, P.G. Agache, Age-Related Mechanical Properties of Human Skin: An In Vivo Study., J. Invest. Dermatol. 93 (1989) 353–357. doi:10.1111/1523-1747.ep12280259.

[90] R. Sanders, Torsional elasticity of human skin in vivo, Pflugers Arch. Eur. J. Physiol. 342 (1973) 255–260. doi:10.1007/BF00591373.

[91] B. Finlay, The torsional characteristics of human skin in vivo, Biomed. Eng. (NY). 6 (1971) 567–73. http://www.ncbi.nlm.nih.gov/pubmed/5158520.

[92] D.C. Vlasblom, Skin Elasticity, University of Utrecht, Netherlands, 1967.

[93] P. Neto, M. Ferreira, F. Bahia, P. Costa, Improvement of the methods for skin mechanical properties evaluation through correlation between different techniques and factor analysis, Ski. Res. Technol. 19 (2013). doi:10.1111/srt.12060.

[94] R. Grahame, P.J. Holt, The influence of ageing on the in vivo elasticity of human skin., Gerontologia. 15 (1969) 121–39. http://www.ncbi.nlm.nih.gov/pubmed/5772167.

[95] R.T. Tregear, Physical Functions of Skin, London: Academic Press, 1966.

[96] L.-C. Gerhardt, V. Strassle, A. Lenz, N.. Spencer, S. Derler, Influence of epidermal hydration on the friction of human skin against textiles, J. R. Soc. Interface. 5 (2008) 1317–1328. doi:10.1098/rsif.2008.0034.

[97] L. Pedersen, B. Hansen, G.B.E. Jemec, Mechanical properties of the skin: a comparison between two suction cup methods., Skin Res. Technol. 9 (2003) 111–115. doi:10.1034/j.1600-0846.2003.00021.x.

[98] G.E. Piérard, S. Piérard, P. Delvenne, C. Piérard-Franchimont, In Vivo Evaluation of the Skin Tensile Strength by the Suction Method: Pilot Study Coping with Hysteresis and Creep Extension, ISRN Dermatol. 2013 (2013) 1–7. doi:10.1155/2013/841217.

[99] H. Dobrev, In vivo study of skin mechanical properties in Raynaud's phenomenon, Ski. Res. Technol. 13 (2007) 91–94. doi:10.1111/j.1600-0846.2007.00197.x.

[100] H. Schade, Untersuchungen zur Organfunction des Bindegewebes, Zeitschrift Für Exp. Pathol. Und Ther. 11 (1912) 369–399. doi:10.1007/BF02622207.

[101] E. Kirk, S.A. Kvorning, Quantitative Measurements of the Elastic Properties of the Skin and Subcutaneous Tissue in Young and Old Individuals, J. Gerontol. 4 (1949) 273–284. doi:10.1093/geronj/4.4.273.

[102] J.E. Kirk, M. Chieffi, Variation with age in elasticity of skin and subcutaneous tissue

in human individuals., J. Gerontol. 17 (1962) 373–80. http://www.ncbi.nlm.nih.gov/pubmed/14032999.

[103] Y. Zheng, A.J. Crosby, S. Cai, Indentation of a stretched elastomer, J. Mech. Phys. Solids. 107 (2017) 145–159. doi:10.1016/j.jmps.2017.07.008.

[104] X. Zhang, J.F. Greenleaf, Estimation of tissue's elasticity with surface wave speed, J. Acoust. Soc. Am. 122 (2007) 2522. doi:10.1121/1.2785045.

[105] A. Tosti, G. Compagno, M.L. Fazzini, S. Villardita, a Ballistometer for the Study of the Plasto-Elastic Properties of Skin, J. Invest. Dermatol. 69 (1977) 315–317. doi:10.1111/1523-1747.ep12507753.

[106] C.G. Fthenakis, D.H. Maes, W.P. Smith, In vivo assessment of skin elasticity using ballistometry, J. Soc. Cosmet. Chem. 42 (1991) 211–222.

[107] T. Jee, K. Komvopoulos, In vitro measurement of the mechanical properties of skin by nano/microindentation methods, J. Biomech. 47 (2014) 1186–1192. doi:10.1016/j.jbiomech.2013.10.020.

[108] M.D. Ridge, V. Wright, The Directional Effects of Skin, J. Invest. Dermatol. 46 (1965) 341–346. doi:10.1038/jid.1966.54.

[109] Y. Lanir, Y.C. Fung, Two-dimensional mechanical properties of rabbit skin—I. Experimental system, J. Biomech. 7 (1974) 29–34. doi:10.1016/0021-9290(74)90067-0.

[110] G. Limbert, A mesostructurally-based anisotropic continuum model for biological soft tissues-Decoupled invariant formulation, J. Mech. Behav. Biomed. Mater. 4 (2011) 1637–1657. doi:10.1016/j.jmbbm.2011.07.016.

[111] E. Kuhl, K. Garikipati, E.M. Arruda, K. Grosh, Remodeling of biological tissue: Mechanically induced reorientation of a transversely isotropic chain network, J. Mech. Phys. Solids. 53 (2005) 1552–1573. doi:10.1016/j.jmps.2005.03.002.

[112] D.C. Schneider, T.M. Davidson, A.M. Nahum, In Vitro Biaxial Stress-Strain Response of Human Skin, Arch. Otolaryngol. - Head Neck Surg. 110 (1984) 329–333. doi:10.1001/archotol.1984.00800310053012.

[113] G.A. Holzapfel, R.W. Ogden, On planar biaxial tests for anisotropic nonlinearly elastic solids. A continuum mechanical framework, Math. Mech. Solids. 14 (2009) 474–489. doi:10.1177/1081286507084411.

[114] G.A. Holzapfel, R.W. Ogden, S. Sherifova, On fibre dispersion modelling of soft biological tissues: A review, Proc. R. Soc. A Math. Phys. Eng. Sci. 475 (2019). doi:10.1098/rspa.2018.0736.

[115] J.C. Dick, The tension and resistance to stretching of human skin and other membranes, with results from a series of normal and oedematous cases., J. Physiol. 112 (1951) 102–13. doi:10.1113/jphysiol.1951.sp004512.

[116] N. Boudeau, P. Malécot, A simplified analytical model for post-processing experimental results from tube bulging test: Theory, experimentations, simulations, Int. J. Mech. Sci. 65 (2012) 1–11. doi:10.1016/j.ijmecsci.2012.08.002.

[117] Y. Li, J.A. Nemes, A.A. Derdouri, Membrane inflation of polymeric materials: Experiments and finite element simulations, Polym. Eng. Sci. 41 (2001) 1399–1412. doi:10.1002/pen.10840.

[118] J.E. Bischoff, E.S. Drexler, A.J. Slifka, C.N. McCowan, Quantifying nonlinear anisotropic elastic material properties of biological tissue by use of membrane inflation, Comput. Methods Biomech. Biomed. Engin. 12 (2009) 353–369. doi:10.1080/10255840802609420.

[119] W.N. Song, F.A. Mirza, J. Vlachopoulos, Finite element analysis of inflation of an axisymmetric sheet of finite thickness, J. Rheol. (N. Y. N. Y). 35 (1991) 93–111. doi:10.1122/1.550211.

[120] Xing Liang, S.A. Boppart, Biomechanical Properties of In Vivo Human Skin From Dynamic Optical Coherence Elastography, IEEE Trans. Biomed. Eng. 57 (2010) 953–959. doi:10.1109/TBME.2009.2033464.

[121] F.M. Hendriks, D. Brokken, C.W.J. Oomens, F.P.T. Baaijens, Influence of hydration and experimental length scale on the mechanical response of human skin in vivo, using optical coherence tomography, Ski. Res. Technol. 10 (2004) 231–241. doi:10.1111/j.1600-0846.2004.00077.x.

[122] S.P. Kearney, A. Khan, Z. Dai, T.J. Royston, Dynamic viscoelastic models of human

skin using optical elastography, Phys. Med. Biol. 60 (2015) 6975–6990. doi:10.1088/0031-9155/60/17/6975.

[123] S. Nesbitt, W. Scott, J. Macione, S. Kotha, Collagen Fibrils in Skin Orient in the Direction of Applied Uniaxial Load in Proportion to Stress while Exhibiting Differential Strains around Hair Follicles, Materials (Basel). 8 (2015) 1841–1857. doi:10.3390/ma8041841.

[124] M.G. Dunn, F.H. Silver, Viscoelastic behavior of human connective tissues: Relative contribution of viscous and elastic components, Connect. Tissue Res. 12 (1983) 59–70. doi:10.3109/03008208309005612.

[125] Y.C. Fung, Elasticity of soft tissues in simple elongation., Am. J. Physiol. 213 (1967) 1532–44. doi:10.1152/ajplegacy.1967.213.6.1532.

[126] D.R. Veronda, R.A. Westmann, Mechanical characterization of skin-Finite deformations, J. Biomech. 3 (1970). doi:10.1016/0021-9290(70)90055-2.

[127] K. Levi, R.J. Weber, J.Q. Do, R.H. Dauskardt, Drying stress and damage processes in human stratum corneum, Int. J. Cosmet. Sci. 32 (2010) 276–293. doi:10.1111/j.1468-2494.2009.00557.x.

[128] Y.S. Papir, K.-H. Hsu, R.H. Wildnauer, The mechanical properties of stratum corneumI. The effect of water and ambient temperature on the tensile properties of newborn rat stratum corneum, Biochim. Biophys. Acta - Gen. Subj. 399 (1975) 170–180. doi:10.1016/0304-4165(75)90223-8.

[129] M.S. Christensen, C.W. Hargens, S. Nacht, E.H. Gans, Viscoelastic properties of intact human skin: instrumentation, hydration effects, and the contribution of the stratum corneum, J. Invest. Dermatol. 69 (1977) 282–286. doi:10.1111/1523-1747.ep12507500.

[130] D.C. Salter, H.C. McArthur, J.E. Crosse, A.D. Dickens, Skin mechanics measured in vivo using torsion: a new and accurate model more sensitive to age, sex and moisturizing treatment, Int. J. Cosmet. Sci. 15 (1993) 200–218. doi:10.1111/j.1467-2494.1993.tb00075.x.

[131] F. Auriol, L. Vaillant, L. Machet, S. Diridollou, G. Lorette, Effects of short-time hydration on skin extensibility., Acta Derm. Venereol. 73 (1993) 344–7.

http://www.ncbi.nlm.nih.gov/pubmed/7904398.

[132] M. Ottenio, D. Tran, A. Ní Annaidh, M.D. Gilchrist, K. Bruyère, Strain rate and anisotropy effects on the tensile failure characteristics of human skin, J. Mech. Behav. Biomed. Mater. 41 (2015) 241–250. doi:10.1016/j.jmbbm.2014.10.006.

[133] Z. Liu, K. Yeung, The Preconditioning and Stress Relaxation of Skin Tissue, J. Biomed. Pharm. Eng. 1 (2008) 22–28. doi:10.1007/s00238-011-0671-1.

[134] M.J. Muñoz, J.A. Bea, J.F. Rodríguez, I. Ochoa, J. Grasa, A. Pérez del Palomar, P. Zaragoza, R. Osta, M. Doblaré, An experimental study of the mouse skin behaviour: Damage and inelastic aspects, J. Biomech. 41 (2008) 93–99. doi:10.1016/j.jbiomech.2007.07.013.

[135] A. Wahlsten, M. Pensalfini, A. Stracuzzi, G. Restivo, R. Hopf, E. Mazza, On the compressibility and poroelasticity of human and murine skin, Biomech. Model. Mechanobiol. 18 (2019) 1079–1093. doi:10.1007/s10237-019-01129-1.

[136] K. Biniek, K. Levi, R.H. Dauskardt, Solar UV radiation reduces the barrier function of human skin, Proc. Natl. Acad. Sci. 109 (2012) 17111–17116. doi:10.1073/pnas.1206851109.

[137] P.A.L.S. Martins, R.M.N. Jorge, A.J.M. Ferreira, A Comparative Study of Several Material Models for Prediction of Hyperelastic Properties: Application to Silicone-Rubber and Soft Tissues, Strain. 42 (2006) 135–147. doi:doi:10.1111/j.1475-1305.2006.00257.x.

[138] R.W. Ogden, Large Deformation Isotropic Elasticity - On the Correlation of Theory and Experiment for Incompressible Rubberlike Solids, Proc. R. Soc. A Math. Phys. Eng. Sci. 326 (1972) 565–584. doi:10.1098/rspa.1972.0026.

[139] M. Mooney, A Theory of Large Elastic Deformation, J. Appl. Phys. 11 (1940) 582–592. doi:10.1063/1.1712836.

[140] A. Ní Annaidh, K. Bruyère, M. Destrade, M.D. Gilchrist, C. Maurini, M. Otténio, G. Saccomandi, Automated Estimation of Collagen Fibre Dispersion in the Dermis and its Contribution to the Anisotropic Behaviour of Skin, Ann. Biomed. Eng. 40 (2012) 1666–1678. doi:10.1007/s10439-012-0542-3.

[141] G.A. Holzapfel, T.C. Gasser, R.W. Ogden, A new constitutive framework for arterial wall mechanics and a comparative study of material models, J. Elast. 61 (2000) 1–48. doi:10.1023/A:1010835316564.

[142] G.A. Holzapfel, Nonlinear Solid Mechanics: a Continuum Approach for Engineering, John Wiley & Sons, 2000.

[143] E.M. Arruda, M.C. Boyce, A three-dimensional constitutive model for the large strech behavior fo rubber elastic materials, J Mech Phys Solids. 41 (1993) 389–412. doi:10.1016/j.commatsci.2011.10.026.

[144] J.E. Bischoff, E.M. Arruda, K. Grosh, Finite element modeling of human skin using an isotropic, nonlinear elastic constitutive model, J. Biomech. 33 (2000) 645–652. doi:10.1016/S0021-9290(00)00018-X.

[145] S.M. Belkoff, R.C. Haut, A structural model used to evaluate the changing microstructure of maturing rat skin, J. Biomech. 24 (1991) 711–720. doi:10.1016/0021-9290(91)90335-K.

[146] C.W. Gunner, W.C. Hutton, T.E. Burlin, The mechanical properties of skin in vivo—a portable hand-held extensometer, Br. J. Dermatol. 100 (1979) 161–163. doi:10.1111/j.1365-2133.1979.tb05555.x.

[147] J.E. Bischoff, E.M. Arruda, K. Grosh, A rheological network model for the continuum anisotropic and viscoelastic behavior of soft tissue, Biomech. Model. Mechanobiol. 3 (2004) 56–65. doi:10.1007/s10237-004-0049-4.

[148] Q. Ma, H. Cheng, K.I. Jang, H. Luan, K.C. Hwang, J.A. Rogers, Y. Huang, Y. Zhang, A nonlinear mechanics model of bio-inspired hierarchical lattice materials consisting of horseshoe microstructures, J. Mech. Phys. Solids. 90 (2016) 179–202. doi:10.1016/j.jmps.2016.02.012.

[149] J.A. Weiss, B.N. Maker, S. Govindjee, Finite element implementation of incompressible, transversely isotropic hyperelasticity, Comput. Methods Appl. Mech. Eng. 135 (1996) 107–128. doi:10.1016/0045-7825(96)01035-3.

[150] S.E. Szczesny, D.M. Elliott, Interfibrillar shear stress is the loading mechanism of collagen fibrils in tendon, Acta Biomater. 10 (2014) 2582–2590. doi:10.1016/j.actbio.2014.01.032.

[151] Y. Gao, A.M. Waas, J.A. Faulkner, T.Y. Kostrominova, A.S. Wineman, Micromechanical modeling of the epimysium of the skeletal muscles, J. Biomech. 41 (2008) 1–10. doi:10.1016/j.jbiomech.2007.08.008.

[152] X.Q. Peng, Z.Y. Guo, B. Moran, An Anisotropic Hyperelastic Constitutive Model With Fiber-Matrix Shear Interaction for the Human Annulus Fibrosus, J. Appl. Mech. 73 (2006) 815. doi:10.1115/1.2069987.

[153] J. Lu, L. Zhang, Physically motivated invariant formulation for transversely isotropic hyperelasticity, 42 (2005) 6015–6031. doi:10.1016/j.ijsolstr.2005.04.014.

[154] Y. Fujita, D.R. Wagner, A.A. Biviji, N.A. Duncan, J.C. Lotz, Anisotropic shear behavior of the annulus fibrosus: Effect of harvest site and tissue prestrain, Med. Eng. Phys. 22 (2000) 349–357. doi:10.1016/S1350-4533(00)00053-9.

[155] G.A. Holzapfel, R.W. Ogden, On planar biaxial tests for anisotropic nonlinearly elastic solids. A continuum mechanical framework, Math. Mech. Solids. 14 (2009) 474–489. doi:10.1177/1081286507084411.

[156] A.N. Annaidh, M. Destrade, Tension Lines of the Skin, in: 2019: pp. 265–280. doi:10.1007/978-3-030-13279-8_9.

[157] G.A. Holzapfel, J.A. Niestrawska, R.W. Ogden, A.J. Reinisch, A.J. Schriefl, Modelling non-symmetric collagen fibre dispersion in arterial walls, J. R. Soc. Interface. 12 (2015) 20150188. doi:10.1098/rsif.2015.0188.

[158] Y. Lanir, Constitutive equations for fibrous connective tissues, J. Biomech. 16 (1983) 1–12. doi:10.1016/0021-9290(83)90041-6.

[159] O. Lokshin, Y. Lanir, Viscoelasticity and Preconditioning of Rat Skin Under Uniaxial Stretch: Microstructural Constitutive Characterization, J. Biomech. Eng. 131 (2009) 31009. doi:10.1115/1.3049479.

[160] R. Meijer, L.F. a. Douven, C.W.J. Oomens, Characterisation of Anisotropic and Non-linear Behaviour of Human Skin In Vivo., Comput. Methods Biomech. Biomed. Engin. 2 (1999) 13–27. doi:10.1080/10255849908907975.

[161] J.W.Y. Jor, M.P. Nash, P.M.F. Nielsen, P.J. Hunter, Estimating material parameters

of a structurally based constitutive relation for skin mechanics, Biomech. Model. Mechanobiol. 10 (2011) 767–778. doi:10.1007/s10237-010-0272-0.

[162] J.F.M. Manschot, A.J.M. Brakkee, The measurement and modelling of the mechanical properties of human skin in vivo—I. The measurement, J. Biomech. 19 (1986) 511–515. doi:10.1016/0021-9290(86)90124-7.

[163] T.K. Tonge, L.M. Voo, T.D. Nguyen, Full-field bulge test for planar anisotropic tissues: Part II-A thin shell method for determining material parameters and comparison of two distributed fiber modeling approaches, Acta Biomater. 9 (2013) 5926–5942. doi:10.1016/j.actbio.2012.11.034.

[164] A.D. Freed, D.R. Einstein, I. Vesely, Invariant formulation for dispersed transverse isotropy in aortic heart valves: An efficient means for modeling fiber splay, Biomech. Model. Mechanobiol. 4 (2005) 100–117. doi:10.1007/s10237-005-0069-8.

[165] N.J.B. Driessen, C.V.C. Bouten, F.P.T. Baaijens, A structural constitutive model for collagenous cardiovascular tissues incorporating the angular fiber distribution, J. Biomech. Eng. 127 (2005) 494–503. doi:10.1115/1.1894373.

[166] S. Federico, T.C. Gasser, Nonlinear elasticity of biological tissues with statistical fibre orientation, J. R. Soc. Interface. 7 (2010) 955–966. doi:10.1098/rsif.2009.0502.

[167] M.S. Sacks, Incorporation of experimentally-derived fiber orientation into a structural constitutive model for planar collagenous tissues., J. Biomech. Eng. 125 (2003) 280–7. doi:10.1115/1.1544508.

[168] A. V. Melnik, H. Borja Da Rocha, A. Goriely, On the modeling of fiber dispersion in fiber-reinforced elastic materials, Int. J. Non. Linear. Mech. 75 (2015) 92–106. doi:10.1016/j.ijnonlinmec.2014.10.006.

[169] T.C. Gasser, R.W. Ogden, G.A. Holzapfel, Hyperelastic modelling of arterial layers with distributed collagen fibre orientations, J. R. Soc. Interface. 3 (2006) 15–35. doi:10.1098/rsif.2005.0073.

[170] A. Buganza-Tepole, J.P. Steinberg, E. Kuhl, A.K. Gosain, Application of Finite Element Modeling to Optimize Flap Design with Tissue Expansion, Plast. Reconstr. Surg. 134 (2014) 785–792. doi:10.1097/PRS.0000000000000553.

[171] C. Flynn, M.B. Rubin, P. Nielsen, A model for the anisotropic response of fibrous soft tissues using six discrete fibre bundles, Int. J. Numer. Method. Biomed. Eng. 27 (2011) 1793–1811. doi:10.1002/cnm.1440.

[172] J.E. Bischoff, Reduced parameter formulation for incorporating fiber level viscoelasticity into tissue level biomechanical models, Ann. Biomed. Eng. 34 (2006) 1164–1172. doi:10.1007/s10439-006-9124-6.

[173] R.C. Haut, R.W. Little, A constitutive equation for collagen fibers, J. Biomech. 5 (1972) 423–430. doi:10.1016/0021-9290(72)90001-2.

[174] Y. Lanir, A structural theory for the homogeneous biaxial stress-strain relationships in flat collagenous tissues, J. Biomech. 12 (1979) 423–436. doi:10.1016/0021-9290(79)90027-7.

[175] B.D. Coleman, W. Noll, Foundations of Linear Viscoelasticity, Rev. Mod. Phys. 33 (1961) 239–249. doi:10.1103/RevModPhys.33.239.

[176] C. Truesdell, W. Noll, The Non-Linear Field Theories of Mechanics, Springer Berlin Heidelberg, Berlin, Heidelberg, 1992. doi:10.1007/978-3-662-13183-1.

[177] G. Limbert, J. Middleton, A transversely isotropic viscohyperelastic material Application to the modeling of biological soft connective tissues, Int. J. Solids Struct. 41 (2004) 4237–4260. doi:10.1016/j.ijsolstr.2004.02.057.

[178] R. Puxkandl, I. Zizak, O. Paris, J. Keckes, W. Tesch, S. Bernstorff, P. Purslow, P. Fratzl, Viscoelastic properties of collagen: synchrotron radiation investigations and structural model., Philos. Trans. R. Soc. Lond. B. Biol. Sci. 357 (2002) 191–197. doi:10.1098/rstb.2001.1033.

[179] J.S. Bergström, M.C. Boyce, Constitutive modeling of the time-dependent and cyclic loading of elastomers and application to soft biological tissues, Mech. Mater. 33 (2001) 523–530. doi:10.1016/S0167-6636(01)00070-9.

[180] C.M. Roland, Network Recovery from Uniaxial Extension: I. Elastic Equilibrium, Rubber Chem. Technol. 62 (1989) 863–879. doi:10.5254/1.3536280.

[181] Y.C. Fung, Biomechanics: Mechanical Properties of Living Tissues, Springer New

York, New York, NY, 1993. doi:10.1007/978-1-4757-2257-4.

[182] M.B. Rubin, S.R. Bodner, A three-dimensional nonlinear model for dissipative response of soft tissue, Int. J. Solids Struct. 39 (2002) 5081–5099. doi:10.1016/S0020-7683(02)00237-8.

[183] E. Mazza, O. Papes, M.B. Rubin, S.R. Bodner, N.S. Binur, Nonlinear elastic-viscoplastic constitutive equations for aging facial tissues, Biomech. Model. Mechanobiol. 4 (2005) 178–189. doi:10.1007/s10237-005-0074-y.

[184] M.B. Rubin, A. Attia, Calculation of hyperelastic response of finitely deformed elastic-viscoplastic materials, Int. J. Numer. Methods Eng. 39 (1996) 309–320. doi:10.1002/(SICI)1097-0207(19960130)39:2<309::AID-NME858>3.0.CO;2-B.

[185] C. Flynn, M.B. Rubin, An anisotropic discrete fiber model with dissipation for soft biological tissues, Mech. Mater. 68 (2014) 217–227. doi:10.1016/j.mechmat.2013.07.009.

[186] Y. Har-Shai, S.R. Bodner, D. Egozy-Golan, E.S. Lindenbaum, O. Ben-Izhak, V. Mitz, B. Hirshowitz, Mechanical Properties and Microstructure of the Superficial Musculoaponeurotic System, Plast. Reconstr. Surg. 98 (1996) 59–70. doi:10.1097/00006534-199607000-00009.

[187] G.G. Barbarino, M. Jabareen, E. Mazza, Experimental and numerical study on the mechanical behavior of the superficial layers of the face, Ski. Res. Technol. 17 (2011) 434–444. doi:10.1111/j.1600-0846.2011.00515.x.

[188] M. Hollenstein, M. Jabareen, M.B. Rubin, Modeling a smooth elastic-inelastic transition with a strongly objective numerical integrator needing no iteration, Comput. Mech. 52 (2013) 649–667. doi:10.1007/s00466-013-0838-7.

[189] P. Ciarletta, M. Ben Amar, A finite dissipative theory of temporary interfibrillar bridges in the extracellular matrix of ligaments and tendons, J. R. Soc. Interface. 6 (2009) 909–924. doi:10.1098/rsif.2008.0487.

[190] A.D. Drozdov, A model of cooperative relaxation in finite viscoelasticity of amorphous polymers, Int. J. Non. Linear. Mech. 35 (2000) 897–909. doi:10.1016/S0020-7462(99)00066-9.

[191] H. Eyring, Viscosity, Plasticity, and Diffusion as Examples of Absolute Reaction Rates, J. Chem. Phys. 4 (1936) 283–291. doi:10.1063/1.1749836.

[192] M.H. Wagner, J. Schaeffer, Constitutive equations from Gaussian slip-link network theories in polymer melt rheology, Rheol. Acta. 31 (1992) 22–31. doi:10.1007/BF00396464.

[193] A.N. Natali, P.G. Pavan, E.L. Carniel, C. Dorow, Viscoelastic Response of the Periodontal Ligament: An Experimental–Numerical Analysis, Connect. Tissue Res. 45 (2004) 222–230. doi:10.1080/03008200490885742.

[194] K.Y. Volokh, Modeling failure of soft anisotropic materials with application to arteries, J. Mech. Behav. Biomed. Mater. 4 (2011) 1582–1594. doi:10.1016/j.jmbbm.2011.01.002.

[195] W. Li, X.Y. Luo, An Invariant-Based Damage Model for Human and Animal Skins, Ann. Biomed. Eng. 44 (2016) 3109–3122. doi:10.1007/s10439-016-1603-9.

[196] H.L. Cox, The elasticity and strength of paper and other fibrous materials, Br. J. Appl. Phys. 3 (1952) 72–79. doi:10.1088/0508-3443/3/3/302.

[197] J. Wu, H. Yuan, L. Li, K. Fan, S. Qian, B. Li, Viscoelastic shear lag model to predict the micromechanical behavior of tendon under dynamic tensile loading, J. Theor. Biol. 437 (2018) 202–213. doi:10.1016/j.jtbi.2017.10.018.

[198] I. Jäger, P. Fratzl, Mineralized collagen fibrils: A mechanical model with a staggered arrangement of mineral particles, Biophys. J. 79 (2000) 1737–1746. doi:10.1016/S0006-3495(00)76426-5.

[199] M. Pensalfini, S. Duenwald-Kuehl, J. Kondratko-Mittnacht, R. Lakes, R. Vanderby, Evaluation of Global Load Sharing and Shear-Lag Models to Describe Mechanical Behavior in Partially Lacerated Tendons, J. Biomech. Eng. 136 (2014) 91006. doi:10.1115/1.4027714.

[200] M.J. Buehler, Atomistic and continuum modeling of mechanical properties of collagen: Elasticity, fracture, and self-assembly, J. Mater. Res. 21 (2006) 1947–1961. doi:10.1557/jmr.2006.0236.

[201] A. Gautieri, A. Russo, S. Vesentini, A. Redaelli, M.J. Buehler, Coarse-grained model of collagen molecules using an extended MARTINI force field, J. Chem. Theory Comput. 6 (2010) 1210–1218. doi:10.1021/ct100015v.

[202] W. Li, Modelling methods for In Vitro biomechanical properties of the skin: A review, Biomed. Eng. Lett. 5 (2015) 241–250. doi:10.1007/s13534-015-0201-3.

[203] T. Gibson, R.M. Kenedi, J.E. Craik, The mobile micro-architecture of dermal collagen: A bio-engineering study, Br. J. Surg. 52 (1965) 764–770. doi:10.1002/bjs.1800521017.

[204] R.T. Tregear, The mechanical properties of skin, J. Soc. Cosmet. Chem. 20 (1969) 467–477. doi:10.1.1.535.5457.

[205] J.F. Ribeiro, E.H.M. dos Anjos, M.L.S. Mello, B. de Campos Vidal, Skin Collagen Fiber Molecular Order: A Pattern of Distributional Fiber Orientation as Assessed by Optical Anisotropy and Image Analysis, PLoS One. 8 (2013) 5–7. doi:10.1371/journal.pone.0054724.

[206] A.G. Ferdman, I. V Yannas, Scattering of Light from Histologic Sections: A New Method for the Analysis of Connective Tissue, J. Invest. Dermatol. 100 (1993) 710–716. doi:10.1111/1523-1747.ep12472364.

[207] J. Diamant, A. Keller, E. Baer, M. Litt, R.G.C. Arridge, Collagen; Ultrastructure and Its Relation to Mechanical Properties as a Function of Ageing, Proc. R. Soc. B Biol. Sci. 180 (1972) 293–315. doi:10.1098/rspb.1972.0019.

[208] X. Markenscoff, I. V. Yannas, On the stress-strain relation for skin, J. Biomech. 12 (1979) 127–129. doi:10.1016/0021-9290(79)90151-9.

[209] J. Kastelic, I. Palley, E. Baer, A structural mechanical model for tendon crimping, J. Biomech. 13 (1980) 887–893. doi:10.1016/0021-9290(80)90177-3.

[210] M. Comninou, I. V. Yannas, Dependence of stress-strain nonlinearity of connective tissues on the geometry of collagen fibres, J. Biomech. 9 (1976) 427–433. doi:10.1016/0021-9290(76)90084-1.

[211] Y. Lanir, Structure-strength relations in mammalian tendon, Biophys. J. 24 (1978)

541–554. doi:10.1016/S0006-3495(78)85400-9.

[212] A.D. Freed, T.C. Doehring, Elastic model for crimped collagen fibrils., J. Biomech. Eng. 127 (2005) 587–93. doi:10.1115/1.1934145.

[213] F. Maceri, M. Marino, G. Vairo, A unified multiscale mechanical model for soft collagenous tissues with regular fiber arrangement, J. Biomech. 43 (2010) 355–363. doi:10.1016/j.jbiomech.2009.07.040.

[214] G.D. Weinstein, R.J. Boucek, Collagen and Elastin of Human Dermis**From the Divisions of Dermatology and Cardiology of the Department of Medicine, University of Miami School of Medicine and Howard Hughes Medical Institute, Miami, Florida.This investigation was supported in part by Gr, J. Invest. Dermatol. 35 (1960) 227–229. doi:10.1038/jid.1960.109.

[215] H. Oxlund, J. Manschot, A. Viidik, The role of elastin in the mechanical properties of skin, J. Biomech. 21 (1988) 213–218. doi:10.1016/0021-9290(88)90172-8.

[216] D.Q.A. Nguyen, T.S. Potokar, P. Price, An objective long-term evaluation of Integra (a dermal skin substitute) and split thickness skin grafts , in acute burns and reconstructive surgery, 36 (2010) 23–28. doi:10.1016/j.burns.2009.07.011.

[217] C.-S. Chu, A.T. McManus, N.P. Matylevich, C.W. Goodwin, B.A. Pruitt, Integra as a dermal replacement in a meshed composite skin graft in a rat model: a one-step operative procedure., J. Trauma. 52 (2002) 122–9. doi:11791062.

[218] N. Brusselaers, A. Pirayesh, H. Hoeksema, C.D. Richters, J. Verbelen, H. Beele, S.I. Blot, S. Monstrey, Skin Replacement in Burn Wounds, J. Trauma Inj. Infect. Crit. Care. 68 (2010) 490–501. doi:10.1097/TA.0b013e3181c9c074.

[219] S. Cadau, D. Rival, V. Andre-Frei, M. Chavan M, D. Fayol, M. Salducci, B. Brisson, F. Guillemot, New bioprinted skin, cosmetic in vitro model., J. Cosmet. Sci. 68 (2017) 85–90. http://www.ncbi.nlm.nih.gov/pubmed/29465388.

[220] K.N. Retting, C.M. O'Neill, D.L.G. N'Guyen, S.C. Presnell, Engineered three-dimensional skin tissues, arrays thereof, and methods of making the same, 2016. https://patents.google.com/patent/US20160122723A1/en.

[221] E.A. Sander, K.A. Lynch, S.T. Boyce, Development of the Mechanical Properties of Engineered Skin Substitutes After Grafting to Full-Thickness Wounds, J. Biomech. Eng. 136 (2014) 51008. doi:10.1115/1.4026290.

[222] J.R. Dias, P.L. Granja, P.J. Bártolo, Advances in electrospun skin substitutes, Prog. Mater. Sci. 84 (2016) 314–334. doi:10.1016/j.pmatsci.2016.09.006.

[223] C. Wang, X. Li, H. Hu, L. Zhang, Z. Huang, M. Lin, Z. Zhang, Z. Yin, B. Huang, H. Gong, S. Bhaskaran, Y. Gu, M. Makihata, Y. Guo, Y. Lei, Y. Chen, C. Wang, Y. Li, T. Zhang, Z. Chen, A.P. Pisano, L. Zhang, Q. Zhou, S. Xu, Monitoring of the central blood pressure waveform via a conformal ultrasonic device, Nat. Biomed. Eng. 2 (2018) 687–695. doi:10.1038/s41551-018-0287-x.

[224] J.T. Whitton, J.D. Everall, On the thickness of the epidermis, Br. J. Dermatol. 89 (1973).

[225] G. Limbert, Mathematical and computational modelling of skin biophysics: a review, Proc. R. Soc. A Math. Phys. Eng. Sci. 473 (2017). http://rspa.royalsocietypublishing.org/content/473/2203/20170257.abstract.

[226] O. Lokshin, Viscoelasticity and Preconditioning of Rat Skin Under Uniaxial Stretch: Microstructural Constitutive Characterization, J. Biomech. Eng. 131 (2009) 31009. doi:10.1115/1.3049479.

[227] A. Ní Annaidh, K. Bruyère, M. Destrade, M.D. Gilchrist, M. Otténio, Characterization of the anisotropic mechanical properties of excised human skin, J. Mech. Behav. Biomed. Mater. 5 (2012) 139–148. doi:10.1016/j.jmbbm.2011.08.016.

[228] C. Lees, J.F. Vincent, J.E. Hillerton, Poisson's ratio in skin., Biomed. Mater. Eng. 1 (1991) 19–23. http://www.ncbi.nlm.nih.gov/pubmed/1842507.

[229] Standard Test Methods for Vulcanized Rubber and Thermoplastic Elastomers—Tension, (n.d.). https://www.astm.org/Standards/D412.htm.

[230] J. Blaber, B. Adair, A. Antoniou, Ncorr: Open-Source 2D Digital Image Correlation Matlab Software, Exp. Mech. 55 (2015) 1105–1122. doi:10.1007/s11340-015-0009-1.

[231] R.H. Pritchard, P. Lava, D. Debruyne, E.M. Terentjev, Precise determination of the

Poisson ratio in soft materials with 2D digital image correlation, Soft Matter. 9 (2013) 6037–6045. doi:10.1039/c3sm50901j.

[232] X. Chen, O. Nadiarynkh, S. Plotnikov, P.J. Campagnola, Second harmonic generation microscopy for quantitative analysis of collagen fibrillar structure, Nat. Protoc. 7 (2012) 654–669. doi:10.1038/nprot.2012.009.

[233] M.A. Meyers, Dynamic Behavior of Materials, John Wiley & Sons, Inc., Hoboken, NJ, USA, 1994. doi:10.1002/9780470172278.

[234] O. Emile, A. Le Floch, F. Vollrath, Time-resolved torsional relaxation of spider draglines by an optical technique, Phys. Rev. Lett. 98 (2007). doi:10.1103/PhysRevLett.98.167402.

[235] Y. Yu, W. Yang, M.A. Meyers, Viscoelastic properties of α-keratin fibers in hair, Acta Biomater. 64 (2017) 15–28. doi:10.1016/j.actbio.2017.09.012.

[236] C.P. Waddington, Viscoelastic parameter determination from cyclic loading tests: application to adhesive flow in the microtensile testing of whisker crystals, J. Phys. D Appl. Phys. 5 (1972) 1531–1539. doi:10.1088/0022-3727/5/9/307.

[237] A.S. Caro-Bretelle, P. Ienny, R. Leger, S. Corn, I. Bazin, F. Bretelle, Constitutive modeling of stress softening and permanent set in a porcine skin tissue: Impact of the storage preservation, J. Biomech. 49 (2016) 2863–2869. doi:10.1016/j.jbiomech.2016.06.026.

[238] W. Van Paepegem, I. De Baere, E. Lamkanfi, J. Degrieck, Monitoring quasi-static and cyclic fatigue damage in fibre-reinforced plastics by Poisson ' s ratio evolution, Int. J. Fatigue. 32 (2010) 184–196. doi:10.1016/j.ijfatigue.2009.02.026.

[239] Y. Yu, W. Yang, B. Wang, M.A. Meyers, Structure and mechanical behavior of human hair, Mater. Sci. Eng. C. 73 (2017) 152–163. doi:10.1016/j.msec.2016.12.008.

[240] Y. Wang, R. Xu, W. He, Z. Yao, H. Li, J. Zhou, J. Tan, S. Yang, R. Zhan, G. Luo, J. Wu, Three-Dimensional Histological Structures of the Human Dermis, Tissue Eng. Part C Methods. 21 (2015) 932–944. doi:10.1089/ten.tec.2014.0578.

[241] V.R. Sherman, Y. Tang, S. Zhao, W. Yang, M.A. Meyers, Structural characterization

and viscoelastic constitutive modeling of skin, Acta Biomater. (2016). doi:10.1016/j.actbio.2017.02.011.

[242] M.J. Buehler, Nature designs tough collagen: explaining the nanostructure of collagen fibrils., Proc. Natl. Acad. Sci. U. S. A. 103 (2006) 12285–12290. doi:10.1073/pnas.0603216103.

[243] M.J. Buehler, Nanomechanics of collagen fibrils under varying cross-link densities: Atomistic and continuum studies, J. Mech. Behav. Biomed. Mater. 1 (2008) 59–67. doi:10.1016/j.jmbbm.2007.04.001.

[244] Z. Qin, M.J. Buehler, Flaw Tolerance of Nuclear Intermediate Filament Lamina under, ACS Nano. 5 (2011) 3034–3042.

[245] Z. Qin, M.J. Buehler, Impact tolerance in mussel thread networks by heterogeneous material distribution., Nat. Commun. 4 (2013) 2187. doi:10.1038/ncomms3187.

[246] W. Yang, V.R. Sherman, B. Gludovatz, M. Mackey, E.A. Zimmermann, E.H. Chang, E. Schaible, Z. Qin, M.J. Buehler, R.O. Ritchie, M.A. Meyers, Protective role of Arapaima gigas fish scales: Structure and mechanical behavior, Acta Biomater. 10 (2014) 3599–3614. doi:10.1016/j.actbio.2014.04.009.

[247] S. Plimpton, Fast Parallel Algorithms for Short-Range Molecular Dynamics, J. Comput. Phys. 117 (1995) 1–19. doi:10.1006/jcph.1995.1039.

[248] A. Stukowski, Visualization and analysis of atomistic simulation data with OVITO-the Open Visualization Tool, Model. Simul. Mater. Sci. Eng. 18 (2010) 0–7. doi:10.1088/0965-0393/18/1/015012.

[249] A. Gautieri, S. Vesentini, A. Redaelli, M.J. Buehler, Hierarchical structure and nanomechanics of collagen microfibrils from the atomistic scale up, Nano Lett. 11 (2011) 757–766. doi:10.1021/nl103943u.

[250] Z.L. Shen, M.R. Dodge, H. Kahn, R. Ballarini, S.J. Eppell, Stress-strain experiments on individual collagen fibrils, Biophys. J. 95 (2008) 3956–3963. doi:10.1529/biophysj.107.124602.

[251] A. Mauri, R. Hopf, A.E. Ehret, C.R. Picu, E. Mazza, A discrete network model to

represent the deformation behavior of human amnion, J. Mech. Behav. Biomed. Mater. 58 (2016) 45–56. doi:10.1016/j.jmbbm.2015.11.009.

[252] H.C. Wells, K.H. Sizeland, N. Kirby, A. Hawley, S. Mudie, R.G. Haverkamp, Acellular dermal matrix collagen responds to strain by intermolecular spacing contraction with fibril extension and rearrangement, J. Mech. Behav. Biomed. Mater. 79 (2018) 1–8. doi:10.1016/j.jmbbm.2017.12.009.

[253] B. Lynch, S. Bancelin, C. Bonod-Bidaud, J.B. Gueusquin, F. Ruggiero, M.C. Schanne-Klein, J.M. Allain, A novel microstructural interpretation for the biomechanics of mouse skin derived from multiscale characterization, Acta Biomater. 50 (2017) 302–311. doi:10.1016/j.actbio.2016.12.051.

[254] K. Bircher, M. Zündel, M. Pensalfini, A.E. Ehret, E. Mazza, Tear resistance of soft collagenous tissues, Nat. Commun. 10 (2019) 1–13. doi:10.1038/s41467-019-08723-y.

[255] U.G.K. Wegst, M.F. Ashby, The mechanical efficiency of natural materials, Philos. Mag. 84 (2004) 2167–2181. doi:10.1080/14786430410001680935.

[256] M.F. Ashby, L.J. Gibson, U. Wegst, R. Olive, The Mechanical Properties of Natural Materials. I. Material Property Charts, Proc. R. Soc. A Math. Phys. Eng. Sci. 450 (1995) 123–140. doi:10.1098/rspa.1995.0075.

[257] L. Rodrigues, EEMCO Guidance to the in vivo Assessment of Tensile Functional Properties of the Skin, Skin Pharmacol. Physiol. 14 (2001) 52–67. doi:10.1159/000056334.

[258] a M. Bauer, a P. Russell, R.E. Shadwick, Mechanical properties and morphological correlates of fragile skin in gekkonid lizards, J. Exp. Biol. 145 (1989) 79–102.

[259] P.P. Purslow, Fracture of non-linear biological materials: some observations from practice relevant to recent theory, J. Phys. D. Appl. Phys. 22 (1989) 854–856. doi:10.1088/0022-3727/22/6/026.

[260] J.F.V. Vincent, Structural Biomaterials, Revised ed, Princeton University Press, 1990. doi:9780691154008.

[261] K. Comley, N.A. Fleck, The toughness of adipose tissue: measurements and physical

basis, J. Biomech. 43 (2010) 1823–1826. doi:10.1016/j.jbiomech.2010.02.029.

[262] R.S. Rivlin, A.G. Thomas, Rupture of rubber. I. Characteristic energy for tearing, J. Polym. Sci. 10 (1953) 291–318. doi:10.1002/pol.1953.120100303.

[263] M. Hollenstein, A.E. Ehret, M. Itskov, E. Mazza, A novel experimental procedure based on pure shear testing of dermatome-cut samples applied to porcine skin, (2011) 651–661. doi:10.1007/s10237-010-0263-1.

[264] W. Yang, H. Quan, M.A. Meyers, R.O. Ritchie, Arapaima Fish Scale: One of the Toughest Flexible Biological Materials, SSRN Electron. J. (2019). doi:10.2139/ssrn.3401845.

[265] Z. Xu, J. Dela Cruz, C. Fthenakis, C. Saliou, A novel method to measure skin mechanical properties with three-dimensional digital image correlation, Ski. Res. Technol. 25 (2019) 60–67. doi:10.1111/srt.12596.

[266] S.L. Evans, C.A. Holt, Measuring the mechanical properties of human skin in vivo using digital image correlation and finite element modelling, J. Strain Anal. Eng. Des. 44 (2009) 337–345. doi:10.1243/03093247JSA488.

[267] I. Jandejsek, L. Gajdoš, M. Šperl, D. Vavřík, Analysis of standard fracture toughness test based on digital image correlation data, Eng. Fract. Mech. 182 (2017) 607–620. doi:10.1016/j.engfracmech.2017.05.045.

[268] S. Yoneyama, S. Arikawa, S. Kusayanagi, K. Hazumi, Evaluating J-integral from Displacement Fields Measured by Digital Image Correlation, Strain. 50 (2014) 147–160. doi:10.1111/str.12074.

[269] T.H. Becker, M. Mostafavi, R.B. Tait, T.J. Marrow, An approach to calculate the J-integral by digital image correlation displacement field measurement, Fatigue Fract. Eng. Mater. Struct. 35 (2012) 971–984. doi:10.1111/j.1460-2695.2012.01685.x.

[270] G.L.G. Gonzáles, J.A.O. González, J.T.P. Castro, J.L.F. Freire, A J-integral approach using digital image correlation for evaluating stress intensity factors in fatigue cracks with closure effects, Theor. Appl. Fract. Mech. 90 (2017) 14–21. doi:10.1016/j.tafmec.2017.02.008.

[271] S.M. Barhli, M. Mostafavi, A.F. Cinar, D. Hollis, T.J. Marrow, J-Integral Calculation by Finite Element Processing of Measured Full-Field Surface Displacements, Exp. Mech. 57 (2017) 997–1009. doi:10.1007/s11340-017-0275-1.

[272] F. Hou, S. Hong, Characterization of R-curve behavior of translaminar crack growth in cross-ply composite laminates using digital image correlation, Eng. Fract. Mech. 117 (2014) 51–70. doi:10.1016/j.engfracmech.2014.01.010.

[273] F. Caimmi, R. Calabrò, F. Briatico-Vangosa, C. Marano, M. Rink, J-Integral from Full Field Kinematic Data for Natural Rubber Compounds, Strain. 51 (2015) 343–356. doi:10.1111/str.12145.

[274] T. Zhang, S. Lin, H. Yuk, X. Zhao, Predicting fracture energies and crack-tip fields of soft tough materials, Extrem. Mech. Lett. 4 (2015) 1–8. doi:10.1016/j.eml.2015.07.007.

[275] S. Mzabi, D. Berghezan, S. Roux, F. Hild, C. Creton, A critical local energy release rate criterion for fatigue fracture of elastomers, J. Polym. Sci. Part B Polym. Phys. 49 (2011) 1518–1524. doi:10.1002/polb.22338.

[276] M. Liu, J. Guo, Z. Li, C.-Y. Hui, A.T. Zehnder, Crack propagation in a PVA dual-crosslink hydrogel: Crack tip fields measured using digital image correlation, Mech. Mater. 138 (2019) 103158. doi:10.1016/j.mechmat.2019.103158.

[277] K.N. Sawyers, R.S. Rivlin, The trousers test for rupture, Eng. Fract. Mech. 6 (1974) 557–562. doi:10.1016/0013-7944(74)90012-5.

[278] J. Lee, S. Lee, J. Chang, M.S. Thompson, D. Kang, S. Park, S. Park, A Novel Method for the Accurate Evaluation of Poisson ' s Ratio of Soft Polymer Materials, 2013 (2013).